



HAL
open science

Modélisation de la dissolution d'une phase solide (UO₂-ZrO₂-Zr) par une phase liquide (Fe) par une approche macroscopique diphasique

Shambhavi Nandan

► **To cite this version:**

Shambhavi Nandan. Modélisation de la dissolution d'une phase solide (UO₂-ZrO₂-Zr) par une phase liquide (Fe) par une approche macroscopique diphasique. Mécanique des fluides [physics.class-ph]. Aix-Marseille Université, 2019. Français. NNT : 2019AIXM0663 . tel-04393909

HAL Id: tel-04393909

<https://irsn.hal.science/tel-04393909>

Submitted on 15 Jan 2024

HAL is a multi-disciplinary open access archive for the deposit and dissemination of scientific research documents, whether they are published or not. The documents may come from teaching and research institutions in France or abroad, or from public or private research centers.

L'archive ouverte pluridisciplinaire **HAL**, est destinée au dépôt et à la diffusion de documents scientifiques de niveau recherche, publiés ou non, émanant des établissements d'enseignement et de recherche français ou étrangers, des laboratoires publics ou privés.

Aix-Marseille Université

Ecole Doctorale: Sciences pour l'Ingénieur: Mécanique, Physique, Micro et Nanoélectronique

UMR 7343 - IUSTI - Institut Universitaire des Systèmes Thermiques Industriels

Laboratoire d'accueil: Laboratoire d'Étude de la Physique du Corium (LEPC)

Institut: Institut de Radioprotection et de Sûreté Nucléaire (IRSN)

Thèse présentée pour obtenir le GRADE de DOCTEUR

Discipline: Doctorat en Sciences pour l'Ingénieur
Spécialité: Mécanique et Physique des Fluides

Par

Shambhavi Nandan

**Modélisation de la Dissolution d'une Phase Solide
($UO_2 - ZrO_2 - Zr$) par une Phase Liquide (Fe) par une
Approche Macroscopique Diphasique**

Sous la direction de Prof. Lounès TADRIST et Prof. Hervé COMBEAU

Soutenance le Décembre 20, 2019 devant le jury composé de:

Prof. Benoît GOYEAU	Centrale-Supélec	Rapporteur
Dr. Romain Le TELLIER	CEA Cadarache	Rapporteur
Dr. Florian FICHOT	IRSN Cadarache	Encadrant de thèse
Dr. Afaque SHAMS	NRG (Pays-Bas)	Examineur
Dr. Olga BUDENKOVA	CNRS / INP Grenoble	Examineur
Prof. Henri NGUYEN THI	Aix-Marseille Université / IM2NP	Président du jury
Prof. Hervé COMBEAU	Institut Jean Lamour	Directeur de thèse
Prof. Lounès TADRIST	Aix-Marseille Université / IUSTI	Directeur de thèse

University of Aix-Marseille

Doctoral School: Sciences for the Engineers: Mechanics, Physics, Micro &
Nano-electronics

UMR 7343 - IUSTI - University Institute of Industrial Thermal Systems

Laboratory of work: Laboratory for the Study of
Physics of Corium (LEPC)

Institute: Institute of Radioprotection &
Nuclear Safety (IRSN)

Thesis presented for the obtainment of DEGREE of the
DOCTORATE in

Discipline: Doctorate in Sciences for the Engineers
Speciality: Physics & Mechanics of Fluids

By

Shambhavi Nandan

**Modelling of Dissolution of a Solid Phase
($UO_2 - ZrO_2 - Zr$) by a Liquid Phase (Fe) with a
Two-Phase Macroscopic Approach**

Under the direction of Prof. Lounès TADRIST and Prof. Hervé
COMBEAU

Defense on December 20, 2019 in front of the jury composed of:

Prof. Benoît GOYEAU	Centrale-Supélec	Reviewer
Dr. Romain Le TELLIER	CEA Cadarache	Reviewer
Dr. Florian FICHOT	IRSN Cadarache	Supervisor of thesis
Dr. Afaque SHAMS	NRG (Netherlands)	Examiner
Dr. Olga BUDENKOVA	CNRS / INP Grenoble	Examiner
Prof. Henri NGUYEN THI	Aix-Marseille Université / IM2NP	President of jury
Prof. Hervé COMBEAU	Institut Jean Lamour	Director of thesis
Prof. Lounès TADRIST	Aix-Marseille Université / IUSTI	Director of thesis

*To my mother Archana Shukla, and father Rakesh Shukla.
They make life beautiful.*

Résumé

Pour la sûreté des réacteurs nucléaires en cas d'accident grave, l'un des problèmes à fort enjeu est la rétention du combustible nucléaire fondu, appelé corium, à l'intérieur de la cuve du réacteur (RPV). Une des façons de refroidir le corium dans le RPV est de refroidir la cuve par l'extérieur. Cette stratégie est appelée rétention du corium en cuve (IVR). En cas de stratégie IVR, on s'attend à ce que le bain de corium soit entouré d'une croûte oxyde qui sera en contact avec de l'acier fondu à la surface supérieure du bain et le long de la cuve. Il a été observé dans les essais CORDEB (financés par IRSN, CEA, EDF et AREVA), que cette croûte devient perméable, ce qui a un impact sur l'épaisseur de la couche d'acier fondu située au-dessus. Pour la stratégie IVR, une fine couche de métal au-dessus de la croûte peut conduire à un flux de chaleur excessif vers la paroi de cuve, conduisant à une rupture éventuelle de la cuve. Ce phénomène est communément appelé *focusing effect*.

Ce travail traite de l'étude de la dissolution d'une telle croûte afin d'estimer le temps pour que l'acier s'écoule à travers elle. D'un point de vue thermochimique, le corium est un mélange d' UO_2 , ZrO_2 et Zr . Les interactions chimiques dans le système quaternaire composé de U, Zr, Fe et O jouent un rôle important dans la stabilité (ou non) de la croûte. Une étude thermochimique faite dans le cadre de cette thèse montre ce système quaternaire peut être réduit à deux systèmes ternaires dans chaque phase : $(U, Zr) + O$ dans la phase oxyde et $(U, Zr) + Fe$ dans la phase métal, où les atomes Fe et O restent respectivement dans les phases métal et oxyde, et les atomes (U, Zr) sont transférés entre les phases, avec une proportion U/Zr approximativement constante.

De plus, il a été montré dans le présent travail que, dans ces systèmes ternaires dans chaque phase, les interactions chimiques entre la croûte et le liquide peuvent être modélisées comme la dissolution d'une zone poreuse diphasique binaire par un liquide. Par conséquent, un modèle macroscopique a été développé par prise de moyenne volumique des équations de transport –masse, espèces, quantité de mouvement, énergie –, sur un volume élémentaire représentatif (VER). Le système final d'équations différentielles a été fermé en déterminant plusieurs relations empiriques pour la diffusivité effective des espèces, les coefficients de transfert de masse, la perméabilité et la conductivité effective. D'abord, le modèle a été résolu numériquement pour étudier la progression de la dissolution dans un domaine $2D$ diphasique sans convection dans la phase métal ($v_m = 0$) avec plusieurs relations de fermeture pour les coefficients de transfert de masse. Cette étude a été faite pour déterminer la relation de fermeture la plus pertinente permettant de décrire la dissolution de la croûte telle qu'observées dans les essais CORDEB. Cette étude de sensibilité a révélé que, pour retrouver une microstructure similaire à celle observée sur les essais CORDEB, le temps caractéristique de diffusion effective doit être beaucoup plus petit que le temps de dissolution.

Après avoir choisi le modèle de fermeture approprié pour le coefficient de transfert de masse, le modèle macroscopique a été résolu pour les situations qui existeraient dans le cas d'une stratégie IVR et donc d'une importance significative. Dans un premier temps, le modèle mathématique est résolu pour le cas avec et sans convection thermosolutale dans un domaine 2D ayant une épaisseur égale de métal et de croûte, la croûte étant orientée verticalement. Par la suite, les résultats numériques avec uniquement la convection thermosolutale ont été obtenus pour un domaine 2D ayant une épaisseur de croûte bien inférieure au cas précédent. Ce cas particulier a été étudié en orientant la croûte à la fois dans le sens vertical et horizontal. Le cas d'une croûte horizontale correspond au cas de la convection de Rayleigh-Bénard et présente donc un intérêt particulier. À la fin du manuscrit, des conclusions générales ont été tirées concernant la faisabilité de l'approche macroscopique en deux phases adoptée dans la présente étude pour étudier la dissolution dans une croûte de corium pendant la stratégie IVR et d'autres questions théoriques liées à la modélisation de la dissolution ont discuté avec le résumé de quelques études complémentaires.

Abstract

With regards to the safety of the Nuclear Power Plants (NPP) in case of a severe nuclear accident, one of the main challenges associated is the retention of the molten nuclear fuel and reactor internals, called corium, within the Reactor Pressure Vessel (RPV). One of the ways of cooling corium within the RPV is by cooling the vessel from outside. This strategy is termed as In-Vessel Retention (IVR). In case of the In-Vessel Retention (IVR) strategy, it is expected that the corium pool will be surrounded by an oxide crust, which will be in contact with molten steel from top of the pool as well as from sides of the vessel. It has been observed in CORDEB experiments (funded by IRSN, CEA and EDF), that this crust becomes permeable, which has an impact on the thickness of molten steel layer, lying on top of it. With respect to the IVR strategy, a thin molten steel layer on top of the crust may lead to an excessive heat flux to the Reactor Pressure Vessel (RPV), resulting in a possible rupture or melt-through. Such phenomenon is commonly known as *focusing effect*.

The present work deals with the study of dissolution of such crust in order to estimate the time for molten steel to flow through the crust. Thermochemically, corium is a mixture of UO_2 , ZrO_2 and Zr . The quaternary chemical interaction between U , Zr , O species and Fe plays an important role in the stability (or not) of the crust. However, a thermochemical study done within the framework of the present thesis, shows that the quaternary system of U , Zr , Fe and O atoms, can be reduced to a ternary in each phase: $(U, Zr) + O$ in the oxide phase and $(U, Zr) + Fe$ in the metal phase, where Fe and O atoms remain in metal and oxide phases respectively, and (U, Zr) atoms as a whole participate in the mass transfer across the interface, having ratio of (U/Zr) atoms always constant.

Further, it has been shown in the present work that, in this ternary-in-each-phase system, chemical interactions between the crust and liquid (Fe) can be modeled as the dissolution of a binary two-phase porous region by a liquid. Consequently, an up-scaled model for binary mixture has been derived by volume averaging transport equations — Mass, Momentum, Species and Energy transport — over a Representative Elementary Volume (REV). The final system of Partial Differential Equations (PDEs) has been closed by deriving several empirical relations for effective species diffusivity, mass transfer coefficients, permeability and effective conductivity. At first the model has been solved numerically to study the progress of dissolution in a two-phase $2D$ domain without convection in the liquid-metal phase ($\mathbf{v}_m = 0$) with several closure relations of mass transfer coefficient. This study is done to identify the closure relation capable of accurately describing the dissolution in the crust by molten steel same as observed in the CORDEB experiments. This sensitivity analysis revealed that in order to reproduce the

microstructure similar to the one observed in CORDEB experiment, the characteristic time of effective diffusion has to be much less than that of dissolution.

After choosing the suitable closure model for mass transfer coefficient the macroscopic model has been solved for the situations that would exist in case of an IVR strategy and thus of significant importance. At first mathematical model is solved for the case with and without thermo-solutal convection in a $2D$ domain having equal thickness of metal and crust, with crust being oriented vertically. Afterwards the numerical results with only thermo-solutal convection have been obtained for a $2D$ domain having a crust thickness much less than the previous case. This particular case has been investigated by orienting crust both in vertical and horizontal direction. The case of a horizontal crust corresponds to the case of Rayleigh-Bénard convection and hence is of specific interest. At the end of the manuscript general conclusions have been drawn regarding the feasibility of the two-phase macroscopic approach adopted in the present study for studying the dissolution in a corium crust during the IVR strategy and further theoretical issues related to the modeling of the dissolution has been discussed along with the summary of some further studies.

Acknowledgements

First and foremost I would like to express my deepest gratitude to my thesis supervisor at IRSN, Dr. Florian Fichot. I thank him very much for choosing me as an ideal candidate for pursuing this PhD. Further I also like to acknowledge his relentless support in this work, which not only made me achieve all the goals of the thesis properly but also on time. Also, regular discussions with him enhanced my knowledge and understanding of the various subjects involved in the thesis.

I would also like to acknowledge the contributions of Dr. Fabien Duval for his guidance on *CALIF³S* software throughout the three years of my thesis. I am also thankful to Dr. Bruno Piar for his constant support on NUCLEA database and for motivating me to learn Python. I am very thankful to everyone in my lab LEPC at IRSN, as well, for providing me a very conducive environment to work and progress in my thesis.

I am grateful to my thesis directors Prof. Hervé Combeau and Prof. Lounés Tadrif for providing their insights in the various theoretical aspects of the thesis work. It definitely helped in the improving the quality of the work. My special thanks to Prof. Benoît Goyeau and Dr. Romain Le Tellier for accepting the offer of being the reviewers of my manuscript. Detailed reports from them has surely helped to enhance the quality of the manuscript. It also helped me to think about some very important questions related to the theoretical and experimental aspects of the work.

My gratitude to Dr. Olga Budenkova, Prof. Henri Nguyen Thi and Dr. Afaque Shams for taking out time to read my manuscript and accepting the offer of being the jury members in my PhD defense.

In the end I would like to thank all my friends who in one way or the other has always helped me during the hard times and provided me rocking company during the good times. My special thanks goes to: Saptarshi Bhattacharjee, Nitendra Singh (IRSN Cadarache), Utkarsh Bajpai (Delaware Univ. USA), Adithya, Alejandro Villarreal Larrauri, Ali Swaidan (Tractebel), Julie-Anne Zambaux (IRSN Cadarache) and Ignacio (CEA Saclay). Thanks and love to all my friends from various labs: Mathilde, Ankita, Tsvetoslav Pavlov, Pietro, Louis Viot (CEA Cadarache), Miloud, Ashkan, Miriam, Mirico, Anthony, Juliana Garcia (IRSN Cadarache), Linkai Wei (IRSN Cadarache), Adrien, Noe, Ronit Panda and Kasi (CEA Cadarache).

This list will be incomplete without mentioning names of some of the very good friends from my *alma mater*, the *University of Delhi*: Shifali Singh, Vaibhav Jaiswal (IRSN), Vaishnvi Tiwari, Savneet (CEA Saclay), Amreen, Lokesh Verma and Neeraj Kumar (Aix-Marseille Univ.). Thank you very much to all of you for being very good friends through thick and thin.

Contents

1	Introduction	1
1.1	Severe Accident in Nuclear Reactors	1
1.1.1	Brief History of PWRs	1
1.1.2	Basic Design of PWRs	2
1.1.3	Accident Initiating Events in Nuclear Reactors	6
1.1.4	Controlled Management of Severe Accident	9
1.1.5	Feasibility of In-Vessel Retention (IVR) strategy for Corium Coolability	11
1.1.6	Dissolution of the Crust Aggravating Focusing Effect . .	17
1.2	Scope of the Thesis	18
2	Experiments	19
2.1	CORDEB and CORDEB-2 Experiments	19
2.2	VITI-CORMET Experiments	22
2.3	Influence of Temperature and Oxidation Degree of the Crust .	25
2.4	Summary and Consequences for Modelling and Safety Studies .	27
3	Mathematical Modeling	28
3.1	Phenomenon of Dissolution	28
3.1.1	Thermodynamics of Dissolution	29
3.2	Past Numerical Studies For Dissolution of Multi-component Mixtures	31
3.3	Corium Crust Modeled As Two-Phase Mushy Zone	32
3.4	Volume Averaged Mathematical Model For Describing Dissolu- tion In Quaternary System (U, Zr, Fe, O)	33
3.4.1	Microscopic System of PDEs, Satisfying Conservation at Local Level	33
3.4.2	Thermochemical study for the Quaternary System (U, Zr, Fe, O)	37
3.4.3	Validity of Liquid-Oxide and Liquid-Metal Thermochem- ical Study for Solid-Oxide and Liquid-Metal (Crust- Molten Metal)	43
3.4.4	Reduction of Quaternary System (U, Zr, Fe, O) to a Ternary in each Phase	44
3.4.5	Summarized Microscopic PDEs for Ternary in each Phase System	52

3.4.6	Volume Averaging	53
3.4.7	Closed Form of Macroscopic Model	58
4	Simplified Thermochemical Model	71
4.1	Recollection of Thermochemical Study Conducted with NUCLEA Toolbox	72
4.1.1	Relation Between n_m^{Fe} , C_{ox} and C_{uz}	72
4.1.2	Derivation of a Simplified Model for the (U, Zr, Fe, O) System	74
4.1.3	Illustration of Fit to NUCLEA Thermochemical Calculations for Various Inventory Compositions	78
4.1.4	Range of Application of Fit model (Range of Data Fitted)	82
4.1.5	An Algorithm for Using Simplified Model For Fast Thermochemical Calculations of n_m^{Fe} , n_m^m , n_{ox}^O	83
5	Application to 0-D and 1-D Cases	84
5.1	Application to 0-D case	84
5.1.1	Calculations of Equilibrium Compositions n_{ox}^{Y*} and n_m^{Y*} from Simplified Thermochemical Model	85
5.1.2	Results for 0-D case	85
5.2	Application to 1-D case and Results	87
6	Topological Relations and Numerical Implementation	89
6.1	Topological Relations	89
6.2	Numerical Implementation	91
7	Model Demonstration for Dissolution Calculations	97
7.1	Geometry 1	99
7.1.1	Without Convection ($\mathbf{v}_m = 0$)	99
7.2	Geometry 2	110
7.2.1	Without Convection ($\mathbf{v}_m = 0$)	110
7.2.2	With Convection ($\mathbf{v}_m \neq 0$)	112
8	Results for Reactor Specific Cases	116
8.1	Metal Layer Dimensions Corresponding to N^{Fe}	116
8.2	Equilibrium Mole fractions	118
8.3	Initial Mole Fractions for n_{ox}^O and n_m^{Fe}	118
8.4	Material Properties for Metal and Oxide	119
8.5	Thermo-solutal Convection	119
8.6	Cases	120
8.6.1	Case 1: Square Domain with Vertical Crust: No Convection ($\mathbf{v}_m = 0$)	120
8.6.2	Case 2: Square Domain with Vertical Crust: Thermo-Solutal Convection	122
8.6.3	Case 3: Rectangular Geometry with Vertical Crust: Thermo-Solutal Convection	125
8.6.4	Case 4: Rayleigh-Bénard Convection	128

9	Conclusions	132
	Annexes	136
A	Discretization of Diffusion Form of Macroscopic Model	137
A.1	System of PDEs	137
A.2	Discretization Methodology	139
A.2.1	Discretized form (Semi-implicit and coupled) for an Internal Finite Volume cell	140
A.3	Numerical Resolution	142
B	Numerical Resolution of Coupled ODEs	143
C	Method of Volume Averaging	146
C.1	Volume Averaging	146
C.2	Theorems	147
C.2.1	Spatial Averaging Theorem	147
C.2.2	General Leibniz Rule	147
D	Discrete Maximum Principle	149
E	Test Cases	153
E.1	Validation of Implemented Navier-Stokes Equation for Partially Porous Domains in case of Forced Convection	153
E.2	Validation Against Solutal Natural Convection in a Uniform Porous Medium	157
F	Different B.C. for Oxygen Atoms	161

List of Figures

1.1	Outline of a typical PWR [113]	3
1.2	A Mitsubishi PWR fuel assembly design [88].	5
1.3	Coolant behavior during cold leg small-break LOCA with Steam-Generator depressurization in a PWR [110]	7
1.4	The Three Mile Island (TMI) reactor 2 after the meltdown. 1) Core inlet A. 2) Core inlet B. 3) Cavity. 4) Core debris. 5) Crust. 6) Previously molten material. 7) Lower plenum debris. 8) Region depleted in Uranium. 9) Ablated in-core instrument guide. 10) Hole in baffle plate. 11) Coating of previously molten material on bypass region interior surfaces. 12) Upper grid damaged top plate. [27]	9
1.5	Severe accident phenomenology and identification of leakage paths to the environment. [107]	10
1.6	Outline of IVR [103]	12
1.7	Position of metal layer in the beginning [36]	13
1.8	Position of metal layer in the long term [36]	13
1.9	Phase interaction zone [36]	14
1.10	Three layer stratified system [36]	14
1.11	Modes of heat transfer in corium. [103]	16
2.1	CORDEB experiment setup. 1 – inductor; 2 – pipes of crucible sections; 3 – multi-section water-cooled bottom calorimeter; 4 – quartz tube; 5 – water-cooled electro- magnetic shield; 6 – water-cooled furnace cover; 7 – port for steel addition, sampling and steel layer temperature measurement by the W-Re thermocouples; 8 – quartz window in the pyrometer shaft; 9 – pyrometer; 10 – video camera; 11 – cooling water in and out; 12 – gas in and out; 13 – oxidic part of corium pool; 14 – metallic part of corium pool; 15 – oxidic crust; 16 – surface steel layer [4] . . .	20
2.2	Post test ingot structure of CD-02 experiment. [4]	21
2.3	Micro-structure of the crust after dissolution, showing oxide crust in Grey and molten steel channels in Black. [4]	22
2.4	Extracted from [4]	23
2.5	Illustration of the molten steel interaction with oxidic crust and oxidic pool. [4]	24
2.6	VITI-CORMET experimental setup. [87]	25

2.7	VITI-CORMET visualization of the interaction zone and dissolution patterns. Solid oxide in Light Grey and Liquid metal channels in Black.[87]	26
2.8	Volume fraction of metal within the oxide phase as a function of Oxygen mole fraction. Dark Grey represents oxide and light grey metal. [4]	26
3.1	A typical binary isomorphous phase diagram (T-C) shown with an equivalent free energy Vs. composition (G-C) diagram at T_0	29
3.2	Growth of liquid phase out of the solid phase	30
3.3	A two phase liquid metal and solid oxide crust with zoomed in Representative Elementary Volume (REV).	34
3.4	NUCLEA Toolbox API for calculating the thermodynamic equilibrium	38
3.5	NUCLEA-17_1 data in the temperature range of existence of two immiscible liquid phases (2900 K - 3100 K) for $C_{uz} = 1.0$ and $C_{ox} = 0.3$	40
3.6	Mole fraction of O in metal phase Vs. Moles of Iron (n_m^O Vs. N^{Fe}) for various inventory compositions (C_{uz}), and degree of oxidation of Zr (C_{ox})	41
3.7	U/Zr molar ratio in oxide phase Vs. Moles of Iron ($\frac{(U/Zr)_{ox}}{C_{uz}}$ Vs. N^{Fe}) for various inventory compositions (C_{uz}) and degree of oxidation of Zr (C_{ox})	42
3.8	U/Zr molar ratio in metal phase Vs. Moles of Iron ($\frac{(U/Zr)_m}{C_{uz}}$ Vs. N^{Fe}) for various inventory compositions (C_{uz}) and degree of oxidation of Zr (C_{ox})	42
3.9	Validity of NUCLEA_17-1 liquid-metal and liquid-oxide thermochemical study for liquid-metal and solid-oxide (crust). Inventory is: $C_{uz} = 1.0$ and $C_{ox} = 0.3$	43
3.10	Summarized microscopic PDEs for ternary in each phase model	52
4.1	Dependence of Fe molar fraction in metal (n_m^{Fe}) on C_{uz}	72
4.2	Dependence of Fe molar fraction in metal (n_m^{Fe}) on C_{ox}	73
4.3	Inventory: $C_{uz} = 1.0$ and $C_{ox} = 0.3$ ($m = 0.0948$)	79
4.4	Inventory: $C_{uz} = 1.0$ and $C_{ox} = 0.6$ ($m = 0.0446$)	79
4.5	Inventory: $C_{uz} = 1.45$ and $C_{ox} = 0.3$ ($m = 0.07176$)	80
4.6	Inventory: $C_{uz} = 1.45$ and $C_{ox} = 0.6$ ($m = 0.034$)	80
4.7	Range of data fitted, shown in (U, Zr, O) form	82
4.8	Range of data fitted, shown in $(U - Zr, Fe, O)$ form	82
4.9	An algorithm to calculate the thermochemical parameters with derived simplified model	83
5.1	Results for 0-D study performed with ODE model, and its comparison with 1-D model	85
5.2	Conservation of total mass of O, Fe, UZ in both oxide and metal phases	86
5.3	Solid volume fraction profiles for 1-D study performed	87

5.4	Results for 1-D study performed	88
6.1	2D Periodic representative cells	91
7.1	Two geometric configurations studied	98
7.2	Computational domain and B.C. for case: 1	99
7.3	Dissolution profile calculated in crust by the model in the crust	100
7.4	Solid volume fraction distribution calculated in crust by the model in the crust at 2000 sec.	101
7.5	Dissolution profile calculated in crust by the model in the crust	101
7.6	Solid volume fraction distribution calculated in crust by the model in the crust at 5000 sec.	102
7.7	Dissolution profile calculated in crust by the model in the crust	102
7.8	Solid volume fraction distribution calculated in crust by the model in the crust at around 2500 sec.	103
7.9	Micro-structure of the crust after dissolution, showing oxide crust in Grey and molten steel channels in Black. CORDEB experiment [4]	103
7.10	Comparison between characteristic time of effective diffusion (τ_{De}) and time of dissolution in liquid phase (τ_{hm}) for Eq. (7.1)	104
7.11	Comparison between characteristic time of effective diffusion (τ_{De}) and time of dissolution in liquid phase (τ_{hm}) for Eq. (7.2)	105
7.12	Comparison between characteristic time of effective diffusion (τ_{De}) and time of dissolution in liquid phase (τ_{hm}) for Eq. (7.3)	105
7.13	Computational domain and B.C. for case: 2	107
7.14	Dissolution profile calculated in crust for <i>case 1</i> and <i>case 2</i> . .	108
7.15	Solid volume fraction distribution calculated in crust for <i>case 1</i> and <i>case 2</i> at around 2500 sec.	108
7.16	Computational domain	110
7.17	Dissolution profile calculated in crust by the model in the crust	111
7.18	Computational domain	112
7.19	Average velocity and solid volume fraction evolution in the crust	113
7.20	State of crust	114
7.21	Flow of molten metal through the crust and effect on the liquid mole fraction profile below the crust	115
8.1	Computational domains for $N^{Fe} = 2.0$	117
8.2	Computational domain for $N^{Fe} = 10.0$	117
8.3	Computational domain for <i>case: 1</i>	120
8.4	Results for dissolution and mole fractions profile evolution in the domain with time in <i>case: 1</i>	121
8.5	State of crust at the beginning and end of time steps in <i>case 1</i>	121
8.6	Computational domain for <i>case: 2</i>	122
8.7	Evolution of the velocity in the domain in <i>case 2</i>	123
8.8	State of crust at three different time steps in <i>case: 2</i>	123
8.9	Results for dissolution and mole fractions profile evolution in the domain with time in <i>case: 2</i>	124

8.10	Physical domains for <i>case: 3</i>	125
8.11	Evolution of the velocity in the domain in <i>case: 3</i>	126
8.12	Evolution of the temperature profile in the domain in <i>case: 3</i>	127
8.13	Evolution of liquid metal <i>channels</i> in the crust in <i>case: 3</i>	127
8.14	Results for dissolution and mole fractions profile evolution in the domain with time in <i>case: 3</i>	128
8.15	Computational domain for <i>case: 4</i>	128
8.16	Evolution of the velocity in the domain in <i>case: 4</i>	129
8.17	Evolution of the temperature profile in the domain in <i>case: 4</i>	130
8.18	Evolution of liquid metal <i>channels</i> in the crust in <i>case: 4</i>	131
8.19	Results for dissolution and mole fractions profile evolution in the domain with time in <i>case: 4</i>	131
A.1	Final system of PDEs	138
A.2	A typical Finite Volume (FV) 2D cell	139
C.1	Position vectors associated with Representative Elementary Volume (REV)	146
D.1	Control volumes representation	150
E.1	Schematic of a partial porous cavity	154
E.2	Effects of the permeability variations on the velocity field	155
E.3	Domain for porous cavity [34]	157
E.4	Liquid concentration contours for case: 1	158
E.5	Non-dimensional vertical velocities for case: 1	159
E.6	Non-dimensional horizontal velocities for case: 1	160
F.1	Results for dissolution profiles with different B.Cs. for <i>O</i> atoms	161
F.2	Results for mole fractions profile evolution in the domain with different B.Cs. for <i>O</i> atoms	162

List of Tables

3.1	Thermochemical study parameters	38
3.2	Global corium composition parameters	39
3.3	Complete macroscopic model	68
3.4	Simplified macroscopic model	70
4.1	m values for various C_{uz} and C_{ox}	78
4.2	m values calculated from Eq. (4.37)	81
8.1	Physical data	119
E.1	Parameters for the porous cavity problem	157

Nomenclature

A_{mox}	interfacial area between metal and oxide phase (m^2)
A_{me}	area of entrance and exit of metal phase (m^2)
A_{oxe}	area of entrance and exit of oxide phase (m^2)
T_{ox}	microscopic temperature of oxide phase (K)
T_m	microscopic temperature of metal phase (K)
v_m	microscopic velocity of metal phase ($msec^{-1}$)
H_{ox}	enthalpy of oxide phase (Jkg^{-1})
H_m	enthalpy of metal phase (Jkg^{-1})
q_{ox}	microscopic heat flux (oxide phase) (Wm^{-2})
q_m	microscopic heat flux (metal phase) (Wm^{-2})
J_{ox}^i	diffusion fluxes of $i = (U, Zr, Fe, O)$ species in oxide phase ($kgm^{-2}sec^{-1}$)
J_m^i	diffusion fluxes of $i = (U, Zr, Fe, O)$ species in metal phase ($kgm^{-2}sec^{-1}$)
w_{mox}	velocity of interface between metal and oxide phases ($msec^{-1}$)
C_{ox}^i	mass fractions of $i = (U, Zr, Fe, O)$ species in oxide phase (-)
C_m^i	mass fractions of $i = (U, Zr, Fe, O)$ species in metal phase (-)
\dot{Q}_{ox}	heat generation per unit mass in oxide phase (Wkg^{-1})
\dot{Q}_m	heat generation per unit mass in metal phase (Wkg^{-1})
P_m	Pressure of liquid phase (Pa)
U, Zr, Fe, O	atoms of Uranium, Zirconium, Iron/Steel and Oxygen (-)
N^i	moles of ($i = U, Zr, Fe, O$) (mol)
N_{ox}^i	moles of ($i = U, Zr, Fe, O$) in oxide phase (-)
N_m^i	moles of ($i = U, Zr, Fe, O$) in metal phase (-)
N^{tot}	total moles of species (mol)
N^{ox}	moles of oxide phase (mol)

N^m	moles of metal phase (<i>mol</i>)
n^m	mole fraction of metal phase (-)
n^{ox}	mole fraction of oxide phase (-)
n_{st}^O	stoichiometric mole fraction of <i>O</i> atoms in oxide phase (-)
n_{ox}^i	mole fraction of ($i = U, Zr, Fe, O$) in oxide phase (-)
n_m^i	mole fraction of ($i = U, Zr, Fe, O$) in metal phase (-)
$(U/Zr)_{ox}$	<i>U/Zr</i> molar ratio in oxide phase (-)
$(U/Zr)_m$	<i>U/Zr</i> molar ratio in metal phase (-)
M_U	molar mass of <i>U</i> ($kgmol^{-1}$)
M_{Zr}	molar mass of <i>Zr</i> ($kgmol^{-1}$)
D_{ox}^i	diffusivities of $i = U, Zr, Fe, O$ in oxide phase (m^2sec^{-1})
D_m^i	diffusivities of $i = U, Zr, Fe, O$ in metal phase (m^2sec^{-1})
D_e	effective diffusivity (m^2sec^{-1})
Y	specie name for <i>for free</i> (<i>U - Zr</i>) (-)
C_{ox}^Y	mass fraction of <i>free</i> (<i>U - Zr</i>) in oxide phase (-)
C_m^Y	mass fraction of <i>free</i> (<i>U - Zr</i>) in metal phase (-)
X	specie name for <i>fixed</i> (<i>U - Zr</i>) (-)
C_{ox}^X	mass fraction of <i>fixed</i> (<i>U - Zr</i>) in oxide phase (-)
V	averaging volume (m^3)
\dot{m}_{ox}	dissolution rate of oxide phase ($Kg^{-3}sec^{-1}$)
\tilde{v}_m	spatial deviation in velocity in oxide phase ($msec^{-1}$)
\tilde{C}_{ox}^Y	spatial deviation in mass fraction of <i>Y</i> in oxide phase (-)
\tilde{C}_m^Y	spatial deviation in mass fraction of <i>Y</i> in metal phase (-)
\tilde{P}_m	spatial deviation in pressure in metal phase (<i>Pa</i>)
\tilde{T}_{ox}	spatial deviation in temperature in oxide phase (<i>K</i>)
\tilde{T}_m	spatial deviation in temperature in metal phase (<i>K</i>)
\tilde{H}_m	spatial deviation in enthalpy in metal phase (Jkg^{-1})

\mathbf{K}	permeability tensor (m^2)
K	permeability scalar (m^2)
\mathbf{F}	2^{nd} order tensor representing Forchheimer correction (–)
h_{ox}	mass exchange/transfer coefficient in oxide phase (sec^{-1})
h_m	mass exchange/transfer coefficient in metal phase (sec^{-1})
\mathbf{D}_m^{fe}	diffusion-dispersion tensor in metal phase ($m^2 sec^{-1}$)
C_{ox}^{Y*}	equilibrium mass fraction of <i>free</i> ($U - Zr$) in oxide phase (–)
C_m^{Y*}	equilibrium mass fraction of <i>free</i> ($U - Zr$) in metal phase (–)
n_{ox}^{Y*}	equilibrium mole fraction of <i>free</i> ($U - Zr$) in oxide phase (–)
n_m^{Y*}	equilibrium mole fraction of <i>free</i> ($U - Zr$) in oxide phase (–)
n_{ox}^{O*}	equilibrium mole fraction of <i>O</i> in oxide phase (–)
n_m^{Fe*}	equilibrium mole fraction of <i>Fe</i> in metal phase (–)
$\langle C_{ox}^Y \rangle^{ox}$	macroscopic mass fraction of <i>free</i> ($U - Zr$) in oxide phase (–)
$\langle C_m^Y \rangle^m$	macroscopic mass fraction of <i>free</i> ($U - Zr$) in metal phase (–)
$\langle n_{ox}^Y \rangle^{ox}$	macroscopic mole fraction of <i>free</i> ($U - Zr$) in oxide phase (–)
$\langle n_m^Y \rangle^m$	macroscopic mole fraction of <i>free</i> ($U - Zr$) in metal phase (–)
$\langle \mathbf{v}_m \rangle^m$	macroscopic velocity of metal phase ($msec^{-1}$)
$\langle P_m \rangle^m$	macroscopic pressure of metal phase (Pa)
$\langle T \rangle$	macroscopic mixture temperature (K)
$\langle H \rangle$	$\varepsilon_{ox}\rho_{ox}\langle H_{ox} \rangle^m + \varepsilon_m\rho_m\langle H_m \rangle^m$ mass enthalpy of total mixture (Jkg^{-1})
m, b	fit parameters
$f(y)$	fit function
l_d	grain size in oxide (m)
L_f	enthalpy of fusion (Jkg^{-1})
C_{Pox}	heat capacity of oxide phase ($Jkg^{-1}K^{-1}$)

C_{Pm} heat capacity of metal phase ($Jkg^{-1}K^{-1}$)

Greek letters

ε_{ox} solid volume fraction of oxide phase (–)
 ε_m liquid volume fraction (porosity) of metal phase (–)
 ρ_{ox} microscopic density of oxide phase (kgm^{-3})
 ρ_m density of metal phase (kgm^{-3})
 $\langle \rho \rangle$ $\varepsilon_{ox}\rho_{ox} + \varepsilon_m\rho_m$ mixture density (kgm^{-3})
 Λ_{ox} thermal conductivity of oxide phase ($Wm^{-1}K^{-1}$)
 Λ_m thermal conductivity of metal phase ($Wm^{-1}K^{-1}$)
 μ_m dynamic viscosity of metal phase ($kgm^{-1}sec^{-1}$)
 Λ_{eff} effective conductivity tensor ($Wm^{-1}K^{-1}$)
 Λ_{eff} effective conductivity scalar ($Wm^{-1}K^{-1}$)
 τ_{hm} characteristic time of dissolution (sec)
 τ_{De} characteristic time of diffusion (sec)
 β_T thermal expansion coefficient (K^{-1})
 β_S solutal expansion coefficient (–)

Subscripts

ox oxide phase
 m metal phase

Superscripts

ox oxide phase
 m metal phase
 $*$ equilibrium values

Chapter 1

Introduction

Chapter 1

Introduction

1.1 Severe Accident in Nuclear Reactors

This section summarizes the severe accident, also known as core degradation accident in Light Water Reactors (LWR). Before stepping directly into the accidental scenarios associated to the LWRs, it is better to understand the basic design and functioning of the LWRs. Generally speaking, LWRs can be categorized into three main categories, namely:

1. Pressurized Water Reactors (PWRs).
2. Boiling Water Reactors (BWRs).
3. Supercritical Water Reactors (SCWR).

Since the present thesis has been carried out in the context of the PWRs, the further description will be constrained to the overview of the history, design and functioning of the Pressurized Water Reactors (PWRs).

1.1.1 Brief History of PWRs

After the discoveries of fission, moderation and of the theoretical possibility of a nuclear chain reaction, early experimental results, rapidly showed that natural uranium could only undergo a sustained chain reaction using graphite or heavy water as a moderator. While the world's first reactors (CP-1, X10 etc.) [5] were successfully reaching criticality, Uranium enrichment began to develop from theoretical concept to practical applications, in order to meet the goal of the Manhattan Project [70], to build a nuclear explosive.

In May 1944, the first grams of enriched Uranium ever produced, reached criticality in the low power (LOPO) [18] reactor at Los Alamos in US, which was used to estimate the critical mass of U^{235} to produce the atomic bomb. However, LOPO cannot be considered as the first light-water reactor because its fuel was not a solid Uranium compound clad with corrosion-resistant material, but was composed of Uranyl Sulfate salt dissolved in water. It is

however the first aqueous homogeneous reactor and the first reactor using enriched Uranium as fuel, and ordinary water as a moderator.

Later, following an idea of Alvin Weinberg, natural Uranium fuel elements were arranged in a lattice, in ordinary water at the top of the X10 [5] reactor to evaluate the neutron multiplication factor [56]. The purpose of this experiment was to determine the feasibility of a nuclear reactor using light water as a moderator and coolant, and cladded solid Uranium as fuel. The results showed that, with a lightly enriched uranium, criticality could be reached. This experiment was the first practical step toward the light-water reactor.

After World War II and with the availability of enriched uranium, new reactor concepts became feasible. In 1946, Eugene Wigner and Alvin Weinberg proposed and developed the concept of a reactor using enriched Uranium as a fuel, and light water as a moderator and coolant. This concept was proposed for a reactor whose purpose was to test the behavior of materials under neutron flux. This reactor was called the Material Testing Reactor (MTR)[72], and was built in Idaho at Idaho National Laboratory (INL), and reached criticality on March 31, 1952. For the design of this reactor, experiments were a necessity, so a mock-up of the MTR was built at Oak Ridge National Laboratory (ORNL), to assess the hydraulic performances of the primary circuit, and then to test its neutronic characteristics. This MTR mock-up, later called the Low Intensity Test Reactor (LITR), reached criticality on February 4, 1950 [40] and was the world's first light-water reactor.

Immediately after the end of World War II, the United States Navy started a program at ORNL, with the goal of using LWRs for nuclear propulsion for submarines. Consequently the program lead to the development of the first Pressurized Water Reactors (PWRs) [94] in the early 1950s, which in turn led to the successful deployment of the first nuclear submarine, the USS Nautilus (SSN-571). The Soviet Union also independently developed a version of the PWR in the late 1950s, under the name of VVER [100]. While functionally very similar to the American effort, it also has certain design distinctions from Western PWRs.

1.1.2 Basic Design of PWRs

The basic design layout the typical PWR is shown in Fig. 1.1. In a typical design concept of a commercial PWR, the following process occurs:

1. The core inside the reactor vessel creates heat.
2. Pressurized water in the primary coolant loop carries the heat to the steam generator.
3. Inside the steam generator, heat from the primary coolant loop vaporizes the water in a secondary loop, producing steam.

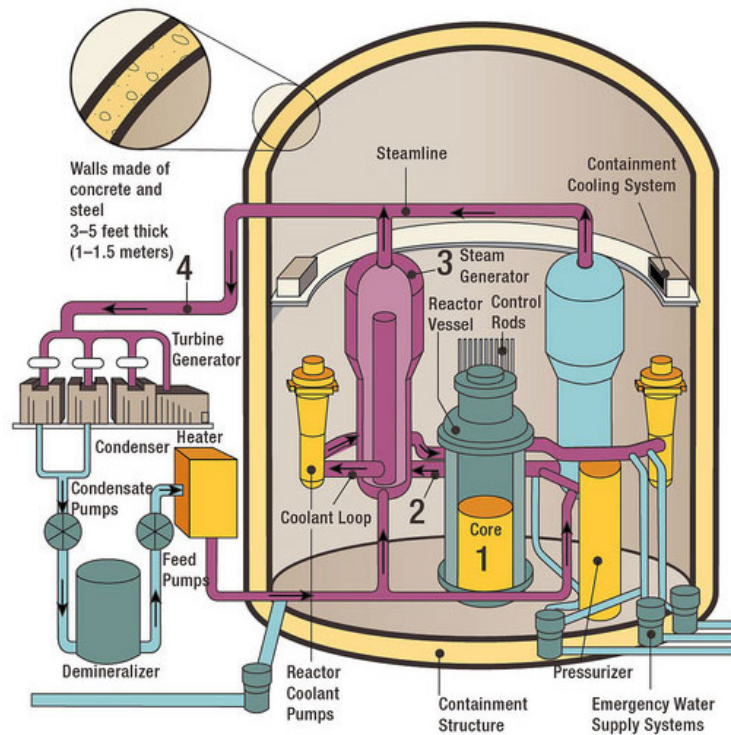


Figure 1.1: Outline of a typical PWR [113]

4. The steam-line directs the steam to the main turbine, causing it to turn the turbine generator, which produces electricity.

The unused steam is exhausted to the condenser, where it is condensed into water. The resulting water is pumped out of the condenser with a series of pumps, reheated, and pumped back to the steam generator. The reactor's core contains fuel assemblies that are cooled by water circulated using electrically powered pumps. These pumps and other operating systems in the plant receive their power from the electrical grid. If offsite power is lost, emergency cooling water is supplied by other pumps, which can be powered by onsite diesel generators.

1.1.2.1 Coolant

Light water is used as the primary coolant in a PWR. Water enters through the bottom of the reactor's core at about 548 K (275 °C) and is heated as it flows upwards through the reactor core to a temperature of about 588 K (315 °C). The water remains liquid despite the high temperature due to the high pressure in the primary coolant loop, usually around 155 bar (15.5 MPa 153 atm, 2,250 psi). In water, the critical point occurs at around 647 K (374 °C; 705 °F) and 22.064 MPa (3200 psi or 218 atm).

1.1.2.2 Pressurizer

Pressure in the primary circuit is maintained by a pressurizer, a separate vessel that is connected to the primary circuit and partially filled with water which is heated to the saturation temperature (boiling point) for the desired pressure by submerged electrical heaters. To achieve a pressure of 155 bars (15.5 MPa), the pressurizer temperature is maintained at 345 °C (653 °F), which gives a sub-cooling margin (the difference between the pressurizer temperature and the highest temperature in the reactor core) of 30 °C (54 °F). As 345 °C is the boiling point of water at 155 bar, the liquid water is at the edge of a phase change. Thermal transients in the reactor coolant system result in large swings in pressurizer liquid/steam volume, and total pressurizer volume is designed around absorbing these transients without uncovering the heaters or emptying the pressurizer. Pressure transients in the primary coolant system manifest as temperature transients in the pressurizer and are controlled through the use of automatic heaters and water spray, which raise and lower pressurizer temperature, respectively.

1.1.2.3 Pumps

The coolant is pumped around the primary circuit by powerful pumps. After picking up heat as it passes through the reactor core, the primary coolant transfers heat in a steam generator to water in a lower pressure secondary circuit, evaporating the secondary coolant to saturated steam — in most designs 6.2 MPa (60 atm, 900 psia), 275 °C (530 °F) — for use in the steam turbine. The cooled primary coolant is then returned to the reactor vessel to be re-heated.

1.1.2.4 Moderator

Pressurized water reactors, like all thermal reactor designs, require the fast fission neutrons to be slowed down (a process called moderation or thermalizing) in order to interact with the nuclear fuel and sustain the chain reaction. In PWRs the coolant water is used as a moderator [54] by letting the neutrons undergo multiple collisions with light hydrogen atoms in the water, losing speed in the process. This "moderating" of neutrons will happen more often when the water is more dense (more collisions will occur). The use of water as a moderator is an important safety feature of PWRs, as an increase in temperature may cause the water to expand, giving greater 'gaps' between the water molecules and reducing the probability of thermalisation—thereby reducing the extent to which neutrons are slowed down and hence reducing the reactivity in the reactor. Therefore, if reactivity increases beyond normal, the reduced moderation of neutrons will cause the chain reaction to slow down, producing less heat. This property, known as the negative temperature coefficient of reactivity [31], makes PWR reactors very stable. This process is referred to as *self-regulating*, i.e. the hotter the coolant becomes, the less reactive the plant becomes, shutting itself down slightly to compensate and vice versa.

1.1.2.5 Fuel

After enrichment, the Uranium dioxide (UO_2) powder is fired in a high-temperature, sintering furnace to create hard, ceramic pellets of enriched Uranium dioxide. The cylindrical pellets are then cladded inside a corrosion-resistant Zirconium metal alloy Zircaloy [81] which are backfilled with helium to aid heat conduction and detect leakages. Zircaloy is chosen because of its mechanical properties and its low neutron absorption cross section. The finished fuel rods are grouped in fuel assemblies, called fuel bundles, that are then used to build the core of the reactor. A typical PWR has fuel assemblies of 200 to 300 rods each, and a large reactor would have about 150~250 such assemblies with 80~100 tonnes of uranium in all. Generally, the fuel bundles consist of fuel rods bundled 14×14 to 17×17 [81]. The power produced by a PWR is around 900 to 1600 MWe (Mega Watt electrical). PWR fuel bundles are about 4 meters in length. Refuelings for most commercial PWRs is on an 18~24 month cycle. Approximately one third of the core is replaced each refueling, though some more modern refueling schemes may reduce refuel time to a few days and allow refueling to occur on a shorter intervals. A Mitsubishi PWR fuel assembly [88] is shown in Fig. 1.2.

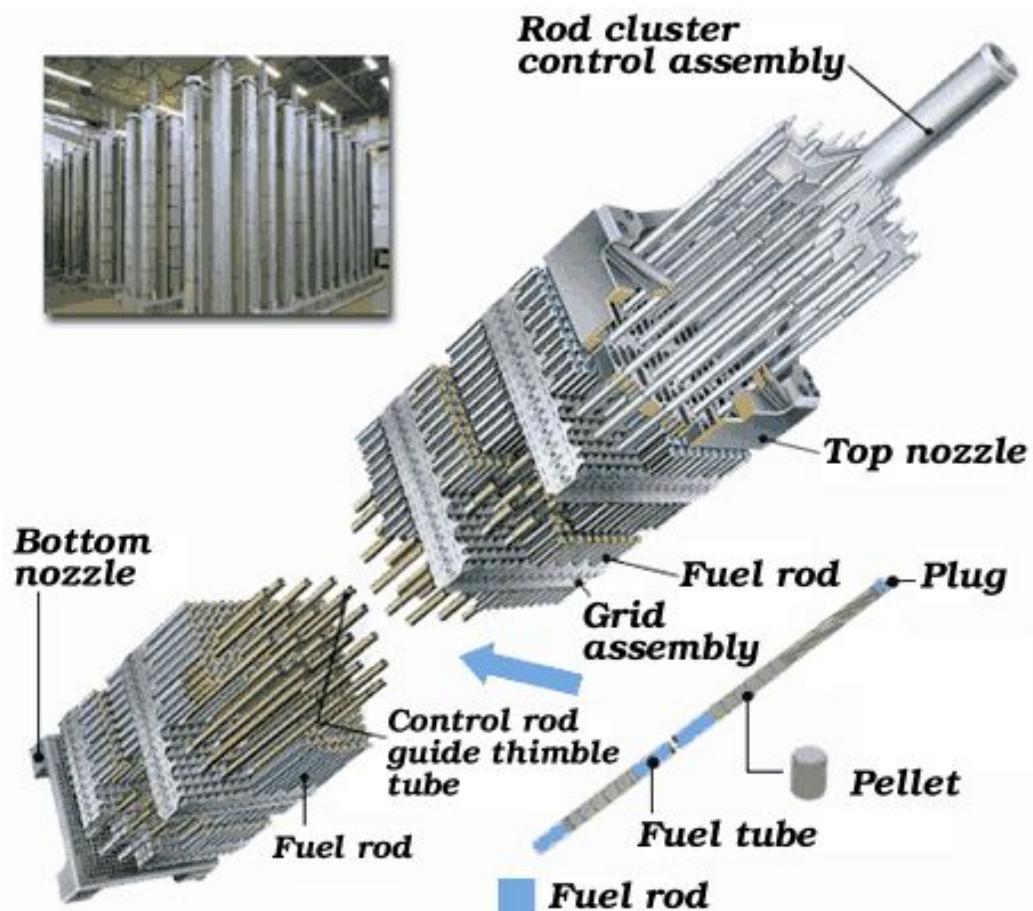


Figure 1.2: A Mitsubishi PWR fuel assembly design [88].

1.1.3 Accident Initiating Events in Nuclear Reactors

Initiating events can be classified according to their frequency of occurrence [51], or in other words their probability. They can either be considered as transients, or accidents. Accidents can be further subdivided into three main categories:

1. Design-Basis Accidents (DBAs): they are postulated accident that a nuclear facility must be designed and built to withstand without loss to the systems, structures, and components necessary to ensure public health and safety.
2. Beyond Design-Basis Accidents (BDBAs): they are accident sequences that are possible but were not fully considered in the design process because they were judged to be too unlikely to occur.
3. Severe Accidents (SAs): they are the type of accidents that may challenge the nuclear facility safety systems at a level much higher than expected.

The adopted analysis methodology for various events mainly differs in the use of diverging acceptance criteria and also in the level of conservatism in the analysis assumptions. A typical categorization for groups of initiating events was proposed by [50] and [51], are as follows:

1. Reactivity induced accidents.
2. Decrease of reactor coolant flow.
3. Increase of reactor coolant inventory.
4. Increase of heat removal by the secondary side.
5. Decrease of heat removal by the secondary side.
6. Loss of coolant accidents (LOCAs).
7. Anticipated transients without SCRAM.

Among all of the above causes of a nuclear accident, LOCA will be elaborated in detail further due to its relevance within the framework of this PhD.

1.1.3.1 Loss of Coolant Accident (LOCA) and Formation of Debris Bed

Due to the loss of coolant during a severe accident, the core gets uncovered and continues to heat up by the decay heat of the fission products in the fuel. As a result, this heating up will cause cooling water to evaporate in the core and it will decrease the water level in reactor pressure vessel. The time range for the core to dry-out varies depending on the accident development and the reactor design, yet the standard period of time is from two to few

hours. The decay of heat produces a continued heat up of the fuel rods and the other core materials. The fuel rod cladding is made of Zirconium material. In this situation, when the temperature is higher than 1200 °C, an exothermic reaction occurs between Zirconium and the super-heated steam, generating around 1.3 MJ per 1 kilogram of Zirconium. This reaction, which is a byproduct of the core heating and water evaporation, accelerates the temperature rise and the core degradation process. Besides that, large amounts of hydrogen are produced and may arrive to the reactor containment through the safety valves of the reactor cooling system or through a leak. Knowing that the reactor containment system is regarded as the 4th passive safety barrier (after the reactor vessel and primary circuit components as 3rd, fuel rods cladding as 2nd, and fuel pellets as 1st safety barrier), the failure of the containment must be avoided. Any failure of the containment would lead to catastrophic consequences in terms of radioactive release to the environment. Moreover, the presence of such high concentrations of hydrogen entering the containment can cause an explosive combustion of the gas mixture, eventually causing serious damage to the containment. Investigations of the oxidation of core metal and hydrogen generation processes can be found in details in [55] and [24].

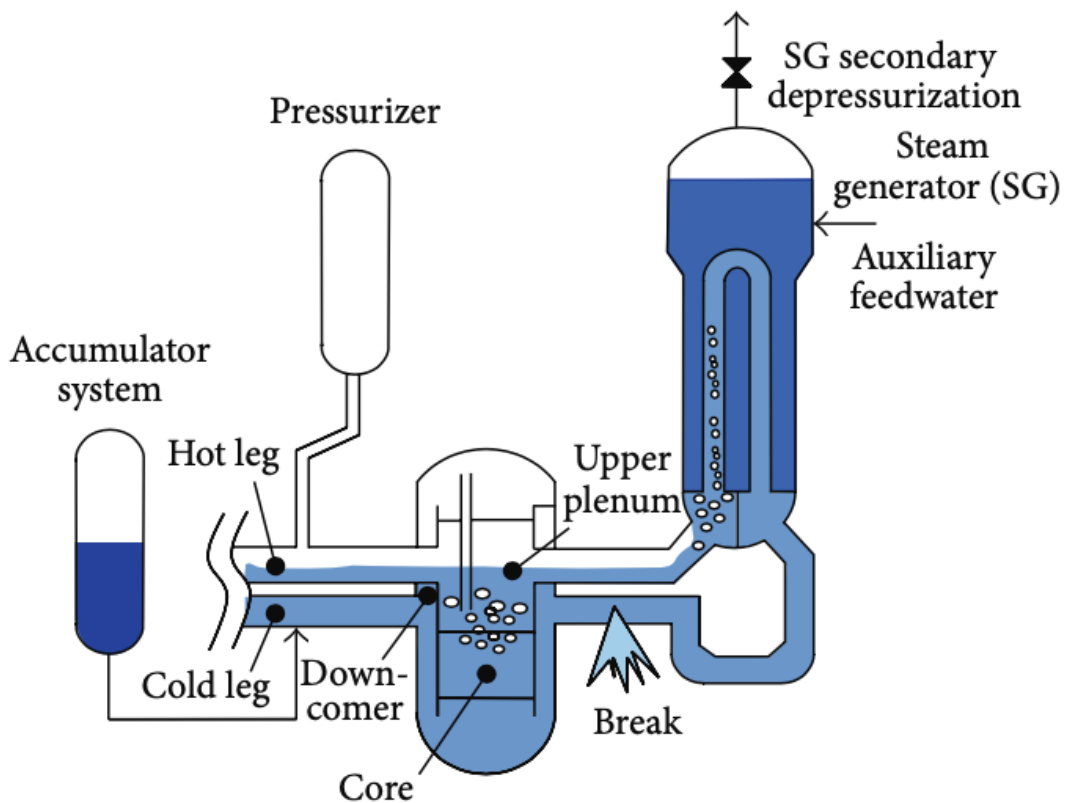


Figure 1.3: Coolant behavior during cold leg small-break LOCA with Steam-Generator depressurization in a PWR [110]

The Loss of Coolant Accident (LOCA), Fig. 1.3, is described by a water leakage in the primary circuit of a nuclear reactor core due to a small or large

pipe break. Once the leak is detected, the safety control rods, are inserted into the core to stop the fission chain reaction. The safety injection systems are then initiated to compensate the loss of coolant through the breach and to ensure the long-term removal of residual heat that continues to accumulate in the core due to the radioactive decay of materials.

Since the LOCA is a design-basis accident, the safety injection systems are designed such that the accident is mitigated without causing damage to the reactor core. However, if the loss of coolant is not compensated by the safety injection systems (as what happened recently in Fukushima Daichi accident), this incident leads to the depressurization in the primary circuit. If the pressure continues to decrease, and drops below the saturation pressure of water, water will then start to vaporize.

If this situation persists, the coolant in the primary circuit continues to vaporize and the reactor core gets uncovered. Due to accumulation of residual heat, the core deteriorates upon temperature increase and its safety is now under question.

Core heating and oxidation of the fuel cladding by the coolant vapor provoke core degradation and a total or partial melting of the hot fuel rods forming a pool of molten fuel and cladding material collectively called *corium*. This corium can relocate to the lower head of the reactor vessel compromising its local integrity which if failed would allow the corium to reach the concrete level which is the last confinement barrier. This will further provoke the danger of a radioactive release to the environment.

Such an accidental scenario was considered impossible in the early times but the severe accidents that occurred in the recent decades: Three Mile Island in USA 1979) and the Fukushima accident in Japan 2011, urged the need to develop awareness and investigate to acquire a deep knowledge of the phenomenology of severe accidents in order to develop and define the means of intervention to mitigate the progression of such events.

Severe accidents resulting from a LOCA (loss of coolant accident) have occurred at the Three Mile Island unit-2 (TMI-2) [80] in the USA (shown in Fig. 1.4), in 1979, and recently in Fukushima, Japan, in 2011, where 3 reactors were destroyed. The Chernobyl accident in 1984 had a different origin (increase of reactivity).

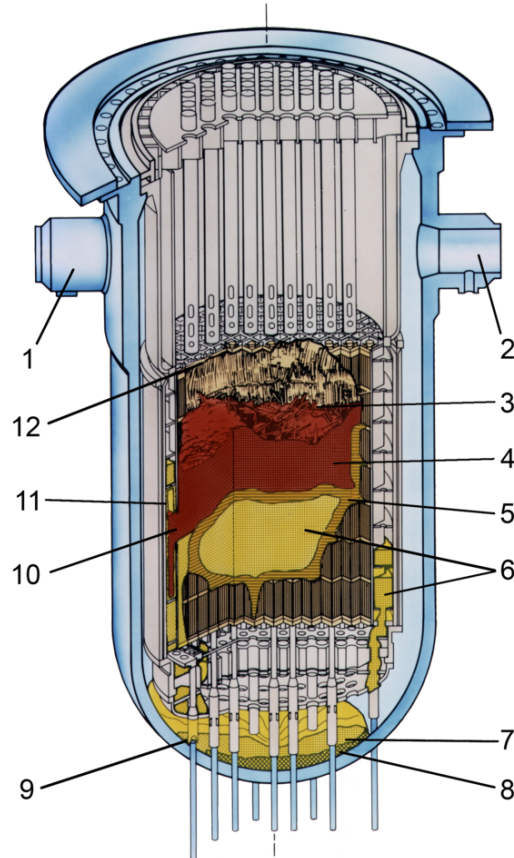


Figure 1.4: The Three Mile Island (TMI) reactor 2 after the meltdown. 1) Core inlet A. 2) Core inlet B. 3) Cavity. 4) Core debris. 5) Crust. 6) Previously molten material. 7) Lower plenum debris. 8) Region depleted in Uranium. 9) Ablated in-core instrument guide. 10) Hole in baffle plate. 11) Coating of previously molten material on bypass region interior surfaces. 12) Upper grid damaged top plate. [27]

1.1.4 Controlled Management of Severe Accident

In a core meltdown accident like LOCA, the main objective is to minimise releases to the environment, exposure of the public to radiation, and long-term contamination. To this end, integrity and leak tightness of the reactor containment must be maintained. An illustration summarizing the overview of the phenomenology of severe accident and leakage paths to environment is shown in Fig. 1.5.

The risk of vessel failure can be minimised with early and sufficiently high-flow injection of water into the vessel to remove the decay heat released by the fuel. The availability of early injection is, however, unlikely since it depends on the operator's capacity, shortly after the beginning of fuel degradation, to find a means of water injection that was not previously available and to maintain it over time.

In addition to water injection into the vessel, which may occur at a later phase, reactor pit flooding increases the possibilities of maintaining the corium in the vessel. The in-vessel corium retention strategy is thus based on sufficiently early water injection into the vessel so that an already degraded core can be cooled at least in part, and on the performance of an external cooling of the vessel.

The decay heat must be evacuated out of the reactor containment to avoid a slow pressure increase. Increased pressure would lead to containment failure, unless there is a venting-filtration system, whose opening time and efficiency in trapping aerosols and gaseous species determine the intensity of environmental releases.

If the corium cannot be maintained in the vessel, dedicated measures or devices protect the basemat. For the EPR, this entails spreading the corium on a large enough surface area to decrease heat flux and promote cooling. Whatever the approach taken (corium in or outside the vessel), water injection and ongoing decay heat evacuation out of the containment are necessary, and the associated risks in terms of containment failure, through pressurisation or dynamic loads, must be examined.

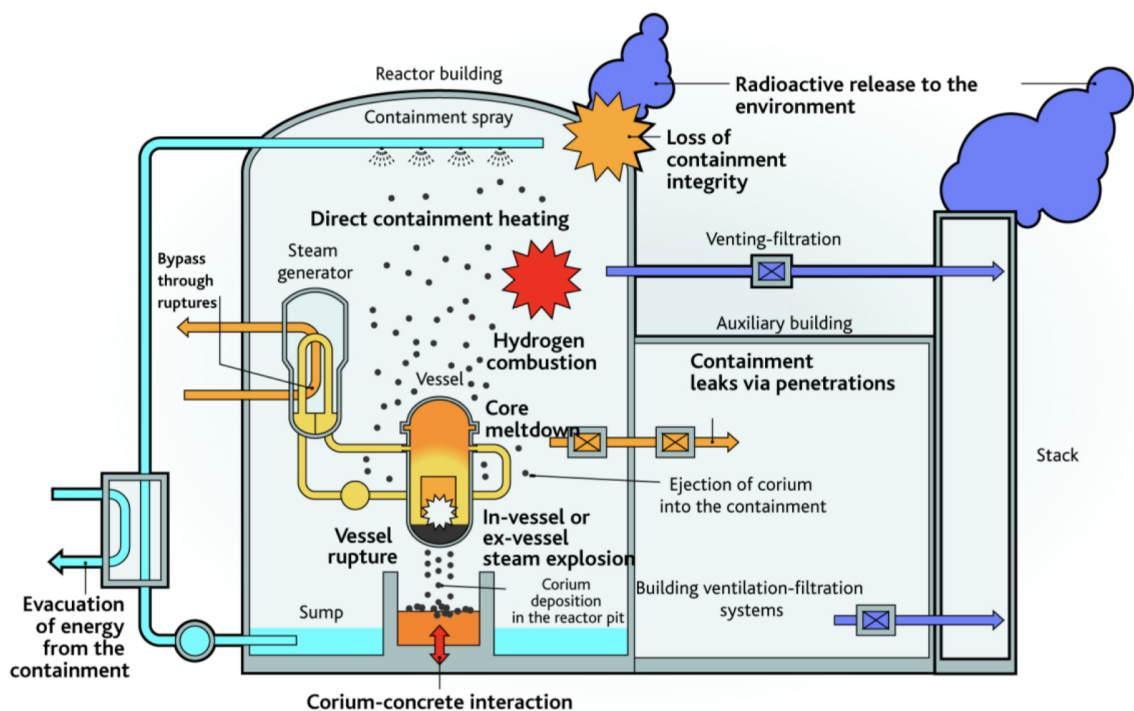


Figure 1.5: Severe accident phenomenology and identification of leakage paths to the environment. [107]

1.1.5 Feasibility of In-Vessel Retention (IVR) strategy for Corium Coolability

Fig. 1.6 illustrates an outline of an IVR strategy. Two main parameters affect the integrity of the Reactor Pressure Vessel (RPV) under core melt accident conditions with molten corium flowing to the bottom of the vessel:

1. The mechanical strength of the Reactor Pressure Vessel (RPV) at all points, particularly in areas subjected to the highest thermal load.
2. The mechanical strength of the RPV to withstand a steam explosion caused by an in-vessel corium water interaction.

Calculations have shown that after core degradation in a PWR, the corium pool would take up a volume similar to the hemispherical reactor pressure vessel bottom. The heat flux associated to this corium pool is extremely high and can only be removed if there is efficient convection at the free surface of the corium pool and the interfaces between the corium pool and the reactor vessel. Even in this case, part of the vessel wall would melt and its residual solid thickness would only be a few centimetres. It is very evident that if this heat flux is not efficiently removed, the reactor vessel will be perforated after only a few minutes. Ensuring vessel integrity therefore requires a way of removing the heat flux from the corium pool at all points in the reactor vessel. This condition is essential, but it is not the only criterion. The weakened vessel also needs to continue to withstand the pressure. Given that the residual thickness of the steel is reduced, the reactor vessel cannot resist high pressure in the Reactor Coolant System (RCS), requiring the RCS to be depressurised. The mechanical strength of the reactor vessel is therefore assessed at final pressure, after depressurisation, taking into account the thermo-mechanical loads caused by the corium pool. It also needs to be evaluated for a peak pressure in the RCS. A pressure peak could, for example, result in an steam production following the inflow of water from the RCS onto the corium pool at the bottom of the reactor vessel [64].

To assess the mechanical strength of the reactor vessel when in contact with a corium pool in core melt accident conditions, vessel behaviour is studied under the worst-case conditions, which are no core reflooding, flow of all corium mass to the vessel bottom and transient addition of the molten steel to the corium pool. These are the conditions in which the highest heat flux is received by the reactor vessel. In such conditions, the integrity of the pressure vessel, will be determined by the peak heat flux distribution across the reactor vessel, which will be in-turn governed by the stratification of corium pool.

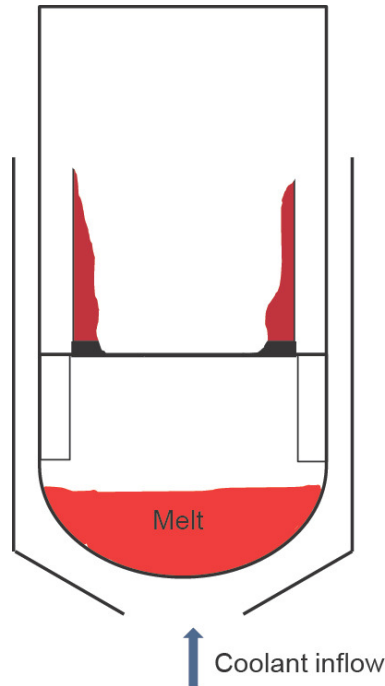


Figure 1.6: Outline of IVR [103]

1.1.5.1 Corium Stratification Governing Peak Heat Flux Distribution

The thermal behaviour of the stratified corium pool is the result of two types of phenomenon. Firstly, the thermo-chemistry defines the segregation of pool in different phases (oxide and metal), secondly, the thermal-hydraulics determines by natural convection the heat flux at the pool interface [32]. In-vessel corium is a multi-phase and multi-component system in terms of phases and species present respectively. Corium is a system of species like UO_2 (oxidised Uranium), ZrO_2 (oxidised Zircaloy), Zr (un-oxidised Zircaloy) and stainless steel elements (Fe, Ni, Cr).

At thermodynamic equilibrium, the miscibility gap in the U-O-Zr-Fe quaternary system [104] leads two immiscible liquid phases that segregate under gravity and results in a two layer stratified corium pool. The position of metal layer in the short term is likely to be at the bottom because of the small amount of molten steel and not fully oxidised corium pool. This situation is shown in Fig. 1.7. In the long term the position of the metal layer is likely to be on top and the corium pool almost fully oxidised. Figure 1.8 illustrates this situation. The evolution of configuration in the corium pool was observed within the framework of MASCA experiment. [8, 7]

Between these two equilibrium states of stratified corium, another intermediate state can occur when there is a three layer stratified system in which light metal is on top, oxidised corium is in center and heavy metal is at the bottom. The formation of heavy metal during transient states of corium layers evolution is the consequence of mass transfer between top steel layer

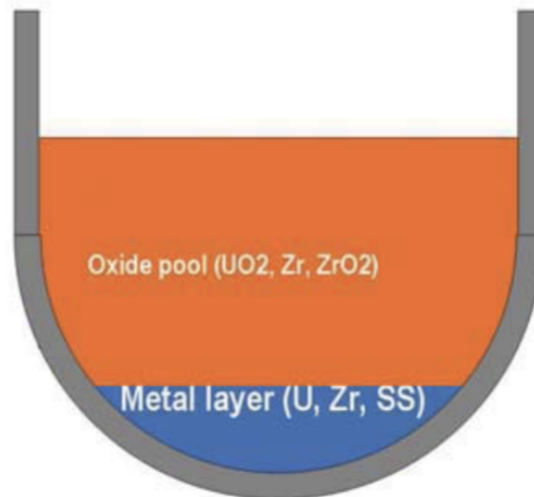


Figure 1.7: Position of metal layer in the beginning [36]

and oxidised corium pool. Specifically when molten steel (mainly Fe) comes in contact with molten corium then U and Zr diffuses in metal. In the oxide phase this produces the phase separation and due to immiscibility of the two phases there is the occurrence of a two phase interaction zone [36]. Such configuration is shown in Fig. 1.9. U and Zr diffusing to metal phase makes the density of the metal phase near the interaction zone heavier than that of oxide. This heavy metal flows to the bottom as soon as its volumetric fraction becomes large enough thus constituting a three layer stratified system. This three layer phenomenon is illustrated in Fig. 1.10.

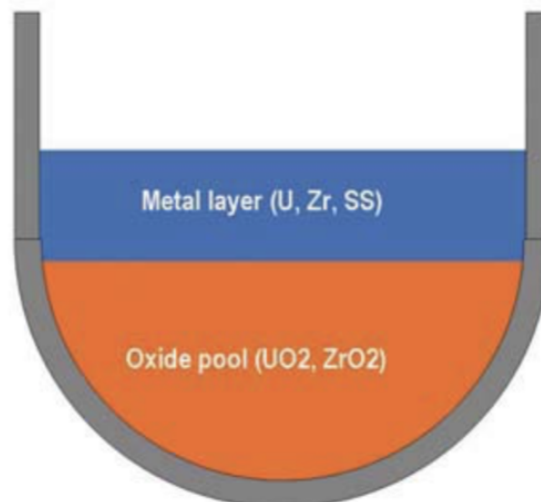


Figure 1.8: Position of metal layer in the long term [36]

Out of these most critical configurations for the reactor vessel is when low-density molten metals (mainly containing steel) float on top of a pool of high-density corium oxides (approximately 8000 kg/m^3) (Fig. 1.8). This configuration was also used to support the first external vessel cooling studies,

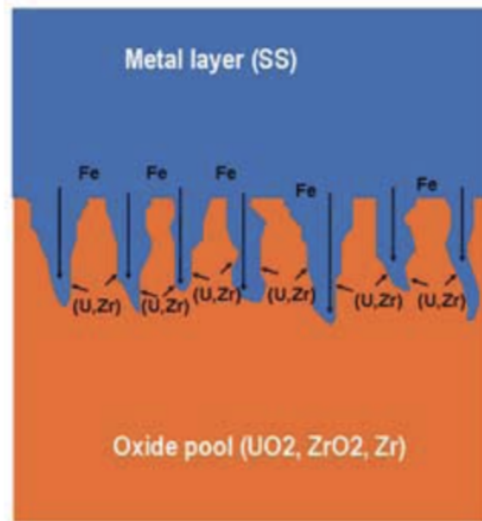


Figure 1.9: Phase interaction zone [36]

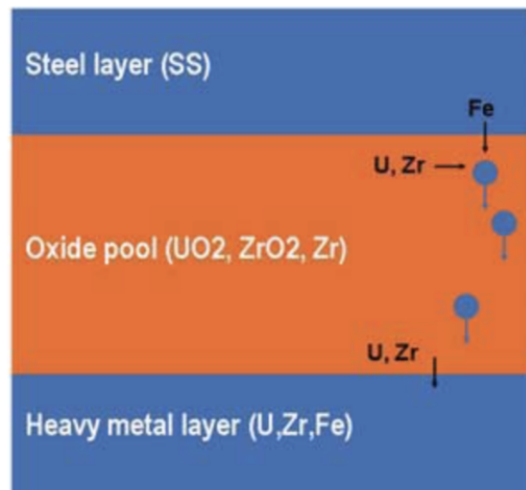


Figure 1.10: Three layer stratified system [36]

in particular the AP600 concept. This configuration will be referred to as the *classical configuration* hereafter.

For any given corium configuration, the heat flux distribution depends on the conditions between the molten pool and the solid wall (either the crust or the steel of the vessel) and the coefficients of heat transfer by natural convection. The temperatures at the edge of a corium pool have been determined in various studies, which are summarised in [106]. The main difficulty in determining the temperatures is related to the fact that the melting materials are a mixture of oxides and metals. These mixtures melt over a relatively wide range of temperatures that depends on the composition of the mixture. Such a mixture may also contain a mushy zone, between the molten pool and the solid crust by the vessel wall, which could affect heat transfer. Reference [106] has shown that in

steady-state thermal-hydraulic conditions (i.e. when the heat fluxes have been established), no such mushy zone can exist, because the pool composition becomes homogeneous and will solidify in the same way as a pure body (with a flat interface between the solid and liquid). In addition, when there is sufficient external cooling, the solid crust has a constant thickness (i.e. the speed of progress of the solidification front is zero). In this case, the temperature at the liquid-solid interface tends towards the liquidus temperature corresponding to the liquid mixture. There is a clear separation between the solid and liquid. Experimental confirmation of this conclusion has been provided by various tests (PHYTHER by the CEA (described in [106]), RASPLAV (Kurchatov Institute, Russia) [2], and SIMECO (Royal Institute of Technology, Sweden). The solidification transient was studied by IRSN in 2005 [96].

The assumption of thermo-chemical equilibrium in determining the interface temperatures also applies to the metallic layer of a stratified corium pool. If the liquidus temperature corresponding to the composition of the metallic layer (chiefly formed of Steel, Zirconium and Uranium) is lower than the melting point of steel, the steel may be dissolved by the molten metal. The interface temperature with the solid steel of the reactor vessel establishes itself at this liquidus temperature. To put things simply, depending on the composition of the liquid metal layer, the temperature of the inner surface of the reactor vessel wall may be substantially lower than the melting point of steel. Temperatures at the liquid-solid interface are calculated with thermodynamic software (such as GEMINI) on the basis of the composition of the liquid layer in question. The corollary of this choice is that the pool is completely liquid and the heat transfer laws identified from tests with simulant materials (pure bodies like water) can be transposed to the real materials.

Heat transfer correlations have been deduced from tests with simulant materials (BALI, COPO, ACOPO, RASPLAV-Salt, etc.) for various geometrical configurations [105]. Efforts have also been made to validate CFD software for natural convection. The results are encouraging, but further improvements to the turbulence model are still required in order to improve the precision of the results. The use of such software at the scale of a power reactor vessel gives results with a wide uncertainty interval. Given the current state of knowledge, it is preferable to use a simpler approach based on correlations from the tests.

1.1.5.2 Focusing Effect

To give an order of magnitude, for the reference configuration shown in Fig. 1.11 the residual heat is distributed as follows, assuming that the entire mass of oxides from the core is at the bottom of the reactor vessel:

1. Half the residual heat released from the pool of oxides is transferred to the bottom of the vessel.

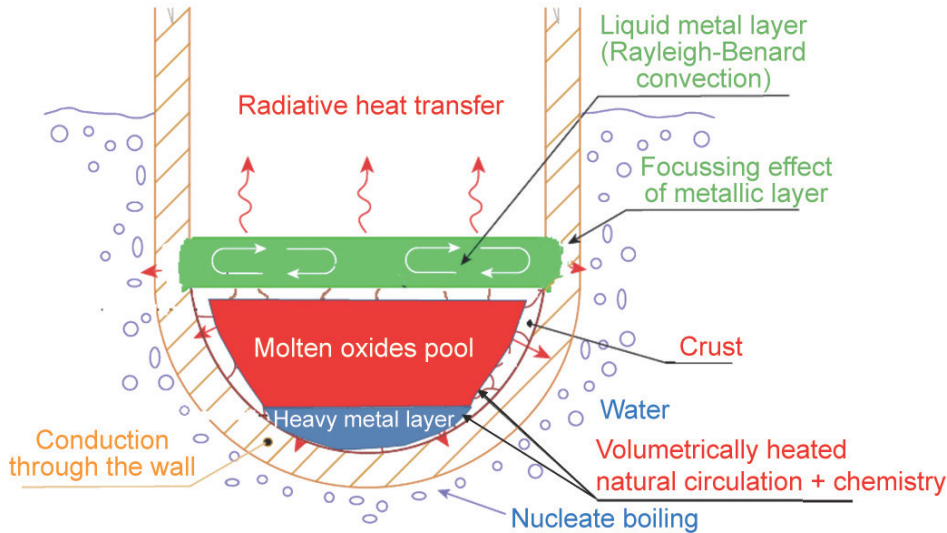


Figure 1.11: Modes of heat transfer in corium. [103]

2. The other half is transferred from the pool of oxides to the upper layer of liquid metals.

If there is no water inside the reactor vessel, the metal layer transfers most of the heat received from the pool of oxides and the internal heat it releases to the steel vessel wall, which is in contact with the liquid metal layer. Because the outer surface of the metal layer is lower than the outer surface of the oxide pool, this produces a higher heat flux along the metal than along the oxide: this is called *focusing effect*. At the point of contact with the metal layer, the heat flux is approximately inversely proportional to the thickness of the metal layer. For a thickness of more than 50 cm (corresponding to approximately 50 tonnes of steel), the heat flux is below 1.5 MW/m^2 . Reactor vessel integrity is only assured if the heat flux transferred to it can be removed by two-phase natural convection from the cooling water outside the vessel. This naturally raises the question of the critical flux on the external vessel wall (upper limit higher than the heat flux that can be removed by external reactor vessel flooding).

1.1.5.3 Critical Heat Flux Condition for External Cooling Channel in IVR

The critical heat flux associated with external cooling of the reactor vessel, in particular in the area around the metallic layer, will therefore be the limiting factor for heat removal from the vessel. Significant efforts have been made around the world to determine this critical flux and to increase it. Various tests have been performed (with 2D or 3D geometries and different wall heating modes). The most interesting of these include ULPU tests (University of California, Santa Barbara) [28], the SULTAN tests (CEA) [95] and tests by KAIST (Korea Advanced Institute of Science and Technology, South Korea). Also, more recently, similar tests were made by UJV for a semi-elliptical geometry corresponding to VVER-1000 reactors (citation of Zdarek et al.).

The first phenomenon that determines the critical flux value if the reactor pit is reflooded is the water circulation by natural convection within the reactor pit. Simply reflooding the reactor pit is not enough to cool the reactor vessel.

The water circulation needs to be organised such as to maximise liquid flow-rate along the vessel walls. This implies the existence of a rising hot leg (the reactor vessel) and a cold leg. The geometry of the vessel (radius and spherical or elliptical shape of the vessel bottom) and the presence of insulating materials around the vessel may affect water circulation and pressure loss. For a geometry that maximises water circulation and in the absence of elements to hinder flow, maximum critical heat flux is obtained when the water flow-rate is high enough to limit boiling close to the wall in the heating zone (no mass boiling in this area). However, above the heating zone, boiling should be higher to create a strong enough *chimney effect* [119], whereby the steam generated drives an increased liquid flow.

If water flow-rate is not high enough, there is film boiling around the heating zone and the critical flux is reduced because the heat is removed less effectively. Having said that, the water flow-rate cannot exceed the flow created by the chimney effect related to mass boiling above the heating zone. This maximum flow-rate corresponds to a maximum critical heat flux of the order of 1.5 MW/m^2 , which can vary between 1. and 2.3 MW/m^2 , depending on the optimization of the channel shape and the surface state of the vessel. Analysis of the test results mentioned above show that the spread of estimated critical flux values is often fairly high. Results from the ULPU tests give values close to 2 MW/m^2 (but with a wide spread of experimental results), whereas results from the SULTAN and KAIST tests show critical flux values on a vertical wall that range from 1.2 to 1.5 MW/m^2 . Various effects have been studied in an attempt to identify provisions that could increase the critical heat flux, in particular effects linked to the condition of the reactor vessel's outer surface. According to some authors, [22], a spray-on porous metal coating on the outer surface of the reactor vessel could significantly increase the critical flux (by a factor of up to 2). However, this conclusion is not universally shared and experimental verification is still required.

1.1.6 Dissolution of the Crust Aggravating Focusing Effect

CORDEB experiments (described in the next chapter 2) have shown that the thickness of the top metal layer can not be assumed to be constant because of the transfer of molten steel through the channels in the crust, due to the dissolution of the crust at high temperature (above 2100 K) by the molten steel. This leads to a significant difficulty for the determination of the maximum heat flux imposed to the vessel by the metal layer. A slow dissolution of the crust, leading to slow mass flow of molten steel through the crust will result in an increasing focusing effect to the vessel wall in time. On the contrary, a fast dissolution will impose less severe focusing effect on the vessel wall. Question of

stability of the crust under dissolution is another important aspect. Situation of fully dissolved crust will be more benign than the stable crust configuration. Nevertheless whatever may be the case, phenomenon of *dissolution* will play a key role in the kinetics of mass transfer of molten steel through the crust and thus in turn in the determination of the focusing effect. This makes the detail study of dissolution of prime importance.

1.2 Scope of the Thesis

The present work can be broadly categorised into two main aspects, namely:

1. Mathematical modeling of the dissolution.
2. Thermochemical study of the quaternary system (U, Zr, Fe, O) .

In particular, the thesis looks into the issue of modeling of mass transfer of molten steel through the oxide crust. In the present work this problem has been modeled as a phenomenon of dissolution of a ternary oxide crust by molten steel. Such an analysis is considered to be a two-phase transport phenomenon with a complex evolution of the interface between solid and liquid phases. Thus, the thesis is built upon a suitable mathematical method to deal with this two phase transport problem. The thesis employs a rigorous thermochemical study for the investigation of quaternary chemical equilibria in the quaternary system (U, Zr, Fe, O) , which backs up the mathematical modeling by providing important simplifications. Thesis also addresses the problem of fast calculations of equilibrium compositions of the species in CFD codes used for the analysis of the severe accidents in the Nuclear Power Reactors (NPP), by deriving a simplified thermochemical model. Further, the thesis presents the numerical results for the various cases. At first the case of diffusion governed dissolution in a 2D crust is presented along with its qualitative comparison with crust morphology observed in CORDEB experiments. Finally, the case of advection-diffusion is studied in 2D, broadly covering the effect of the convection on the dissolution of the crust and also on the associated heat transfer.

Chapter 2

Experimental observations of
interactions between solid
oxide and molten steel

Chapter 2

Experimental Observations of Dissolution

The first clear evidence of molten steel interacting with the solid oxide crust was observed in CORDEB experiments. Those experiments are described in the following sub-section. Complementary experiments VITI-CORMET were performed to provide more data about the kinetics of dissolution and the physical mechanisms governing it. They are also described in a sub-section. Finally, the consequences of that chemical interaction for the safety analysis in case of IVR are briefly discussed.

2.1 CORDEB and CORDEB-2 Experiments

CORDEB (CORium DEBris) experiments [4] were performed in NITI Russia and funded by IRSN, CEA, EDF and Framatome. The experiments were performed with prototypical nuclear materials $UO_2 + ZrO_2 + Zr$ to analyse the three-liquid oxidic-metallic corium pool. The first tests series of CORDEB program was devoted to study a possible reactor configuration where the oxide/metal pool, resulting from the melting of oxidic corium and steel internal structures, would be cooled from the top by radiative heat transfer towards the core plate and the top of the vessel leading to the formation of an oxidic crust and where molten steel would arrive above this crust due to further melting of the vessel wall and upper structures. A first objective was to determine if such a configuration would be stable or if the crust would let molten steel go through it (by dissolution or through cracks). A second objective was to determine the kinetics of mass transfer through the crust.

Therefore, two tests, CD1-01 and CD1-02, were performed in three steps. First, a prototype $UO_2 - ZrO_2 - Zr$ corium (oxidation index $C_{ox} = 0.3$, $U/Zr = 1.2$) was formed. Second, a first portion of stainless steel was added and, when the thermo-chemical equilibrium was reached, the oxidic crust was formed by decreasing the temperature of the top. Third, the second portion of stainless steel was added and the established three-layer pool was exposed for unchanged furnace parameters for approximately one hour in CD1-01 and

three hours in CD1-02. The relative steel mass was around 0.15 after the first steel addition and 0.29 after the second one. These tests were performed in an inert atmosphere. The complete description and the results and material analyses of both tests are detailed in [4]. The RASPLAV-3 test facility of the RASPLAV platform was used. Corium was heated up and melted using the technology of induction melting in the cold crucible in the argon atmosphere. Fig. 2.1 shows the schematic of the induction furnace and oxidic-metallic pool at the moment of formation of the initial two layer structure. The post test ingot structure of CD1-02 experiment, shown in Fig. 2.2, shows the formation of crust between top metal layer and bottom oxide corium. In CD1-02 experiment, the presence of two Heavy Metal (HM) layers, namely HM1 and HM2, was observed.

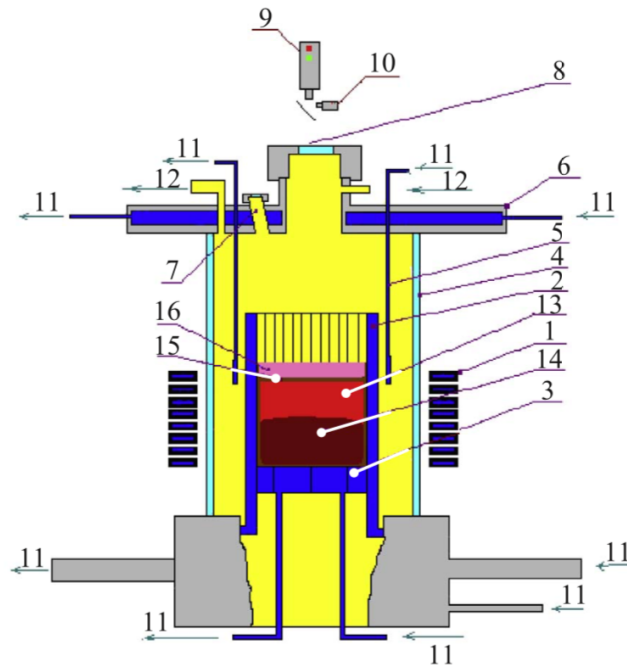


Figure 2.1: CORDEB experiment setup. 1 – inductor; 2 – pipes of crucible sections; 3 – multi-section water-cooled bottom calorimeter; 4 – quartz tube; 5 – water-cooled electro- magnetic shield; 6 – water-cooled furnace cover; 7 – port for steel addition, sampling and steel layer temperature measurement by the W-Re thermocouples; 8 – quartz window in the pyrometer shaft; 9 – pyrometer; 10 – video camera; 11 – cooling water in and out; 12 – gas in and out; 13 – oxidic part of corium pool; 14 – metallic part of corium pool; 15 – oxidic crust; 16 – surface steel layer [4]

Mass and composition of upper metal ingots of both tests indicate that thermo-chemical interactions between upper steel and oxidic crust has occurred because U and Zr are present in the upper steel. Both upper metallic ingots have similar composition but the percentage of upper steel which

went through the crust is much higher in CD1-02 (57.2 w-%) than in CD1-01 (7.4 w-%). After the first steel addition, some Uranium and Zirconium relocate in the metallic phase and the oxidation index of the oxidic layer increases up to $C_{ox} = 0.78$. However, during the first steel addition, some steel relocates in the oxidic layer and, the thermo-chemical equilibrium calculated with *NUCLEA* – 18_1 database at 1600°C with the whole inventory of the oxidic layer gives a three-phase equilibrium containing the same $UO_2 - ZrO_2$ phases and a liquid phase. This liquid phase contains all steel atoms but its major part is made of *Zr* (around 38 mol-%) and *U* (around 28 mol-%). And thus, this liquid phase represents around 4 w-% of the oxide crust.

Looking at the micro-structure of the crust in Fig. 2.3 in CD1-02 experiment, channels of molten metal can be seen in black color and oxide crust is represented by grey color. This shows that in CORDEB experiments, molten steel was able to *dissolve* the crust at high temperature of around 2100 K and above, creating the micro channels of molten metal. Tests performed at lower temperature of the crust (1800 K) show that dissolution is not visible. Therefore, dissolution appeared only at high temperature (above 2000 K), which corresponds to the typical situation in case of IVR.

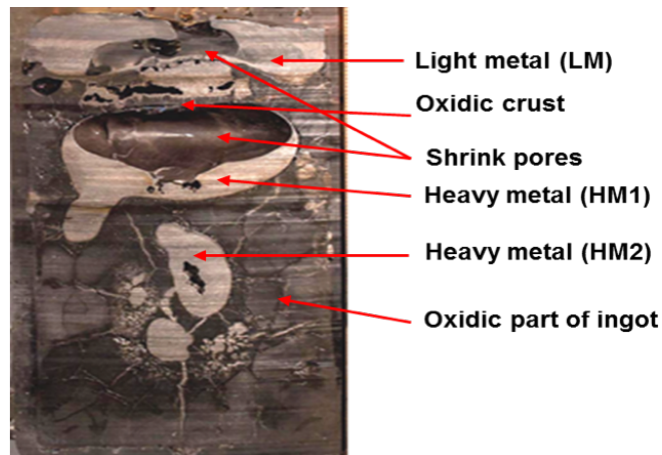


Figure 2.2: Post test ingot structure of CD-02 experiment. [4]

Regarding the kinetics, CD1-01 and CD1-02 give two pictures of the same configuration at two different times. Formation of channels seems to last a little less than one hour as only 7.4 w-% of the second steel addition was transferred through the crust in CD1-01 whereas 57.2 w-% was transferred in CD1-02. This transferred metal formed droplets which joined the heavy metal which became lighter and went up in the oxidic pool.

Based on the post test analysis of CD1-01 and CD1-02 ingot fragments, the following mechanism of the transient processes is assumed in [4]: During and after the molten steel addition to the crust, the molten steel starts to dissolve the crust, which consists of the crystallized sub-oxidized corium melt. This

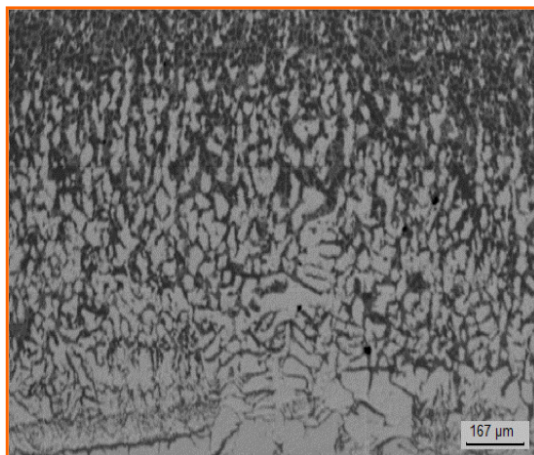
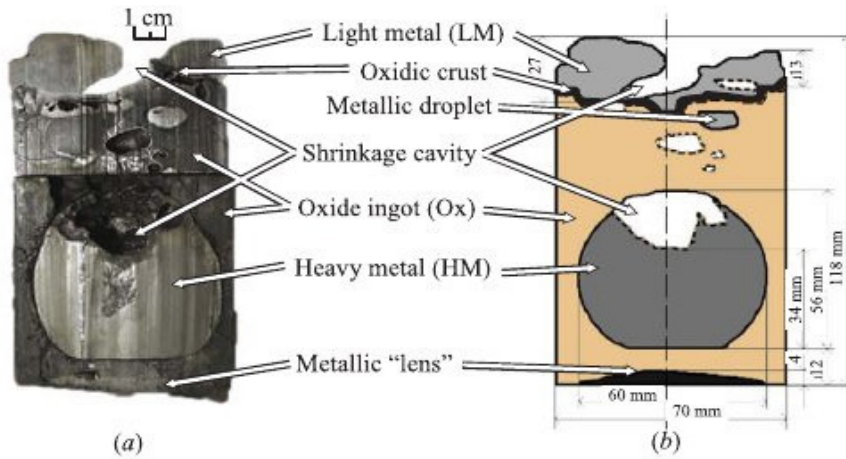


Figure 2.3: Micro-structure of the crust after dissolution, showing oxide crust in Grey and molten steel channels in Black. [4]

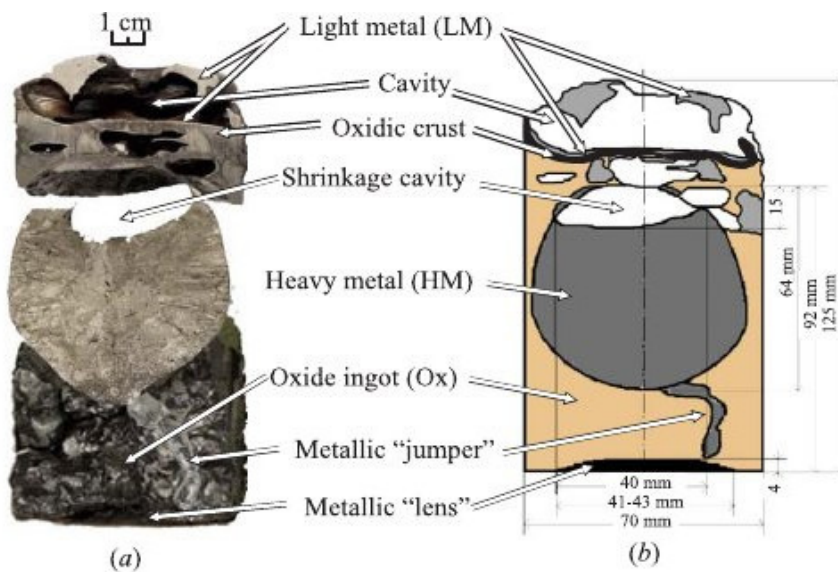
interaction first brings the formation of liquid metallic phase in the crust, following these interactions open channels are formed as shown in Fig. 2.3. These channels connect the metallic melt above the crust with the oxidic melt under it. The mass transfer of molten steel and oxidic melt component goes through these transport channels. This results in the formation of mixed metallic-oxidic zone with prevailing liquid metallic phase in the bottom (hot) crust layer. After the U accumulation in the metallic part of that zone, which is caused by the redistribution of U and oxide components, the metallic melt becomes heavier, it separates from the crust and, as droplets, relocates to the oxidic-metallic melt and joins the HM layer. Also, Light Metal (LM) can be transported through cracks formed in the crust because of mechanical stresses. These processes lead to increase the volume of liquid under the crust, which separates the oxidic-metallic pool and LM layer. On the other hand, as a result of components redistribution the oxide phase crystallizes on the crust upper boundary (which is colder), while the crust dissolves on the lower (hotter) boundary. As a result the crust gradually shifts in upper direction without own average thickness changing. After a longer exposure at a certain moment of time, due to the increase of the SS component fraction (mass) and decrease of the U fraction in the HM layer, its density becomes lower than that of oxide, and the inversion of oxide and HM layers position takes place. Fig. 2.5 shows the aforementioned process.

2.2 VITI-CORMET Experiments

The VITI-CORMET experiments were performed by CEA in Cadarache research center. Following the first observations made on CORDEB tests, CEA investigated in more details the interaction of molten steel with a solid phase made of $UO_2 + ZrO_2 + Zr$. The objectives were to identify the characteristic structures appearing during the interaction (like preferential channels), to measure local compositions of the phases and to estimate the



(a) CD1-01 ingot axial section (a) and schematics (b)



(b) CD1-02 ingot axial section (a) and schematics (b)

Figure 2.4: Extracted from [4]

kinetics of dissolution and the kinetics of progression of the dissolution front. Those experiments are still on-going and publications are limited. The only reference used here is [87]. The facility is represented in Fig. 2.6. It is made of a Tungsten crucible where an oxide crust is formed at the bottom. It is heated by induction, providing quasi isothermal conditions, in the range between 1600°C and 1800°C . The U/Zr ratio is $C_{UZ} = 1.2$. The oxidation index of the solid phase (crust) is $C_{ox} = 0.7$. The interaction is initiated by depositing a Steel droplet (2 gram) over the solid crust. Local examinations of the interaction zone show two different modes of progression of the liquid steel within the oxide crust: penetration through small preexisting cracks and dissolution of the crust. The patterns observed in the dissolution zones are very similar to the one already observed in CORDEB tests. They are shown in Fig. 2.7. The authors of VITI-CORMET tests have identified three different zones. In the area close to the metal layer, there are discontinuous small islands of oxide

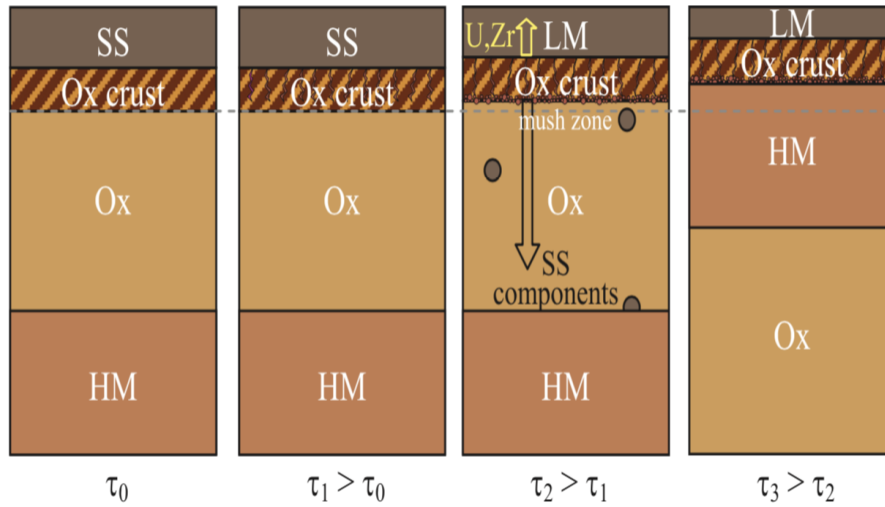


Figure 2.5: Illustration of the molten steel interaction with oxidic crust and oxidic pool. [4]

crust surrounded by liquid metal. Further into the crust, an intermediate zone shows an interconnected channel structure filled by metal between large discontinuous islands of oxide crust. Then, at the end of the interaction zone, interconnected metallic inclusions are observed within a continuous oxide phase. Following [87], this behaviour indicates a heterogeneous penetration of molten metal through the crust and thus existence of preferential paths or channels. This supposes the existence of fast diffusion pathways (grain boundaries, porosities). The formation of (U, Zr) metallic pockets by reduction of $(UZr)O_{(2-x)}$, may also be assumed, as already observed by [58] in the dissolution of UO_2 by molten Zr . The preferential extraction of Zr is also observed.

From the kinetics point of view, it was observed a progressive decrease of the dissolution rate up to an apparent stop after 6 hours of exposure. This indicates that one of the phases has reached its equilibrium composition or that diffusion of an element has become very slow (due to a very low gradient of composition for example).

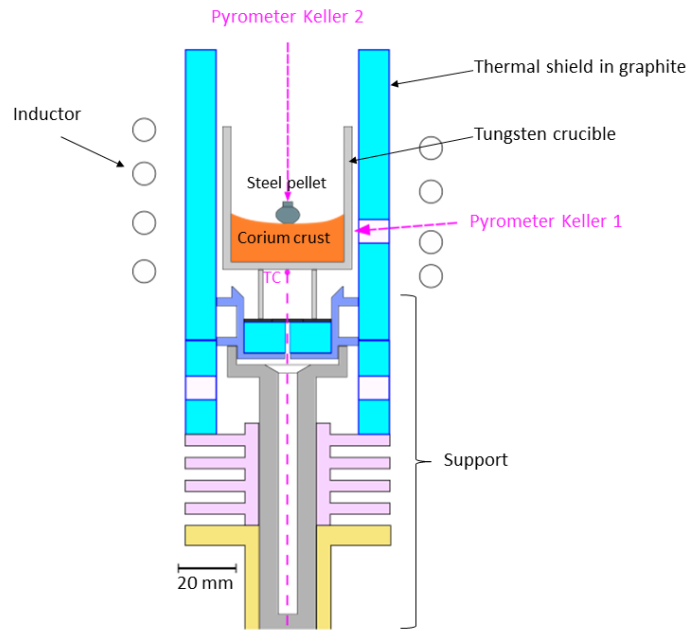


Figure 2.6: VITI-CORMET experimental setup. [87]

2.3 Influence of Temperature and Oxidation Degree of the Crust

In the other tests of the CORDEB-2 series, the temperature was varied from very low values (1470 °C) to quite high values (2150 °C). It was found that, at low temperature, there is no transfer of Fe through the crust which remains almost intact. No metallic channels are visible in that case. But there is a transfer of U and Zr towards the top metal layer. On the contrary, at high temperature, all the steel elements are quickly transferred through the crust (in less than 45 *mn* for the highest temperature). This indicates that dissolution strongly depends on temperature.

The oxidation degree of the crust also has an influence on the kinetics. The higher the oxidation degree, the slower the mass transfer through the crust. This is probably related to the volume fraction of metal in the crust. At thermochemical equilibrium with the oxide phase, the metallic phase has a lower volume fraction when the Oxygen content increases. It is even zero when the oxide is stoichiometric (atomic fraction near 0.667). This is illustrated in Fig. 2.8.

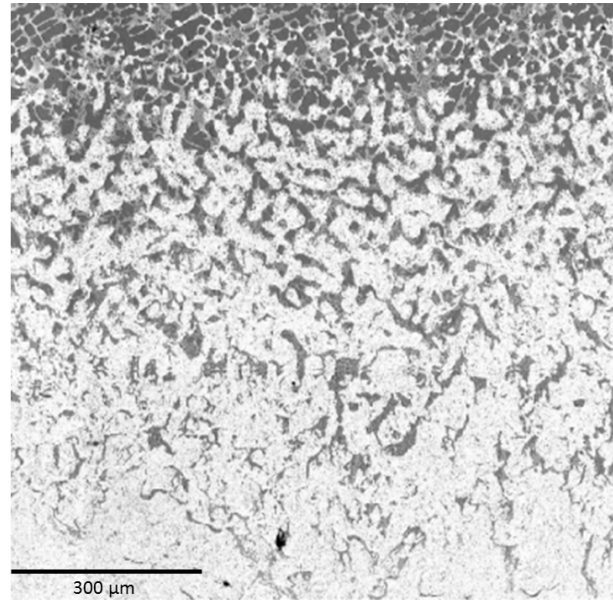


Figure 2.7: VITI-CORMET visualization of the interaction zone and dissolution patterns. Solid oxide in Light Grey and Liquid metal channels in Black. [87]

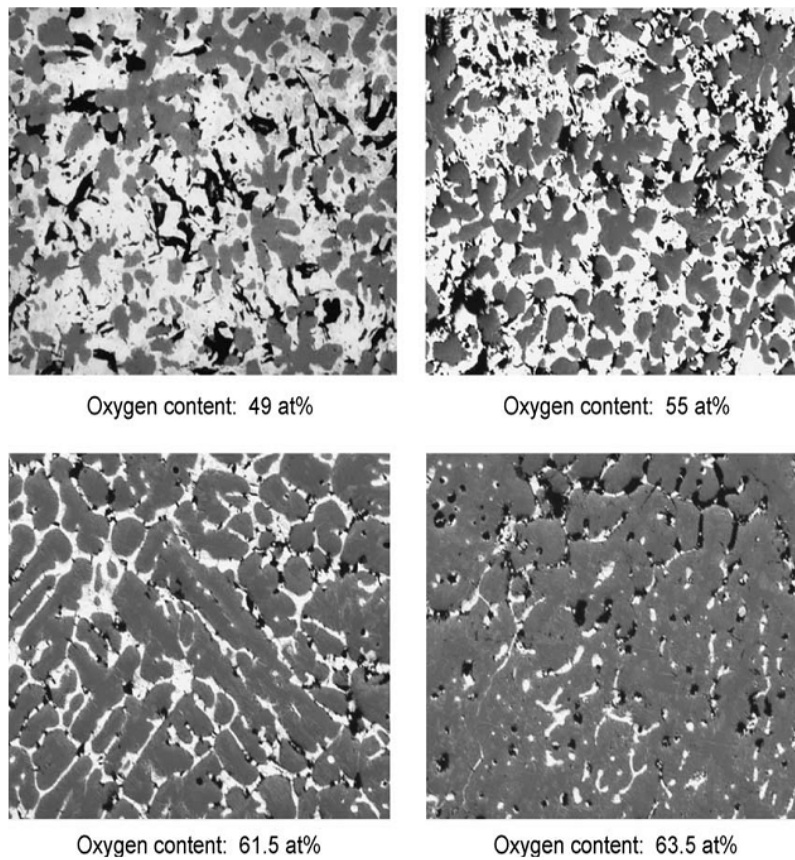


Figure 2.8: Volume fraction of metal within the oxide phase as a function of Oxygen mole fraction. Dark Grey represents oxide and light grey metal. [4]

2.4 Summary and Consequences for Modelling and Safety Studies

It was observed in both CORDEB and VITI-CORMET experiments that dissolution of the crust is associated to the formation and growth of metal channels inside the crust. This means that the diffusion of Fe in the liquid metal may play a limiting role in the dissolution process. The observed impact of the oxidation degree of the crust indicates the diffusion of Oxygen in the solid phase may also play a limiting role. The strong reduction (or even the absence) of dissolution observed when decreasing the crust temperature seems to be a confirmation that the process is driven by molecular diffusion of Fe and O in the liquid and solid phases respectively (since diffusion coefficients decrease when temperature decreases).

Boundary conditions also play an important role, in particular the conditions on the side of the crust which is not in contact with steel. If there is no way for Oxygen to go out of the crust, this will limit the dissolution. Similarly, if there is not enough convection in the liquid metal to avoid saturation of the metal near the crust, dissolution may be limited.

From a modelling point of view, this means that a relevant model should include the diffusion of several species (at least Fe and O) and consider relevant boundary conditions on both sides of the crust. This implies that taking into account the convective motion in the metal is also necessary, as it determines the boundary condition on one side of the crust. With respect to the metal channels formed in the crust, their scale seems to be related to the grain size but it may not be exactly proportional. As illustrated in Fig. 2.8, the channels seems to have a more or less periodic structure. This is a difficult point to model.

At the reactor scale, the extrapolation of these results implies that molten steel would be able to flow through the crust if it is not fully oxidised. This has a consequence on the relocation of molten steel in the pool, in particular for steel that is melted at the inner surface of the vessel wall which is always in contact with an oxide crust. An important consequence is that a three-layer pool configuration in a reactor is possible, at least during the time that is necessary for Fe to be transferred through the crust. During this time the focusing effect may be increased and the heat flux to the vessel wall may be high.

Chapter 3

Mathematical Modeling

Chapter 3

Mathematical Modeling

3.1 Phenomenon of Dissolution

Before moving on to the mathematical aspects involved in the modeling of dissolution, it is worth to get a primer of the phenomenon of dissolution and the basic thermodynamics associated with it. The phenomenon of dissolution is an important naturally occurring phenomenon in nature. It is a fundamental phenomenon that governs some of the simplest things we do in our day to day life, like mixing of sugar in tea, salt in water, chocolate in milk, so on and so forth. The physics associated with the phenomenon of dissolution is the change of state. The process of such change of state encompasses myriad branches of sciences and engineering namely thermodynamics, chemistry, physics of transport of chemical species etc. The dissolution results in the modifications of thermodynamic variables like temperature, concentration etc., which leads to the evolution of the equilibrium state of matter from a solid state to a liquid state below the melting point of the solid.

The understanding of the dissolution phenomenon is crucial for plenty of applications, particularly for the geophysical mechanics of the planets, for the evolution of the fractures in the soil, for the extraction of petroleum products from the cavities within the earth and also for the study of the contamination of the aquifers by the partially miscible fluids or Non-Aqueous Liquid Phase (NAPL) such as hydrocarbons.

Another example is the dissolution of $NaCl$ by water. On addition to water, the Na^+ part of $NaCl$ is attracted to the oxygen side of the bi-polar water molecules, while the Cl^- part is attracted to the hydrogen's side of the water molecule. This causes the sodium chloride to split in water, and the $NaCl$ dissolves into separate Na^+ and Cl^- atoms. A hydration shell is formed around them which prevents Na^+ and Cl^- to form ionic bonds.

Metallurgy is another field where phenomenon of dissolution can be very easily encountered. Most of the processes associated are related to the dissolution of binary or ternary alloys, ceramic materials etc. by liquid metals

at a temperature much lower than the melting point of the constituent solutes. Several studies related to the dissolution of the alloys by the molten metals has been documented in [47, 61, 82], [83, 84], [74, 86], [85, 102] and [101, 120].

3.1.1 Thermodynamics of Dissolution

In this section thermodynamical aspect of the dissolution at constant temperature is discussed with respect to the binary alloys. To keep the analysis simple binary alloy having isomorphous phase diagrams has been considered. One such system exhibiting the isomorphous characteristics is shown in Fig. 3.1.

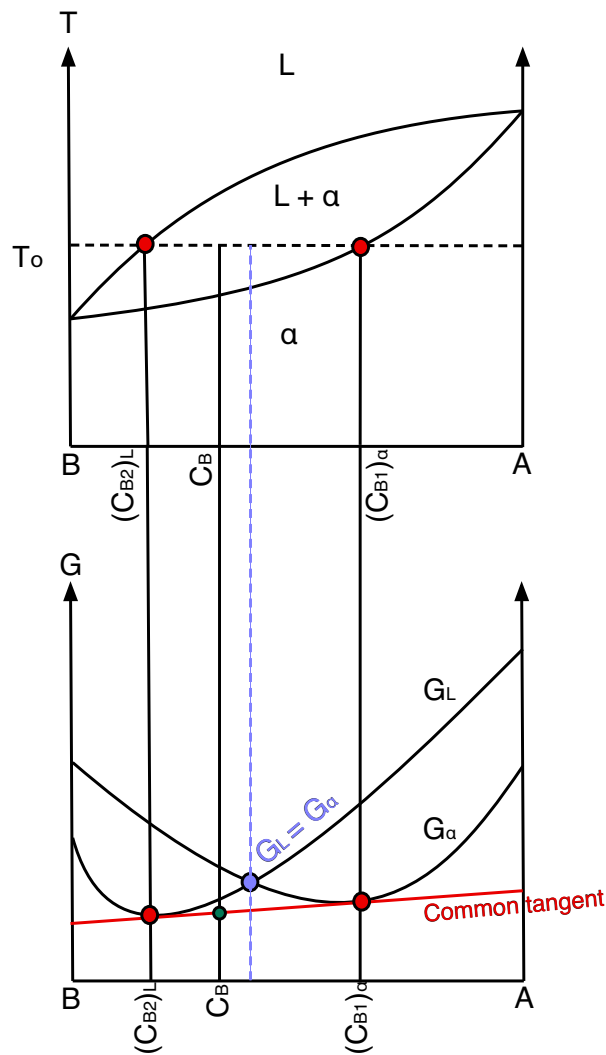


Figure 3.1: A typical binary isomorphous phase diagram (T-C) shown with an equivalent free energy Vs. composition (G-C) diagram at T_0 .

The dashed purple line in the Fig. 3.1 represents the composition in T-C and G-C diagrams at which the Gibbs energy of liquid and alpha phase is identical. Further, If an alloy initially solid, having a composition C_B – which falls on the left side of the $G_α = G_L$ line – is chosen, and kept at the temperature T_0 , the G-C phase diagram then tells that such an alloy with C_B composition can not

stay completely solid at T_o . This is evident from the G-C diagram showing that on the left of the $G_\alpha = G_L$ line, $G_L < G_\alpha$. Thus, making liquid more stable.

However, at the temperature T_o , the complete solid alloy will not transform into liquid even though $G_L < G_\alpha$. This is because at the temperature T_o and composition C_B , the minimum Gibbs free energy of the mixture will be given by the green dot on the *common tangent* represented in red in G-C diagram. This shows that a solid alloy of C_B composition has to split into a solid phase, having composition $(C_{B1})_\alpha$ (represented by right red dot), and into a liquid phase, having composition $(C_{B2})_L$ (represented by left red dot). Consequently, liquid phase of composition $(C_{B2})_L$ has to nucleate out of the solid initially having a composition C_B .

Apparently, it is interesting to see that because a liquid phase with $(C_{B2})_L$ composition, nucleating out of the solid with C_B composition can only be in equilibrium with solid of $(C_{B1})_\alpha$ composition, thus, a *local equilibrium* at the interface between liquid and solid has to be maintained. In other words, the solid in the very close vicinity of the liquid will have the composition $(C_{B1})_\alpha$ and rest of the solid still be having composition C_B . To even out the composition of the solid from C_B to $(C_{B1})_\alpha$, long range diffusion has to take place. This will result in the growth of liquid phase till the equilibrium is reached.

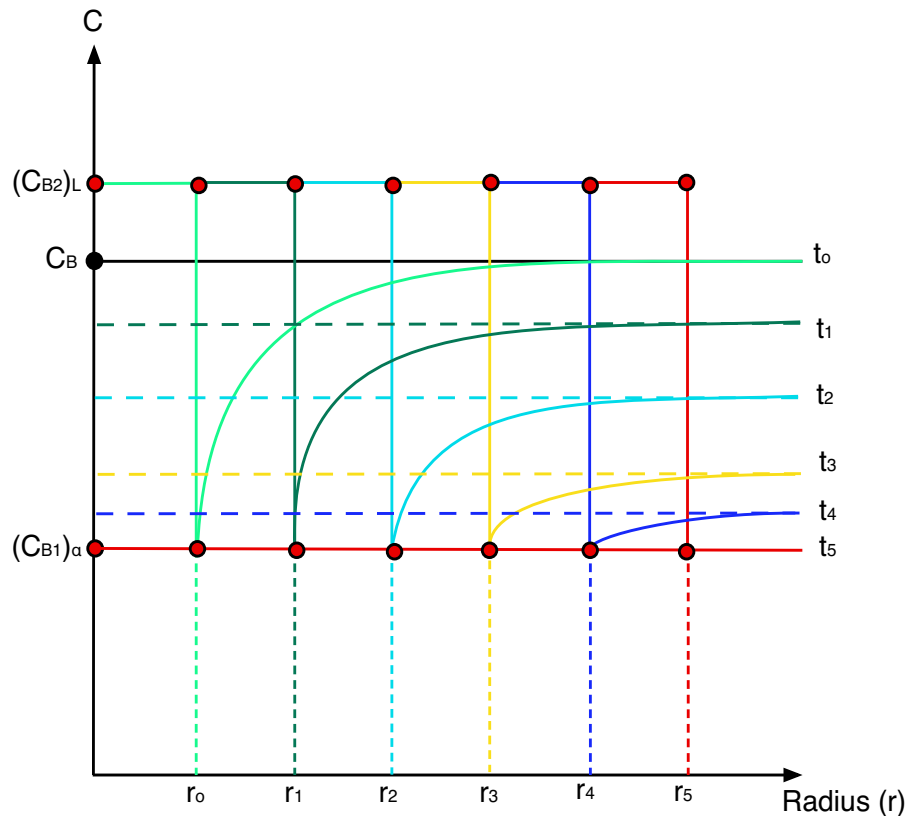


Figure 3.2: Growth of liquid phase out of the solid phase

Fig. 3.2 shows an initial (time = t_0) nucleus of liquid of radius r_0 , with $(C_{B2})_L$ composition, is in *local equilibrium* with solid of composition $(C_{B1})_\alpha$ at the interface. The rest of the solid still being at initial composition C_B . Further it can be seen from Fig. 3.2 that to maintain equilibrium composition of $(C_{B1})_\alpha$ in whole solid, *mass transfer* takes place into the liquid phase, making it grow, and thus concentration in the solid phase eventually comes down to the equilibrium value of $(C_{B1})_\alpha$ from initial C_B . This process of redistribution of mass between two phases resulting in the increase of the liquid phase at the constant temperature of T_0 , is termed as *Dissolution*.

3.2 Past Numerical Studies For Dissolution of Multi-component Mixtures

Several mathematical models for the kinetics of dissolution of alloys have been developed over time. Most of the work for the modeling of dissolution kinetics has been carried out by considering the dissolution as Stefan problem [108]. Works of Whelan [53] incorporate the long range diffusion for describing the dissolution kinetics. His model was based on the analytical solutions for the interfacial positions as a function of time. Crank [26] in his work has also worked out the analytical solutions for the time dependent interfacial position. Similarly the effect of the long range diffusion had also been incorporated in the works of Baty et al. [63] for studying the dissolution of CuAl_2 in an Al-4Cu alloy and in the works of Tundal and Ryum [112] for studying the dissolution of particles in binary alloys. These authors have applied Finite Difference Model with bounded volume for studying dissolution. Nolfi [78] model incorporated the non-equilibrium conditions at the interface but lacked the interface migration. The non-equilibrium condition in [78] was modelled as Robin boundary condition at the interface and the solution was in form of Fourier series. Aron and Kotler [1] had combined the Whelan's solution with the incorporation of the Gibbs-Thomson effect to deal with the influence of curvature on the movement of interface. In the works of [1] the Robin boundary condition of [78] was transformed to the Dirichlet condition.

The kinetics of dissolution transformations with mechanical and chemical forces exerted on the interface had been studied by Svoboda et al. [109]. Their approach is based on the thermodynamics concepts that can be found in [48]. The dissolution of multi-component particles in multi-component alloys has been studied by Hubert [49] and Vitek et al. [118]. Reiso et al. [93] investigated the dissolution of Mg_2Si alloys in the aluminum alloys. Works of Vermolen et al. [117] has given mathematical insight in to the qualitative behavior of solutions of Stefan problem associated with the particle dissolution in multi-component alloys. Further they have used Finite Element method based on the moving grid method to analyse the Stefan problem. Other studies conducted by Vermolen on dissolution kinetics can be found in [115, 116]. Phase field modeling [73] for the dissolution kinetics has been adapted

in the works of [60] and [44]. Dissolution study of ZrO_2 by molten Zircaloy using Moving Particle Semi-Implicit (MPS) method can be found in [21].

Dissolution of multi-component mixtures being a two-phase transport phenomenon, has some inherent mathematical modeling issues, which are related to the accurate representation of the geometry of the evolving interface between liquid (dissolving phase) and solid phases (dissolved phase). Effect of evolving shape of the interface on dissolution has been studied in [68, 77, 6]. It has been seen that the effect of interface topology during dissolution process has been often taken care of, in studies concerned with the modeling of dissolution of porous crystals. With regard to the dissolution of porous crystals, macroscopic models are given in [33, 35, 59, 69, 30]. The analysis in these papers however does not take into account the pore geometry of evolving micro-structures. This missing link of representation of interface topology at pore scale for porous media dissolution can be found in macroscopic models developed by [79, 46].

In recent years, dissolution studies of multi-component mixtures has also been quite effectively done with the use of up-scaled macroscopic models primarily developed for studying micro-structure evolution in binary mixtures during the process of solidification of dendritic [43, 16, 17], columnar and equiaxed mushy zones [98, 99, 97]. Belloni et al. [13, 14] in their studies of dissolution of ZrO_2 by molten Zr has used an up-scaled mathematical model, which was inspired from the solidification model developed by Bousquet-Mélou et al. [43, 16, 17] for quantitative treatment of solidifying dendritic mushy-zone in case of binary mixtures. The efficacy of these solidification models for describing dissolution lies in the type of up-scaling procedure chosen for their derivation. All the aforementioned solidification models [43, 16, 17, 98, 99, 97, 13, 14] have been derived using an up-scaling procedure called *volume averaging* [124].

3.3 Corium Crust Modeled As Two-Phase Mushy Zone

It is observed in the CORDEB experiment [4] that dissolution of the crust creates channels of molten steel in the solid oxide crust. Owing to such a solid-liquid morphology of the crust, it has been modeled as porous medium in the present study. In general from the physics point of view the dissolution in the present work is modeled as two-phase transport phenomenon of mass, momentum, species and energy in the reacting porous medium. Due to this the modeling issue lies in the accurate micro-macroscopic description of transport phenomenon in the crust. Among all the mathematical methods summarised in the section 3.2, the method of *volume averaging* has been chosen in the present work to derive an up-scaled mathematical model for study of dissolution in the crust. It is however shown in the studies of [15, 75, 19] that *mixture*

theory can be used to postulate a macroscopic system of equations without any reference to the microscopic system of equations. Although it may be possible to deduce the necessary terms in the macroscopic model without any sort of averaging of microscopic equations, there are various advantages to the averaging procedure of microscopic model, as discussed by [29]. In a nutshell it can be summarised that due to its ability to incorporate complex microscopic information in the averaged system of equations and effective transport properties (like permeability, thermal and species diffusivity and mass diffusion coefficients), the method of volume averaging is often chosen for the derivation of macroscopic models.

3.4 Volume Averaged Mathematical Model For Describing Dissolution In Quaternary System (U, Zr, Fe, O)

The following analysis is concerned with the volume averaged [124] model development for the study of dissolution of ternary (U, Zr, O) solid crust by molten steel (mainly Fe). Since the mathematical analysis is based on the theoretical work done by Bousquet-Mélou et. al. [43, 16, 17] for the solidification of binary columnar dendritic mushy zone, the complete derivation of the model is not given in this work and the rigorous mathematics can be referred from works of Bousquet-Mélou et. al. [43, 16, 17] and Roux et. al. [98, 99, 97]. However, for the sake of understanding of physics behind the mathematical modeling, the important assumptions, geometrical restrictions, important mathematical theorems are properly invoked throughout this analysis either in the main document or in the Appendices.

The mathematical modeling is formally introduced next, starting with the writing of microscopic Partial Differential Equations (PDEs) for mass, momentum, species and energy, and later moving on to the macroscopic volume averaged model from this microscopic system of PDEs.

3.4.1 Microscopic System of PDEs, Satisfying Conservation at Local Level

A two phase crust of length scale l_s is considered as shown in Fig. 3.3. Within this crust, a Representative Elementary Volume (REV) of characteristic length scale (λ) is taken as averaging volume, and following assumptions has been made:

1. Thermochemical equilibrium exists at the interface between oxide and metal phase i.e.

$$\mu_{ox}^i = \mu_m^i \quad (i = U, Zr, Fe, O) \quad \text{at} \quad A_{moz} \quad (3.1)$$

$$T_{ox} = T_m \quad \text{at} \quad A_{moz} \quad (3.2)$$

where: A_{mox} is the interfacial area between oxide and metal phase. μ_k^i is the chemical potential of an i^{th} species in the k^{th} phase.

2. The advection of solid oxide phase (ox) is not considered.

$$\mathbf{v}_{ox} = 0 \quad (3.3)$$

3. Flow of metal phase (m) within the porous matrix has been considered to be laminar and incompressible.

$$\nabla \cdot \mathbf{v}_m = 0 \quad (3.4)$$

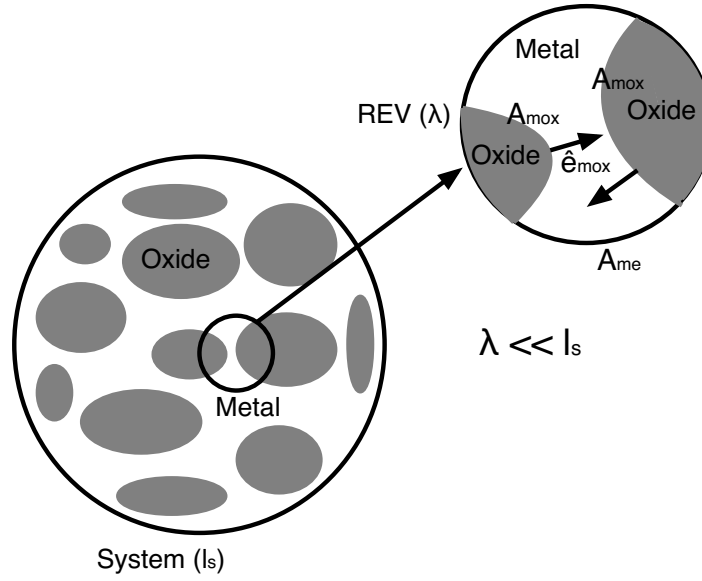


Figure 3.3: A two phase liquid metal and solid oxide crust with zoomed in Representative Elementary Volume (REV).

With this, the system of conservation equations for mass, momentum and energy at microscopic scale for four species (U, Zr, Fe, O) is written as:

3.4.1.1 Solid Oxide Phase (ox):

Mass Conservation

$$\frac{\partial}{\partial t}(\rho_{ox}) = 0 \quad (3.5)$$

Energy Conservation

$$\frac{\partial}{\partial t}(\rho_{ox} H_{ox}) = -\nabla \cdot \mathbf{q}_{ox} + \rho_{ox} \dot{Q}_{ox} \quad (3.6)$$

Species Conservation

$$\frac{\partial}{\partial t}(\rho_{ox} C_{ox}^U) = -\nabla \cdot \mathbf{J}_{ox}^U \quad (3.7)$$

$$\frac{\partial}{\partial t}(\rho_{ox}C_{ox}^{Zr}) = -\nabla \cdot \mathbf{J}_{ox}^{Zr} \quad (3.8)$$

$$\frac{\partial}{\partial t}(\rho_{ox}C_{ox}^{Fe}) = -\nabla \cdot \mathbf{J}_{ox}^{Fe} \quad (3.9)$$

$$\frac{\partial}{\partial t}(\rho_{ox}C_{ox}^O) = -\nabla \cdot \mathbf{J}_{ox}^O \quad (3.10)$$

3.4.1.2 Liquid Metal Phase (m):

Mass Conservation

$$\frac{\partial}{\partial t}(\rho_m) + \nabla \cdot (\rho_m \mathbf{v}_m) = 0 \quad (3.11)$$

Momentum Conservation

$$\frac{\partial}{\partial t}(\rho_m \mathbf{v}_m) + \nabla \cdot (\rho_m \mathbf{v}_m \mathbf{v}_m) = -\nabla P_m + \mu_m \nabla^2 \mathbf{v}_m + \rho_m \mathbf{g} \quad (3.12)$$

Energy Conservation

$$\frac{\partial}{\partial t}(\rho_m H_m) + \nabla \cdot (\rho_m H_m \mathbf{v}_m) = -\nabla \cdot \mathbf{q}_m + \rho_m \dot{Q}_m \quad (3.13)$$

Species Conservation

$$\frac{\partial}{\partial t}(\rho_m C_m^U) + \nabla \cdot (\rho_m C_m^U \mathbf{v}_m) = -\nabla \cdot \mathbf{J}_m^U \quad (3.14)$$

$$\frac{\partial}{\partial t}(\rho_m C_m^{Zr}) + \nabla \cdot (\rho_m C_m^{Zr} \mathbf{v}_m) = -\nabla \cdot \mathbf{J}_m^{Zr} \quad (3.15)$$

$$\frac{\partial}{\partial t}(\rho_m C_m^{Fe}) + \nabla \cdot (\rho_m C_m^{Fe} \mathbf{v}_m) = -\nabla \cdot \mathbf{J}_m^{Fe} \quad (3.16)$$

$$\frac{\partial}{\partial t}(\rho_m C_m^O) + \nabla \cdot (\rho_m C_m^O \mathbf{v}_m) = -\nabla \cdot \mathbf{J}_m^O \quad (3.17)$$

where: $\mathbf{J}_k^i = -\rho_k D_k^i \nabla C_k^i$ and $\mathbf{q}_k = -\Lambda_k \nabla T_k$ ($i = U, Zr, Fe, O; k = ox, m$) are diffusive and conductive fluxes given by Fick's and Fourier laws [52] respectively.

3.4.1.3 Continuity of Fluxes at the Interface Between Oxide and Metal:

$$\hat{\mathbf{e}}_{mox} \cdot \left[-\rho_{ox} \mathbf{w}_{mox} \right] = \hat{\mathbf{e}}_{mox} \cdot \left[\rho_m (\mathbf{v}_m - \mathbf{w}_{mox}) \right] \quad \text{at } \mathbf{A}_{mox} \quad (3.18)$$

$$\hat{\mathbf{e}}_{mox} \cdot \left[(-\rho_{ox} C_{ox}^U \mathbf{w}_{mox}) + \mathbf{J}_{ox}^U \right] = \hat{\mathbf{e}}_{mox} \cdot \left[\rho_m C_m^U (\mathbf{v}_m - \mathbf{w}_{mox}) + \mathbf{J}_m^U \right] \quad \text{at } \mathbf{A}_{mox} \quad (3.19)$$

$$\hat{\mathbf{e}}_{mox} \cdot \left[(-\rho_{ox} C_{ox}^{Zr} \mathbf{w}_{mox}) + \mathbf{J}_{ox}^{Zr} \right] = \hat{\mathbf{e}}_{mox} \cdot \left[\rho_m C_m^{Zr} (\mathbf{v}_m - \mathbf{w}_{mox}) + \mathbf{J}_m^{Zr} \right] \quad \text{at } \mathbf{A}_{mox} \quad (3.20)$$

$$\hat{\mathbf{e}}_{mox} \cdot \left[(-\rho_{ox} C_{ox}^{Fe} \mathbf{w}_{mox}) + \mathbf{J}_{ox}^{Fe} \right] = \hat{\mathbf{e}}_{mox} \cdot \left[\rho_m C_m^{Fe} (\mathbf{v}_m - \mathbf{w}_{mox}) + \mathbf{J}_m^{Fe} \right] \quad \text{at } \mathbf{A}_{mox} \quad (3.21)$$

$$\hat{\mathbf{e}}_{mox} \cdot \left[(-\rho_{ox} C_{ox}^O \mathbf{w}_{mox}) + \mathbf{J}_{ox}^O \right] = \hat{\mathbf{e}}_{mox} \cdot \left[\rho_m C_m^O (\mathbf{v}_m - \mathbf{w}_{mox}) + \mathbf{J}_m^O \right] \quad \text{at } \mathbf{A}_{mox} \quad (3.22)$$

$$\hat{\mathbf{e}}_{mox} \cdot \left[(-\rho_{ox} H_{ox} \mathbf{w}_{mox}) + \mathbf{q}_{ox} \right] = \hat{\mathbf{e}}_{mox} \cdot \left[\rho_m H_m (\mathbf{v}_m - \mathbf{w}_{mox}) + \mathbf{q}_m \right] \quad \text{at } \mathbf{A}_{mox} \quad (3.23)$$

where: \mathbf{w}_{mox} is the velocity of the dissolving/solidifying interface between the solid-oxide phase and liquid-metal phase, \mathbf{A}_{mox} is the interfacial area vector and $\hat{\mathbf{e}}_{mox}$ is the unit normal vector at the solid liquid interface, pointing from solid oxide phase to liquid metal phase, as shown in Fig. 3.3.

3.4.1.4 Relationship Among the Diffusive Fluxes of Quaternary Species (U, Zr, Fe, O)

One immediate problem which is encountered while moving from the volume averaging of binary microscopic system of PDEs [43, 16, 17, 98, 99, 97, 76] to ternary or even quaternary system of PDEs, is the knowing of the relationship among diffusive fluxes of species. The simplicity of binary system is, that the transport equations in each phase and flux condition at the interface has to be volume averaged and then solved, only for one species. The evolution of the other species towards its equilibrium can be calculated by the following constraint:

$$C_k^n = 1 - C_k^{n-1} \quad (3.24)$$

where: $k = m, ox$ phases; $n = 2$ in a binary system, and it is assumed that diffusivities of both the species in both the phases are known.

However such a constraint can not be written for a ternary or quaternary system. In other words, in a ternary or quaternary system the equilibrium values of each species in a phase can be known by the thermodynamical calculations but there is no elementary constraint like Eq. (3.24), through which the evolution of $(n - 1)$ species can be deduced from the n^{th} species. One of the ways to overcome this problem in the present work, is done by performing a thermochemical study of the quaternary system (U, Zr, Fe, O) , in order to derive some relationship between the diffusive fluxes (J_k^i) . Following section gives the details of the thermochemical calculations for the quaternary (U, Zr, Fe, O) system.

3.4.2 Thermochemical study for the Quaternary System (U, Zr, Fe, O)

The current equilibrium thermochemical calculations of (U, Zr, Fe, O) species are performed with IRSN's NUCLEA Toolbox. At first a brief introduction of the NUCLEA Toolbox in section (3.4.2.1) has been given, followed by the details of the thermochemical calculations in section (3.4.2.2).

3.4.2.1 The NUCLEA Toolbox for Simulation of the Thermochemical Equilibria

NUCLEA is an IRSN owned project, providing the following two functionalities:

1. A set of non-ideal solution based thermodynamic database, called NUCLEA database.
2. A Toolbox of computational thermodynamics, referred to as NUCLEA Toolbox.

Simply put, NUCLEA is a self-sufficient database-cum-computational Tool designed for the calculation of thermochemical equilibria. It is specially developed for in- and ex-vessel nuclear applications, related to severe accident scenario. NUCLEA database contains $18 + 2$ elements: $O - U - Zr - Ag - In - B - C - Fe - Cr - Ni - Ba - La - Sr - Ru - Al - Ca - Mg - Si + Ar - H$ and includes the following 15 oxide systems: $UO_2 - ZrO_2 - In_2O_3 - B_2O_3 - FeO - Fe_2O_3 - Cr_2O_3 - NiO - BaO - La_2O_3 - SrO - Al_2O_3 - CaO - MgO - SiO_2$. This database covers the entire range, from metal to oxide domains. The quaternary system (U, Zr, Fe, O) was developed from binary data, later completed by the ternary (U, Zr, O) [23, 11]. The whole database was recently improved, as explained in [10]. It is useful to mention the importance of data from the MASCA experiments for the validation of the quaternary system. After the MASCA program, several alternative thermochemical models of the quaternary were proposed in [9, 38, 37]. To supplement the database, NUCLEA also comes with a Gibbs function minimization solver. Such a solver with all its functionalities are integrated within NUCLEA Toolbox in the form of a

Python Application Program Interface (API). Because of this API, a user can write codes in Python, and access Gibbs solver to compute the thermochemical equilibrium for known initial moles and mass fractions of the system of species. An example of calculating the thermodynamic equilibrium for given initial moles of species at a particular temperature and pressure is illustrated in Fig. 3.4.

```
import nuclea

initial_composition = { 'U'   : 0.8,
                       'Zr'  : 1.0,
                       'O'   : 0.3,
                       'Fe'  : 0.1
                       }

eqp = nuclea.EqPhases()
db = eqp.define_data_base('NUCLEA-17_1')
pro = eqp.define_process('isobaric')
pro.set_pressure(1)
pro.set_temperature(2900)

#original equilibrium
eqp.set_nb_moles('U', initial_composition['U'])
eqp.set_nb_moles('Zr', initial_composition['Zr'])
eqp.set_nb_moles('O', initial_composition['O'])
eqp.set_nb_moles('Fe', initial_composition['Fe'])
|
#compute equilibrium
eq = eqp.compute_equilibrium()

#save equilibrium
eqp.save_equilibrium()
```

Figure 3.4: NUCLEA Toolbox API for calculating the thermodynamic equilibrium

3.4.2.2 Details of Thermochemical Calculations

Table 3.1 shows the variables for which thermochemical calculations has been performed. The study has been carried out to see the variation in parameters listed in Table 3.1, with the increasing moles of Iron (Fe). Moles of Iron (Fe) represented by (N^{Fe}) have been chosen as independent variable in order to simulate the accident scenario, where there is a continuous addition of molten Steel — coming mainly from the melting of reactor internals — to the relocated corium pool in the lower head of the reactor vessel.

n_m^O	mole fraction of O in metal phase
n_{ox}^{Fe}	mole fraction of Fe in oxide phase
n_{ox}^O	mole fraction of O in oxide phase
n_m^{Fe}	mole fraction of Fe in metal phase
$(U/Zr)_{ox}$	U/Zr molar ratio in oxide phase
$(U/Zr)_m$	U/Zr molar ratio in metal phase

Table 3.1: Thermochemical study parameters

With respect to the composition, the corium initially contains oxidised Uranium (UO_2), oxidised Zircaloy (ZrO_2), and unoxidised Zircaloy (Zr). Global corium composition can be described by following three parameters, listed in Table 3.2. To keep the analysis relevant to the broad range of

C_{uz}	It is the global ratio of U to Zr atoms in the corium. This value, depends mainly on the reactor design and accident scenario. Typically, for a Pressurised Water Reactor (PWR) it may go up to 1.45, and for a typical Boiling Water Reactor (BWR) it may go down to 0.8.
C_{ox}	It is the global degree of oxidation of Zr. The parameter depends on accidental scenario. For instance in a slow scenario like Small Break Loss Of Coolant Accident (SBLOCA), the degree of oxidation would be larger than in a fast scenario like Large Break Loss Of Coolant Accident (LBLOCA).
C_{sz}	It is the global ratio of Fe to Zr atoms. Depending on local configurations and timing in the accident scenario, the value of C_{sz} may vary between 0 and rather large values, although the global is typically around 1 for many reactors designs and accident scenario.

Table 3.2: Global corium composition parameters

reactors — PWR, BWR etc. — the thermochemical analysis has considered several values of C_{uz} and C_{ox} , which corresponds to different core inventory compositions, and degrees of oxidation of Zirconium (Zr).

Since, in the present study, the thermochemical study has been performed by prescribing different values of C_{uz} and C_{ox} , it is important to relate these two parameters with moles of U , Zr and O . This conversion of C_{uz} , C_{ox} , C_{sz} to N^U , N^{Zr} , N^O and N^{Fe} , is important because NUCLEA takes moles/mole fractions/mass fractions as a input, to calculate an equilibrium. This conversion is done by identifying the global inventory as given below by Eqs. (3.25, 3.26, 3.27, 3.28). All the global mole numbers of the three other species are normalised by the number of moles of Zr :

$$N^{Zr} = 1 \quad (3.25)$$

$$N^U = N^{Zr} C_{uz} = C_{uz} \quad (3.26)$$

$$N^O = 2(C_{uz} + C_{ox}) \quad (3.27)$$

$$N^{Fe} = N^{Zr} C_{sz} = C_{sz} \quad (3.28)$$

$$N^{tot} = N^{Zr} + N^U + N^O + N^{Fe} \quad (3.29)$$

where N_{tot} is the total number of moles and C_{sz} is the global Fe/Zr ratio.

For all thermochemical analysis, the version of thermochemical database used is NUCLEA-17_1. The present study deals with the miscibility gap where two liquid phases (oxide + metal) coexist. NUCLEA-17_1 calculations show that two liquid phases are obtained only in the temperature range

between 2900K and 3100K. Thus, this study is valid in this range of temperature. Result depicted in Fig. 3.5 shows that the equilibrium mole fractions do not depend visibly on temperature in that range. Therefore, all the calculations presented thereafter were performed at 2900K.

The main findings of the thermochemical calculations performed with NUCLEA are summarised in the following sections (3.4.2.3, 3.4.2.4, 3.4.2.5).

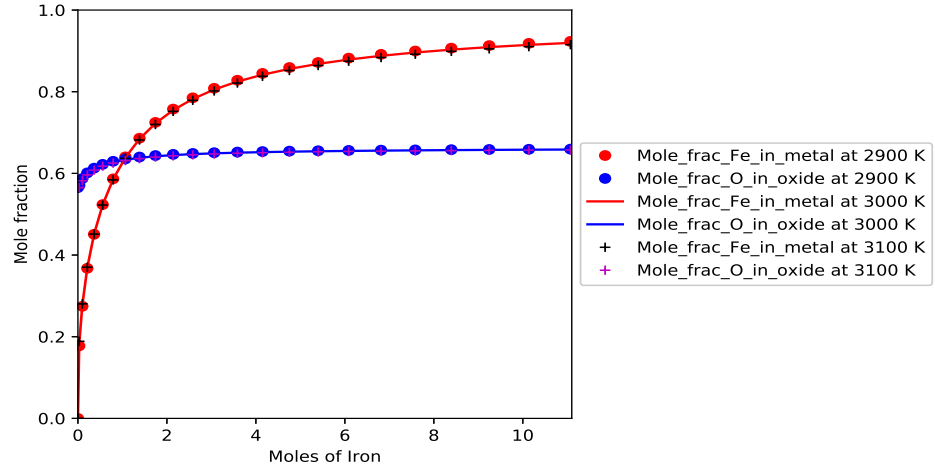


Figure 3.5: NUCLEA-17_1 data in the temperature range of existence of two immiscible liquid phases (2900 K - 3100 K) for $C_{uz} = 1.0$ and $C_{ox} = 0.3$

3.4.2.3 Absence of Fe in the Oxide Phase

For all the thermochemical calculations, no trace of Fe is predicted in the oxide phase. This is due to the immiscibility of Fe in UO_2 . Therefore, $n_{ox}^{Fe} = 0$ in all cases of interest. Thus, it is assumed that moles of Fe in oxide phase (N_{ox}^{Fe}) are zero:

$$N_{ox}^{Fe} = 0 \quad (3.30)$$

3.4.2.4 Solubility of Oxygen in the Metal Phase

From Fig. 3.6, it can be seen that only a small amount of O is found in the metal phase. This shows the limited solubility of O in metal phase. So, it can be neglected with respect to the mole fraction of the other elements, and the assumption that moles of O in metal phase (N_m^O) are zero can be made:

$$N_m^O = 0 \quad (3.31)$$

3.4.2.5 Invariance of U/Zr Ratio

Looking in detail at the variation of U/Zr ratio in the metal, it can be seen in Fig. 3.8, that it is slightly lower than the global value of C_{uz} in each case

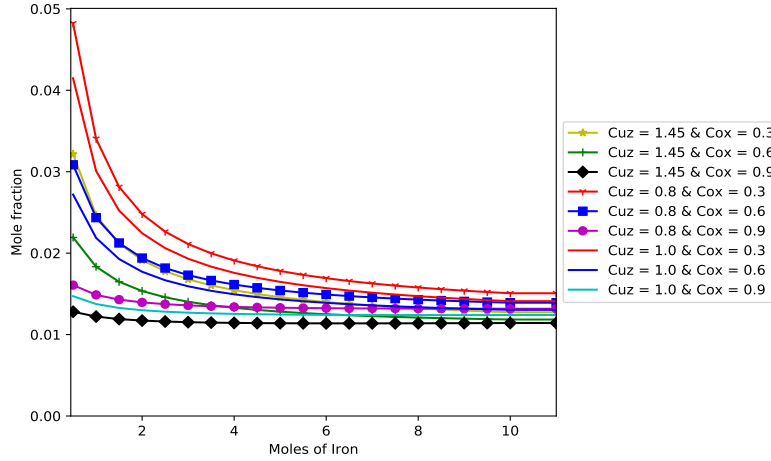


Figure 3.6: Mole fraction of O in metal phase Vs. Moles of Iron (n_m^O Vs. N^{Fe}) for various inventory compositions (C_{uz}), and degree of oxidation of Zr (C_{ox})

shown, and this deviation is more important when C_{uz} is greater than 1. This indicates a preferential extraction of Zr in the metal. However, this deviation remains small, especially in the asymptotic limit where the number of moles of iron is large. Figs. 3.7 and 3.8 show the evolution of U/Zr with the number of moles of Iron in oxide and metal phase respectively. It can be seen that U/Zr ratio almost remains constant in both phases. This shows that as a first approximation, it may be estimated that in both oxide and metal phases there is a C_{uz} atom of U , for one atom of Zr . It also means that there is the same partitioning coefficient K for both U and Zr atoms. This partitioning coefficient K , thus can be written as:

$$K = \frac{N_m^U}{N^U} = \frac{N_m^{Zr}}{N^{Zr}} = \frac{N_m^{Zr} + N_m^U}{(1 + C_{uz})} \quad (3.32)$$

Role of this partitioning coefficient K will be discussed in chapter 4.

3.4.2.6 Main Outcomes of the Thermochemical Study

Based on the observations made in section (3.4.2.3), it can be seen that no trace of Fe is found in oxide phase. Further, from section (3.4.2.4) small trace of O in metal phase can be neglected, and from section (3.4.2.5) the U/Zr ratio in both metal and oxide phase can be taken to be almost constant. Thus, these findings implies that during the dissolution of the oxide crust by molten steel, Fe atoms does not leave metal phase, O atoms does not leave oxide phase, and it is only $(U - Zr)$ atoms as a whole (because U/Zr ratio remains constant) gets transferred across the interface between the metal and oxide phases. Thus, the quaternary system (U, Zr, Fe, O) dispersed across metal and oxide phases, can be decomposed into *ternary in each phase* as:

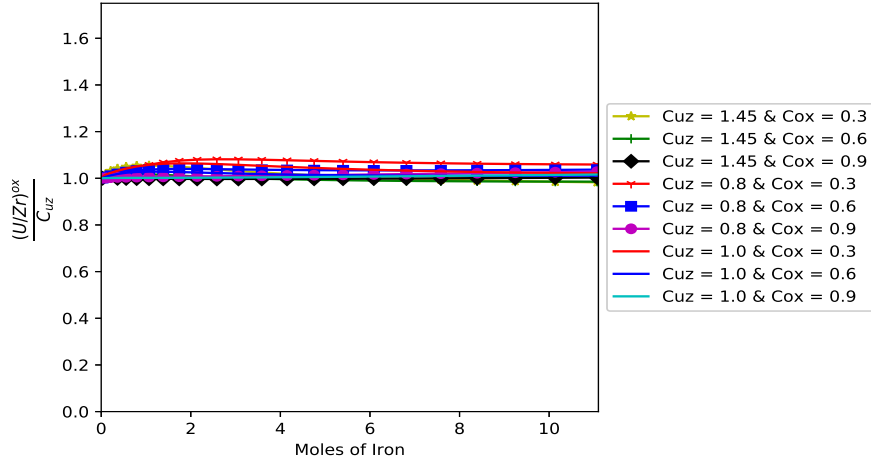


Figure 3.7: U/Zr molar ratio in oxide phase Vs. Moles of Iron ($\frac{(U/Zr)_{ox}}{C_{uz}}$ Vs. N^{Fe}) for various inventory compositions (C_{uz}) and degree of oxidation of Zr (C_{ox})

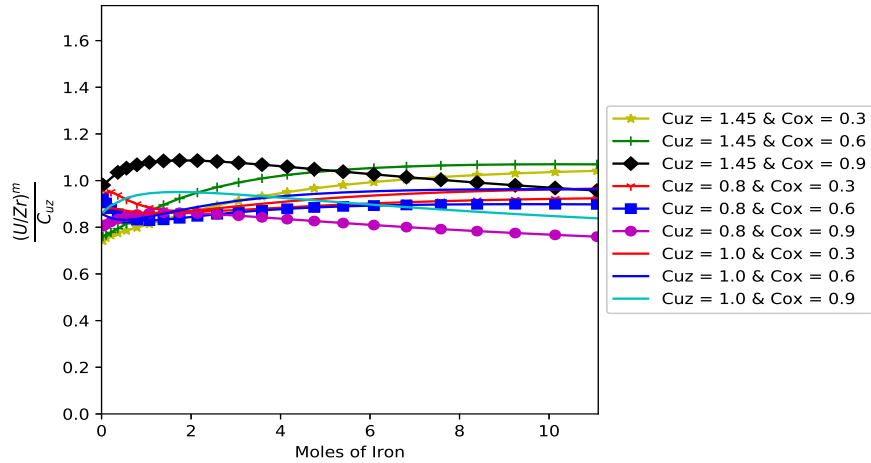


Figure 3.8: U/Zr molar ratio in metal phase Vs. Moles of Iron ($\frac{(U/Zr)_m}{C_{uz}}$ Vs. N^{Fe}) for various inventory compositions (C_{uz}) and degree of oxidation of Zr (C_{ox})

1. $(U - Zr) + Fe$ in metal phase.
2. $(U - Zr) + O$ in oxide phase.

The implications for such a *ternary in each phase* system for the full quaternary system (U, Zr, Fe, O) are discussed in the following sections.

3.4.3 Validity of Liquid-Oxide and Liquid-Metal Thermochemical Study for Solid-Oxide and Liquid-Metal (Crust-Molten Metal)

It is important to note again that the aforementioned thermochemical study is done for two immiscible liquid-oxide and liquid-metal system. This already has been explained in the previous section (3.4.2.2), where this liquid-liquid system was found to be valid over the temperature ranging from $2900K$ to $3100K$ (see Fig. 3.5).

However, the actual system of interest in the present thesis is the corium crust and liquid metal, which is a liquid-solid system, where crust being solid-oxide. Thus, it is important to validate the analysis of liquid-liquid system for liquid-solid system. Ideally, there should not be large difference between the equilibrium mole fractions of the species in liquid-liquid and liquid-solid system. Fig. 3.9, shows for an inventory of $C_{uz} = 1.0$ and $C_{ox} = 0.3$, the equilibrium mole fractions for Fe in metal phase and O in oxide phase for both the liquid-liquid and liquid-solid (crust) system. The liquid-solid (crust) system is found to exist in the temperature range of $2500 K$ to $2700 K$. Accordingly the present calculations of NUCLEA for liquid-solid system are done at $2700 K$. It can be observed from Fig. 3.9, that the equilibrium mole fractions for Fe in metal phase and O in oxide phase for both the liquid-liquid and liquid-solid (crust) system, has negligible difference. Thus, the present thermochemical study done for liquid-metal and liquid-oxide case, can be safely extrapolated to liquid-metal and solid-oxide crust case.

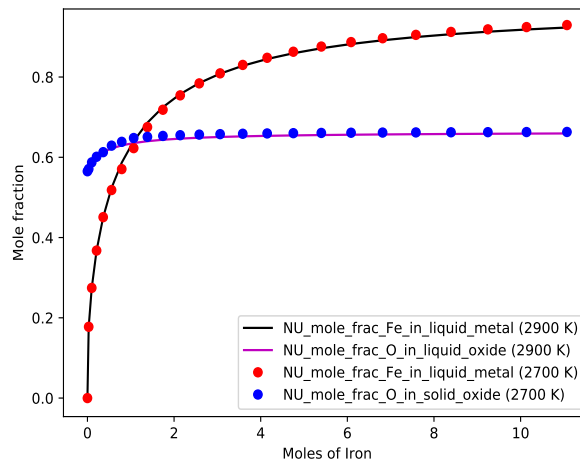


Figure 3.9: Validity of NUCLEA_17-1 liquid-metal and liquid-oxide thermochemical study for liquid-metal and solid-oxide (crust). Inventory is: $C_{uz} = 1.0$ and $C_{ox} = 0.3$

3.4.4 Reduction of Quaternary System (U, Zr, Fe, O) to a Ternary in each Phase

Based upon the main findings of the thermochemical study performed, following expressions are straight forward to write:

1. The outcome of the invariability of the (U/Zr) ratio, leads to the following relationship between n_{ox}^U and n_{ox}^{Zr} in oxide phase:

$$n_{ox}^U = \left(\frac{U}{Zr}\right)^{ox} n_{ox}^{Zr} \quad (3.33)$$

and in form of mass fractions it is:

$$\frac{C_{ox}^U}{M_U} = \left(\frac{U}{Zr}\right)^{ox} \frac{C_{ox}^{Zr}}{M_{Zr}} \quad (3.34)$$

since, $\left(\frac{U}{Zr}\right)^{ox}$ remains equal to global C_{uz} :

$$\boxed{\frac{C_{ox}^U}{M_U} = C_{uz} \frac{C_{ox}^{Zr}}{M_{Zr}}} \quad (3.35)$$

2. The outcome of the invariability of the (U/Zr) ratio, leads to the following relationship between n_m^U and n_m^{Zr} in metal phase:

$$n_m^U = \left(\frac{U}{Zr}\right)^m n_m^{Zr} \quad (3.36)$$

and in form of mass fractions it is:

$$\frac{C_m^U}{M_U} = \left(\frac{U}{Zr}\right)^m \frac{C_m^{Zr}}{M_{Zr}} \quad (3.37)$$

also since, $\left(\frac{U}{Zr}\right)^m$ remains equal to global C_{uz} :

$$\boxed{\frac{C_m^U}{M_U} = C_{uz} \frac{C_m^{Zr}}{M_{Zr}}} \quad (3.38)$$

3. The outcome of:

$$n_{ox}^{Fe} = 0 \quad (3.39)$$

in oxide phase leads to:

$$\boxed{C_{ox}^{Fe} = 0} \quad (3.40)$$

4. The outcome of:

$$n_m^O = 0 \quad (3.41)$$

in metal phase leads to:

$$\boxed{C_m^O = 0} \quad (3.42)$$

3.4.4.1 Reduction to Ternary Form in Oxide Phase

From section (3.4.1.1), substituting:

$$\mathbf{J}_{ox}^i = -\rho_{ox} D_{ox}^i \nabla C_{ox}^i \quad (3.43)$$

where: $i = (U, Zr, Fe, O)$

in the Eqs. (3.7, 3.8, 3.9, 3.10), and rewrite the microscopic system of PDEs for oxide phase like:

$$\frac{\partial}{\partial t}(\rho_{ox} C_{ox}^U) = \nabla \cdot (\rho_{ox} D_{ox}^U \nabla C_{ox}^U) \quad (3.44)$$

$$\frac{\partial}{\partial t}(\rho_{ox} C_{ox}^{Zr}) = \nabla \cdot (\rho_{ox} D_{ox}^{Zr} \nabla C_{ox}^{Zr}) \quad (3.45)$$

$$\frac{\partial}{\partial t}(\rho_{ox} C_{ox}^{Fe}) = \nabla \cdot (\rho_{ox} D_{ox}^{Fe} \nabla C_{ox}^{Fe}) \quad (3.46)$$

$$\frac{\partial}{\partial t}(\rho_{ox} C_{ox}^O) = \nabla \cdot (\rho_{ox} D_{ox}^O \nabla C_{ox}^O) \quad (3.47)$$

Further, substituting the Eq. (3.40) in Eq. (3.46), makes it redundant. Also, substitution of (3.35) in Eqs. (3.44, 3.45), gives the following set of equations:

$$\frac{\partial}{\partial t}(\rho_{ox} C_{ox}^{Zr}) = \nabla \cdot (\rho_{ox} D_{ox}^U \nabla C_{ox}^{Zr}) \quad (3.48)$$

$$\frac{\partial}{\partial t}(\rho_{ox} C_{ox}^{Zr}) = \nabla \cdot (\rho_{ox} D_{ox}^{Zr} \nabla C_{ox}^{Zr}) \quad (3.49)$$

This makes the Eqs. (3.48, 3.49) identical in the sense that with known diffusivities, D_{ox}^U and D_{ox}^{Zr} , either of the equation, Eq. (3.48) or Eq. (3.49), can be used to track concentration of Zr . Subsequently, with the known concentration of Zr , it is straightforward to calculate concentration of U from relation (3.35). Therefore, it can be seen that the oxide phase is identified by ternary system (U, Zr, O) with following PDEs:

$$\frac{\partial}{\partial t}(\rho_{ox} C_{ox}^U) = \nabla \cdot (\rho_{ox} D_{ox}^U \nabla C_{ox}^U) \quad (3.50)$$

and

$$\frac{\partial}{\partial t}(\rho_{ox}C_{ox}^{Zr}) = \nabla \cdot (\rho_{ox}D_{ox}^{Zr}\nabla C_{ox}^{Zr}) \quad (3.51)$$

and

$$\frac{\partial}{\partial t}(\rho_{ox}C_{ox}^O) = \nabla \cdot (\rho_{ox}D_{ox}^O\nabla C_{ox}^O) \quad (3.52)$$

where Eq. (3.50) and Eq. (3.51) are related by the constraint Eq. (3.35), as explained above.

However, the analysis in oxide phase is not that simpler, because in the oxide phase, the atoms are not independent, owing to the fact that oxide phase is a mixture of oxide species (UO_2 and ZrO_2) and metal species (U and Zr). Since, it has already been seen from Eq. (3.42) that O has a negligible solubility in metal phase, and hence, remains in the oxide phase, therefore, it is required to track the transfer of only *free* ($U - Zr$) atoms (U , Zr without any association with O atoms) from the oxide phase to metal phase, and vice-versa. In order to quantify the free U and Zr , the mass fractions in oxide phase can be written as following:

$$C_{ox}^{Zr} + C_{ox}^U + C_{ox}^O = 1 \quad (3.53)$$

Because there will be 2 atoms of O for every atom of U and Zr in oxide phase, the above expression can be written as:

$$C_{ox}^{Zr} + C_{ox}^U - \frac{1}{2}C_{ox}^O + \frac{3}{2}C_{ox}^O = 1 \quad (3.54)$$

Consequently, to track this transfer of *free* ($U - Zr$), a new species Y is defined, and its concentration in oxide phase (C_{ox}^Y) will be given as:

$$C_{ox}^Y = C_{ox}^{Zr} + C_{ox}^U - \frac{1}{2}C_{ox}^O \quad (3.55)$$

which is the total concentration of *free* U and *free* Zr . It can be rewritten as:

$$C_{ox}^Y = 1 - \frac{3}{2}C_{ox}^O \quad (3.56)$$

Also, the fixed atoms (UO_2 , ZrO_2) mass fractions in oxide phase is defined by a new species X , whose concentration in oxide phase is given by:

$$C_{ox}^X = \frac{3}{2}C_{ox}^O \quad (3.57)$$

Substituting, Eqs. (3.56, 3.57) in Eq. (3.54):

$$C_{ox}^Y + C_{ox}^X = 1 \quad (3.58)$$

Now, it can be understood from above analysis that to correctly describe the mass transfer of (U, Zr) across the phases, it is necessary to solve for C_{ox}^Y , which is *free* (U, Zr) , instead of Eqs. (3.50, 3.51). One of the ways to get the PDE for C_{ox}^Y is to use the PDE for O i.e. Eq. (3.52) and carry out the substitution of Eq. (3.56). This will give result into a change of variable from O to *free* (U, Zr) in the Eq. (3.52) to give a governing PDE for *free* (U, Zr) i.e. for C_{ox}^Y . This new PDE reads as:

$$\frac{\partial}{\partial t}(\rho_{ox}C_{ox}^Y) = \nabla \cdot (\rho_{ox}D_{ox}^O \nabla C_{ox}^Y) \quad (3.59)$$

Therefore, it can be concluded that diffusive transport in the oxide phase is described by the single species Y with concentration C_{ox}^Y .

Thus, summarising the analysis of going from quaternary system to a ternary system in this section, based upon the thermochemical study performed, it can be concluded that that the transport in the oxide phase will be governed by a single microscopic PDEs, which are given as :

Governing microscopic PDEs in oxide phase:

$$\boxed{\frac{\partial}{\partial t}(\rho_{ox}C_{ox}^Y) = \nabla \cdot (\rho_{ox}D_{ox}^O \nabla C_{ox}^Y)} \quad (3.60)$$

Governing microscopic PDE in oxide phase for *free* $(U - Zr)$ atoms (C_{ox}^Y), where Y , takes part in transport across the oxide-metal interface.

3.4.4.2 Reduction to Ternary Form in Metal Phase

From section (3.4.1.2), substituting:

$$\mathbf{J}_m^i = -\rho_m D_m^i \nabla C_m^i \quad (3.61)$$

where: $i = (U, Zr, Fe, O)$

in the Eqs. (3.14, 3.15, 3.16, 3.17), and rewrite the microscopic system of PDEs for metal phase like:

$$\frac{\partial}{\partial t}(\rho_m C_m^U) + \nabla \cdot (\rho_m C_m^U \mathbf{v}_m) = \nabla \cdot (\rho_m D_m^U \nabla C_m^U) \quad (3.62)$$

$$\frac{\partial}{\partial t}(\rho_m C_m^{Zr}) + \nabla \cdot (\rho_m C_m^{Zr} \mathbf{v}_m) = \nabla \cdot (\rho_m D_m^{Zr} \nabla C_m^{Zr}) \quad (3.63)$$

$$\frac{\partial}{\partial t}(\rho_m C_m^{Fe}) + \nabla \cdot (\rho_m C_m^{Fe} \mathbf{v}_m) = \nabla \cdot (\rho_m D_m^{Fe} \nabla C_m^{Fe}) \quad (3.64)$$

$$\frac{\partial}{\partial t}(\rho_m C_m^O) + \nabla \cdot (\rho_m C_m^O \mathbf{v}_m) = \nabla \cdot (\rho_m D_m^O \nabla C_m^O) \quad (3.65)$$

Further, substituting the Eq. (3.42) in Eq. (3.65), makes it redundant. Also, substitution of (3.38) in Eqs. (3.62, 3.63), gives the following set of equations:

$$\frac{\partial}{\partial t}(\rho_m C_m^{Zr}) + \nabla \cdot (\rho_m C_m^{Zr} \mathbf{v}_m) = \nabla \cdot (\rho_m D_m^U \nabla C_m^{Zr}) \quad (3.66)$$

$$\frac{\partial}{\partial t}(\rho_m C_m^{Zr}) + \nabla \cdot (\rho_m C_m^{Zr} \mathbf{v}_m) = \nabla \cdot (\rho_m D_m^{Zr} \nabla C_m^{Zr}) \quad (3.67)$$

This makes the Eqs. (3.66, 3.67) identical for the same reasons already explained for oxide phase. Therefore, it can be seen that the system becomes equivalent to a ternary mixture in the metal phase as well, like:

$$\frac{\partial}{\partial t}(\rho_m C_m^U) + \nabla \cdot (\rho_m C_m^U \mathbf{v}_m) = \nabla \cdot (\rho_m D_m^U \nabla C_m^U) \quad (3.68)$$

and

$$\frac{\partial}{\partial t}(\rho_m C_m^{Zr}) + \nabla \cdot (\rho_m C_m^{Zr} \mathbf{v}_m) = \nabla \cdot (\rho_m D_m^{Zr} \nabla C_m^{Zr}) \quad (3.69)$$

and

$$\frac{\partial}{\partial t}(\rho_m C_m^{Fe}) + \nabla \cdot (\rho_m C_m^{Fe} \mathbf{v}_m) = \nabla \cdot (\rho_m D_m^{Fe} \nabla C_m^{Fe}) \quad (3.70)$$

Unlike the oxide phase, the analysis for identifying the concentration of free ($U - Zr$) in metal phase (C_m^Y) is simpler, because the atoms are independent in this phase. Similar to oxide phase analysis, a new species Y representing the *free* (U, Zr) in metal phase is being chosen. Consequently, concentration for Y will be given represented by C_m^Y , which in this case is simply:

$$C_m^Y = 1 - C_m^{Fe} \quad (3.71)$$

To obtain the PDE for C_m^Y , the PDE for Fe i.e. Eq. (3.70) is used with the substitution of Eq. (3.71). This will give result into a change of variable from Fe to *free* (U, Zr) in the Eq. (3.70) to give a governing PDE for *free* (U, Zr) i.e. for C_m^Y in metal phase. This new PDE reads as:

$$\frac{\partial}{\partial t}(\rho_m C_m^Y) + \nabla \cdot (\rho_m C_m^Y \mathbf{v}_m) = \nabla \cdot (\rho_m D_m^{Fe} \nabla C_m^Y) \quad (3.72)$$

Therefore, it can be concluded that diffusive transport in the metal phase is described by the single species Y , with concentration C_m^Y .

Thus, summarising the analysis of going from quaternary system to a ternary system in this section, based upon the thermochemical study performed, it can be concluded that the transport in the metal phase will be governed by a single microscopic PDEs, which are given as :

Governing microscopic PDEs in metal phase:

$$\boxed{\frac{\partial}{\partial t}(\rho_m C_m^Y) + \nabla \cdot (\rho_m C_m^Y \mathbf{v}_m) = \nabla \cdot (\rho_m D_m^{Fe} \nabla C_m^Y)} \quad (3.73)$$

Governing microscopic PDE in metal phase for *free* ($U - Zr$) atoms (C_m^Y), where Y , takes part in transport across the oxide-metal interface

3.4.4.3 Reformulation of Interfacial Species' Flux Equations for Ternary in each Phase System

From section (3.4.1.1):

$$\mathbf{J}_{ox}^i = -\rho_{ox} D_{ox}^i \nabla C_{ox}^i \quad (3.74)$$

and from section (3.4.1.2):

$$\mathbf{J}_m^i = -\rho_m D_m^i \nabla C_m^i \quad (3.75)$$

where: $i = (U, Zr, Fe, O)$

substituting Eqs. (3.74, 3.75) in Eqs. (3.19, 3.20, 3.22), the system of species flux balance at the interface can be rewritten as the following:

$$\begin{aligned} \hat{\mathbf{e}}_{mox} \cdot [(-\rho_{ox} C_{ox}^U \mathbf{w}_{mox}) + (-\rho_{ox} D_{ox}^U \nabla C_{ox}^U)] = \\ \hat{\mathbf{e}}_{mox} \cdot [\rho_m C_m^U (\mathbf{v}_m - \mathbf{w}_{mox}) + (-\rho_m D_m^U \nabla C_m^U)] \quad at \quad \mathbf{A}_{mox} \quad (3.76) \end{aligned}$$

$$\begin{aligned} \hat{\mathbf{e}}_{mox} \cdot [(-\rho_{ox} C_{ox}^{Zr} \mathbf{w}_{mox}) + (-\rho_{ox} D_{ox}^{Zr} \nabla C_{ox}^{Zr})] = \\ \hat{\mathbf{e}}_{mox} \cdot [\rho_m C_m^{Zr} (\mathbf{v}_m - \mathbf{w}_{mox}) + (-\rho_m D_m^{Zr} \nabla C_m^{Zr})] \quad at \quad \mathbf{A}_{mox} \quad (3.77) \end{aligned}$$

$$\begin{aligned} \hat{\mathbf{e}}_{mox} \cdot [(-\rho_{ox} C_{ox}^{Fe} \mathbf{w}_{mox}) + (-\rho_{ox} D_{ox}^{Fe} \nabla C_{ox}^{Fe})] = \\ \hat{\mathbf{e}}_{mox} \cdot [\rho_m C_m^{Fe} (\mathbf{v}_m - \mathbf{w}_{mox}) + (-\rho_m D_m^{Fe} \nabla C_m^{Fe})] \quad at \quad \mathbf{A}_{mox} \quad (3.78) \end{aligned}$$

$$\begin{aligned} \hat{\mathbf{e}}_{mox} \cdot [(-\rho_{ox} C_{ox}^O \mathbf{w}_{mox}) + (-\rho_{ox} D_{ox}^O \nabla C_{ox}^O)] = \\ \hat{\mathbf{e}}_{mox} \cdot [\rho_m C_m^O (\mathbf{v}_m - \mathbf{w}_{mox}) + (-\rho_m D_m^O \nabla C_m^O)] \quad at \quad \mathbf{A}_{mox} \quad (3.79) \end{aligned}$$

Substitution of Eqs. (3.40, 3.42) in Eqs. (3.78, 3.79), gives:

$$\hat{\mathbf{e}}_{mox} \cdot [\rho_m C_m^{Fe} (\mathbf{v}_m - \mathbf{w}_{mox}) + (-\rho_m D_m^{Fe} \nabla C_m^{Fe})] = 0 \quad at \quad \mathbf{A}_{mox} \quad (3.80)$$

$$\hat{\mathbf{e}}_{mox} \cdot [(-\rho_{ox} C_{ox}^O \mathbf{w}_{mox}) + (-\rho_{ox} D_{ox}^O \nabla C_{ox}^O)] = 0 \quad at \quad \mathbf{A}_{mox} \quad (3.81)$$

which means that the gradients in each phase are related with O staying in oxide phase and Fe in metal phase. Further, substituting Eqs. (3.35, 3.38) in Eqs. (3.76) gives:

$$\begin{aligned} \hat{\mathbf{e}}_{mox} \cdot \left[(-\rho_{ox} C_{ox}^{Zr} \mathbf{w}_{mox}) + (-\rho_{ox} D_{ox}^U \nabla C_{ox}^{Zr}) \right] = \\ \hat{\mathbf{e}}_{mox} \cdot \left[\rho_m C_m^{Zr} (\mathbf{v}_m - \mathbf{w}_{mox}) + (-\rho_m D_m^U \nabla C_m^{Zr}) \right] \quad \text{at } \mathbf{A}_{mox} \end{aligned} \quad (3.82)$$

which is identical to Eq. (3.77). Thus, transport across the interface can be either described by Eq. (3.76) or by Eq. (3.77), because the ratio of U/Zr i.e. C_{uz} remains constant. However, these two equations do not completely describe the diffusive and advective fluxes of *free* ($U - Zr$) across the interface. Thus, similar to sections (3.4.4.1, 3.4.4.2), in this section as well the condition at the interface for *free* ($U - Zr$) can be derived. In order to work out the derivation, substitution of Eqs. (3.71, 3.56) in Eqs. (3.80, 3.81) respectively leads to the following set of equations:

$$\hat{\mathbf{e}}_{mox} \cdot \left[-\rho_m C_m^Y (\mathbf{v}_m - \mathbf{w}_{mox}) + (\rho_m D_m^{Fe} \nabla C_m^Y) + \rho_m (\mathbf{v}_m - \mathbf{w}_{mox}) \right] = 0 \quad (3.83)$$

$$\hat{\mathbf{e}}_{mox} \cdot \left[(\rho_{ox} C_{ox}^Y \mathbf{w}_{mox}) + (\rho_{ox} D_{ox}^O \nabla C_{ox}^Y) - (\rho_{ox} \mathbf{w}_{mox}) \right] = 0 \quad (3.84)$$

Since, *free* atoms of ($U - Zr$) are the one participating in the transport in and across the interface, Eq. (3.83, 3.84) should match at the interface, thus, equating the Eq. (3.83) and Eq. (3.84), and using the mass flux balance at the interface, Eq. (3.18), yields:

$$\begin{aligned} \hat{\mathbf{e}}_{mox} \cdot \left[-\rho_m C_m^Y (\mathbf{v}_m - \mathbf{w}_{mox}) + (\rho_m D_m^{Fe} \nabla C_m^Y) \right] = \\ \hat{\mathbf{e}}_{mox} \cdot \left[(\rho_{ox} C_{ox}^Y \mathbf{w}_{mox}) + (\rho_{ox} D_{ox}^O \nabla C_{ox}^Y) \right] \quad \text{at } \mathbf{A}_{mox} \end{aligned} \quad (3.85)$$

Continuity of advective and diffusive fluxes of *free* ($U - Zr$) or Y , at the interface is given by following relation:

$$\boxed{\begin{aligned} \hat{\mathbf{e}}_{mox} \cdot \left[-\rho_m C_m^Y (\mathbf{v}_m - \mathbf{w}_{mox}) + (\rho_m D_m^{Fe} \nabla C_m^Y) \right] = \\ \hat{\mathbf{e}}_{mox} \cdot \left[(\rho_{ox} C_{ox}^Y \mathbf{w}_{mox}) + (\rho_{ox} D_{ox}^O \nabla C_{ox}^Y) \right] \quad \text{at } \mathbf{A}_{mox} \end{aligned}} \quad (3.86)$$

3.4.5 Summarized Microscopic PDEs for Ternary in each Phase System

Oxide Phase:	
Mass Conservation	
$\frac{\partial}{\partial t}(\rho_{ox}) = 0$	(3.87)
Energy Conservation	
$\frac{\partial}{\partial t}(\rho_{ox} H_{ox}) = -\nabla \cdot \mathbf{q}_{ox} + \rho_{ox} \dot{Q}_{ox}$	(3.88)
Species Conservation	
$\frac{\partial}{\partial t}(\rho_{ox} C_{ox}^Y) = \nabla \cdot (\rho_{ox} D_{ox}^O \nabla C_{ox}^Y)$	(3.89)
Metal Phase:	
Mass Conservation	
$\frac{\partial}{\partial t}(\rho_m) + \nabla \cdot (\rho_m \mathbf{v}_m) = 0$	(3.90)
Momentum Conservation	
$\frac{\partial}{\partial t}(\rho_m \mathbf{v}_m) + \nabla \cdot (\rho_m \mathbf{v}_m \mathbf{v}_m) = -\nabla P_m + \mu_m \nabla^2 \mathbf{v}_m + \rho_m \mathbf{g}$	(3.91)
Energy Conservation	
$\frac{\partial}{\partial t}(\rho_m H_m) + \nabla \cdot (\rho_m H_m \mathbf{v}_m) = -\nabla \cdot \mathbf{q}_m + \rho_m \dot{Q}_m$	(3.92)
Species Conservation	
$\frac{\partial}{\partial t}(\rho_m C_m^Y) + \nabla \cdot (\rho_m C_m^Y \mathbf{v}_m) = \nabla \cdot (\rho_m D_m^{Fe} \nabla C_m^Y)$	(3.93)
Flux Balance at the Oxide-Metal Interface:	
$\hat{\mathbf{e}}_{mox} \cdot [-\rho_{ox} \mathbf{w}_{mox}] = \hat{\mathbf{e}}_{mox} \cdot [\rho_m (\mathbf{v}_m - \mathbf{w}_{mox})] \quad \text{at } \mathbf{A}_{mox}$	(3.94)
$\hat{\mathbf{e}}_{mox} \cdot [-\rho_m C_m^Y (\mathbf{v}_m - \mathbf{w}_{mox}) + (\rho_m D_m^{Fe} \nabla C_m^Y)] =$	(3.95)
$\hat{\mathbf{e}}_{mox} \cdot [(\rho_{ox} C_{ox}^Y \mathbf{w}_{mox}) + (\rho_{ox} D_{ox}^O \nabla C_{ox}^Y)] \quad \text{at } \mathbf{A}_{mox}$	
$\hat{\mathbf{e}}_{mox} \cdot [(-\rho_{ox} H_{ox} \mathbf{w}_{mox}) + \mathbf{q}_{ox}] = \hat{\mathbf{e}}_{mox} \cdot [\rho_m H_m (\mathbf{v}_m - \mathbf{w}_{mox}) + \mathbf{q}_m] \quad \text{at } \mathbf{A}_{mox}$	(3.96)

Figure 3.10: Summarized microscopic PDEs for ternary in each phase model

3.4.6 Volume Averaging

Next it is required to derive a macroscopic volume averaged model to describe dissolution as a two-phase transport phenomenon. The mathematical analysis presented in this section will be an excerpt from the works of Bousquet-Mélou et al. [43, 16, 17]. Before starting the formal averaging, it is now important to identify the boundary conditions at area of entrances and exit of metal (\mathbf{A}_{me}) and oxide phase (\mathbf{A}_{oxe}) shown in Fig. 3.3. The boundary conditions are:

$$\mathbf{v}_m = F_v(\mathbf{r}, t) \text{ at } \mathbf{A}_{me} \quad (3.97)$$

At this point, the functions F_v is unknown. Also, along with the already identified assumptions in section (3.4.1), an other important assumption concerning the independence of concentration from temperature at the oxide metal interface is brought up in the analysis of dissolution. Thus:

$$C_k^Y \neq f(T_k), \quad k = (ox, m) \text{ at } \mathbf{A}_{mox} \quad (3.98)$$

This essentially means that C_k^Y is not a function or decoupled from T_k at the metal oxide interface \mathbf{A}_{mox} .

Prior to the formal averaging it is now important to introduce the *Gray's decomposition* [45] for all microscopic fields. This decomposition reads:

$$\Psi_k = \langle \Psi_k \rangle^k + \tilde{\Psi}_k, \quad k = (ox, m) \quad (3.99)$$

where any microscopic field represented as Ψ_k is decomposed into its intrinsic phase averaged field given as $\langle \Psi_k \rangle^k$, and the corresponding deviation field represented as $\tilde{\Psi}_k$.

With these assumptions and using the definition of *Gray's decomposition*, the Eqs. (3.87 - 3.96) are volume averaged using the *Spatial averaging theorem* [121], general Leibniz integral rule [111], explained in Appendix (C), to obtain the unclosed form of macroscopic equations. The rigorous mathematical analysis can be referred from the theoretical works of Bousquet-Mélou et. al [43, 16, 17]. The summary of unclosed volume averaged form of the Eqs. (3.87 - 3.96) and closure work is jotted down in the following sections.

3.4.6.1 Mass Conservation Equation

First, volume averaging the jump condition Eq. (3.94) gives:

$$-\frac{1}{V} \int_{A_{mox}(t)} \hat{\mathbf{e}}_{mox} \cdot \rho_{ox} \mathbf{w}_{mox} dA - \frac{1}{V} \int_{A_{mox}(t)} \hat{\mathbf{e}}_{mox} \cdot \rho_m (\mathbf{v}_m - \mathbf{w}_{mox}) dA = 0 \quad (3.100)$$

further defining:

$$\dot{m}_{ox} = -\frac{1}{V} \int_{A_{mox}(t)} \hat{\mathbf{e}}_{mox} \cdot \rho_{ox} \mathbf{w}_{mox} dA \quad (3.101)$$

and

$$\dot{m}_m = -\frac{1}{V} \int_{A_{mox}(t)} \hat{\mathbf{e}}_{mox} \cdot \rho_m (\mathbf{v}_m - \mathbf{w}_{mox}) dA \quad (3.102)$$

it can be written as:

$$\dot{m}_m + \dot{m}_{ox} = 0 \quad (3.103)$$

or

$$\sum_{k=ox}^m \dot{m}_k = 0, \quad k = (ox, m) \quad (3.104)$$

Here, \dot{m}_{ox} being negative is termed as *rate of dissolution*. Secondly, volume averaging the mass conservation equations for both oxide and metal phase, Eqs. (3.87, 3.90), and using the Eq. (3.101), gives the volume averaged equation for the metal-oxide mixture as a whole:

$$\frac{\partial}{\partial t} (\varepsilon_m \rho_m) + \nabla \cdot (\varepsilon_m \rho_m \langle \mathbf{v}_m \rangle^m) = -\dot{m}_{ox} \quad (3.105)$$

$$\dot{m}_{ox} = \frac{\partial}{\partial t} (\varepsilon_{ox} \rho_{ox}) \quad (3.106)$$

3.4.6.2 Momentum Conservation Equation

Volume averaging Navier-Stokes equation, Eq. (3.91), after simplifications explained in [124], gives unclosed macroscopic NS equation:

$$\begin{aligned}
 & \frac{\partial}{\partial t}(\varepsilon_m \rho_m \langle \mathbf{v}_m \rangle^m) + \nabla \cdot (\varepsilon_m \rho_m \langle \mathbf{v}_m \rangle^m \langle \mathbf{v}_m \rangle^m) + \nabla \cdot (\varepsilon_m \rho_m \langle \tilde{\mathbf{v}}_m \tilde{\mathbf{v}}_m \rangle^m) \\
 & \quad + \frac{1}{V} \int_{A_{mox}(t)} \hat{\mathbf{e}}_{mox} \cdot (\mathbf{v}_m - \mathbf{w}_{mox}) \rho_m \mathbf{v}_m \, dA \\
 & = -\varepsilon_m \nabla \langle P_m \rangle^m + \varepsilon_m \mu_m \nabla^2 \langle \mathbf{v}_m \rangle^m + \varepsilon_m \rho_m \mathbf{g} \quad (3.107) \\
 & \quad + \frac{1}{V} \int_{A_{mox}(t)} \hat{\mathbf{e}}_{mox} \cdot (-\tilde{P}_m \mathbf{I} + \mu_m \nabla \tilde{\mathbf{v}}_m) \, dA \\
 & \quad + \mu_m \nabla \cdot \left\{ \frac{1}{V} \int_{A_{mox}(t)} \hat{\mathbf{e}}_{mox} \cdot \tilde{\mathbf{v}}_m \, dA \right\}
 \end{aligned}$$

3.4.6.3 Species Conservation Equation

In this analysis of dissolution, the solute transport is considered separately in oxide and metal phase, and no specific assumption has been made regarding the diffusion in solid oxide phase. This gives rise to two individual species transport equations, one in oxide phase and the other one is metal phase. The unclosed volume averaged form of microscopic species conservation equations, Eqs. (3.89, 3.93), are presented below:

Oxide Phase:

$$\begin{aligned}
 & \frac{\partial}{\partial t}(\varepsilon_{ox} \rho_{ox} \langle C_{ox}^Y \rangle^{ox}) + \frac{1}{V} \int_{A_{mox}(t)} \rho_{ox} C_{ox}^Y \hat{\mathbf{e}}_{mox} \cdot (-\mathbf{w}_{mox}) \, dA \\
 & \quad = \rho_{ox} \varepsilon_{ox} \nabla \cdot (D_{ox}^O \nabla \langle C_{ox}^Y \rangle^{ox}) \\
 & \quad \quad + \frac{\rho_{ox} D_{ox}^O}{V} \int_{A_{mox}(t)} \hat{\mathbf{e}}_{mox} \cdot \nabla \tilde{C}_{ox}^Y \, dA \quad (3.108) \\
 & \quad + \nabla \cdot \left\{ \frac{\rho_{ox} D_{ox}^O}{V} \int_{A_{mox}(t)} \hat{\mathbf{e}}_{mox} \tilde{C}_{ox}^Y \, dA \right\}
 \end{aligned}$$

Metal Phase:

$$\begin{aligned}
 & \frac{\partial}{\partial t} (\varepsilon_m \rho_m \langle C_m^Y \rangle^m) + \nabla \cdot (\varepsilon_m \rho_m \langle C_m^Y \rangle^m \langle \mathbf{v}_m \rangle^m) + \nabla \cdot (\varepsilon_m \rho_m \langle \tilde{\mathbf{v}}_m \tilde{C}_m^Y \rangle^m) \\
 & + \frac{1}{V} \int_{A_{mox}(t)} \rho_m C_m^Y \hat{\mathbf{e}}_{mox} \cdot (\mathbf{v}_m - \mathbf{w}_{mox}) dA \\
 & = \rho_m \varepsilon_m \nabla \cdot (D_m^{Fe} \nabla \langle C_m^Y \rangle^m) \\
 & + \frac{\rho_{ox} D_m^{Fe}}{V} \int_{A_{mox}(t)} \hat{\mathbf{e}}_{mox} \cdot \nabla \tilde{C}_m^Y \\
 & + \nabla \cdot \left\{ \frac{\rho_m D_m^{Fe}}{V} \int_{A_{mox}(t)} \hat{\mathbf{e}}_{mox} \tilde{C}_m^Y dA \right\}
 \end{aligned} \tag{3.109}$$

3.4.6.4 Rate of Dissolution

Volume averaging the Eq. (3.95) gives the unclosed form of dissolution rate (\dot{m}_{ox}):

$$\begin{aligned}
 & -\frac{1}{V} \int_{A_{mox}(t)} \rho_m C_m^Y \hat{\mathbf{e}}_{mox} \cdot (\mathbf{v}_m - \mathbf{w}_{mox}) dA + \frac{1}{V} \int_{A_{mox}(t)} \rho_m D_m^{Fe} \hat{\mathbf{e}}_{mox} \cdot \nabla C_m^Y dA \\
 & = \frac{1}{V} \int_{A_{mox}(t)} \rho_{ox} C_{ox}^Y \hat{\mathbf{e}}_{mox} \cdot \mathbf{w}_{mox} dA \\
 & + \frac{1}{V} \int_{A_{mox}(t)} \rho_{ox} D_{ox}^O \hat{\mathbf{e}}_{mox} \cdot \nabla C_{ox}^Y dA
 \end{aligned} \tag{3.110}$$

3.4.6.5 Energy Conservation Equation

Similarly, the unclosed volume averaged form of microscopic energy equations, Eqs. (3.88, 3.92), are given by:

Oxide Phase:

$$\begin{aligned}
 \frac{\partial}{\partial t}(\varepsilon_{ox}\rho_{ox}\langle H_{ox}\rangle^{ox}) + \frac{1}{V}\int_{A_{mox}(t)}\rho_{ox}H_{ox}\hat{\mathbf{e}}_{mox}\cdot(-\mathbf{w}_{mox})dA \\
 = \nabla\cdot(\varepsilon_{ox}\Lambda_{ox}\nabla\langle T_{ox}\rangle^{ox}) \\
 + \frac{\Lambda_{ox}}{V}\int_{A_{mox}(t)}\hat{\mathbf{e}}_{mox}\cdot\nabla T_{ox} \\
 + \nabla\cdot\left\{\frac{\Lambda_{ox}}{V}\int_{A_{mox}(t)}\hat{\mathbf{e}}_{mox}\tilde{T}_{ox}dA\right\}
 \end{aligned} \tag{3.111}$$

Metal Phase:

$$\begin{aligned}
 \frac{\partial}{\partial t}(\varepsilon_m\rho_m\langle H_m\rangle^m) + \frac{1}{V}\int_{A_{mox}(t)}\rho_{ox}H_m\hat{\mathbf{e}}_{mox}\cdot(\mathbf{v}_m - \mathbf{w}_{mox})dA \\
 + \nabla\cdot(\varepsilon_m\rho_m\langle H_m\rangle^m\langle \mathbf{v}_m\rangle^m) + \nabla\cdot(\varepsilon_m\rho_m\langle \tilde{\mathbf{v}}_m\tilde{H}_m\rangle^m) \\
 = \nabla\cdot(\varepsilon_m\Lambda_m\nabla\langle T_m\rangle^m) \\
 + \frac{\Lambda_m}{V}\int_{A_{mox}(t)}\hat{\mathbf{e}}_{mox}\cdot\nabla T_m \\
 + \nabla\cdot\left\{\frac{\Lambda_m}{V}\int_{A_{mox}(t)}\hat{\mathbf{e}}_{mox}\tilde{T}_m dA\right\}
 \end{aligned} \tag{3.112}$$

Assuming that there exist a thermal equilibrium between oxide and metal phase [67], i.e. ($\langle T_m \rangle^m \simeq \langle T_{ox} \rangle^{ox} \simeq \langle T \rangle$), the above two averaged equations can be combined into one single energy equation of the metal-oxide mixture. With this assumption adding Eqs. (3.111, 3.112), and making use of the volume averaged form of Eq. (3.96), the unclosed volume averaged form of energy conservation reduces to:

$$\begin{aligned} \frac{\partial}{\partial t}(\langle \rho \rangle \langle H \rangle) + \nabla \cdot (\varepsilon_m \rho_m \langle H_m \rangle^m \langle \mathbf{v}_m \rangle^m) + \nabla \cdot (\varepsilon_m \rho_m \langle \tilde{\mathbf{v}}_m \tilde{H}_m \rangle^m) \\ = \nabla \cdot (\Lambda_{mix} \nabla \langle T \rangle) \\ + \nabla \cdot \left\{ \frac{1}{V} \int_{A_{mox}(t)} \hat{\mathbf{e}}_{mox} (\Lambda_m \tilde{T}_m + \Lambda_{ox} \tilde{T}_{ox}) dA \right\} \end{aligned} \quad (3.113)$$

where:

$$\langle \rho \rangle = \varepsilon_{ox} \rho_{ox} + \varepsilon_m \rho_m \quad (3.114)$$

$$\langle H \rangle = \frac{\varepsilon_{ox} \rho_{ox} \langle H_{ox} \rangle^{ox} + \varepsilon_m \rho_m \langle H_m \rangle^m}{\langle \rho \rangle} \quad (3.115)$$

$$\Lambda_{mix} = \varepsilon_{ox} \Lambda_{ox} + \varepsilon_m \Lambda_m \quad (3.116)$$

3.4.7 Closed Form of Macroscopic Model

To carry out the closure analysis it is again required to invoke Gray's decomposition detailed in section (3.4.6). This decomposition has been carried out for all the microscopic fields in the set of Eqs. (3.87 - 3.93) giving rise to the microscopic set of PDEs having partial derivatives of intrinsic phase average fields ($\langle \Psi_k \rangle^k$) and deviation fields ($\tilde{\Psi}_k$).

These new set of microscopic PDEs are then subtracted from unclosed macroscopic Eqs. (3.105 - 3.113). This gives rise to set of complex deviation equations. Bousquet M elou [16] has shown that this set of complex deviation equations can be simplified on the basis of several assumptions detailed in [43] and order of magnitude analysis detailed in [17, 16, 124, 43], to finally produce the following deviation problems for momentum (section (3.4.7.1)), species (section (3.4.7.2)) and temperature (section(3.4.7.3)).

3.4.7.1 Momentum Deviation Relations and Closure

$$\nabla \cdot \tilde{\mathbf{v}}_m = 0 \quad (3.117)$$

$$\begin{aligned} \rho_m \mathbf{v}_m \cdot \nabla \tilde{\mathbf{v}}_m &= -\nabla \tilde{P}_m + \mu_m \nabla^2 \tilde{\mathbf{v}}_m \\ -\frac{1}{V_m} \int_{A_{mox}(t)} \hat{\mathbf{e}}_{mox} \cdot (-\tilde{P}_m \mathbf{I} + \mu_m \nabla \tilde{\mathbf{v}}_m) dA \end{aligned} \quad (3.118)$$

$$\tilde{\mathbf{v}}_m = -\langle \mathbf{v}_m \rangle^m \text{ at } \mathbf{A}_{mox} \quad (3.119)$$

$$\tilde{\mathbf{v}}_m = \mathbf{Y} \cdot \langle \mathbf{v}_m \rangle^m \text{ at } \mathbf{A}_{me} \quad (3.120)$$

It is assumed here that the B.C. given by Eq. (3.97) is equivalent to $\mathbf{v}_m = \mathbf{X} \cdot \langle \mathbf{v}_m \rangle^m$, where \mathbf{X} is a second order tensor given by: $\mathbf{Y} = \mathbf{X} - \mathbf{I}$. This closure problem given by Eqs. (3.117 - 3.120) indicates that $\langle \mathbf{v}_m \rangle^m$ is source of velocity fluctuations ($\tilde{\mathbf{v}}_m$) and pressure fluctuations (\tilde{P}_m). Thus, following the analysis given in Whitaker [124, 122] and Goyeau et al. [43], the expression for $\tilde{\mathbf{v}}_m$ and \tilde{P}_m can be written as:

$$\tilde{\mathbf{v}}_m = \mathbf{M} \cdot \langle \mathbf{v}_m \rangle^m \quad (3.121)$$

$$\tilde{P}_m = \mu_m \mathbf{m} \cdot \langle \mathbf{v}_m \rangle^m \quad (3.122)$$

Further, the following decomposition from Whitaker [124, 122] has been considered to separate linear friction and inertial effect:

$$\mathbf{M} = \mathbf{b}(\varepsilon_m) + \mathbf{c}(\varepsilon_m, \langle \mathbf{v}_m \rangle^m) \quad (3.123)$$

$$\mathbf{m} = \mathbf{B}(\varepsilon_m) + \mathbf{C}(\varepsilon_m, \langle \mathbf{v}_m \rangle^m) \quad (3.124)$$

Thus, the Eqs. (3.121, 3.122) takes the following form:

$$\tilde{\mathbf{v}}_m = \mathbf{B}(\varepsilon_m) \cdot \langle \mathbf{v}_m \rangle^m + \mathbf{C}(\varepsilon_m, \langle \mathbf{v}_m \rangle^m) \cdot \langle \mathbf{v}_m \rangle^m \quad (3.125)$$

$$\tilde{P}_m = \mu_m \mathbf{b}(\varepsilon_m) \cdot \langle \mathbf{v}_m \rangle^m + \mu_m \mathbf{c}(\varepsilon_m, \langle \mathbf{v}_m \rangle^m) \cdot \langle \mathbf{v}_m \rangle^m \quad (3.126)$$

where \mathbf{B} , \mathbf{b} , \mathbf{C} and \mathbf{c} are solutions to the following boundary value problems, Problem 1 and Problem 2.

Problem 1:

$$\nabla \cdot \mathbf{B} = 0 \quad (3.127)$$

$$-\nabla \mathbf{b} + \nabla^2 \mathbf{B} - \frac{1}{V_m} \int_{A_{moz}(t)} \hat{\mathbf{e}}_{moz} \cdot (\nabla \mathbf{B} - \mathbf{bI}) dA = 0 \quad (3.128)$$

$$\mathbf{B} = -\mathbf{I} \text{ at } \mathbf{A}_{moz} \quad (3.129)$$

$$\mathbf{b}(\mathbf{r} + \lambda_i) = \mathbf{b}(\mathbf{r}) \text{ at } \mathbf{A}_{me} \quad (3.130)$$

$$\mathbf{B}(\mathbf{r} + \lambda_i) = \mathbf{B}(\mathbf{r}) \text{ at } \mathbf{A}_{me} \quad (3.131)$$

$$\langle \mathbf{B} \rangle^m = 0 \quad (3.132)$$

Problem 2:

$$\nabla \cdot \mathbf{C} = 0 \quad (3.133)$$

$$-\nabla \mathbf{c} + \nabla^2 \mathbf{C} - \frac{1}{V_m} \int_{A_{moz}(t)} \hat{\mathbf{e}}_{moz} \cdot (\nabla \mathbf{C} - \mathbf{cI}) dA = \rho_m \mu_m^{-1} \mathbf{v}_m \cdot \nabla (\mathbf{B} + \mathbf{C}) \quad (3.134)$$

$$\mathbf{C} = 0 \text{ at } \mathbf{A}_{moz} \quad (3.135)$$

$$\mathbf{c}(\mathbf{r} + \lambda_i) = \mathbf{c}(\mathbf{r}) \text{ at } \mathbf{A}_{me} \quad (3.136)$$

$$\mathbf{C}(\mathbf{r} + \lambda_i) = \mathbf{C}(\mathbf{r}) \text{ at } \mathbf{A}_{me} \quad (3.137)$$

$$\langle \mathbf{C} \rangle^m = 0 \quad (3.138)$$

In Whitaker [124, 122, 123], the following terms:

$$-\frac{1}{V_m} \int_{A_{moz}(t)} \hat{\mathbf{e}}_{moz} \cdot (\nabla \mathbf{C} - \mathbf{cI}) dA \quad (3.139)$$

and

$$-\frac{1}{V_m} \int_{A_{moz}(t)} \hat{\mathbf{e}}_{moz} \cdot (\nabla \mathbf{B} - \mathbf{bI}) dA \quad (3.140)$$

in Eq. (3.134) and Eq. (3.128) respectively has been related to the Forchheimer correction tensor (\mathbf{F}) and permeability tensor (\mathbf{K}) as:

$$\varepsilon_m \mathbf{K}^{-1} = -\frac{1}{V_m} \int_{A_{moz}(t)} \hat{\mathbf{e}}_{moz} \cdot (\nabla \mathbf{B} - \mathbf{bI}) dA \quad (3.141)$$

$$\varepsilon_m \mathbf{K}^{-1} \cdot \mathbf{F} = -\frac{1}{V_m} \int_{A_{mox}(t)} \hat{\mathbf{e}}_{mox} \cdot (\nabla \mathbf{C} - \mathbf{cI}) dA \quad (3.142)$$

Finally, making use of deviation relations given by Eqs. (3.125, 3.126) and definition of Forchheimer correction tensor (\mathbf{F}) and permeability tensor (\mathbf{K}), in unclosed Navier-Stokes Eq. (3.107), it is easy to see the following closed form of Navier-Stokes equation:

Closed Navier-Stokes Equation

$$\begin{aligned} \frac{\partial}{\partial t}(\varepsilon_m \rho_m \langle \mathbf{v}_m \rangle^m) + \nabla \cdot (\varepsilon_m \rho_m \langle \mathbf{v}_m \rangle^m \langle \mathbf{v}_m \rangle^m) &= -\varepsilon_m \nabla \langle P_m \rangle^m \\ &+ \varepsilon_m \mu_m \nabla^2 \langle \mathbf{v}_m \rangle^m + \mu_m \nabla \varepsilon_m \cdot \langle \mathbf{v}_m \rangle^m \\ &+ \mu_m (\nabla^2 \varepsilon_m) \langle \mathbf{v}_m \rangle^m - \varepsilon_m^2 \mu_m \mathbf{K}^{-1} \cdot \langle \mathbf{v}_m \rangle^m \\ &- \varepsilon_m^2 \mu_m \mathbf{K}^{-1} \cdot \mathbf{F} \cdot \langle \mathbf{v}_m \rangle^m + \varepsilon_m \rho_m \mathbf{g} \end{aligned} \quad (3.143)$$

3.4.7.2 Species Deviation Relations and Closure

Deviation equations for the species system in metal and oxide phase after following the simplifications explained in Bousquet-Mélou [16] are:

$$D_{ox}^O \nabla^2 \tilde{C}_{ox}^Y - \frac{1}{\varepsilon_{ox}} \left\{ \frac{1}{V} \int_{A_{mox}(t)} D_{ox}^O \hat{\mathbf{e}}_{mox} \cdot \nabla \tilde{C}_{ox}^Y \right\} dA = 0 \quad (3.144)$$

$$\tilde{C}_{ox}^Y = C_{ox}^{Y*} - \langle C_{ox}^Y \rangle^{ox} \text{ at } \mathbf{A}_{mox} \quad (3.145)$$

$$\langle \tilde{C}_{ox}^Y \rangle = 0 \quad (3.146)$$

$$\tilde{C}_{ox}^Y(\mathbf{r} + \lambda_i) = \tilde{C}_{ox}^Y(\mathbf{r}), \quad i = 1, 2, 3 \text{ at } \mathbf{A}_{oxe} \quad (3.147)$$

$$\begin{aligned} \mathbf{v}_m \cdot \nabla \tilde{C}_m^Y + \tilde{\mathbf{v}}_m \cdot \nabla \langle C_m^Y \rangle^m &= D_m^{Fe} \nabla^2 \tilde{C}_m^Y \\ - \frac{1}{\varepsilon_m} \left\{ \frac{1}{V} \int_{A_{mox}(t)} D_m^{Fe} \hat{\mathbf{e}}_{mox} \cdot \tilde{C}_m^Y \right\} dA & \end{aligned} \quad (3.148)$$

$$\tilde{C}_m^Y = C_m^{Y*} - \langle C_m^Y \rangle^m \text{ at } \mathbf{A}_{mox} \quad (3.149)$$

$$\langle \tilde{C}_m^Y \rangle = 0 \quad (3.150)$$

$$\tilde{C}_m^Y(\mathbf{r} + \lambda_i) = \tilde{C}_m^Y(\mathbf{r}), \quad i = 1, 2, 3 \text{ at } \mathbf{A}_{oxe} \quad (3.151)$$

C_{ox}^{Y*} and C_m^{Y*} are equilibrium mass fractions in oxide and metal phase.

The constraints given by Eq. (3.146, 3.150) are necessary to obtain the solution to the closure problem [89]. The conditions given by Eqs. (3.147, 3.151) are the boundary condition at the boundary of the volume set by the periodicity of the medium [43, 16, 90, 91, 92, 67]. The form of the Eqs. (3.144 - 3.151) suggest that the quantities $C_{ox}^{Y*} - \langle C_{ox}^Y \rangle^{ox}$, $C_m^{Y*} - \langle C_m^Y \rangle^m$ and $\nabla \langle C_m^Y \rangle^m$ are the source of the deviations generated \tilde{C}_{ox}^Y , \tilde{C}_m^Y . In general for these deviations, it has been shown in [16] that they can be written as:

$$\tilde{C}_{ox}^Y = \alpha_{ox} (C_{ox}^{Y*} - \langle C_{ox}^Y \rangle^m) \quad (3.152)$$

$$\tilde{C}_m^Y = \alpha_m (C_m^{Y*} - \langle C_m^Y \rangle^m) + \mathbf{b}_m \cdot \nabla \langle C_m^Y \rangle^m \quad (3.153)$$

where α_{ox} , α_m and \mathbf{b}_m are obtained by solving following three problems which are obtained by integrating the Eqs. (3.152, 3.153) in the system of equations given by Eqs. (3.144 - 3.151).

Problem 1:

$$\mathbf{v}_m \cdot \nabla \mathbf{b}_m + \tilde{\mathbf{v}}_m = D_m^{Fe} \nabla^2 \mathbf{b}_m - \varepsilon_m^{-1} \mathbf{u}_m \quad (3.154)$$

$$\mathbf{b}_m = 0 \text{ at } \mathbf{A}_{mox} \quad (3.155)$$

$$\langle \mathbf{b}_m \rangle = 0 \quad (3.156)$$

$$\mathbf{b}_m(\mathbf{r} + \lambda_i) = \mathbf{b}_m(\mathbf{r}), \quad i = 1, 2, 3 \text{ at } \mathbf{A}_{oxe} \quad (3.157)$$

where:

$$\mathbf{u}_m = \frac{1}{V} \int_{A_{mox}(t)} D_m^{Fe} \hat{\mathbf{e}}_{mox} \cdot \nabla \mathbf{b}_m \, dA \quad (3.158)$$

Problem 2:

$$\mathbf{v}_m \cdot \nabla \alpha_m + \tilde{\mathbf{v}}_m = D_m^{Fe} \nabla^2 \alpha_m - \varepsilon_m^{-1} h_m \quad (3.159)$$

$$\alpha_m = 1 \text{ at } \mathbf{A}_{mox} \quad (3.160)$$

$$\langle \alpha_m \rangle = 0 \quad (3.161)$$

$$\alpha_m(\mathbf{r} + \lambda_i) = \alpha_m(\mathbf{r}), \quad i = 1, 2, 3 \text{ at } \mathbf{A}_{oxe} \quad (3.162)$$

where:

$$h_m = \frac{1}{V} \int_{A_{mox}(t)} D_m^{Fe} \hat{\mathbf{e}}_{mox} \cdot \nabla \alpha_m \, dA \quad (3.163)$$

Problem 3:

$$D_{ox}^O \nabla^2 \alpha_{ox} - \varepsilon_{ox}^{-1} h_{ox} = 0 \quad (3.164)$$

$$\alpha_{ox} = 1 \text{ at } \mathbf{A}_{mox} \quad (3.165)$$

$$\langle \alpha_{ox} \rangle = 0 \quad (3.166)$$

$$\alpha_{ox}(\mathbf{r} + \lambda_i) = \alpha_{ox}(\mathbf{r}), \quad i = 1, 2, 3 \text{ at } \mathbf{A}_{oxe} \quad (3.167)$$

where:

$$h_{ox} = \frac{1}{V} \int_{A_{mox}(t)} D_{ox}^O \hat{\mathbf{e}}_{mox} \cdot \nabla \alpha_{ox} dA \quad (3.168)$$

The quantities \mathbf{u}_m play the role of velocity of transport of macroscopic fields $\langle C_m^Y \rangle$, whereas the coefficients h_m and h_{ox} play the role of mass exchange due to diffusion and advection across the interface between solid-oxide and liquid-metal.

Using Eqs. (3.145, 3.146, 3.149, 3.150) and Eqs. (3.152, 3.153) along with Eqs. (3.154, 3.166) in the unclosed volume averaged equations for species conservation in oxide and metal phase (Eqs. (3.108, 3.109)) and in the unclosed form of rate of dissolution expression (3.110), gives the closed form of species conservation and rate of dissolution:

Closed Species Conservation Equation in Oxide Phase

$$\begin{aligned} \frac{\partial}{\partial t} (\varepsilon_{ox} \rho_{ox} \langle C_{ox}^Y \rangle^{ox}) - C_{ox}^{Y*} \frac{\partial}{\partial t} (\varepsilon_{ox} \rho_{ox}) &= \nabla \cdot (\varepsilon_{ox} \rho_{ox} D_{ox}^O \nabla \langle C_{ox}^Y \rangle^{ox}) \\ &\quad - \rho_{ox} D_{ox}^O (\nabla \varepsilon_{ox}) \cdot \nabla \langle C_{ox}^Y \rangle^{ox} \\ &\quad - \nabla \cdot [\rho_{ox} D_{ox}^O (\nabla \varepsilon_{ox}) (C_{ox}^{Y*} - \langle C_{ox}^Y \rangle^{ox})] \\ &\quad + \rho_{ox} h_{ox} (C_{ox}^{Y*} - \langle C_{ox}^Y \rangle^{ox}) \end{aligned} \quad (3.169)$$

Closed Species Conservation Equation in Metal Phase

$$\begin{aligned} \frac{\partial}{\partial t} (\varepsilon_m \rho_m \langle C_m^Y \rangle^m) + \nabla \cdot (\varepsilon_m \rho_m \langle C_m^Y \rangle^m \langle \mathbf{v}_m \rangle^m) + C_m^{Y*} \frac{\partial}{\partial t} (\varepsilon_{ox} \rho_{ox}) \\ &= \nabla \cdot (\varepsilon_m \rho_m \mathbf{D}_m^{Fe} \nabla \langle C_m^Y \rangle^m) \\ &\quad - \rho_m \mathbf{D}_m^{Fe} (\nabla \varepsilon_m) \cdot \nabla \langle C_m^Y \rangle^m \\ &\quad - \nabla \cdot [\rho_m \mathbf{D}_m^{Fe} (\nabla \varepsilon_m) (C_m^{Y*} - \langle C_m^Y \rangle^m)] + \rho_m h_m (C_m^{Y*} - \langle C_m^Y \rangle^m) \end{aligned} \quad (3.170)$$

Rate of Dissolution

$$\underbrace{\frac{\partial}{\partial t}(\rho_{ox}\varepsilon_{ox})}_{\dot{m}_{ox}} = \frac{1}{(C_m^{Y*} - C_{ox}^{Y*})} \left[\rho_m h_m (C_m^{Y*} - \langle C_m^Y \rangle^m) + \rho_{ox} h_{ox} (C_{ox}^{Y*} - \langle C_{ox}^Y \rangle^{ox}) \right. \\ \left. - \rho_{ox} D_{ox}^O (\nabla \varepsilon_{ox}) \cdot \nabla \langle C_{ox}^Y \rangle^{ox} \right. \\ \left. - \rho_m D_m^{Fe} (\nabla \varepsilon_m) \cdot \nabla \langle C_m^Y \rangle^m \right] \quad (3.171)$$

In above equations of conservation of species in metal phase and rate of dissolution, the quantity D_m^{Fe} is a diffusion-dispersion tensor, which is written as:

$$D_m^{Fe} = \underbrace{\varepsilon_m D_m^{Fe} I}_{Diffusion} - \underbrace{\langle \tilde{v}_m \mathbf{b}_m \rangle}_{Dispersion} \quad (3.172)$$

3.4.7.3 Temperature Deviation Relations and Closure

The deviation equations after simplifications detailed by Bousquet-Mélou [16] are:

$$\Lambda_{ox} \nabla^2 \tilde{T}_{ox} - \frac{\Lambda_{ox}}{\varepsilon_{ox}} \left\{ \frac{1}{V} \int_{A_{mox}(t)} \hat{\mathbf{e}}_{mox} \cdot \nabla \tilde{T}_{ox} \right\} dA = 0 \quad (3.173)$$

$$\begin{aligned} & \rho_m c_{pm} \mathbf{v}_m \cdot \nabla \tilde{T}_m + \rho_m c_{pm} \tilde{\mathbf{v}}_m \cdot \nabla \langle T \rangle \\ & = \Lambda_m \nabla^2 \tilde{T}_m - \frac{\Lambda_{ox}}{\varepsilon_m} \left\{ \frac{1}{V} \int_{A_{mox}(t)} \hat{\mathbf{e}}_{mox} \cdot \nabla \tilde{T}_m \right\} dA \end{aligned} \quad (3.174)$$

$$\Lambda_{ox} \hat{\mathbf{e}}_{mox} \cdot \nabla \tilde{T}_{ox} - \Lambda_m \hat{\mathbf{e}}_{mox} \cdot \nabla \tilde{T}_m = (\Lambda_m - \Lambda_{ox}) \hat{\mathbf{e}}_{mox} \cdot \nabla \langle T \rangle \text{ at } \mathbf{A}_{mox} \quad (3.175)$$

$$\nabla \tilde{T}_{ox} = \nabla \tilde{T}_m \text{ at } \mathbf{A}_{mox} \quad (3.176)$$

$$\tilde{T}_{ox}(\mathbf{r} + \lambda_i) = \tilde{T}_{ox}(\mathbf{r}), \quad i = 1, 2, 3 \text{ at } \mathbf{A}_{oxe} \quad (3.177)$$

$$\tilde{T}_m(\mathbf{r} + \lambda_i) = \tilde{T}_m(\mathbf{r}), \quad i = 1, 2, 3 \text{ at } \mathbf{A}_{me} \quad (3.178)$$

Further, it is shown in the work of Bousquet-Mélou [16] that deviation term can be written as:

$$\tilde{\mathbf{T}}_k = \mathbf{e}_k \langle T \rangle, \quad k = (ox, m) \quad (3.179)$$

where \mathbf{e}_k is another closure variable having an associated closure problem with it. The details of the closure problem of \mathbf{e}_k can be directly found in the works of Bousquet-Mélou et al. [17, 16]. Further, it has been shown in Goyeau [43] and Bousquet-Mélou et al. [17, 16] that using deviations equations summarised above and Eq. (3.179) in unclosed energy conservation equation given by Eq. (3.113), a closed energy conservation is given by Eq. (3.180).

Closed Energy Conservation Equation

$$\frac{\partial}{\partial t}(\langle \rho \rangle \langle H \rangle) + \nabla \cdot (\varepsilon_m \rho_m \langle H_m \rangle^m \langle \mathbf{v}_m \rangle^m) = \nabla \cdot (\Lambda_{eff} \nabla \langle T \rangle) \quad (3.180)$$

where:

$$\langle \rho \rangle = \varepsilon_{ox} \rho_{ox} + \varepsilon_m \rho_m \quad (3.181)$$

$$\langle H \rangle = \frac{\varepsilon_{ox} \rho_{ox} \langle H_{ox} \rangle^{ox} + \varepsilon_m \rho_m \langle H_m \rangle^m}{\langle \rho \rangle} \quad (3.182)$$

$$\Lambda_{eff} = \Lambda_{mix} \mathbf{I} + \frac{\Lambda_m - \Lambda_{ox}}{V} \underbrace{\int_{A_{mox}(t)} \hat{\mathbf{e}}_{mox} \cdot \mathbf{e}_m \, dA}_{Tortuosity} - \underbrace{\rho_m c_{pm} \langle \tilde{\mathbf{v}}_m \mathbf{e}_m \rangle}_{Dispersion} \quad (3.183)$$

$$\Lambda_{mix} = \varepsilon_{ox} \Lambda_{ox} + \varepsilon_m \Lambda_m \quad (3.184)$$

Usage of Temperature as a Pseudo Field in Dissolution Study:

It is important to mention at this point that in the present study of dissolution, the temperature is used as a pseudo field. It essentially means that the dissolution is studied at a fixed temperature. Thus, making the analysis of dissolution thermodynamically a study of diffusion facilitated redistribution or partitioning of species between liquid (metal) and solid (oxide) phase. The thermodynamics of this kind of dissolution has already been explained in section (3.1.1). This means that just for the dissolution sake, it is not required to solve the energy equation. However, the energy equation will still be a part of the solution routine in the present study, to take into account the velocity generated, due to change in density resulting from the gradients in the temperature field. In other words, in the present study, the coupling of temperature with species transport equation will not be considered but the coupling of temperature equation with Navier-Stokes equation will be considered. This fact will be evident in the chapter 8, where the results of dissolution with natural convection flow in the metal-oxide system due to thermo-solutal gradients will be shown.

The complete macroscopic dissolution model for oxide-metal phase is summarized in Table 3.3.

Table 3.3: Complete macroscopic model

$$\underbrace{\frac{\partial}{\partial t}(\rho_{ox}\varepsilon_{ox})}_{\dot{m}_{ox}} = \frac{1}{(C_m^{Y*} - C_{ox}^{Y*})} \left[\rho_m h_m (C_m^{Y*} - \langle C_m^Y \rangle^m) + \rho_{ox} h_{ox} (C_{ox}^{Y*} - \langle C_{ox}^Y \rangle^{ox}) - \rho_{ox} D_{ox}^O (\nabla \varepsilon_{ox}) \cdot \nabla \langle C_{ox}^Y \rangle^{ox} - \rho_m \mathbf{D}_m^{Fe} (\nabla \varepsilon_m) \cdot \nabla \langle C_m^Y \rangle^m \right]$$

$$\frac{\partial}{\partial t}(\varepsilon_m \rho_m) + \nabla \cdot (\varepsilon_m \rho_m \langle \mathbf{v}_m \rangle^m) = - \underbrace{\frac{\partial}{\partial t}(\rho_{ox}\varepsilon_{ox})}_{\dot{m}_{ox}}$$

$$\begin{aligned} \frac{\partial}{\partial t}(\varepsilon_m \rho_m \langle \mathbf{v}_m \rangle^m) + \nabla \cdot (\varepsilon_m \rho_m \langle \mathbf{v}_m \rangle^m \langle \mathbf{v}_m \rangle^m) = & -\varepsilon_m \nabla \langle P_m \rangle^m + \varepsilon_m \mu_m \nabla^2 \langle \mathbf{v}_m \rangle^m + \mu_m \nabla \varepsilon_m \cdot \langle \mathbf{v}_m \rangle^m + \mu_m (\nabla^2 \varepsilon_m) \langle \mathbf{v}_m \rangle^m - \varepsilon_m^2 \mu_m \mathbf{K}^{-1} \cdot \langle \mathbf{v}_m \rangle^m \\ & - \varepsilon_m^2 \mu_m \mathbf{K}^{-1} \cdot \mathbf{F} \cdot \langle \mathbf{v}_m \rangle^m + \varepsilon_m \rho_m \mathbf{g} \end{aligned}$$

$$\begin{aligned} \frac{\partial}{\partial t}(\varepsilon_{ox} \rho_{ox} \langle C_{ox}^Y \rangle^{ox}) - C_{ox}^{Y*} \underbrace{\frac{\partial}{\partial t}(\rho_{ox}\varepsilon_{ox})}_{\dot{m}_{ox}} = & \nabla \cdot (\varepsilon_{ox} \rho_{ox} D_{ox}^O \nabla \langle C_{ox}^Y \rangle^{ox}) - \rho_{ox} D_{ox}^O (\nabla \varepsilon_{ox}) \cdot \nabla \langle C_{ox}^Y \rangle^{ox} - \nabla \cdot [\rho_{ox} D_{ox}^O (\nabla \varepsilon_{ox}) (C_{ox}^{Y*} - \langle C_{ox}^Y \rangle^{ox})] \\ & + \rho_{ox} h_{ox} (C_{ox}^{Y*} - \langle C_{ox}^Y \rangle^{ox}) \end{aligned}$$

$$\begin{aligned} \frac{\partial}{\partial t}(\varepsilon_m \rho_m \langle C_m^Y \rangle^m) + \nabla \cdot (\varepsilon_m \rho_m \langle C_m^Y \rangle^m \langle \mathbf{v}_m \rangle^m) + C_m^{Y*} \underbrace{\frac{\partial}{\partial t}(\rho_{ox}\varepsilon_{ox})}_{\dot{m}_{ox}} = & \nabla \cdot (\varepsilon_m \rho_m \mathbf{D}_m^{Fe} \nabla \langle C_m^Y \rangle^m) - \rho_m \mathbf{D}_m^{Fe} (\nabla \varepsilon_m) \cdot \nabla \langle C_m^Y \rangle^m + \rho_m h_m (C_m^{Y*} - \langle C_m^Y \rangle^m) \\ & - \nabla \cdot [\rho_m \mathbf{D}_m^{Fe} (\nabla \varepsilon_m) (C_m^{Y*} - \langle C_m^Y \rangle^m)] \end{aligned}$$

$$\frac{\partial}{\partial t}(\langle \rho \rangle \langle H \rangle) + \nabla \cdot (\varepsilon_m \rho_m \langle H_m \rangle^m \langle \mathbf{v}_m \rangle^m) = \nabla \cdot (\Lambda_{eff} \nabla \langle T \rangle)$$

Further, in the works of Roux et al. [25, 96, 98, 99, 97] and Bousquet-Mélou et al. [17, 16] it has been shown that the non-classical terms like deviations of fields terms ($\tilde{\psi}$) can be neglected. Roux in his work [97] has found out that gradient in porosity ($\nabla\varepsilon$) terms has negligible effect on the final solution of the macroscopic model, and thus can be neglected as well. Also, in the present work all the calculations are carried out with *mole fractions*, instead of *mass fractions*. Thus, with these simplifications and taking into account the conversion from *mass fractions* to *mole fractions*, the simplified macroscopic model is given in Table 3.4.

Table 3.4: Simplified macroscopic model

$$\underbrace{\frac{\partial}{\partial t}(\rho_{ox}\varepsilon_{ox})}_{\dot{m}_{ox}} = \frac{1}{(n_m^{Y*} - n_{ox}^{Y*})} \left[\rho_m h_m (n_m^{Y*} - \langle n_m^Y \rangle^m) + \rho_{ox} h_{ox} (n_{ox}^{Y*} - \langle n_{ox}^Y \rangle^{ox}) \right] \quad (3.185)$$

$$\frac{\partial}{\partial t}(\varepsilon_m \rho_m) + \nabla \cdot (\varepsilon_m \rho_m \langle \mathbf{v}_m \rangle^m) = - \underbrace{\frac{\partial}{\partial t}(\rho_{ox}\varepsilon_{ox})}_{\dot{m}_{ox}} \quad (3.186)$$

$$\frac{\partial}{\partial t}(\varepsilon_m \rho_m \langle \mathbf{v}_m \rangle^m) + \nabla \cdot (\varepsilon_m \rho_m \langle \mathbf{v}_m \rangle^m \langle \mathbf{v}_m \rangle^m) = -\varepsilon_m \nabla \langle P_m \rangle^m + \varepsilon_m \mu_m \nabla^2 \langle \mathbf{v}_m \rangle^m - \varepsilon_m^2 \mu_m \mathbf{K}^{-1} \cdot \langle \mathbf{v}_m \rangle^m - \varepsilon_m^2 \mu_m \mathbf{K}^{-1} \cdot \mathbf{F} \cdot \langle \mathbf{v}_m \rangle^m + \varepsilon_m \rho_m \mathbf{g} \quad (3.187)$$

$$\frac{\partial}{\partial t}(\varepsilon_{ox} \rho_{ox} \langle n_{ox}^Y \rangle^{ox}) - n_{ox}^{Y*} \underbrace{\frac{\partial}{\partial t}(\rho_{ox}\varepsilon_{ox})}_{\dot{m}_{ox}} = \nabla \cdot (\varepsilon_{ox} \rho_{ox} D_{ox}^O \nabla \langle n_{ox}^Y \rangle^{ox}) + \rho_{ox} h_{ox} (n_{ox}^{Y*} - \langle n_{ox}^Y \rangle^{ox}) \quad (3.188)$$

$$\frac{\partial}{\partial t}(\varepsilon_m \rho_m \langle n_m^Y \rangle^m) + \nabla \cdot (\varepsilon_m \rho_m \langle n_m^Y \rangle^m \langle \mathbf{v}_m \rangle^m) + n_m^{Y*} \underbrace{\frac{\partial}{\partial t}(\rho_{ox}\varepsilon_{ox})}_{\dot{m}_{ox}} = \nabla \cdot (\varepsilon_m \rho_m \mathbf{D}_m^{Fe} \nabla \langle n_m^Y \rangle^m) + \rho_m h_m (n_m^{Y*} - \langle n_m^Y \rangle^m) \quad (3.189)$$

$$\frac{\partial}{\partial t}(\langle \rho \rangle \langle H \rangle) + \nabla \cdot (\varepsilon_m \rho_m \langle H_m \rangle^m \langle \mathbf{v}_m \rangle^m) = \nabla \cdot (\boldsymbol{\Lambda}_{eff} \nabla \langle T \rangle) \quad (3.190)$$

Chapter 4

Simplified Thermochemical Model

Chapter 4

Simplified Thermochemical Model

In the process of simulating various phenomena related to the severe accidents – like dissolution in present study – with the help of the mathematical models, there is an inherent need to calculate the equilibrium compositions while numerically solving the mathematical models. This problem of calculating the equilibrium compositions in real time in the numerical simulations can be broadly dealt in two ways, namely:

1. Using a full fledged Gibbs minimization solver like IRSN’s NUCLEA Toolbox during runtime of CFD calculations.
2. Using a simplified model, which can be used for fast calculations of the equilibrium compositions of species in phases during large CFD simulations.

Due to its own internal iterations, calling a full Gibbs solver like NUCLEA during numerical calculations comes with a CPU cost over already memory demanding simulations. This CPU overhead cost can be significantly reduced by the use of a suitable model. A simplified model thus can serve as a fast tool for calculating the equilibrium compositions, at the same time reducing the CPU time.

A simplified model is generally given by a fit function ($f(y)$; y being some independent variable). This fit function $f(y)$ can then be used to fit the NUCLEA equilibria composition data in order to evaluate the fit parameters in the fit function $f(y)$. Thus, once the fit parameters are known, the fit function $f(y)$ can be used to quickly produce the equilibrium compositions during real time CFD simulations.

The present chapter, thus deals with the derivation of a simplified thermochemical model, which can efficiently fit the thermochemical equilibria compositions produced by NUCLEA thermochemical Toolbox. To proceed with the development of simplified model, it is important to first recollect the some preliminary results of the thermochemical study of quaternary system (U, Zr, Fe, O) conducted with NUCLEA-17_1 from section (3.4.2).

4.1 Recollection of Thermochemical Study Conducted with NUCLEA Toolbox

In section (3.4.2) one of the important outcomes was the invariability of global molar ratio of U/Zr in both oxide and metal phases. Such invariability has already been shown in Fig. (3.7) and in Fig. (3.8). In section (3.4.2.5) because of this important result, it was possible to formulate a partitioning coefficient K for $(U - Zr)$. This partitioning coefficient K was given by Eq. (3.32) and is invoked again below:

$$K = \frac{N_m^U}{N^U} = \frac{N_m^{Zr}}{N^{Zr}} = \frac{N_m^{Zr} + N_m^U}{(1 + C_{uz})} \quad (4.1)$$

The thermochemical study with NUCLEA Toolbox is further extended to study the relationship between n_m^{Fe} and C_{ox} , and, n_m^{Fe} and C_{uz} for different moles of Iron (N^{Fe}).

4.1.1 Relation Between n_m^{Fe} , C_{ox} and C_{uz}

Referring to Fig. 4.1, it can be seen that the molar concentration of Fe in the metal becomes asymptotically independent of C_{uz} as soon as the number of moles of Iron (N^{Fe}) becomes more than 5, and even for lower values, the dependence is weak.

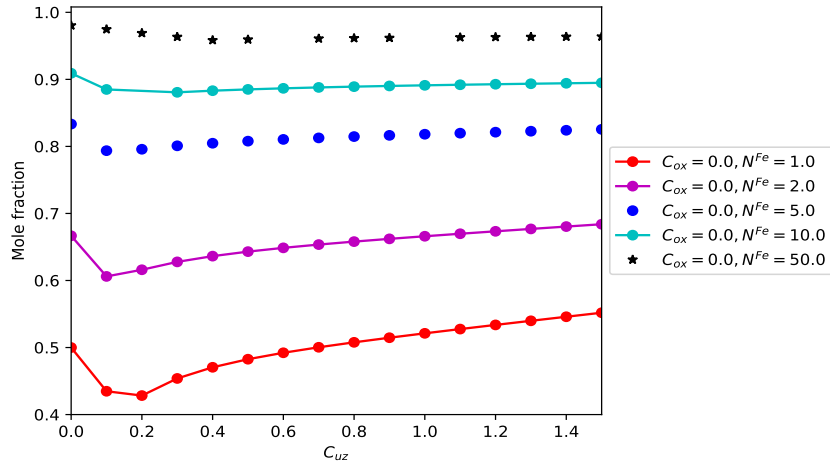


Figure 4.1: Dependence of Fe molar fraction in metal (n_m^{Fe}) on C_{uz}

Looking at Fig. 4.2, it clearly appears that there is a linear dependence of the mole fraction of Fe in the metal (n_m^{Fe}) with C_{ox} , for $N^{Fe} = 1$. This linear dependence can be written as:

$$n_m^{Fe} = 1 - n_m^*(1 - C_{ox}) \quad (4.2)$$

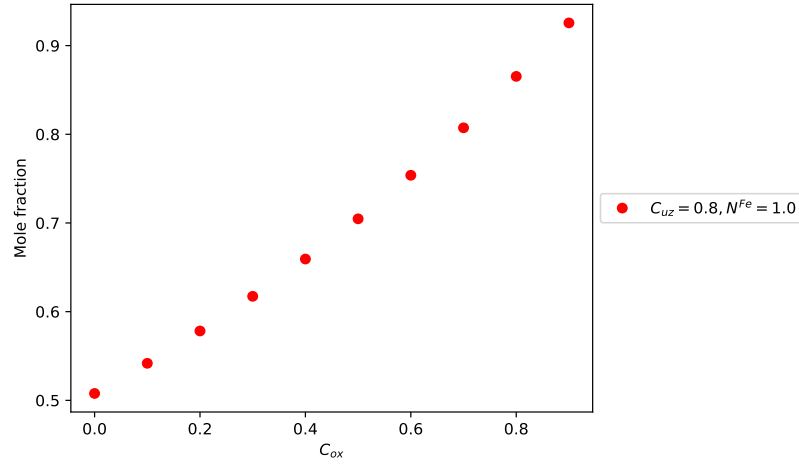


Figure 4.2: Dependence of Fe molar fraction in metal (n_m^{Fe}) on C_{ox}

$$n_m^U + n_m^{Zr} = n_m^*(1 - C_{ox}) \quad (4.3)$$

$$N_m^U + N_m^{Zr} = n_m^* N^m (1 - C_{ox}) \quad (4.4)$$

And, using the partitioning coefficient K , we can write that:

$$K(C_{ox}, C_{uz}, C_{sz})(1 + C_{uz}) = n_m^* N^m (1 - C_{ox}) \quad (4.5)$$

From the previous equation, it can be seen that the unknown partition coefficient K is not only related to input variables C_{uz} and C_{ox} but also to n_m^* , which is another unknown. This relation will be used to derive the simple analytical model in the following section (4.1.2).

4.1.2 Derivation of a Simplified Model for the (U, Zr, Fe, O) System

The analysis starts with the identification of the global inventory (recalling from section 3.4.2.2) as:

$$N^{Zr} = 1 \quad (4.6)$$

$$N^U = C_{uz} \quad (4.7)$$

$$N^O = 2(C_{uz} + C_{ox}) \quad (4.8)$$

$$N^{Fe} = C_{sz} \quad (4.9)$$

$$N^{tot} = N^{Zr} + N^U + N^O + N^{Fe} \quad (4.10)$$

4.1.2.1 Expressions for n_m^{Fe} , n_{ox}^O and n^m

The inventory of the metal phase is:

$$N^m = N_m^{Zr} + N_m^U + N^{Fe} \quad (4.11)$$

and n_m^{Fe} is given by:

$$n_m^{Fe} = \frac{N^{Fe}}{N_m^{Zr} + N_m^U + N^{Fe}} \quad (4.12)$$

The inventory of the oxide phase is:

$$N^{ox} = N_{ox}^{Zr} + N_{ox}^U + N^O \quad (4.13)$$

and n_{ox}^O is given by:

$$n_{ox}^O = \frac{N^O}{N_{ox}^{Zr} + N_{ox}^U + N^O} \quad (4.14)$$

It is straightforward to see that:

$$\frac{N^{Fe}}{n_m^{Fe}} + \frac{N^O}{n_{ox}^O} = N^m + N^{ox} = N^{tot} \quad (4.15)$$

which may also be written as:

$$\frac{n_m^{Fe}}{n_m^{Fe}} + \frac{n_{ox}^O}{n_{ox}^O} = 1 \quad (4.16)$$

Thus, the conservation of the total number of atoms gives the relation between n_m^{Fe} and n_{ox}^O :

$$n_{ox}^O = n^O \left(1 - \frac{n_m^{Fe}}{n_m^{Fe}}\right)^{-1} \quad (4.17)$$

Then, the mole fraction of metal phase is simply obtained by:

$$n^m = \frac{N^m}{N^{tot}} = \frac{N^m}{N^{Fe}} \frac{N^{Fe}}{N^{tot}} = \frac{n_m^{Fe}}{n_m^{Fe}} \quad (4.18)$$

Therefore, it can be seen that, in principle, only one of the three variables n_m^{Fe} , n_{ox}^O or n^m has to be fitted.

4.1.2.2 Choice of the Fitting Function and Parameters

Assuming that O is present only in the oxide phase, as discussed previously, a relation between C_{ox} and n_{ox}^O can be derived from Eqs. (3.25, 3.26, 3.27, 3.29). The relation can be written as:

$$n_{ox}^O = \frac{N^O}{N^{ox}} = \frac{2(C_{uz} + C_{ox})}{(1 - K)(1 + C_{uz}) + 2(C_{uz} + C_{ox})} \quad (4.19)$$

After some algebraic transformations, the previous expression is equivalent to:

$$1 - C_{ox} = (1 + C_{uz}) \frac{1 - \frac{3-K}{2} n_{ox}^O}{1 - n_{ox}^O} \quad (4.20)$$

Substituting the left-hand side term in Eq. (4.20), with Eq. (4.2):

$$n_m^{Fe} = 1 - n_m^*(1 + C_{uz}) \frac{1 - \frac{3-K}{2} n_{ox}^O}{1 - n_{ox}^O} \quad (4.21)$$

At this point, it is interesting to remember that, when C_{ox} tends to 1, the partition coefficient K tends asymptotically to 0, and n_{ox}^O tends asymptotically to $n_{st}^O = 2/3$. Thus, in general n_{ox}^O can be written as $n_{ox}^O = n_{st}^O - x$ or $n_{ox}^O = 2/3 - x$, where x is some unknown. This is also true when C_{sz} becomes large. Writing the Eq. (4.21) as a function of x , and setting $K = 0$, the following expression is obtained:

$$\frac{2}{3n_m^*(1 + C_{uz})} n_m^{Fe} = \frac{2}{3n_m^*(1 + C_{uz})} - \frac{x}{\frac{1}{3} + x} \quad (4.22)$$

Making an approximation that $\frac{1}{3} + x \approx \frac{1}{3}$, and defining the two constants m and b as:

$$m = \frac{2}{9n_m^*(1 + C_{uz})} \quad (4.23)$$

$$b = \frac{2}{3} - m = n_{st}^O - m \quad (4.24)$$

The Eq. (4.22) can then be re-written as:

$$mn_m^{Fe} \approx \left(m - \frac{2}{3}\right) + \left(\frac{2}{3} - x\right) = n_{ox}^O - b \quad (4.25)$$

From the Eq. (4.25), it can be seen that:

$$n_m^{Fe} = \frac{n_{ox}^O - b}{m} \quad (4.26)$$

and:

$$n_{ox}^O = mn_m^{Fe} + b \quad (4.27)$$

The previous relation is asymptotically correct when $C_{ox} = 1$ or when C_{sz} is large. Therefore, it can be generalized, and additionally it can be assumed that both n_m^{Fe} and n_{ox}^O can be written as a function of some fitting function $f(y)$, as:

$$n_m^{Fe} = \frac{1}{m} f(y) \quad (4.28)$$

$$n_{ox}^O = b + f(y) \quad (4.29)$$

From constraint given by Eq. (4.16), it can be written:

$$\frac{mn^{Fe}}{f(y)} + \frac{n^O}{b + f(y)} = 1 \quad (4.30)$$

which gives a second order equation:

$$f(y)^2 + (b - n^O - mn^{Fe})f(y) - bmn^{Fe} = 0 \quad (4.31)$$

We define the variable y as:

$$y = \frac{1}{2}(n^O + mn^{Fe} - b) \quad (4.32)$$

Then, the previous equation can be written as:

$$f(y)^2 - 2yf(y) - bmn^{Fe} = 0 \quad (4.33)$$

Selecting the positive solution:

$$f(y) = y + \sqrt{y^2 + bmn^{Fe}} \quad (4.34)$$

Finally, the two unknown concentrations are given by the Eqs. (4.32, 4.34, 4.28, 4.29). And it is easy to check that the last unknown variable n^m is given

by:

$$n^m = \frac{mn^{Fe}}{f(y)} \quad (4.35)$$

4.1.2.3 Behavior of the Fitting Function $f(y)$

The fitting function given by Eq. (4.34), starts from 0 for $n^{Fe} = 0$ (mole fraction of iron) and tends to m , very quickly, in an asymptotic way when n^{Fe} increases. Therefore the asymptotic solution for n_m^{Fe} is 1 and for n_{ox}^O is $b + m$. This gives the following constraint:

$$b + m = n_{st}^O \quad (4.36)$$

Thus the fit is made only with one fitting parameter (either b or m), the other being deduced from Eq. (4.36).

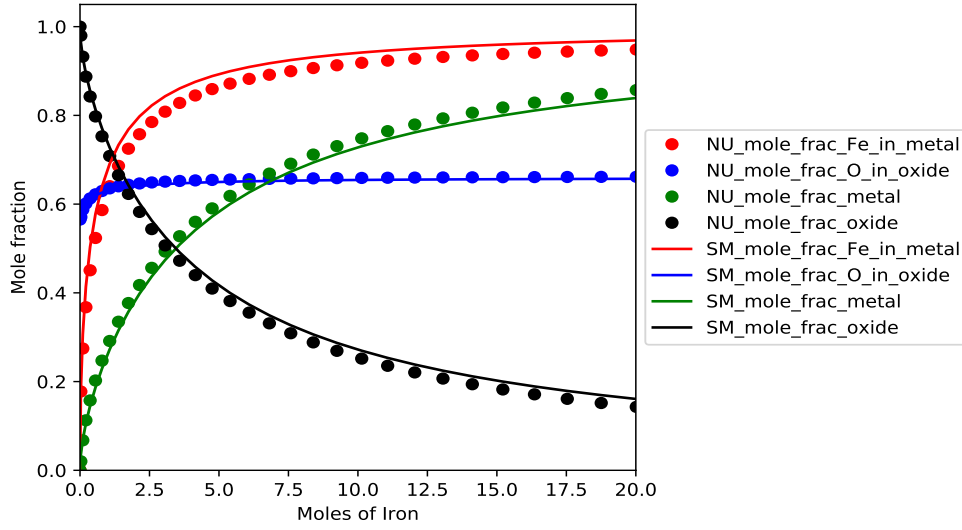
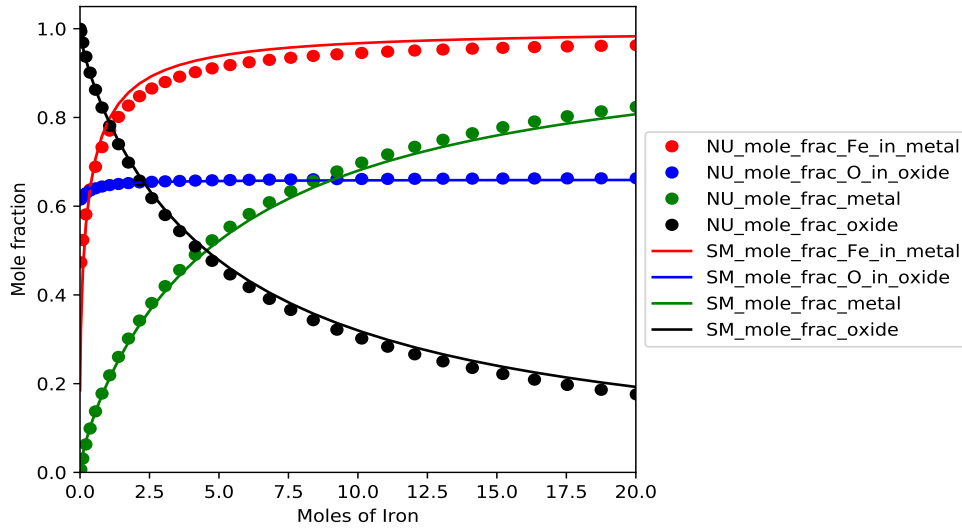
4.1.3 Illustration of Fit to NUCLEA Thermochemical Calculations for Various Inventory Compositions

In this section the quality of fit, made by the derived simplified model, for the NUCLEA calculations has been shown. Method of Least Squares have been used to fit the NUCLEA data by the derived simplified model, which has lead to the deduction of the values of fit parameter (m). Fig. 4.3, shows fit data (coloured lines) to the NUCLEA data (coloured dots), corresponding to $C_{uz} = 1.0$ and $C_{ox} = 0.3$. It can be seen that the model fits quite well to the thermochemical calculations. The value of fit parameter (m) for this case is found to be 0.0948. The value of other fit parameter (b) can be calculated from Eq. (4.36). Similarly, fits for thermochemical calculations, obtained for other values of C_{uz} and C_{ox} , can be seen in Figs. 4.4, 4.5 and 4.6, respectively.

$C_{ox} \backslash C_{uz}$	0.8	1.0	1.45
0.3	$m = 0.11000$	$m = 0.0948$	$m = 0.07176$
0.6	$m = 0.05130$	$m = 0.0446$	$m = 0.03400$
0.9	$m = 0.00615$	$m = 0.0048$	$m = 0.00266$

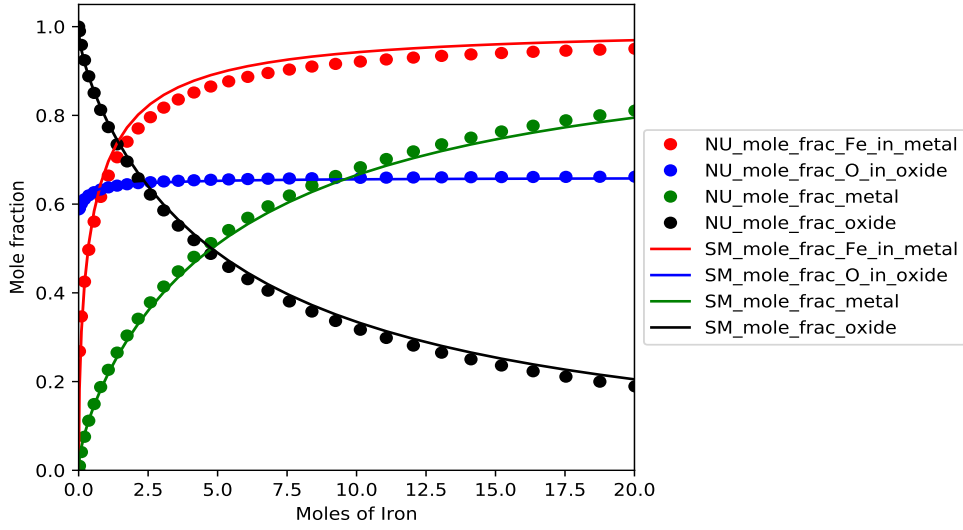
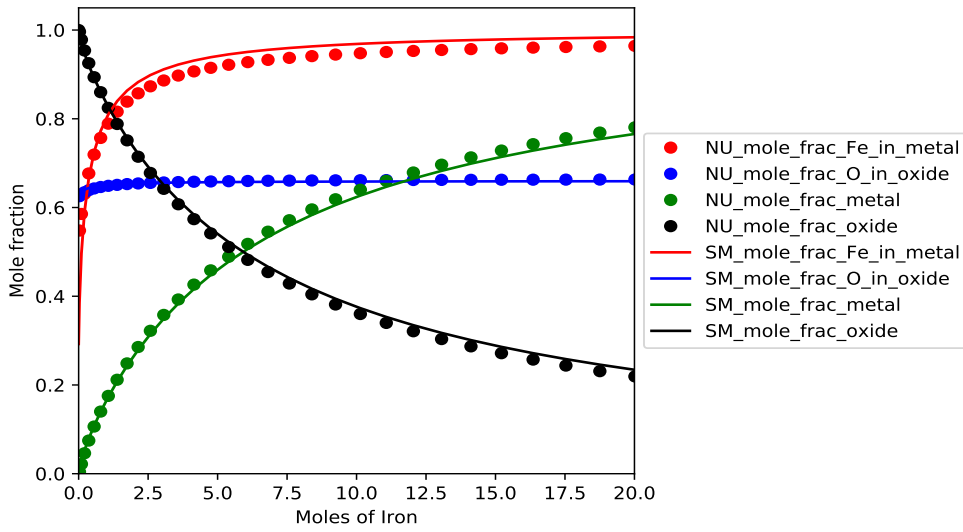
Table 4.1: m values for various C_{uz} and C_{ox}

The values of fit parameter (m) found after fitting the NUCLEA data, for other important values of C_{uz} and C_{ox} , can be seen in Table 4.1.


 Figure 4.3: Inventory: $C_{uz} = 1.0$ and $C_{ox} = 0.3$ ($m = 0.0948$)

 Figure 4.4: Inventory: $C_{uz} = 1.0$ and $C_{ox} = 0.6$ ($m = 0.0446$)

To calculate the values of the fit parameter (m), for other values of C_{uz} and C_{ox} , apart from the one given in Table 4.1, we found in our study, that for a given C_{ox} , m follows a simple dependence on C_{uz} . This dependence is expressed as:

$$m(C_{uz}) = m^{ref} \frac{1 + C_{uz}^{ref}}{1 + C_{uz}} \quad (4.37)$$


 Figure 4.5: Inventory: $C_{uz} = 1.45$ and $C_{ox} = 0.3$ ($m = 0.07176$)

 Figure 4.6: Inventory: $C_{uz} = 1.45$ and $C_{ox} = 0.6$ ($m = 0.034$)

where, $m(C_{uz})$ is the unknown for a given C_{uz} at a fixed C_{ox} , m^{ref} is a reference value of m , which can be taken to be any already known value of m from Table 4.1, at a fixed C_{ox} . Similarly, C_{uz}^{ref} is the value of C_{uz} , corresponding to m^{ref} , at a fixed C_{ox} , and C_{uz} is the value for which $m(C_{uz})$ is to be determined.

Table 4.2, shows the use of Eq. (4.37), to determine the value of m for various values of C_{uz} at a given value of C_{ox} . In this analysis, C_{uz} is varied from 0.8 to 1.45 at a given $C_{ox} = 0.3$, chosen $m^{ref} = 0.11$ (from Table 4.1) and the C_{uz}^{ref} corresponding to $m^{ref} = 0.11$ is $C_{uz}^{ref} = 0.8$ (from Table 4.1).

C_{oz} \ C_{uz}	0.8	0.9	1.0	1.2	1.3	1.45
	m	m	m	m	m	m
0.3	0.11	0.104	0.0948	0.09	0.086	0.07176

Table 4.2: m values calculated from Eq. (4.37)

In Table 4.2, the values of m in bold corresponds to the already known values given in Table 4.1, and non-bold m values are the one calculated by using Eq. (4.37). In a similar way, values of m for other values of various C_{uz} , at $C_{oz} = 0.6$ and $C_{oz} = 0.9$ can be approximated by using Eq. (4.37).

4.1.4 Range of Application of Fit model (Range of Data Fitted)

Figure 4.7 shows the range of fitted thermochemical data obtained from NUCLEA database. Clearly it can be seen that fitting covers values of C_{uz} ranging from 0.8 to 1.5 and C_{ox} ranging from 0.3 to 0.9. This data set is larger than the available experimental data points, thus making the fitting relevant to various inventory compositions found in different nuclear reactors like PWR, BWR, etc. Another illustration, showing the globalness of the fit data can be seen in Fig. 4.8, which is showing a full quaternary system ($U - Zr, Fe, O$) in a cross-sectional ternary phase diagram. Yet again, it can be seen that the fit data covers broader range than the experimental data.

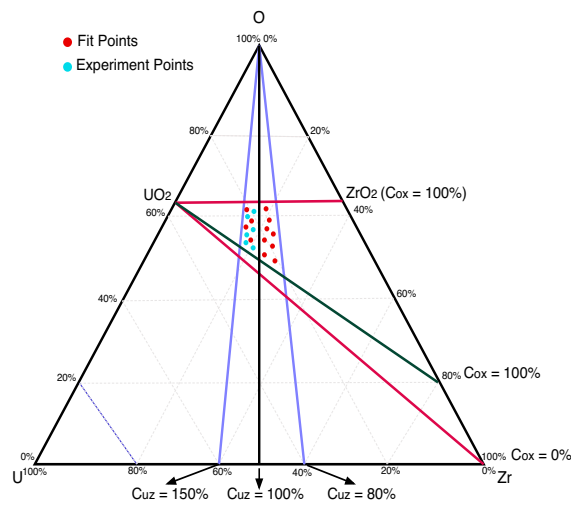


Figure 4.7: Range of data fitted, shown in (U, Zr, O) form

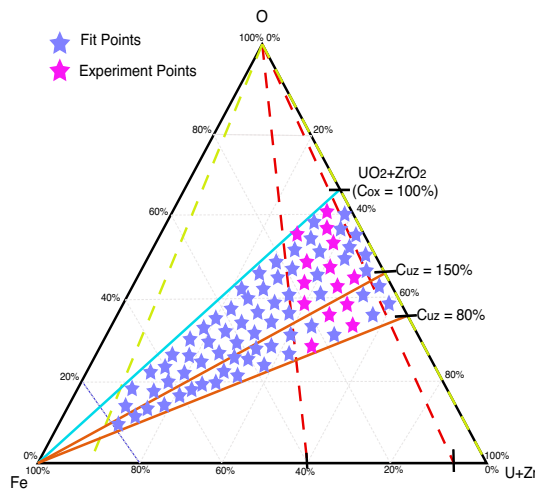


Figure 4.8: Range of data fitted, shown in ($U - Zr, Fe, O$) form

4.1.5 An Algorithm for Using Simplified Model For Fast Thermochemical Calculations of n_m^{Fe} , n^m , n_{ox}^O

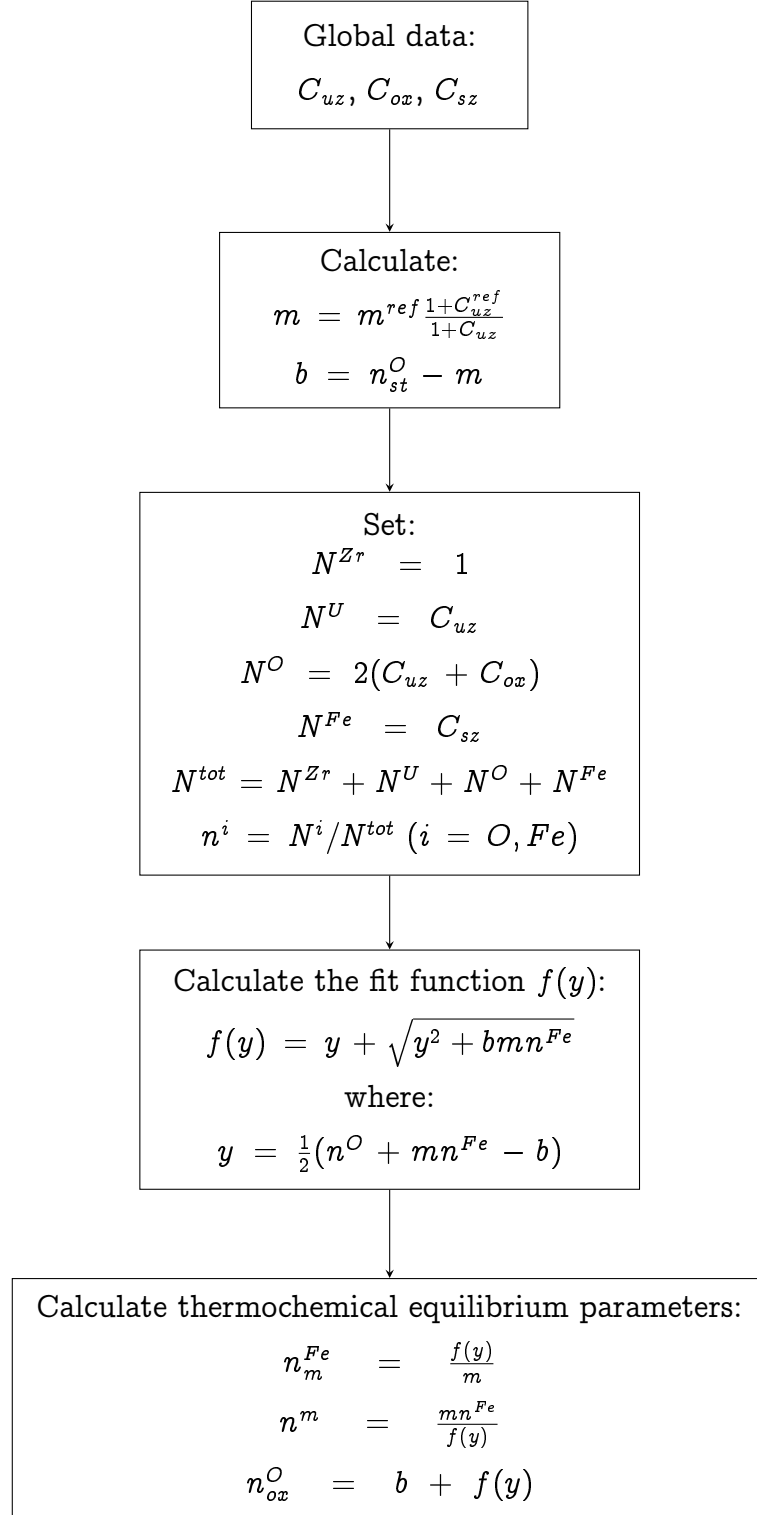


Figure 4.9: An algorithm to calculate the thermochemical parameters with derived simplified model

Chapter 5

Application to 0-D and 1-D Cases

Chapter 5

Application to 0-D and 1-D Cases

5.1 Application to 0-D case

In this chapter, an application of the ternary in each phase model to predict the quaternary equilibria in a stratified metal-oxide system is presented. At first, a 0-D model by neglecting the diffusion terms from Eqs. (3.188) and (3.189) is considered. Consequently, the Eqs. (3.188) and (3.189), reduces to system of Ordinary Differential Equations (ODEs) given below:

$$\frac{d(\rho_{ox}\varepsilon_{ox}\langle n_{ox}^Y \rangle^{ox})}{dt} - n_{ox}^{Y*}\dot{m} = \rho_{ox}h_{ox}(n_{ox}^{Y*} - \langle n_{ox}^Y \rangle^{ox}) \quad (5.1)$$

$$\frac{d(\rho_m\varepsilon_m\langle n_m^Y \rangle^m)}{dt} + n_m^{Y*}\dot{m} = \rho_m h_m(n_m^{Y*} - \langle n_m^Y \rangle^m) \quad (5.2)$$

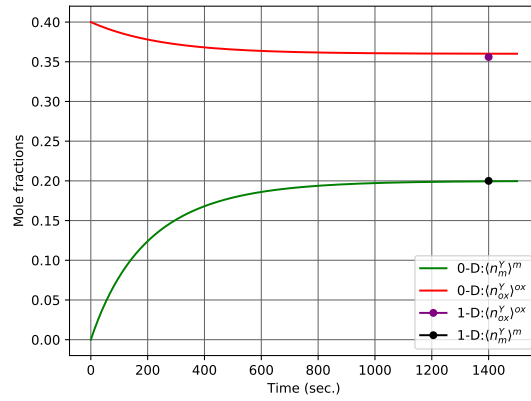
$$\begin{aligned} \dot{m} &= \frac{d(\rho_{ox}\varepsilon_{ox})}{dt} \\ &= \frac{1}{(n_m^{Y*} - n_{ox}^{Y*})} \left[\rho_m h_m(n_m^{Y*} - \langle n_m^Y \rangle^m) + \rho_{ox}h_{ox}(n_{ox}^{Y*} - \langle n_{ox}^Y \rangle^{ox}) \right] \end{aligned} \quad (5.3)$$

To solve the above system of ODEs, it is required to know the equilibrium mole fractions values represented by n_{ox}^{Y*} and n_m^{Y*} . In order to know the mole fractions values, derived simplified thermochemical model is to be used as demonstrated in the next section (5.1.1).

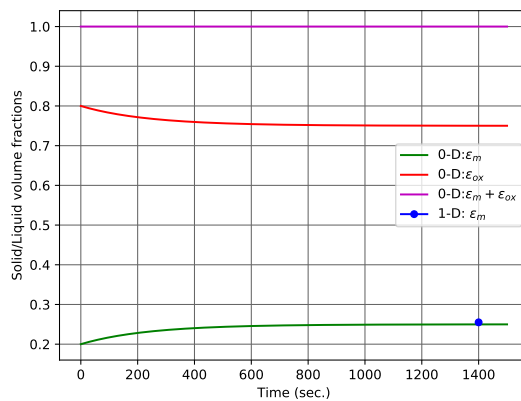
5.1.1 Calculations of Equilibrium Compositions n_{ox}^{Y*} and n_m^{Y*} from Simplified Thermochemical Model

In order to determine the equilibrium composition in the 0-D model, the algorithm explained in section (4.1.5) needs to be followed. At first, global values of C_{uz} , C_{ox} , C_{sz} or N^{Fe} has been chosen to be 1, 0.3 and 2.0 respectively. Secondly, for these C_{uz} and C_{ox} , values of m and b are found to be 0.0948 and 0.572. With these values of C_{uz} , C_{ox} , C_{sz} , m , b , and following the third, fourth and fifth steps of the algorithm (Fig. 4.9), the equilibrium values of n_{ox}^O and n_m^{Fe} are calculated to be 0.65 and 0.8. Finally the equilibrium values n_{ox}^{Y*} and n_m^{Y*} are calculated to be 0.35 and 0.2, respectively.

5.1.2 Results for 0-D case



(a) Variation of Y in oxide and metal phases



(b) Variation of oxide and metal volume fractions

Figure 5.1: Results for 0-D study performed with ODE model, and its comparison with 1-D model

The initial values of $\langle n_{ox}^Y \rangle^{ox}$ and $\langle n_m^Y \rangle^m$ are taken as 0.4 and 0, respectively. The system of coupled ODEs given by Eqs. (5.1, 5.2, 5.3) has been solved by a split algorithm elaborated in Appendix (B). It can be seen from Fig. 5.1 (a) that $\langle n_m^Y \rangle^m$ reach its equilibrium value at around 1400 seconds and $\langle n_{ox}^Y \rangle^{ox}$ has almost reached to its equilibrium by 1400 seconds. Also, from Fig. 5.1 (b), it can be inferred that by starting with 80% oxide (shown in red curve in Fig. 5.1 (b)), there will be a reduction of about 5% in oxide volume fraction, hence, metal volume fraction (shown in green curve in Fig. 5.1 (b)) increases to 25% from initial 20%, at around 1400 seconds. It is also interesting to see the conservativeness of the ternary in each phase model (here represented by an ODE model) from Fig. 5.2, where mass of O and Fe remains conserved in respective oxide phase and metal phase, and the mass of $(U - Zr)$ remains conserved in oxide-metal phase.

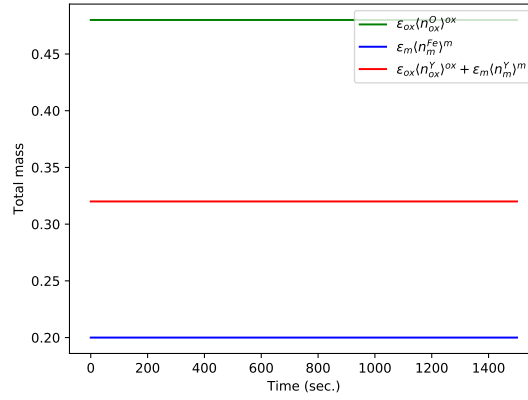


Figure 5.2: Conservation of total mass of O , Fe , UZ in both oxide and metal phases

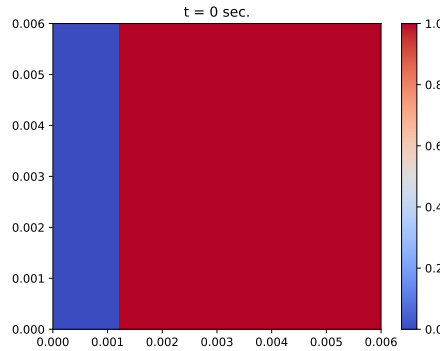
5.2 Application to 1-D case and Results

Analysis carried out with 0-D model is also repeated with a 1-D model. For this, the diffusion terms in Eqs. (3.188) and (3.189) are retained. Thus, the system of PDEs read as:

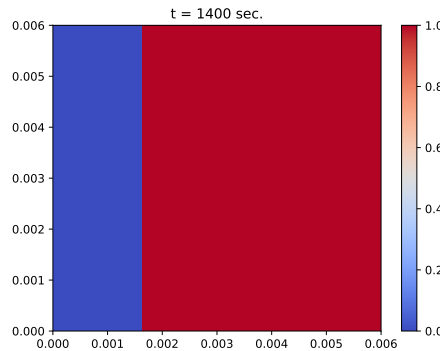
$$\frac{\partial}{\partial t}(\rho_{ox}\varepsilon_{ox}\langle n_{ox}^Y \rangle^{ox}) - n_{ox}^{Y*} \frac{\partial}{\partial t}(\rho_{ox}\varepsilon_{ox}) = \nabla \cdot (\rho_{ox}\varepsilon_{ox}D_{ox}^O \nabla \langle n_{ox}^Y \rangle^{ox}) + \rho_{ox}h_{ox}(n_{ox}^{Y*} - \langle n_{ox}^Y \rangle^{ox}) \quad (5.4)$$

$$\frac{\partial}{\partial t}(\rho_m\varepsilon_m\langle n_m^Y \rangle^m) + n_m^{Y*} \frac{\partial}{\partial t}(\rho_{ox}\varepsilon_{ox}) = \nabla \cdot (\rho_m\varepsilon_mD_m^{Fe} \nabla \langle n_m^Y \rangle^m) + \rho_mh_m(n_m^{Y*} - \langle n_m^Y \rangle^m) \quad (5.5)$$

$$\dot{m} = \frac{d(\rho_{ox}\varepsilon_{ox})}{dt} = \frac{1}{(n_m^{Y*} - n_{ox}^{Y*})} \left[\rho_mh_m(n_m^{Y*} - \langle n_m^Y \rangle^m) + \rho_{ox}h_{ox}(n_{ox}^{Y*} - \langle n_{ox}^Y \rangle^{ox}) \right] \quad (5.6)$$



(a) $\varepsilon_{ox} = 80\%$ at $t = 0$ sec.



(b) $\varepsilon_{ox} = 75\%$ at $t = 1400$ sec.

Figure 5.3: Solid volume fraction profiles for 1-D study performed

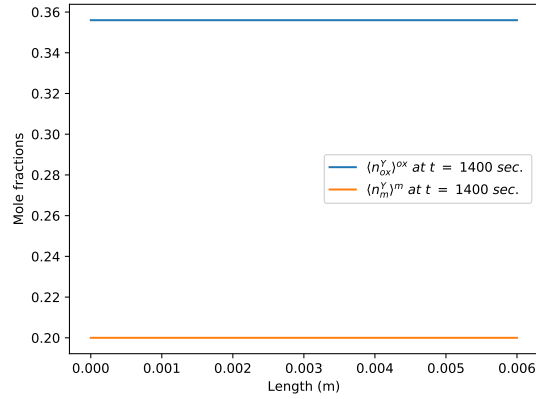
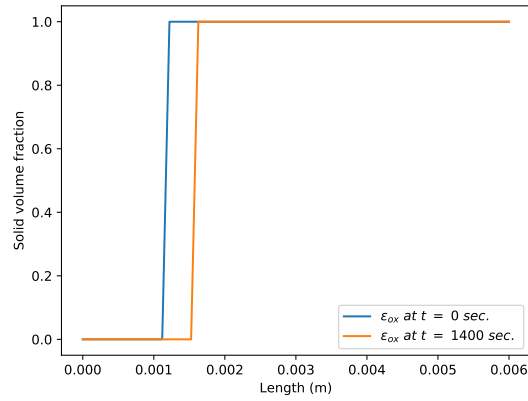

 (a) Mole fraction $\langle n_{ox}^Y \rangle^{ox}$ at $t = 1400$ sec.

 (b) ϵ^{ox} at $t = 0$ and $t = 1400$ sec.

Figure 5.4: Results for 1-D study performed

The above system of coupled PDEs has been solved numerically by a semi-implicit Finite Volume scheme adopted in a fully coupled solver, explained in Appendix (A). Further, the value of diffusivity, D_m^{Fe} , is chosen to be $10^{-6} \text{ m}^2/\text{sec}$. [65], and it is $10^{-9} \text{ m}^2/\text{sec}$. [3, 62] for D_{ox}^O . Fig. 5.3 illustrates the 1-D analysis with the same thermochemical data used for 0-D study. For the sake of comparison with 0-D model, the initial oxide volume fraction (ϵ_{ox}) in Fig. 5.3 (a) is taken to be 80% in a square domain. Fig. 5.3 (b) and Fig. 5.4 (b) shows the state of the system at 1400 seconds, when the interface between oxide and metal phase has moved by around 5% because of the dissolution of the oxide phase, making oxide phase to have around 75% volume fraction, similar to one observed in 0-D model (shown in Fig. 5.1 (b)). Similarly, the mole fraction of $(U - Zr)$ in metal phase (i.e. $\langle n_m^Y \rangle^m$) has attained an equilibrium value of $\langle n_m^Y \rangle^m = 0.2$ by 1400 seconds, shown in Fig. 5.4 (a), which is also in good agreement with 0-D model (Fig. 5.1 (a)).

Chapter 6

Topological Relations and Numerical Implementation

Chapter 6

Topological Relations and Numerical Implementation

6.1 Topological Relations

The derivation of volume averaged model in section (3.4.6) in chapter 3, lead to the system of closed PDEs. The closure problems detailed there, were concerned with the closure of following variables:

1. Mass transfer coefficient in solid-oxide phase represented by h_{ox} .
2. Mass transfer coefficient in liquid-metal phase represented by h_m .
3. Diffusion coefficient in solid-oxide phase represented by D_{ox}^O .
4. Diffusion coefficient tensor in liquid-metal phase represented by \mathbf{D}_m^{Fe} .
5. Forchheimer correction tensor represented by \mathbf{F} .
6. Permeability tensor represented by \mathbf{K} .

Ideally, whole set of PDEs along with the derived closure problems can be numerically solved. In fact, at least for \mathbf{K} and \mathbf{F} , the associated closure problems Eqs. (3.128 - 3.138) was solved by [16] for representative cells of dendrite equiaxed structures in solidification. These are still to be solved for representative cells of solid grains saturated with liquid, illustrated in Fig. (2.3). The case of stratified cells will be acceptable for this study. In the case of solidification, [41, 42] had solved these closure problems by considering the parallel and transverse flows on primary axis of dendrites. These cases are not very appropriate for the present problem of dissolution. In fact, the present problem of dissolution does not involve the dendrite structures, the problem in hand in this study is more like classical porous media. Consequently, in the present thesis, these closure problems can be solved for special type of representative cells appropriate for dissolution, however, it will arise an extra level of numerical complexity, which is not a primary aim of the present thesis.

Therefore, an alternate simpler approach of closure of variables detailed above has been worked out in the present work by choosing various empirical relations for the unclosed variables. These empirical relations are generally termed as *topological relations*, outlined by [76]. On going enumeration summarizes some important assumptions and the closure of variables.

1. At first it is assumed that the Forchheimier correction tensor (\mathbf{F}), representing the inertial effects in flow through porous media, is negligible [14]. Further, the permeability tensor (\mathbf{K}) is assumed to be a scalar (K) and closed by Kozeny-Carman relation [12].

$$K = \frac{l_d^2}{180} \frac{\varepsilon_m^3}{(1 - \varepsilon_m)^2} \quad (6.1)$$

Also, it is important to note that, as the porosity (ε_m) increases to some higher values of 40% or above, due to the dissolution in the crust, the grains becomes quite mobile and can not be assumed to be connected anymore. Hence, in order to simulate the rate of increase of permeability, consistent with the rate of increase of porosity, beyond a certain limiting value of porosity, a new expression is proposed, which retains the dimension of Eq. (6.1) but is more relaxed for higher porosities. This expression reads as.

$$K_r = \frac{l_d^2 \varepsilon_m}{(1 - \varepsilon_m)^4} \quad (6.2)$$

2. For diffusivity in liquid phase it is assumed that the dispersion in diffusion-dispersion tensor (\mathbf{D}_m^{Fe}) is negligible [14] reducing it to a scalar (D_m^{Fe}). Further, this diffusivity in liquid-metal phase along with diffusivity in solid-oxide phase is represented by an effective diffusivity obtained from the homogenization of the diffusion equation [57] for periodic grains shown in Fig. (6.1), where: $l_d^2 = \varepsilon_{ox} l_v^2$.

$$D_e = \frac{(2 - \varepsilon_m) D_{ox}^O + D_m^{Fe}}{2 - \varepsilon_m + \frac{D_{ox}^O}{D_m^{Fe}}} \quad (6.3)$$

3. In effective conductivity tensor (Λ_{eff}), the contribution from dispersion and tortuosity are neglected and the resulting scalar effective conductivity is closed by Eq. (6.4) [57].

$$\Lambda_{eff} = \frac{(2 - \varepsilon_m) \Lambda_{ox} + \Lambda_m}{2 - \varepsilon_m + \frac{\Lambda_{ox}}{\Lambda_m}} \quad (6.4)$$

4. For mass transfer coefficients, several models from the literature has been tested to correctly reproduce the morphology of the crust observed in

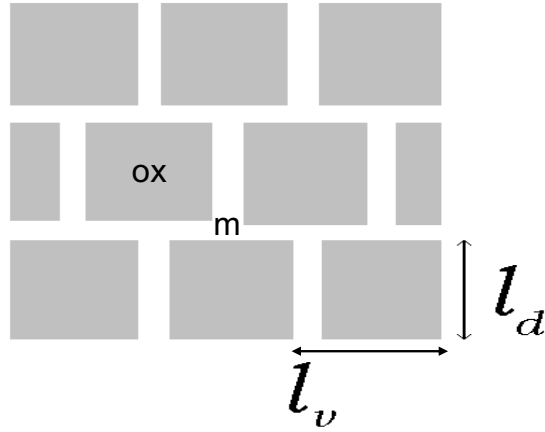


Figure 6.1: 2D Periodic representative cells

CORDEB experiment [4] after dissolution by molten steel. The complete analysis about the physics of these equations will be discussed in chapter 7. Here, the form of several models of mass transfer coefficients in oxide and metal phases are given by Eq. (6.5) [16], Eq. (6.6) [14] and Eq. (6.7).

$$h_k = \frac{h_{k0} D_k \left[256\varepsilon_k - 300\varepsilon_k - 653\varepsilon_k + 1320\varepsilon_k - 623\varepsilon_k \right]}{l_d^2} \quad (6.5)$$

$$h_k = \frac{h_{k0} D_k \varepsilon_k (1 - \varepsilon_k)}{l_d^2} \quad (6.6)$$

$$h_k = \frac{h_{k0} \varepsilon_k (1 - \varepsilon_k)}{\tau} \quad (6.7)$$

where: $k = (ox, m)$, h_{k0} is some constant whose value will be discussed in chapter 7, and τ is like an effective time of dissolution.

6.2 Numerical Implementation

For the sake of clarity the simplified set of PDEs from Table 3.4 along with the modified rate of dissolution term (\dot{m}_{ox}) explained in chapter 5, is presented again below.

$$\begin{aligned} \frac{\partial}{\partial t} (\varepsilon_m \rho_m \langle \mathbf{v}_m \rangle^m) + \nabla \cdot (\varepsilon_m \rho_m \langle \mathbf{v}_m \rangle^m \langle \mathbf{v}_m \rangle^m) = & -\varepsilon_m \nabla \langle P_m \rangle^m + \varepsilon_m \mu_m \nabla^2 \langle \mathbf{v}_m \rangle^m \\ & -\varepsilon_m^2 \mu_m K^{-1} \cdot \langle \mathbf{v}_m \rangle^m + \varepsilon_m \rho_m \mathbf{g} \end{aligned} \quad (6.8)$$

$$\begin{aligned} \frac{\partial}{\partial t}(\varepsilon_{ox}\rho_{ox}\langle n_{ox}^Y \rangle^{ox}) - n_{ox}^{Y*}\dot{m}_{ox} &= \nabla \cdot (\varepsilon_{ox}\rho_{ox}D_{ox}^O \nabla \langle n_{ox}^Y \rangle^{ox}) \\ &+ \rho_{ox}h_{ox}(n_{ox}^{Y*} - \langle n_{ox}^Y \rangle^{ox}) \end{aligned} \quad (6.9)$$

$$\begin{aligned} \frac{\partial}{\partial t}(\varepsilon_m\rho_m\langle n_m^Y \rangle^m) + \nabla \cdot (\varepsilon_m\rho_m\langle n_m^Y \rangle^m \langle \mathbf{v}_m \rangle^m) + n_m^{Y*}\dot{m}_{ox} \\ = \nabla \cdot (\varepsilon_m\rho_m D_m^{Fe} \nabla \langle n_m^Y \rangle^m) \\ + \rho_m h_m (n_m^{Y*} - \langle n_m^Y \rangle^m) \end{aligned} \quad (6.10)$$

$$\dot{m}_{ox} = \frac{1}{(n_m^{Y*} - n_{ox}^{Y*})} \left[\rho_m h_m (n_m^{Y*} - \langle n_m^Y \rangle^m) + \rho_{ox} h_{ox} (n_{ox}^{Y*} - \langle n_{ox}^Y \rangle^{ox}) \right] \quad (6.11)$$

$$\frac{\partial}{\partial t}(\langle \rho \rangle \langle H \rangle) + \nabla \cdot (\varepsilon_m\rho_m \langle H_m \rangle^m \langle \mathbf{v}_m \rangle^m) = \nabla \cdot (\Lambda_{eff} \nabla \langle T \rangle) \quad (6.12)$$

where:

$$\langle \rho \rangle = \varepsilon_{ox}\rho_{ox} + \varepsilon_m\rho_m \quad (6.13)$$

$$\langle H \rangle = \frac{\varepsilon_{ox}\rho_{ox}\langle H_{ox} \rangle^{ox} + \varepsilon_m\rho_m\langle H_m \rangle^m}{\langle \rho \rangle} \quad (6.14)$$

Further implementing following assumptions from [16, 14, 97]:

1. The density of continuous liquid-metal phase is equal to a constant reference density ρ_0 in all the terms except in the body force per unit volume term, $\varepsilon_m\rho_m\mathbf{g}$, in momentum equation. In this body force term, *Boussinesq approximation* [125] is assumed to be valid i.e.

$$\rho_m = \rho_0 \left[1 - \beta_T(\langle T \rangle - T_0) - \beta_S(\langle n_m^Y \rangle^m - n_0) \right] \text{ in } \varepsilon_m\rho_m\mathbf{g} \quad (6.15)$$

$$\rho_m = \rho_0 \text{ in all other terms} \quad (6.16)$$

where: β_T and β_S are the respective thermal and solutal expansion coefficients defined as:

$$\beta_T = -\frac{1}{\rho_m} \left(\frac{\partial \rho_m}{\partial T} \right) \quad (6.17)$$

$$\beta_S = -\frac{1}{\rho_m} \left(\frac{\partial \rho_m}{\partial n} \right) \quad (6.18)$$

Further, it is also assumed from [14] that density in solid-oxide phase is equal to density of liquid-metal phase i.e.

$$\rho_{ox} = \rho_m = \rho_0 \quad (6.19)$$

2. The macroscopic enthalpies in oxide and metal phases are independent of the mole fractions and vary linearly with the temperature of the mixture as:

$$\langle H_{ox} \rangle^{ox} = C_{P_{ox}} \langle T \rangle \quad (6.20)$$

$$\langle H_m \rangle^m = C_{P_m} \langle T \rangle + L_f \quad (6.21)$$

where: $C_{P_{ox}}$, C_{P_m} and L_f are the respective heat capacity of oxide phase, heat capacity of metal phase and latent heat of fusion. Further, it is also assumed [14]:

$$C_{P_{ox}} = C_{P_m} = C_{P_0} \quad (6.22)$$

Further, with the implementation of above assumptions and with following simplifications of the notations :

1. $\varepsilon_m \rho_m = \varepsilon_m \rho_0 = \tilde{\rho}_m$, termed as apparent density of liquid-metal phase.
2. $\langle \mathbf{v}_m \rangle^m = \mathbf{v}_m$
3. $\langle P_m \rangle^m = P_m$
4. $\varepsilon_{ox} \rho_{ox} = \varepsilon_{ox} \rho_0 = \tilde{\rho}_{ox}$, termed as apparent density of solid-oxide phase.
5. $\langle n_{ox}^Y \rangle^{ox} = n_{ox}$
6. $n_{ox}^{Y*} = n_{ox}^*$
7. $D_{ox}^O = D_{ox}$
8. $\langle n_m^Y \rangle^m = n_m$

9. $n_m^{Y*} = n_m^*$
10. $D_m^{Fe} = D_m$
11. $\langle T \rangle = T$

The final set of PDEs, ready for numerical implementation read as:

$$\begin{aligned} \frac{\partial}{\partial t}(\tilde{\rho}_m \mathbf{v}_m) + \nabla \cdot (\tilde{\rho}_m \mathbf{v}_m \mathbf{v}_m) &= -\frac{\tilde{\rho}_m}{\rho_0} \nabla P_m + \frac{\tilde{\rho}_m}{\rho_0} \mu_m \nabla^2 \mathbf{v}_m \\ &- \left(\frac{\tilde{\rho}_m}{\rho_0} \right)^2 \mu_m K^{-1} \cdot \mathbf{v}_m + \tilde{\rho}_m \left[1 - \beta_T (T - T_0) - \beta_S (n_m - n_0) \right] \mathbf{g} \end{aligned} \quad (6.23)$$

$$\begin{aligned} \frac{\partial}{\partial t}(\tilde{\rho}_{ox} n_{ox}) - n_{ox}^* \dot{m}_{ox} &= \nabla \cdot (\tilde{\rho}_{ox} D_{ox} \nabla n_{ox}) \\ &+ \rho_0 h_{ox} (n_{ox}^* - n_{ox}) \end{aligned} \quad (6.24)$$

$$\begin{aligned} \frac{\partial}{\partial t}(\tilde{\rho}_m n_m) + \nabla \cdot (\tilde{\rho}_m n_m \mathbf{v}_m) + n_m^* \dot{m}_{ox} \\ &= \nabla \cdot (\tilde{\rho}_m D_m \nabla n_m) \\ &+ \rho_0 h_m (n_m^* - n_m) \end{aligned} \quad (6.25)$$

$$\dot{m}_{ox} = \frac{\partial}{\partial t}(\tilde{\rho}_{ox}) = \frac{1}{(n_m^* - n_{ox}^*)} \left[\rho_0 h_m (n_m^* - n_m) + \rho_0 h_{ox} (n_{ox}^* - n_{ox}) \right] \quad (6.26)$$

$$\begin{aligned} \frac{\partial}{\partial t}(\tilde{\rho}_m C_{P0} T) + \nabla \cdot (\tilde{\rho}_m C_{P0} T \mathbf{v}_m) &= \nabla \cdot (\Lambda_{eff} \nabla T) \\ &- L_f \dot{m}_{ox} - \frac{\partial}{\partial t}(\tilde{\rho}_{ox} C_{P0} T) \end{aligned} \quad (6.27)$$

The numerical implementation of the above system of PDEs has been done in IRSN's high fidelity C++ CFD solver *CALIF³S* [20]. The main highlight of the numerical scheme implemented in *CALIF³S* is the use of *time semi-discretization* scheme. One of the main highlights of this *time semi-discretization* scheme is that it ensures the conservativeness and *discrete maximum principle* for the scalar transport equations like species

and temperature. The mathematical proof for the satisfaction of *discrete maximum principle* is given in Appendix (D). Below is the summarised algorithm with *time semi-discretization* of the system of PDEs given by Eqs. (6.23 - 6.27).

Considering a partition; $0 = t^0 < t^1 < \dots < t^K = T$; of the time interval $(0, T)$, which for the sake of simplicity, is taken uniform. Let Δt be a constant time step; $\Delta t = t^{k+1} - t^k$ for $k = 0, 1, 2, \dots, K - 1$. The *time semi-discretization* of Eqs. (6.23 - 6.27) reads:

Knowing $\tilde{\rho}_{ox}^{k-1}, \tilde{\rho}_m^{k-1}, \tilde{\rho}_{ox}^k, \tilde{\rho}_m^k, \mathbf{v}_m^k, P^k, n_{ox}^k$ and n_m^k :

1. *Step 1*: Solve for $\tilde{\rho}_{ox}^{k+1}$ and \dot{m}_{ox}

$$\frac{\tilde{\rho}_{ox}^{k+1} - \tilde{\rho}_{ox}^k}{\Delta t} = \frac{1}{(n_m^* - n_{ox}^*)} \left[\rho_0 h_m(n_m^* - n_{ox}^k) + \rho_0 h_{ox}(n_{ox}^* - n_{ox}^k) \right] \quad (6.28)$$

$$\dot{m}_{ox} = \frac{1}{(n_m^* - n_{ox}^*)} \left[\rho_0 h_m(n_m^* - n_m^k) + \rho_0 h_{ox}(n_{ox}^* - n_{ox}^k) \right] \quad (6.29)$$

2. *Step 2*: Solve for n_{ox}^{k+1}

$$\frac{\tilde{\rho}_{ox}^k n_{ox}^{k+1} - \tilde{\rho}_{ox}^{k-1} n_{ox}^k}{\Delta t} - n_{ox}^* \dot{m}_{ox} = \nabla \cdot (\tilde{\rho}_{ox}^k D_{ox} \nabla n_{ox}^{k+1}) + \rho_0 h_{ox}(n_{ox}^* - n_{ox}^{k+1}) \quad (6.30)$$

3. *Step 3*: Solve for n_m^{k+1}

$$\begin{aligned} \frac{\tilde{\rho}_m^k n_m^{k+1} - \tilde{\rho}_m^{k-1} n_m^k}{\Delta t} + \nabla \cdot (\tilde{\rho}_m^k n_m^{k+1} \mathbf{v}_m^k) + n_m^* \dot{m}_{ox} &= \nabla \cdot (\tilde{\rho}_m^k D_m \nabla n_m^{k+1}) \\ &+ \rho_0 h_m(n_m^* - n_m^{k+1}) \end{aligned} \quad (6.31)$$

4. *Step 4*: Solve for T^{k+1}

$$\begin{aligned} \frac{\tilde{\rho}_m^k C_{P0} T^{k+1} - \tilde{\rho}_m^{k-1} C_{P0} T^k}{\Delta t} + \nabla \cdot (\tilde{\rho}_m^k C_{P0} T^{k+1} \mathbf{v}_m^k) &= \nabla \cdot (\Lambda_{eff} \nabla T^{k+1}) \\ L_f \dot{m}_{ox} - \frac{\tilde{\rho}_{ox}^k C_{P0} T^{k+1} - \tilde{\rho}_{ox}^{k-1} C_{P0} T^k}{\Delta t} & \end{aligned} \quad (6.32)$$

5. *Step 5:* Solve for $\tilde{\rho}_m^{k+1}$

$$\frac{\tilde{\rho}_m^{k+1} - \tilde{\rho}_m^k}{\Delta t} + \nabla \cdot (\tilde{\rho}_m^{k+1} \mathbf{v}_m^k) = -\dot{m}_{ox} \quad (6.33)$$

6. *Step 6:* Solve for $\tilde{\mathbf{v}}_m^{k+1}$ (predicted velocity)

$$\begin{aligned} \frac{\tilde{\rho}_m^k \tilde{\mathbf{v}}_m^{k+1} - \tilde{\rho}_m^{k-1} \mathbf{v}_m^k}{\Delta t} + \nabla \cdot (\tilde{\rho}_m^k \tilde{\mathbf{v}}_m^{k+1} \mathbf{v}_m^k) = & -\frac{\tilde{\rho}_m^k}{\rho_0} \nabla P_m^k + \frac{\tilde{\rho}_m^k}{\rho_0} \mu_m \nabla^2 \tilde{\mathbf{v}}_m^{k+1} \\ & - \left(\frac{\tilde{\rho}_m^k}{\rho_0} \right)^2 \mu_m K^{-1} \cdot \tilde{\mathbf{v}}_m^{k+1} + \tilde{\rho}_m^k \left[1 - \beta_T (T^k - T_0) - \beta_S (n_m^k - n_0) \right] \mathbf{g} \end{aligned} \quad (6.34)$$

7. *Step 7:* Solve for P^{k+1} , \mathbf{v}_m^{k+1} , where: $\rho = \tilde{\rho}_m + \tilde{\rho}_{ox}$

$$\frac{\rho^k (\mathbf{v}_m^{k+1} - \tilde{\mathbf{v}}_m^{k+1})}{\Delta t} + \nabla (P^{k+1} - P^n) = 0 \quad (6.35)$$

$$\frac{\rho^{k+1} - \rho^k}{\Delta t} + \nabla \cdot (\rho^{k+1} \mathbf{v}_m^{k+1}) = 0 \quad (6.36)$$

Step 2, Step 3 and Step 4 are the semi-implicit solution of the balance equations for n_{ox}^{k+1} , n_m^{k+1} and T^{k+1} , which is classical except the fact that the density is shifted backward with respect to time, this will yield a discretization satisfying a discrete-maximum principle (see Appendix (D)). Step 6 consist in a semi-implicit solution of the momentum balance equation to obtain a predicted velocity, with once again a shift in density. Step 7 is a pressure correction step, which is a standard projection step used in constant density incompressible flow solving algorithm [71]. At the discrete level, taking the divergence of Eq. (6.35) and using the Eq. (6.36) to eliminate the unknown velocity \mathbf{v}_m^{k+1} gives a linear elliptic problem for the pressure. Once pressure is known, the Eq. (6.35) gives the \mathbf{v}_m^{k+1} .

Several test cases from the literature, testing the numerical accuracy of the implemented Navier-Stokes equation in handling the flow through partially porous medium and further calculating the solutal natural convection in coupling with the implemented species transport equations for uniform porous media has been shown in Appendix (E).

Chapter 7

Model Demonstration for Dissolution Calculations

Chapter 7

Model Demonstration for Dissolution Calculations

The main aim of this chapter is to present a demonstration of the 2D dissolution calculated by the macroscopic model in the crust with various closure relations for the mass transfer coefficients. The closure models tested in the present chapter are already been mentioned in chapter 6 under the section (6.1). This sensitivity study is important to study the strong dependency of mass transfer coefficients on the evolving micro-structures in the crust.

In the regard of this important sensitivity study with different closure relations for mass transfer coefficients, the numerical results are compared qualitatively in this chapter with the morphology of the crust produced by CORDEB experiments [4]. This is done, in order to identify a unique closure model for mass transfer coefficient, which can be used for all subsequent calculations for reactor specific cases, detailed in chapter 8. It is important to mention that a quantitative validation of the model with respect to CORDEB results was not possible because there are several elements or phenomena in CORDEB tests which could not be taken into account in the model developed: the formation of cracks in the crust, the changes of volume due to changes of composition and density, the existence of a liquid oxide phase.

Further, after identifying the appropriate closure model for mass transfer coefficient, some calculations have also been shown with different boundary conditions below the crust. Capability of the mathematical model for calculating the dissolution under the influence of the advection is also demonstrated at the end of this chapter.

It is important to note that the present chapter only serves the purpose of identifying the appropriate closure relation for mass transfer coefficient capable of producing the morphology of the crust same as observed in CORDEB experiments, and demonstrating the capability of the mathematical model to compute dissolution for various cases with or without convection. Thus, the dimensions of the molten metal layer in the computational domains

taken for the study of the $2D$ dissolution may not correspond to the moles of molten steel (N^{Fe}) present in the metal-oxide system. Also, the present chapter does not cover the thermo-solutal convection in the metal domain. These, more concrete reactor-specific cases are elaborated and discussed in chapter 8.

Throughout this chapter, all the numerical results will be shown mainly for two geometric configurations which are as follows:

1. A single liquid-metal domain above the two phase solid-oxide and liquid-metal crust, henceforth called *Geometry 1* and shown in Fig. 7.1 (a).
2. Two liquid-metal domains, one above and other below the crust, henceforth called *Geometry 2* and shown in Fig. 7.1 (b).

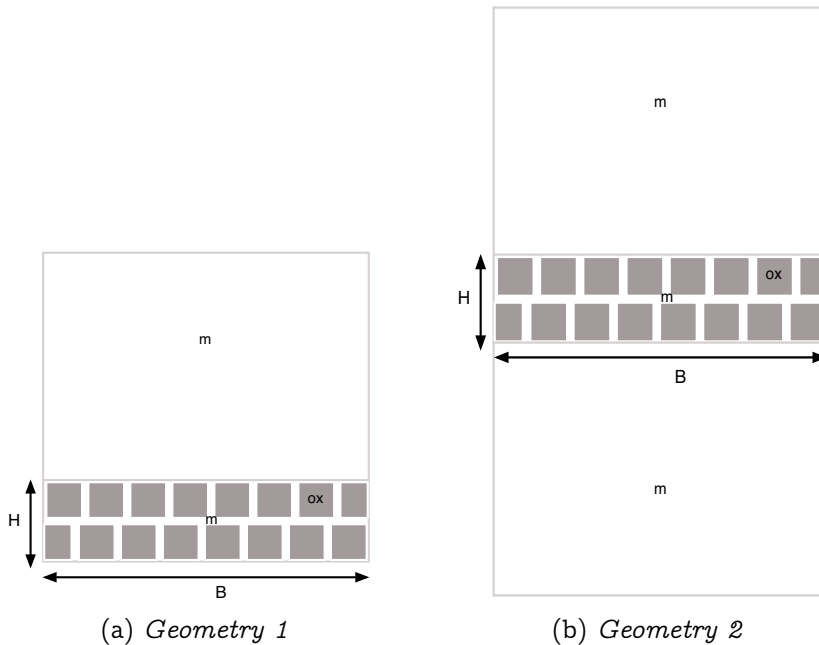


Figure 7.1: Two geometric configurations studied

7.1 Geometry 1

7.1.1 Without Convection ($\mathbf{v}_m = 0$)

The case of no convection in the liquid phase $\mathbf{v}_m = 0$ has been studied for two cases. The two cases corresponds to the different boundary conditions below the crust. The computational domains with the boundary conditions and the numerical results has been elaborated in the following sections.

7.1.1.1 Case 1: Initial, Equilibrium and Boundary Conditions (B.C.)

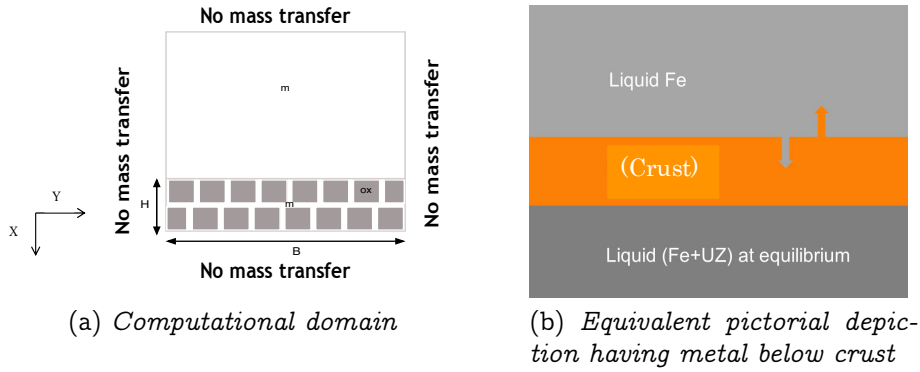


Figure 7.2: Computational domain and B.C. for case: 1

The dimensions indicated in Fig. 7.2(b) are: $H = 0.01 \text{ m}$ and $B = 0.06 \text{ m}$.

No mass transfer is taken on lateral boundaries in Fig. 7.2(a). In this case liquid metal is taken to be at equilibrium below the crust. To simulate a case of liquid at equilibrium below crust as shown in Fig. 7.2(b), *No mass transfer* has been taken as the B.C below crust ($m + ox$) in Fig. 7.2(a). In order not to impose any B.C. at the interface between the crust ($m + ox$) and the liquid-metal (m), computational domain includes a purely liquid zone at the top shown in Fig. 7.2(a), where again, *No mass transfer* has been taken.

The initial mole fractions of (U, Zr) in the liquid-metal phase is: $\langle n_m^Y \rangle^m = 0$. The initial mole fractions of (U, Zr) in solid-oxide grains corresponds to $\langle n_{ox}^Y \rangle^{ox} = 0.45$. The equilibrium mole fractions in liquid-metal and solid-oxide phase as determined from simplified model for reactor case of $C_{uz} = 1$, $C_{ox} = 0.3$ and C_{sz} or $N^{Fe} = 2.0$ are $n_m^{Y*} = 0.2$ and $n_{ox}^{Y*} = 0.35$ respectively.

The initial porosity field ε_m is initialized randomly in the range $10\% \pm 5\%$, in order to represent the non-uniform distribution of interstitial spaces between the solid-oxide grains.

7.1.1.2 Case 1: Numerical Results

The first set of numerical results has been produced by using the expression of mass transfer coefficients given by Eq. (6.5) [16] and read as:

$$h_k = \frac{h_{k0} D_k^i \left[256\varepsilon_k - 300\varepsilon_k^2 - 653\varepsilon_k^3 + 1320\varepsilon_k^4 - 653\varepsilon_k^5 \right]}{l_d^2} \quad (7.1)$$

where $k = (ox, m)$, $i = O$ for $k = ox$ and $i = Fe$ for $k = m$. The value of h_{k0} is 10^{-3} for $k = m$, and 10^{-6} for $k = ox$. The value of diffusivities D_k^i are $10^{-6} \text{ m}^2/\text{sec}$. [65] for $k = m$ and $i = Fe$, and $10^{-9} \text{ m}^2/\text{sec}$. [3, 62] for $k = ox$ and $i = O$. The value of l_d corresponds to the average grain size which is about 10^{-4} m [13].

Fig. 7.3 shows the dissolution profile obtained in the crust by using the Eq. (7.1). From Fig. 7.3 it appears that the dissolution progresses as plane front in the crust. Further this front is quite sharp as the crust is fully dissolved in around 4000 seconds. This corresponds to an average velocity of 0.025 mm/sec. for a 1 cm of crust. Other important observation can be made for the evolution of porosity in the two-phase crust. It is quite evident that the initial variation in porosity field subsides within crust in time. Also, there is a simultaneous solidification of initial pores in the region not yet affected by dissolution. Hence, no occurrence of liquid channels same as Fig. 2.3 from CORDEB experiment [4] can be seen in these results obtained by use of Eq. (7.1). The same can be seen from Fig. 7.4 as well.

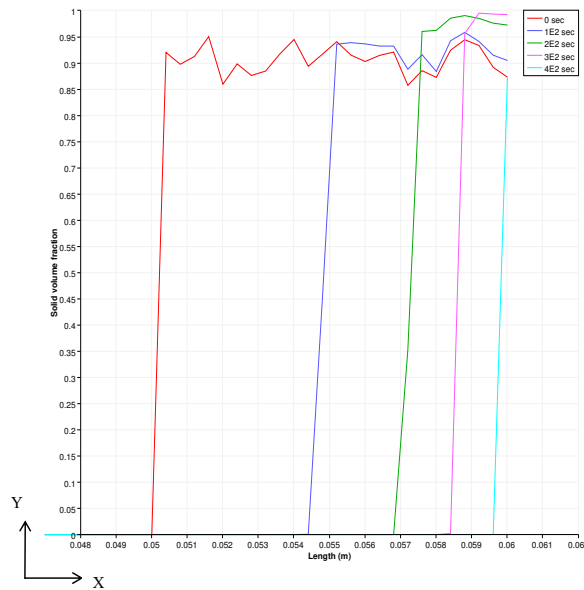


Figure 7.3: Dissolution profile calculated in crust by the model in the crust

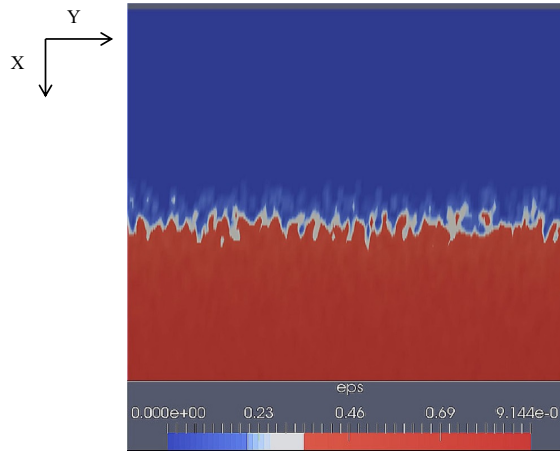


Figure 7.4: Solid volume fraction distribution calculated in crust by the model in the crust at 2000 sec.

The second set of results corresponds to the use of the expression of mass transfer coefficient given by Eq. (6.6) [13], which read as:

$$h_k = \frac{h_{k0} D_k^i \varepsilon_k (1 - \varepsilon_k)}{l_d^2} \quad (7.2)$$

where $k = (ox, m)$, $i = O$ for $k = ox$ and $i = Fe$ for $k = m$. The values of h_{k0} , D_k^i , l_d are same as the one given below Eq. (7.1).

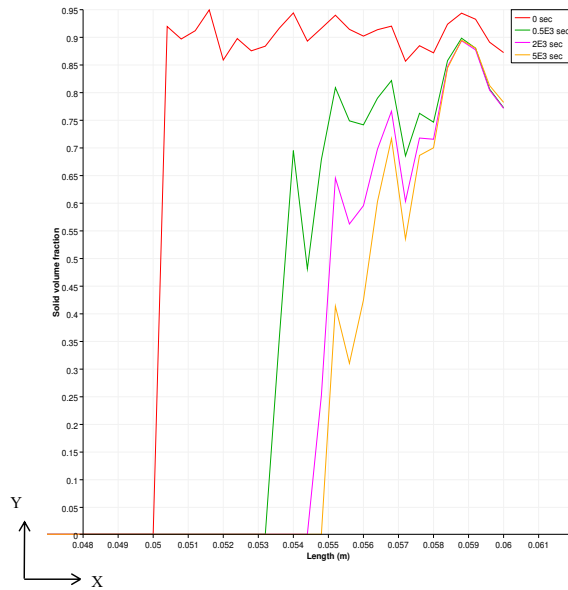


Figure 7.5: Dissolution profile calculated in crust by the model in the crust

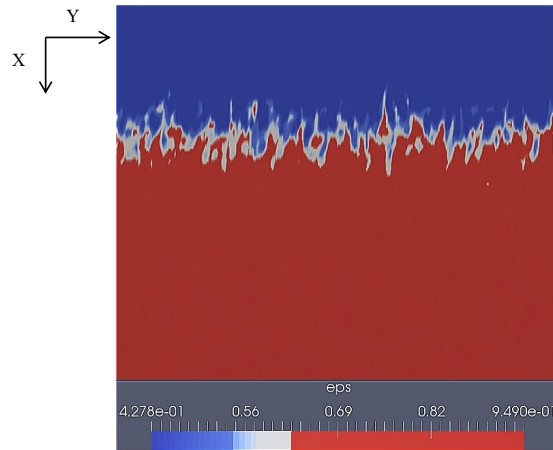


Figure 7.6: Solid volume fraction distribution calculated in crust by the model in the crust at 5000 sec.

From Fig. 7.5 it can be seen that the dissolution occurs almost like plane front in this case, as well. But the front is not as sharp as the one observed in the previous case because at the end of the 5000 sec. it seems that less than half of the crust is dissolved. Some amplification of initial porosities can be seen near the top part of the crust. But the solidification of initial porosities near the bottom part of the crust renders the amplification ineffective to produce the liquid channels. Fig. 7.6 shows that the use of Eq. (7.2) turns out to be ineffective to reproduce the microstructure of the crust same as observed in Fig. 2.3.

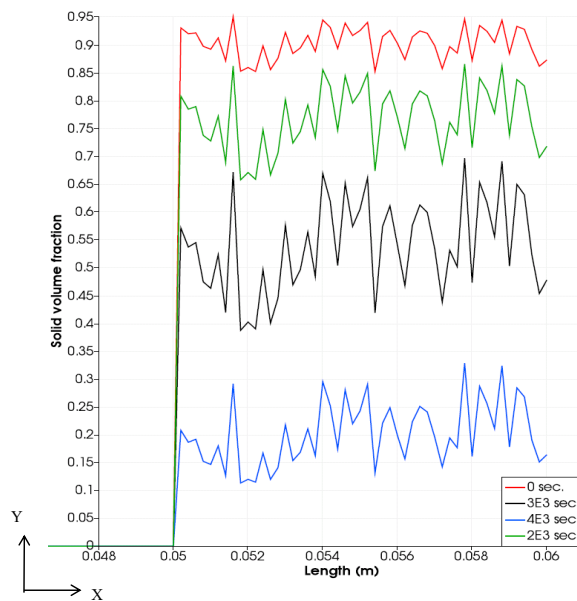


Figure 7.7: Dissolution profile calculated in crust by the model in the crust

The third set of results are obtained with the use of Eq. (6.7), which is proposed in this work. This expression reads as:

$$h_k = \frac{h_{k0} \varepsilon_k (1 - \varepsilon_k)}{\tau} \quad (7.3)$$

where $k = (ox, m)$, $i = O$ for $k = ox$ and $i = Fe$ for $k = m$. The values of h_{k0} are same as the one given below Eq. (7.1). The value of τ is chosen to be 1 sec.

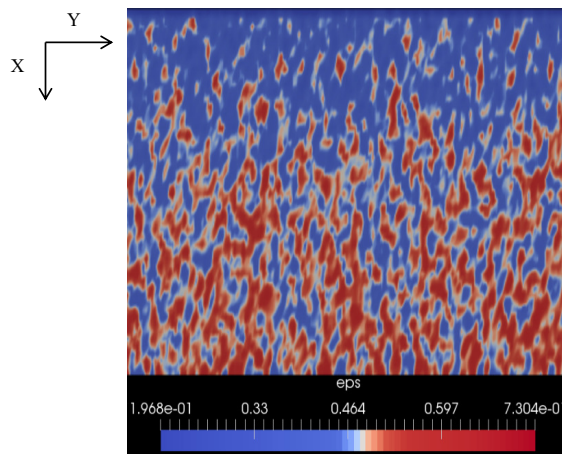


Figure 7.8: Solid volume fraction distribution calculated in crust by the model in the crust at around 2500 sec.

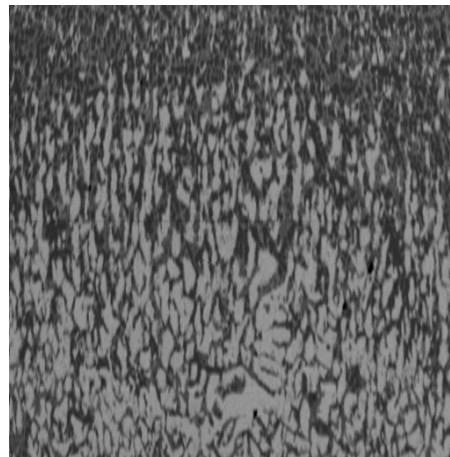


Figure 7.9: Micro-structure of the crust after dissolution, showing oxide crust in Grey and molten steel channels in Black. CORDEB experiment [4]

From Fig. 7.8 it is observed that the dissolution occurs uniformly in the whole crust with no distinct front. In this case it can be clearly seen that the initial variation of porosity field gets amplified to create visible molten steel channels in the crust. The same has been observed in the Fig. 7.9 from CORDEB experiment [4].

7.1.1.3 Discussions About the Effect of Liquid Mass Transfer Coefficients on Dissolution in Crust

It is evident from section (7.1.1.2) that the closure model used for the mass transfer coefficients have significant effect on the microstructure evolution in the crust while dissolution. An insight on this issue can be derived by looking into the comparison of characteristic times of dissolution in liquid and effective diffusion. The characteristic time of dissolution in liquid is given by:

$$\tau_{h_m} = \frac{1}{h_m} \quad (7.4)$$

Likewise, the characteristic time of effective diffusion can be estimated as:

$$\tau_{De} = \frac{l_d^2}{D_e} \quad (7.5)$$

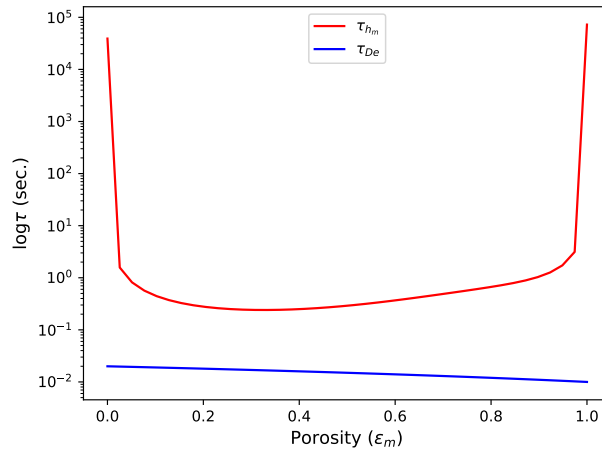


Figure 7.10: Comparison between characteristic time of effective diffusion (τ_{De}) and time of dissolution in liquid phase (τ_{h_m}) for Eq. (7.1)

Keeping these two expressions in mind, the characteristic times can be plotted. The characteristic times for dissolution in liquid and effective diffusion for Eq. (7.1) is shown in Fig. (7.10). Similarly, the characteristic times for dissolution in liquid and effective diffusion for Eq. (7.2) and Eq. (7.3) are shown in Fig. (7.11) and Fig. (7.12), respectively.

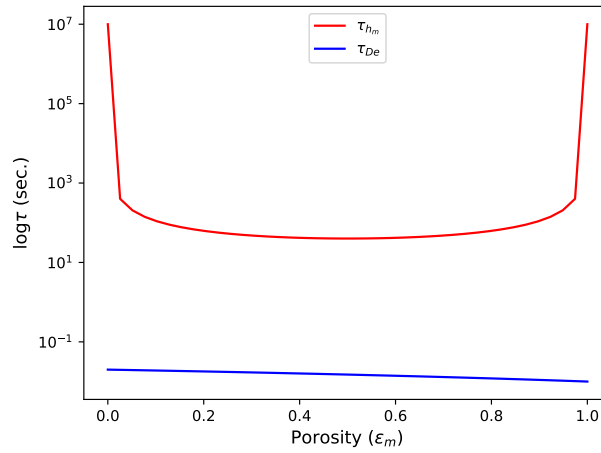


Figure 7.11: Comparison between characteristic time of effective diffusion (τ_{De}) and time of dissolution in liquid phase (τ_{hm}) for Eq. (7.2)

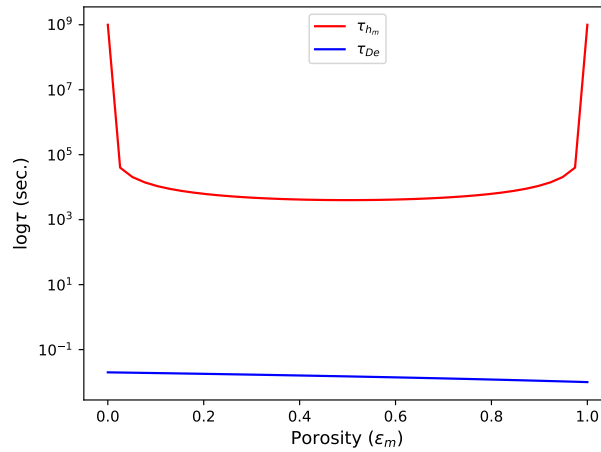


Figure 7.12: Comparison between characteristic time of effective diffusion (τ_{De}) and time of dissolution in liquid phase (τ_{hm}) for Eq. (7.3)

Comparing the Fig. 7.12, Fig. 7.10 and Fig. 7.11, it can be seen that diffusion is much faster than the dissolution in the case of using the expression of mass transfer coefficient given by Eq. (7.3) and illustrated by Fig. 7.12. This is evident from the fact that the relative difference between the characteristic time of dissolution in liquid-metal and effective diffusivity is highest in Fig. 7.12 (outcome of Eq. (7.3)) when compared with Fig. 7.10 (outcome of Eq. (7.1)) and Fig. 7.11 (outcome of Eq. (7.2)).

This very large relative difference between the characteristic time of effective diffusion and dissolution in liquid-metal phase obtained from Eq. (7.3), making the effective diffusion much faster than the dissolution, can be one of the reasons explaining the manifestation of liquid-metal channels (see Fig. 7.8) similar to the one observed in CORDEB experiment [4]. Consequently, for the same reason, when the relative difference between the time of effective diffusion and time of dissolution in liquid-metal phase decreases, as observed from the trend produced by Eq. (7.2) and Eq. (7.1), the liquid-metal channels become less and less visible in Fig. 7.11 and Fig. 7.10 respectively. Thus, for the cases represented by Eq. (7.2) and Eq. (7.1), plane front is one of the characteristics of the dissolution, but for the case represented by Eq. (7.3), dissolution is prominently uniform in the crust, leading to the creation of liquid-metal channels.

From the preceding analysis, done with the comparison of effective time of diffusion and time of dissolution in liquid-metal, it can be concluded that, in order to reproduce experimental observations, it is necessary to assume a very fast diffusion of atoms through the crust, with a value of the effective diffusion well above the standard molecular diffusion in solids. The reason for that remains an open question at the moment and more investigations, both numerical and experimental, are necessary.

7.1.1.4 Case 2: Initial, Equilibrium and Boundary Conditions (B.C)

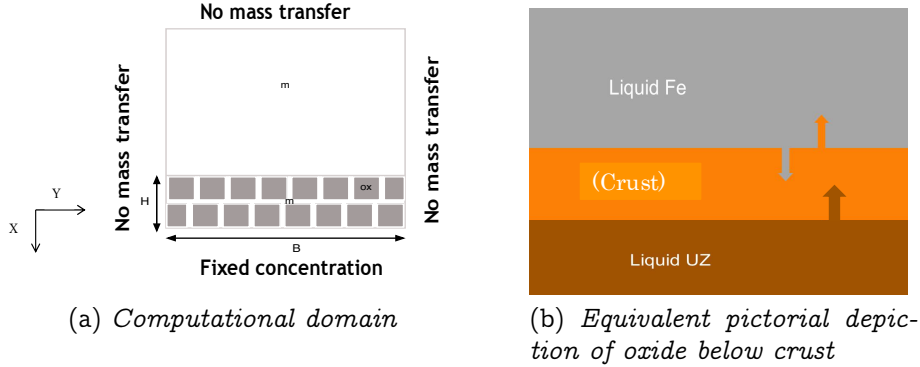


Figure 7.13: Computational domain and B.C. for case: 2

The dimensions of the computational domain shown in Fig. 7.13 (a) are the same as *case 1*. The initial and equilibrium conditions for mole fractions in this case are exactly the same as *case 1*, detailed in section (7.1.1.1). The initial porosity distribution is also the same as *case 1*. This case corresponds to the presence of a liquid oxide below the crust. Consequently in order to simulate the presence of liquid oxide below the crust, as shown in Fig. 7.13 (b), the *Fixed* B.C. has been imposed on the bottom boundary in the computational domain, which is shown in Fig. 7.13 (a). This *Fixed* B.C. corresponds to fixed value of mole fractions of (U, Zr) on the bottom boundary i.e. $\langle n_{ox}^Y \rangle^{ox} = 0.35$ which is also the equilibrium value.

7.1.1.5 Case 2: Numerical Results

The expression of mass transfer coefficient used to generate the numerical results for *case 2* is the one, which worked for reproducing the microstructure of the crust after dissolution in CORDEB experiment [4]. This mass transfer expression was identified to be Eq. (7.3) in section (7.1.1.2), and reads as:

$$h_k = \frac{h_{k0} \varepsilon_k (1 - \varepsilon_k)}{\tau} \quad (7.6)$$

where $k = (ox, m)$, $i = O$ for $k = ox$ and $i = Fe$ for $k = m$. The value of h_{k0} are same as the one given below Eq. (7.1). The value of τ is 1 sec.

Fig. 7.14 (a) depicts the dissolution profiles in the crust for *case 2*. Comparing the dissolution profiles for *case 2* with *case 1*, shown in Fig. 7.14 (b), some similarities and differences can be accounted for. In general in both cases, there is an amplification of initial distribution of porosities. However, looking at the solid volume fraction calculated by the model it can be seen that only in *case 1*, the liquid channels are observed (Fig. 7.15 (b)) but not in *case 2*

(Fig. 7.15 (a)), despite the amplification of initial porosity distribution seen in both the cases. This is because the dissolution in *case 2* is non-uniform in the crust. From Fig.7.14 (a), it can be seen that it is more on the top part of the crust and less at the bottom part of the crust. In fact the dissolution is not only less in the bottom part of the crust but also there is occurrence of solidification in the initial pores very close to the bottom part of the crust. Due to this gradient in the dissolution profile with solidification close to the bottom part of the crust, the amplification in the initial porosity distribution rendered ineffective to give rise to the liquid channels in the crust.

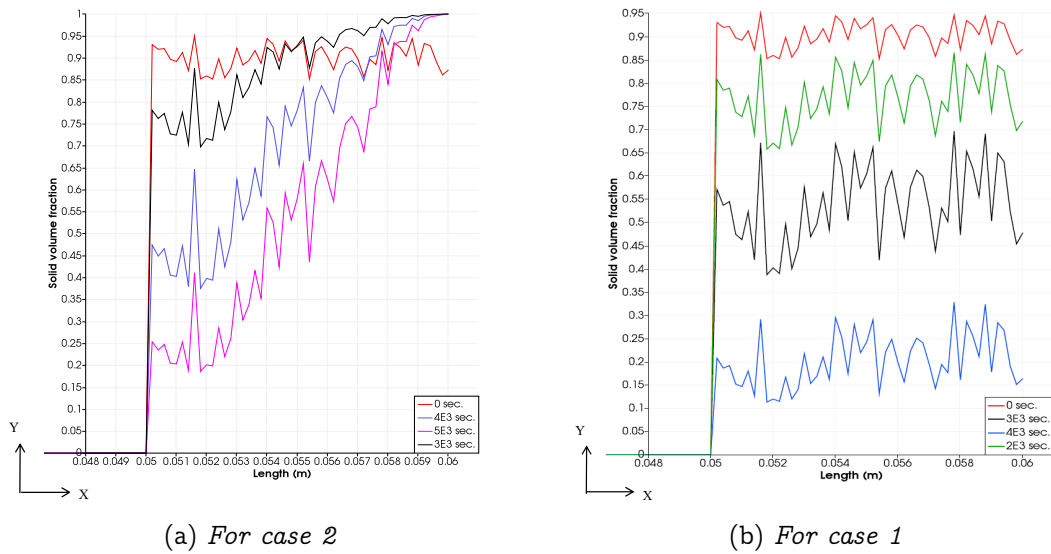


Figure 7.14: Dissolution profile calculated in crust for *case 1* and *case 2*

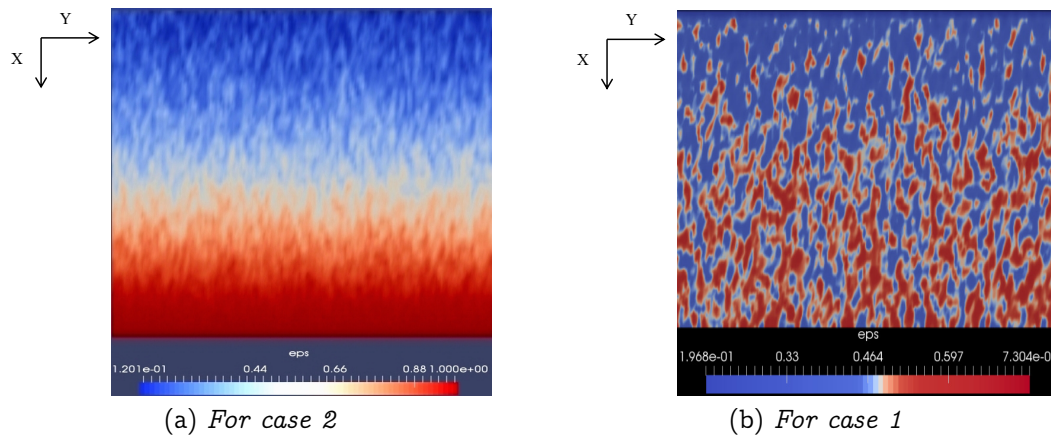


Figure 7.15: Solid volume fraction distribution calculated in crust for *case 1* and *case 2* at around 2500 sec.

It is clear in *case 2* that the crust becomes stable after some time and dissolution is no more effective. This is due to the supply of O atoms into the oxide phase in crust from the bottom liquid oxide phase. Due to this transfer of O atoms, the crust seems to become stable. Thus, the composition of liquid phase present below the crust has an impact on the stability of the crust. If there is liquid metal at equilibrium below the crust, the crust seems to dissolve eventually as seen in Fig. 7.15 (b), but having a liquid oxide below the crust, seems to make it stable, especially at the bottom part of the crust as seen in Fig. 7.15 (a).

7.2 Geometry 2

The case with *geometry 2* has been studied both with convection ($v_m \neq 0$) and without convection ($v_m = 0$).

7.2.1 Without Convection ($v_m = 0$)

7.2.1.1 Initial, Equilibrium and Boundary Conditions (B.C)

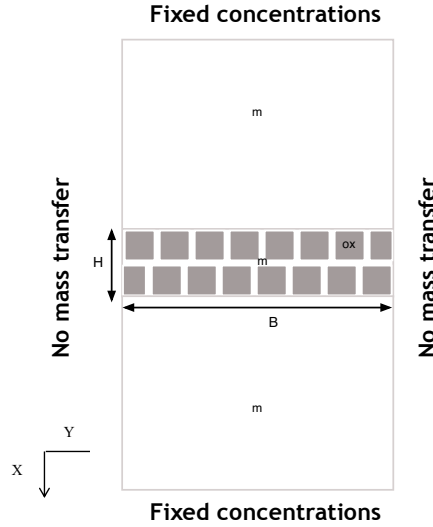


Figure 7.16: Computational domain

The dimensions indicated in Fig. 7.16 are: $H = 0.02 \text{ m}$ and $B = 0.06 \text{ m}$.

In Fig. 7.16, the initial mole fractions of (U, Zr) in top liquid-metal phase is: $\langle n_m^Y \rangle^m = 0$. The initial mole fractions of (U, Zr) in solid-oxide grains in crust corresponds to $\langle n_{ox}^Y \rangle^{ox} = 0.45$. The equilibrium mole fractions in liquid-metal and solid-oxide phase as determined from simplified model for reactor case of $C_{uz} = 1$, $C_{ox} = 0.3$ and C_{sz} or $N^{Fe} = 2.0$ are $n_m^{Y*} = 0.2$ and $n_{ox}^{Y*} = 0.35$ respectively. Further, in Fig. 7.16, the initial mole fractions of (U, Zr) in bottom liquid-metal phase is at equilibrium i.e. $\langle n_m^Y \rangle^m = n_m^{Y*}$.

No mass transfer is taken on lateral boundaries in Fig. 7.16. The top B.C. corresponds to the *Fixed* mole fractions of (U, Zr) in both solid-oxide and liquid-metal phase, which are: $\langle n_{ox}^Y \rangle^{ox} = 0.45$ and $\langle n_m^Y \rangle^m = 0$. The bottom B.C. also corresponds to the *Fixed* value of mole fraction, where $\langle n_{ox}^Y \rangle^{ox} = 0.45$, however, $\langle n_m^Y \rangle^m = n_m^{Y*}$.

The porosity field ε_m is initialized randomly in the range $10\% \pm 5\%$, in order to represent the non-uniform distribution of interstitial spaces between the solid-oxide grains.

7.2.1.2 Numerical Results

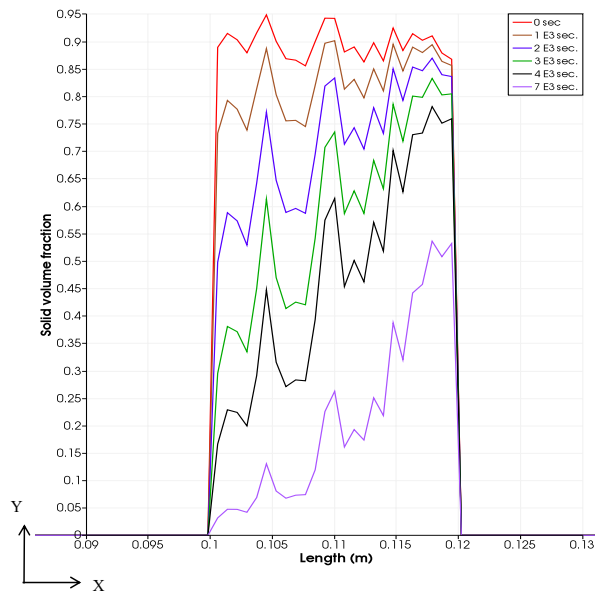


Figure 7.17: Dissolution profile calculated in crust by the model in the crust

The dissolution computed by the model in the present case by using the Eq. (7.6) is shown in Fig. 7.17. It can be seen that the dissolution occurs everywhere in the domain but is faster on the left side in Fig. 7.17 (top in the Fig. 7.16) than the right side (bottom in Fig. 7.16).

This is due to the different liquid mole fractions below the crust, where liquid is already at equilibrium. This obviously means that there is no dissolution (or very less) below the crust (right side in Fig. 7.17) in the beginning.

Similar to the results in the section (7.1.1.2) obtained by using Eq. (7.3), here as well an amplification of porosities is observed, with formation of channels. The important comparative study between the present case and the case with convection is given in the following section.

7.2.2 With Convection ($v_m \neq 0$)

7.2.2.1 Initial, Equilibrium and Boundary Conditions (B.C)

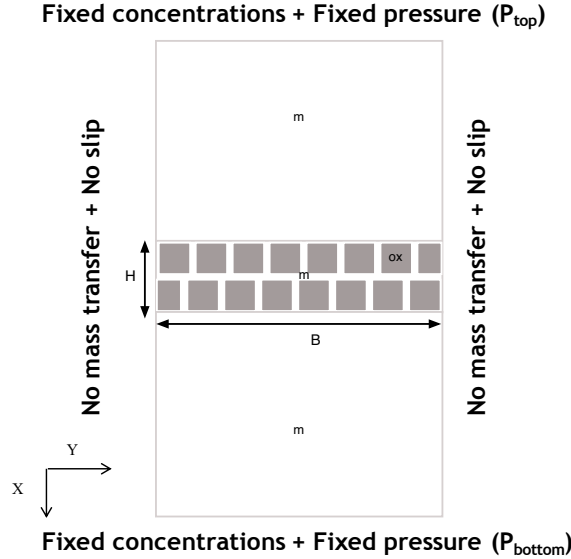


Figure 7.18: Computational domain

The initial, equilibrium values of mole fractions are same as one identified in section (7.2.1.1) for the case of no convection ($v_m = 0$). The porosity field in the crust is randomly initialized, similar to all above cases.

The B.C. with respect to the mole fractions on lateral, top and bottom boundaries are similar to the case of no convection described in section (7.2.1.1). For velocity, *No slip* B.C. is imposed on the lateral boundaries, as shown in Fig. (7.18). Additionally, for this case, in order to generate a flow, after creation of the liquid channels, a pressure gradient is applied between top and bottom boundary, such that, $P_{top} > P_{bottom}$.

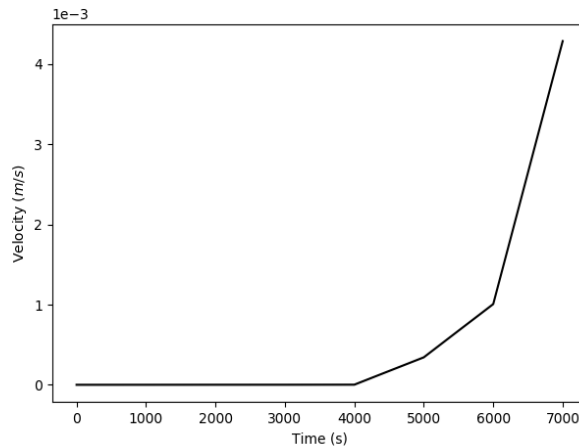
7.2.2.2 Numerical Results

In the calculations with convection, it is observed that in the beginning till $t < 5000 \text{ sec}$, due to the low porosity in the crust, depicted by black curve in Fig. 7.19 (b), the velocity across the crust remains small as seen in Fig. 7.19 (a). However, at 5000 sec , when the average solid volume fraction ϵ_s in the crust becomes less than 60 % i.e. ($\epsilon_s < 60 \%$), the velocity (of the order 10^{-3} m/sec) becomes significant in the crust. After $t > 5000 \text{ sec}$, it can be seen that dissolution becomes much faster, as observed from the black curve in Fig. 7.19 (b).

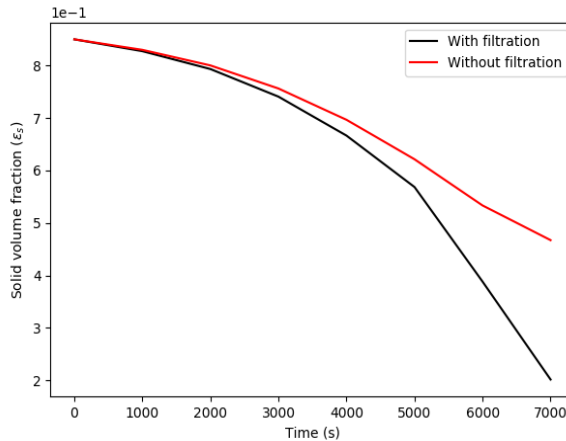
This is due to the penetration of *fresh* steel, which replaces the saturated steel within the pores. Looking at the Fig. 7.19 (a)-(b), it can also be observed that the average velocity evolution along the cross-section in

the crust, shows a sharp increase after 5000 *sec*, which is the beginning of percolation, and is quickly followed by the *breakthrough* of metal through the crust.

Finally, at around 7000 *sec*, almost complete dissolution of the crust is observed. In Fig. 9 (b), it can be observed that convection has enhanced the dissolution in the present case, unlike the case with no convection, described in section (7.2.1). The red curve in Fig. 7.19 (b) shows the case with no convection, and the black curve depicts the present case with convection.



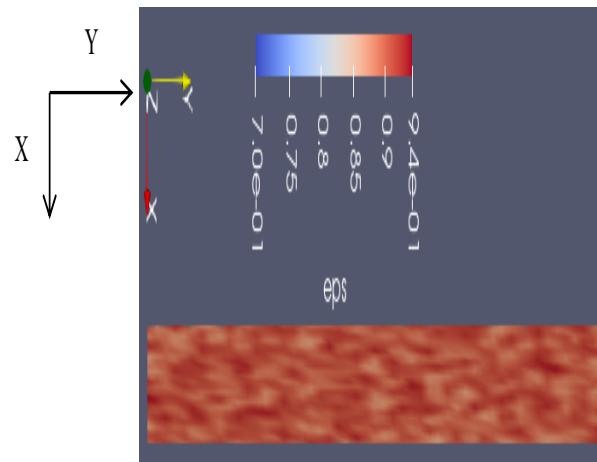
(a) Average velocity evolution along the cross-section in the crust



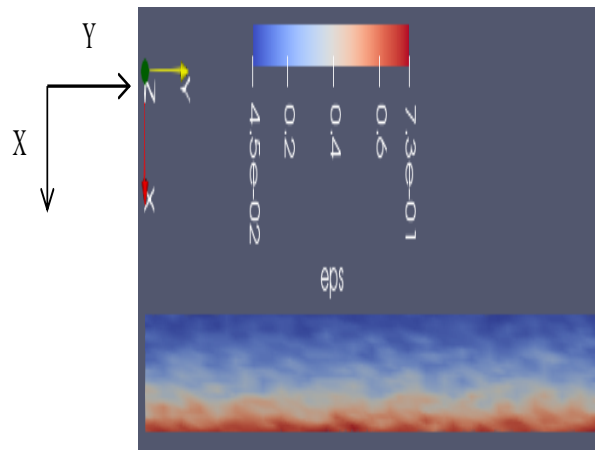
(b) Evolution of average solid volume fraction for the case, with and without convection

Figure 7.19: Average velocity and solid volume fraction evolution in the crust

Fig. 7.20 (a)-(b) shows the picture of the crust at $t = 0$ *sec* and $t = 5000$ *sec*. At $t = 5000$ *sec*, it can be seen that the crust has almost completely dissolved from the top, and solid volume fraction has an average value of about 60% near the bottom part of the crust.



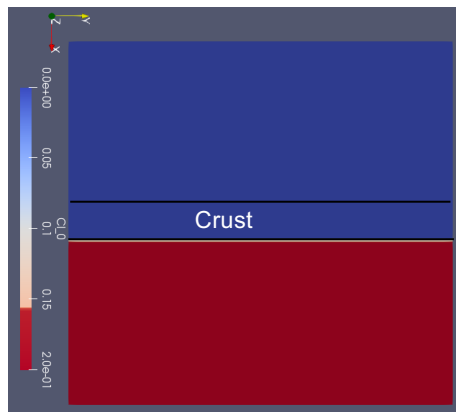
(a) Crust at 0 sec.



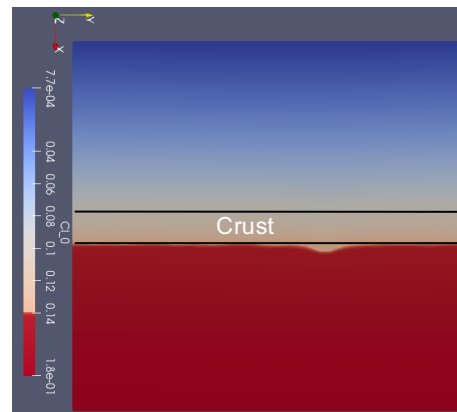
(b) Crust at 5000 sec. with average $\epsilon_{ox} < 60\%$

Figure 7.20: State of crust

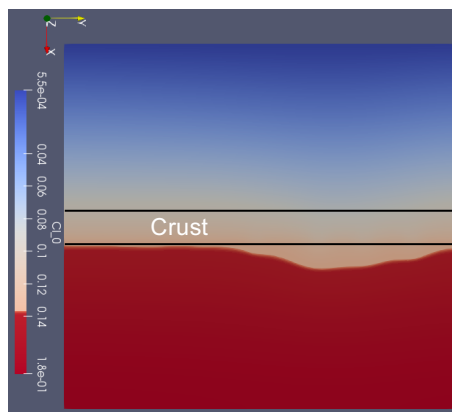
It can also be seen from the numerical results, that at 5000 sec, the point of the first *breakthrough* (first point across the length of the crust to allow flow of molten metal), corresponds to the small *bulge* in liquid mole fraction distribution ($\langle n_m^Y \rangle$), below the crust, shown in Fig. 7.21 (b). This *bulge* occurs as soon as there is a breach in the crust, due to high porosity, and simultaneously, the liquid mole fractions is modified below the crust, due to the advection of molten metal mass from top. Further, at 5400 sec, shown in Fig. 7.21 (c), an even bigger region below the crust, shows a change in liquid mole fractions, due to flow of molten steel from the top. Similar observations were also made in the CORDEB experiment [4], shown in Fig. 7.21 (d), where a similar *bulge* of molten metal can be seen below crust.



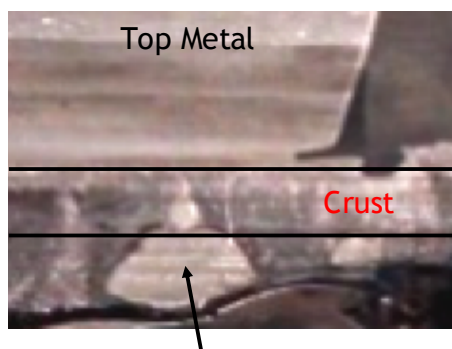
(a) *Liquid mole fraction profile above and below the crust at 0 sec.*



(b) *Liquid mole fraction profile above and below the crust at 5000 sec.*



(c) *Liquid mole fraction profile above and below the crust at 5400 sec.*



Metal below crust as seen

In CORDEB experiment

(d) *Flow of metal through a percolation in the crust observed in CORDEB experiment [4]*

Figure 7.21: Flow of molten metal through the crust and effect on the liquid mole fraction profile below the crust

Chapter 8

Results for Reactor Specific Cases

Chapter 8

Results for Reactor Specific Cases

This chapter shows the CFD calculations, which are both physically consistent and relevant to reactor cases, unlike chapter 7. The numerical results are made relevant to the reactor specific cases by improving upon the following parameters:

1. Dimensions of the molten metal layer, which will now correspond to the mass of steel, or moles of Fe in present analysis (N^{Fe}) present in the metal-oxide system.
2. Choosing more accurate initial mole fractions for O atoms in oxide phase (n_{ox}^O) and Fe atoms in metal phase (n_m^{Fe}), which will be relevant to reactor scenario.
3. Choosing accurate material properties for metal and oxide phases.
4. Taking into account the thermo-solutal convection in the molten metal layer.

8.1 Metal Layer Dimensions Corresponding to N^{Fe}

This chapter broadly covers two values of moles of Fe (N^{Fe}), that are:

1. $N^{Fe} = 2.0$
2. $N^{Fe} = 10.0$

2D computational domain corresponding to $N^{Fe} = 2.0$ have equal width of metal and crust layers. The corresponding geometry looks like Fig. 8.1 (a)-(b), where, A is the width of the metal layer and B is the width of the crust.

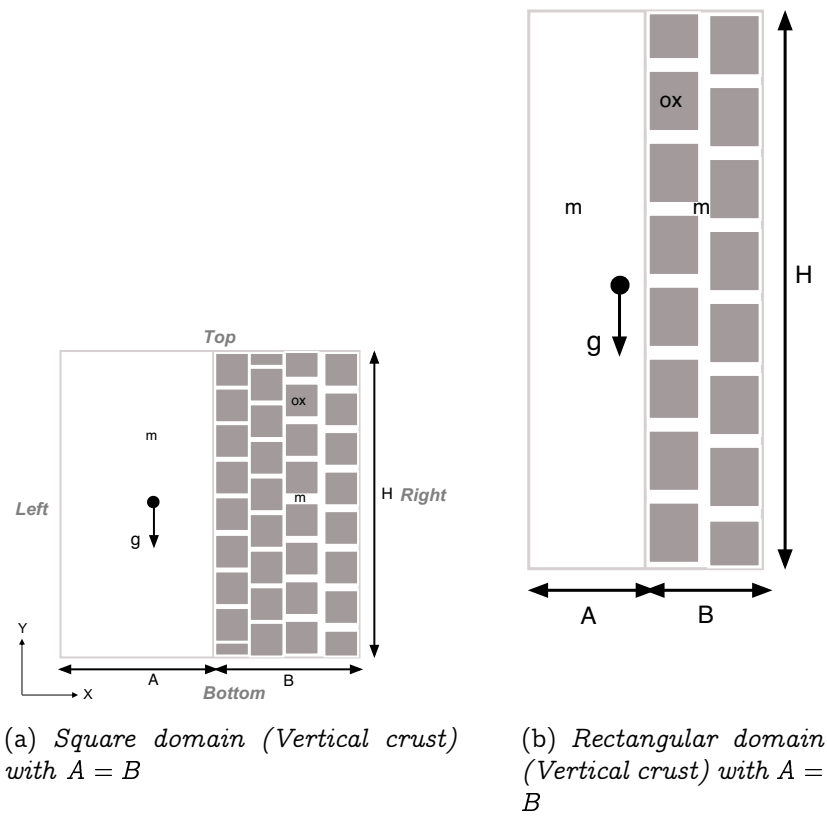


Figure 8.1: Computational domains for $N^{Fe} = 2.0$

Computational domain corresponding to $N^{Fe} = 10.0$ have width of metal layer greater than the crust layer. The corresponding geometry looks like Fig. 8.2 (a), where, A and B are the width of metal layer and crust, respectively.

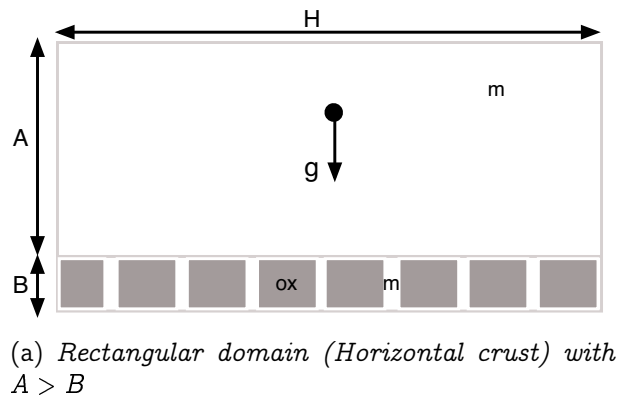


Figure 8.2: Computational domain for $N^{Fe} = 10.0$

8.2 Equilibrium Mole fractions

For the calculation of the equilibrium mole fractions of Fe atoms in metal phase (n_m^{Fe*}) and O atoms in oxide phase (n_{ox}^{O*}), similar to chapter 7, the global ratio of U/Zr atoms i.e C_{uz} and global degree of oxidation of Zr atoms i.e. C_{ox} are taken to be:

1. $C_{uz} = 1.0$.
2. $C_{ox} = 0.3$.

From the above values, it is easy to calculate the equilibrium values from the simplified model derived in chapter 4 for $N^{Fe} = 2.0$ and $N^{Fe} = 10.0$.

For $N^{Fe} = 2.0$, equilibrium values are calculated to be:

1. $n_{ox}^{O*} = 0.65$.
2. $n_m^{Fe*} = 0.8$.

Similarly, for $N^{Fe} = 10.0$, equilibrium values are calculated to be:

1. $n_{ox}^{O*} = 0.65$.
2. $n_m^{Fe*} = 0.94$.

8.3 Initial Mole Fractions for n_{ox}^O and n_m^{Fe}

Unlike chapter 7, the initial mole fractions here are taken to be the ones consistent with the reactor scenario, where initially no molten steel is present in the crust. Thus accordingly, the initial mole fractions of O atoms in oxide phase ($\langle n_{ox}^O \rangle^{ox}$) and Fe atoms in metal phase ($\langle n_m^{Fe} \rangle^m$) are as follows:

1. $\langle n_m^{Fe} \rangle^m = 1.0$ in pure liquid domain and $\langle n_m^{Fe} \rangle^m = 0$ in the crust region.
2. $\langle n_{ox}^O \rangle^{ox} = n_{ox}^{O*}$ in pure liquid domain and $\langle n_{ox}^O \rangle^{ox} = 0.6$ in the crust region. This value, $\langle n_{ox}^O \rangle^{ox} = 0.6$, corresponds to the reactor case where global degree of oxidation of Zr atoms is 30%, or $C_{ox} = 0.3$.

These values will be used throughout this chapter for the initialization of mole fraction fields.

8.4 Material Properties for Metal and Oxide

The complete list of thermo-physical data used in the calculations for molten steel or oxide is given in the Table 8.1.

Density (metal or oxide) [66]	$\rho_m = \rho_{ox} = \rho_0 = 7000 \text{ kgm}^{-3}$
Specific heat (metal or oxide) [66]	$C_{Pm} = C_{Pox} = C_{P0} = 720 \text{ Jkg}^{-1}\text{K}^{-1}$
Molecular diffusion (metal) [65]	$D_m^{Fe} = D_m = 1.0 \times 10^{-6} \text{ m}^2\text{s}^{-1}$
Molecular diffusion (oxide) [3, 62]	$D_{ox}^O = D_{ox} = 1.0 \times 10^{-9} \text{ m}^2\text{s}^{-1}$
Dynamic viscosity (metal) [66]	$\mu_m = 8.0 \times 10^{-3} \text{ kgm}^{-1}\text{s}^{-1}$
Thermal conductivity (metal) [39]	$\Lambda_m = 30.0 \text{ Wm}^{-1}\text{K}^{-1}$
Thermal conductivity (oxide) [13]	$\Lambda_{ox} = 3.54 \text{ Wm}^{-1}\text{K}^{-1}$
Thermal expansion coefficient (metal) [66]	$\beta_T = 1.0 \times 10^{-4} \text{ K}^{-1}$
Solutal expansion coefficient (metal) [66]	$\beta_S = 4.0 \times 10^{-3} -$
Gravity	$g = 9.81 \text{ m/s}^2$

Table 8.1: Physical data

8.5 Thermo-solutal Convection

The convection in the present chapter will be studied due to the combined effects of the thermal and solutal gradients. The thermal and solutal convection are generally quantified by the thermal and solutal Rayleigh numbers, Ra_T and Ra_S , respectively. At this point, it is important to mention that the role of Darcy number (Da) in both mode of convection is not taken into account, because here the metal flow will not be considered in the porous region, which is crust. Of course, metal flow will take place in the crust region once there is sufficient percolation due to the dissolution.

Thus, thermal and solutal Rayleigh numbers without Darcy number (Da) contribution, are given by the following relations:

$$Ra_T = \frac{\rho_0 g \beta_T \Delta T L^3}{\mu_m \alpha} \quad (8.1)$$

$$Ra_S = \frac{\rho_0 g \beta_S \Delta n L^3}{\mu_m D_m} \quad (8.2)$$

where: $\alpha = \frac{\Lambda_m}{\rho_0 C_{P0}}$ is the thermal diffusivity.

In the subsequent sections showing numerical results, the relative dominance of the mode of convection, thermal over solutal or vice-versa, will be checked by comparing the order of magnitudes of the two Rayleigh numbers, Ra_T and Ra_S . Also, in the context of convection, the square domain with vertical crust, shown in Fig. 8.1 (a) is studied both with and without

thermo-solutal convection. Further, closer reactor cases represented by the rectangular domains with vertical and horizontal crusts, shown in Fig. 8.1 (b) and 8.2 (a), respectively, are studied only with thermo-solutal convection.

8.6 Cases

8.6.1 Case 1: Square Domain with Vertical Crust: No Convection ($v_m = 0$)

The first case shown here is the illustration of dissolution in the case of a vertical crust having a square geometry with equal width of metal layer and crust, as shown in Fig. 8.3. From the discussion in section (8.1), this case corresponds to $N^{Fe} = 2.0$. Thus, from section (8.2), for $N^{Fe} = 2.0$, the calculated equilibrium mole fractions of O in oxide and Fe in metal phase are: $n_{ox}^{O*} = 0.65$ and $n_m^{Fe*} = 0.8$. The dimensions of Fig. 8.3 are: $H = 6\text{ cm}$ and $A = B = 3\text{ cm}$. Here, the porosity field ε_m is initialized randomly in the range $10\% \pm 5\%$, in order to represent the non-uniform distribution of interstitial spaces between the solid-oxide grains. The boundary conditions in Fig. 8.3 are: $Top = Bottom = Left = Right = No\ mass\ transfer$.

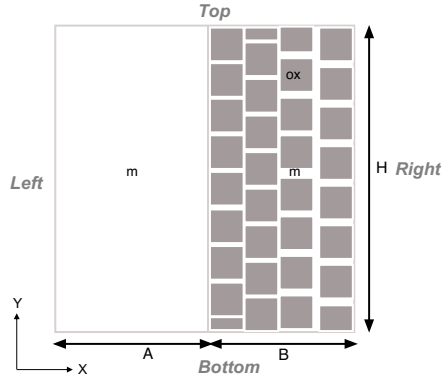
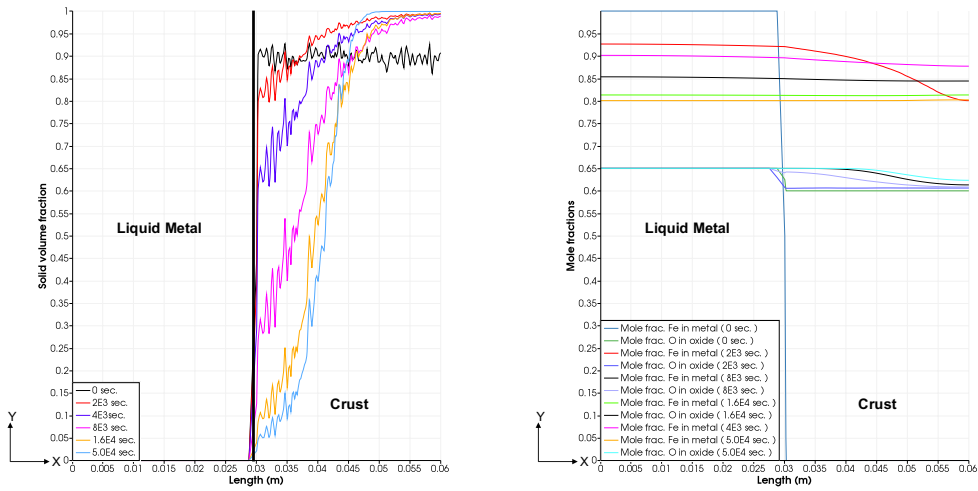


Figure 8.3: Computational domain for case: 1

8.6.1.1 Results

In this case it can be seen from Fig. 8.4 (a) that the dissolution is more prominent in the left region of the crust with initial porosity distribution getting amplified. On the contrary, the right region in the crust is experiencing the precipitation with the diminishing of initial porosity distribution. This precipitation is due to the increase in the mole fraction of O in oxide phase in the right region of the crust. This is evident from the Fig. 8.4 (b), where it can be seen that the mole fraction of O in oxide goes quickly to the equilibrium value in the dissolved region of the crust, but on the right region the mole fraction of O is evolving slowly towards equilibrium because of the mole fraction gradient. The 2D pictures of the crust at the initial and final time steps can be seen in

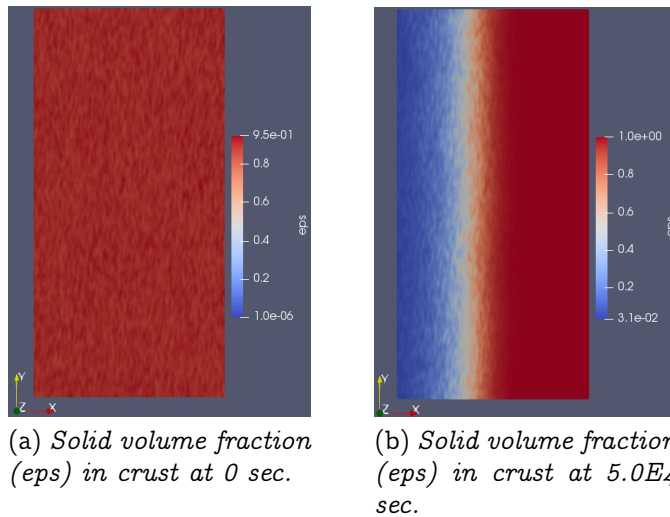
Fig. 8.5. In Fig. 8.5 (b) the dissolved left part of crust can be observed along with the precipitated right part.



(a) Dissolution profiles at the mid-section of the domain $y = 3$ cm

(b) Mole fraction profiles of Fe in metal and O in oxide at mid-section of the domain $y = 3$ cm

Figure 8.4: Results for dissolution and mole fractions profile evolution in the domain with time in case: 1



(a) Solid volume fraction (eps) in crust at 0 sec.

(b) Solid volume fraction (eps) in crust at 5.0E4 sec.

Figure 8.5: State of crust at the beginning and end of time steps in case 1

8.6.2 Case 2: Square Domain with Vertical Crust: Thermo-Solutal Convection

In this case, the physical problem explained in *case: 1* is studied with thermo-solutal convection. The computational domain for this case is shown in Fig. 8.6. Fig. 8.6 has the same dimensions as *case: 1* with *Left* boundary maintained at temperature of $T = 1400^\circ\text{C}$, *Right* boundary at $T = 2500^\circ\text{C}$, *Top* and *Bottom* are taken to be adiabatic boundaries. For species: $Top = Bottom = Left = Right = No\ mass\ transfer$, and for velocity: $Top = Bottom = Left = Right = No\ slip$. The ΔT and Δn in the definition of thermal and solutal Rayleigh numbers are: $\Delta T = 1100^\circ\text{C}$ and $\Delta n = 1$, respectively. This gives the Ra_T of the order of 10^7 and Ra_S of the order of 10^6 . Thus, for this case, the thermal convection will be dominant over solutal convection.

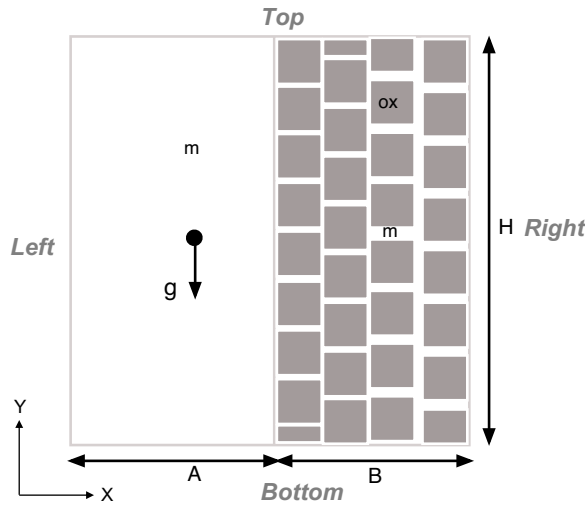


Figure 8.6: Computational domain for *case: 2*

8.6.2.1 Results

Fig. 8.7 (a) shows the flow pattern generated by thermo-solutal convection at time $t = 400\ sec.$. The flow sets in motion in an anti-clockwise direction with the peak velocity of $3.2\ cm/sec.$. Due to the low porosity in the crust, there is a negligible flow in that region. The anti-clockwise flow direction results in the erosion of the crust surface from bottom to top with velocity at the bottom inflection point in the range $1.5\ to\ 2.5\ cm/sec.$, which subsequently results in more dissolution near the bottom left part of the crust. This can be observed in Fig. 8.8 (b). Also, looking at the solid volume fraction values near the bottom left part of Fig. 8.8 (b) at $4000\ sec.$, the approximate values are in the range $0 < \epsilon_{ox}(eps) < 0.75$. Interestingly, at this instance of time there can be seen flow penetration in the crust, as shown in Fig. 8.7 (b).

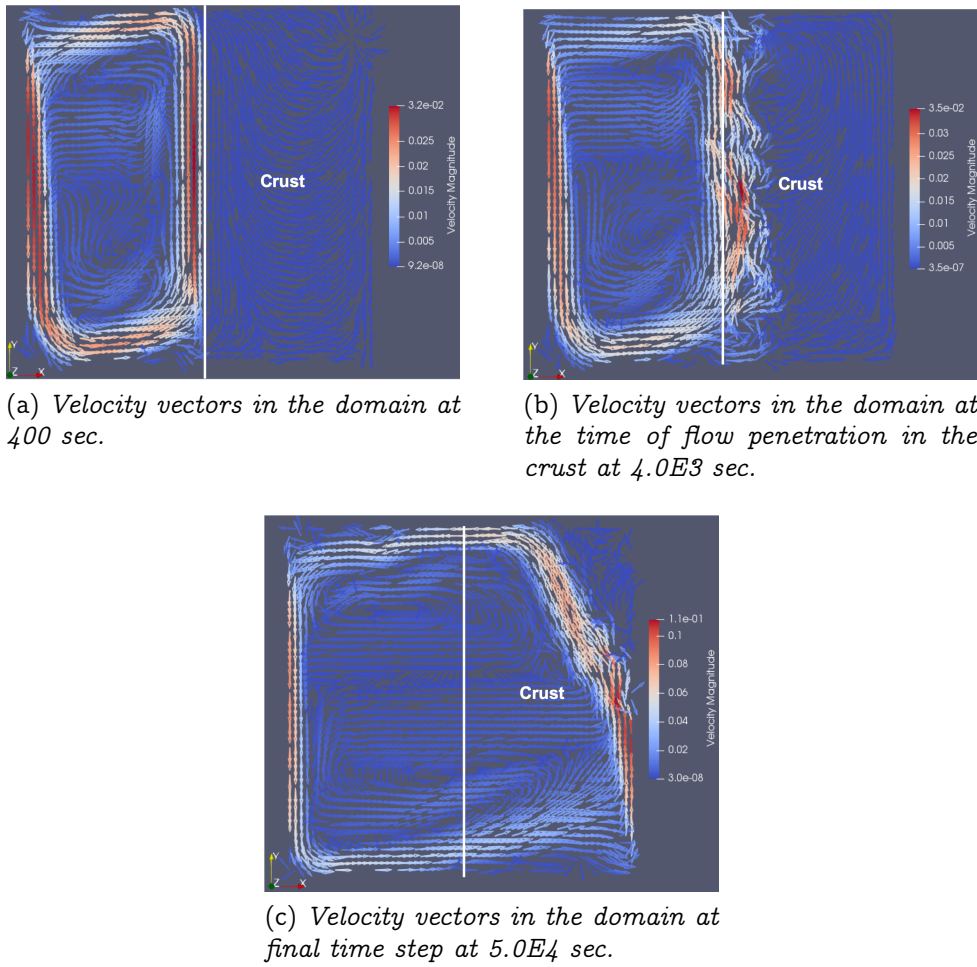


Figure 8.7: Evolution of the velocity in the domain in *case 2*

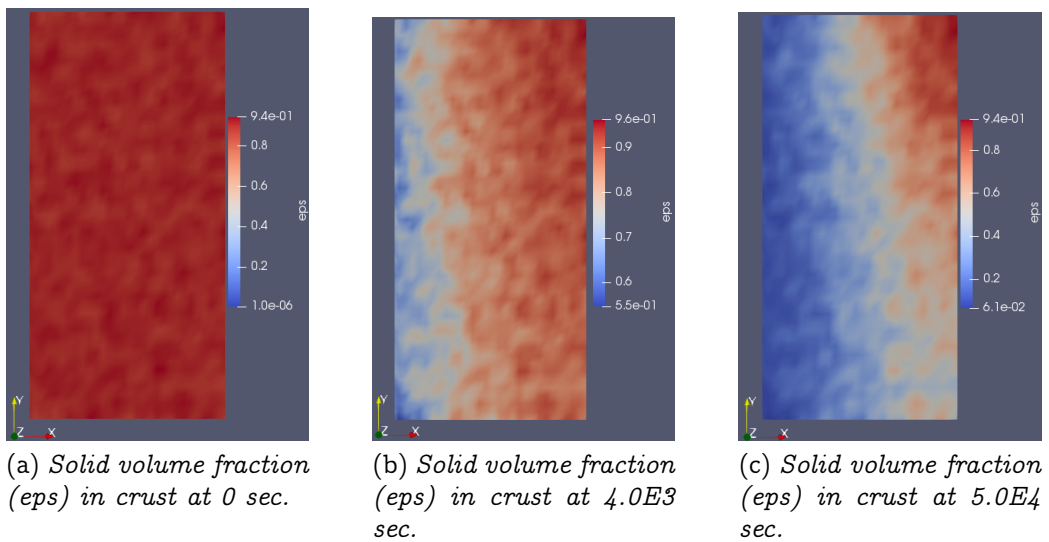


Figure 8.8: State of crust at three different time steps in *case: 2*

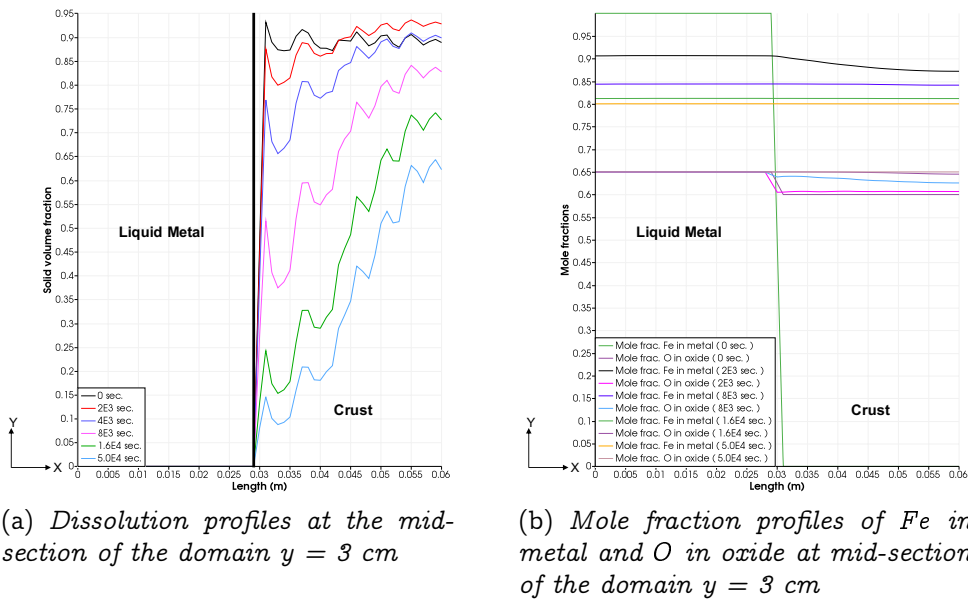


Figure 8.9: Results for dissolution and mole fractions profile evolution in the domain with time in *case: 2*

Further, the effect of the convection on the dissolution can be seen in Fig. 8.9 (a), where the dissolution takes place in the whole crust, with more dissolution in the left that the right part. This is different from the results of the *case: 1*, where precipitation was observed in the right part of the crust (see Fig. 8.4 (a)) in the absence of any convection in the liquid-metal. The corresponding mole fraction profiles in the whole domain can be seen in Fig. 8.9 (b). In 8.9 (b) the behaviour of mole fraction of Fe in metal is more or less same as *case: 1* but the difference is more evident in the evolution of the O mole fraction in the oxide, which unlike *case: 1*, goes to the equilibrium more uniformly, following the progress of dissolution. Thus, there is less effect of diffusion of O atoms. Finally, at the end of the time step, at $50,000$ sec., it can be observed from Fig. 8.8 (c) that almost complete crust (except some part in the top right corner) becomes permeable and hence, the molten metal flow loop covers almost the whole domain, as shown in Fig. 8.7 (c).

8.6.3 Case 3: Rectangular Geometry with Vertical Crust: Thermo-Solutal Convection

This case corresponds to the computational domain shown in Fig. 8.10. Again, from the discussion in section (8.1), this case corresponds to $N^{Fe} = 2.0$. Hence, from section (8.2), for $N^{Fe} = 2.0$, the calculated equilibrium mole fractions are: $n_{ox}^{O*} = 0.65$ and $n_m^{Fe*} = 0.8$. The dimensions of Fig. 8.10 are: $H = 10\text{ cm}$ and $A = B = 3\text{ mm}$. The B.Cs. are identical to *case: 2*. In this case as well $Ra_T > Ra_S$, with Ra_T in the order of 10^8 and Ra_S having the order of 10^7 .

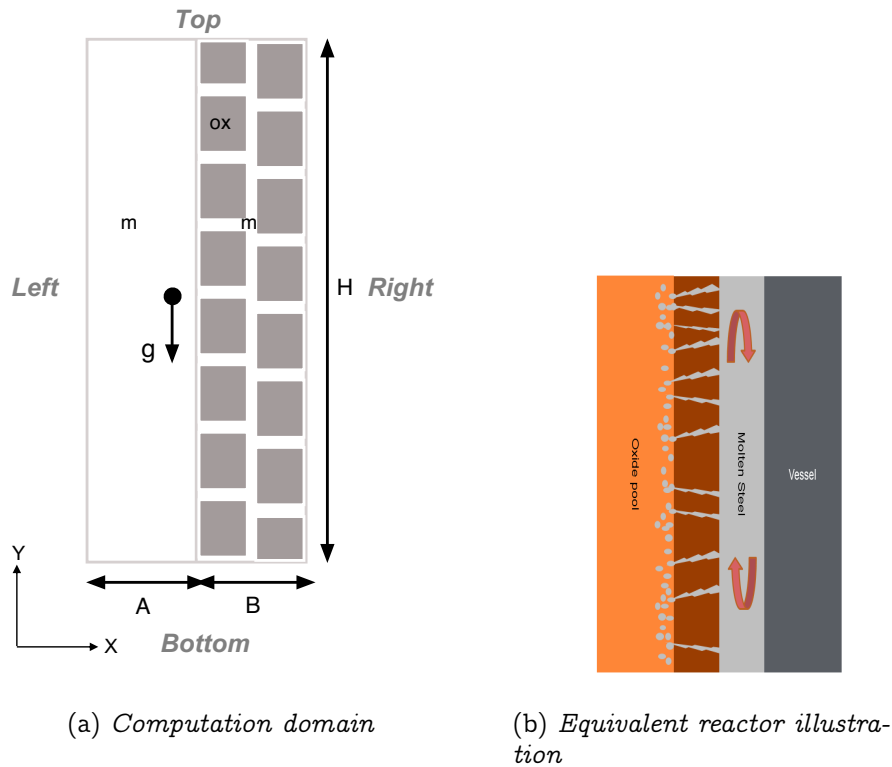


Figure 8.10: Physical domains for *case: 3*

8.6.3.1 Results

Looking at the flow patterns at time $t = 400\text{ sec.}$ shown in Fig. 8.11 (a), it can be observed that here as well the flow sets in an anti-clockwise direction with peak velocity 3.9 cm/sec. . Even though in this case as well the flow hits the crust from top to bottom but the more dissolution is not observed near the bottom left part of the crust (dissolution is uniform in Fig. 8.13) unlike *case: 2*. This is due to the very small velocity at the bottom inflection point, which is approximately 5 mm/sec. . However, the convection has an impact on the dissolution in the whole crust, where a uniform dissolution profile is observed. This is evident from Fig. 8.14 (a). It is interesting to note that even though in *case: 2* the dissolution was observed in the whole crust but it was not uniform like the present case. This is may be due to the thin crust in the present case

($B = 3 \text{ mm}$) as opposed to *case: 2*, where crust thickness was $B = 3 \text{ cm}$. Due to the thin crust, diffusion is fast enough to make mole fractions of Fe in metal phase and O in oxide phase uniform in the whole crust. Consequently, both Fe mole fraction in metal and O in oxide phase evolve very uniformly towards their equilibrium values as seen in Fig. 8.14 (b), making dissolution uniform in the whole crust.

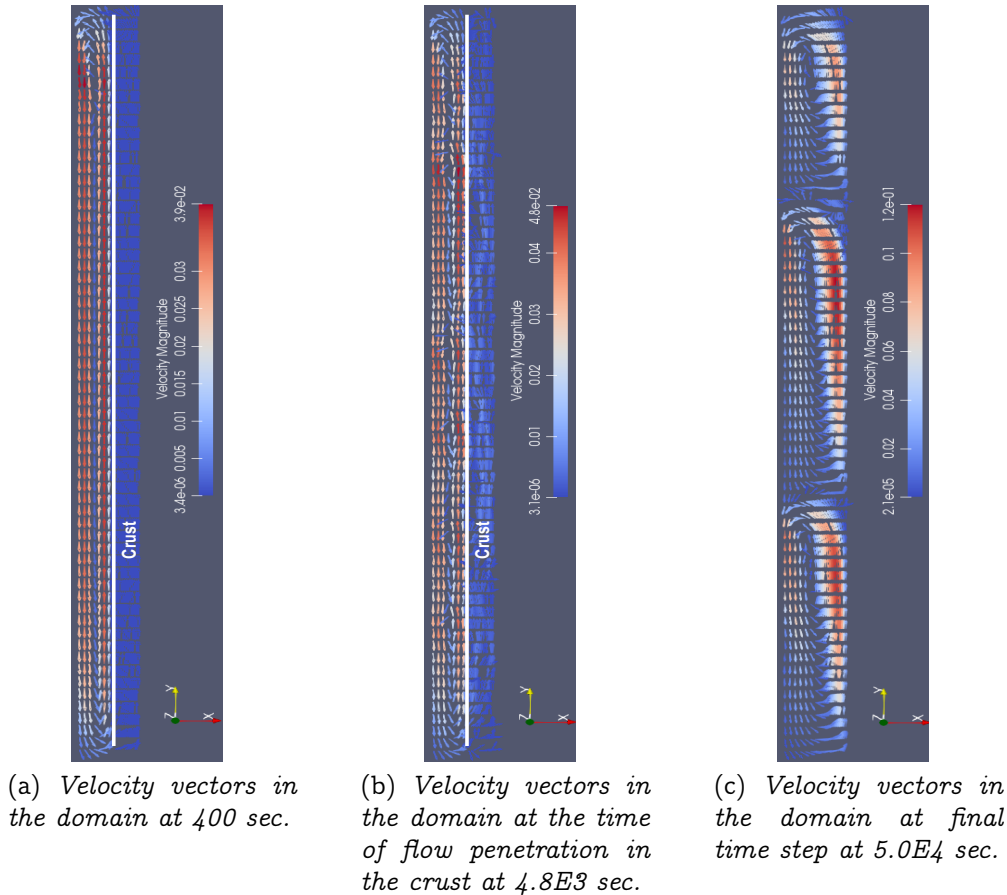


Figure 8.11: Evolution of the velocity in the domain in *case: 3*

The flow penetration in the crust is shown at 4000 *sec.* in Fig. 8.11 (b). Also, it is interesting to see from Fig. 8.11 (c) that the initial single flow loop breaks into three smaller flow loops. This is because when metal flow enters the whole crust region, it directly comes in contact with the right hot boundary. Thus, as soon as the metal reaches the right boundary temperature (i.e. 2500°C), it reaches its maximum value and turns downwards and gets cooled.

Further, from Fig. 8.14 (a) it can also be observed that due to the uniform dissolution in the present case there is an amplification of the initial porosity field distribution, which consequently leads to the creation of liquid metal *channels* in the crust. This can be observed from Fig. 8.13, where no *channels* are observed in 8.13 (a) and the deepest *channels* are observed at the end time step in 8.13 (c).

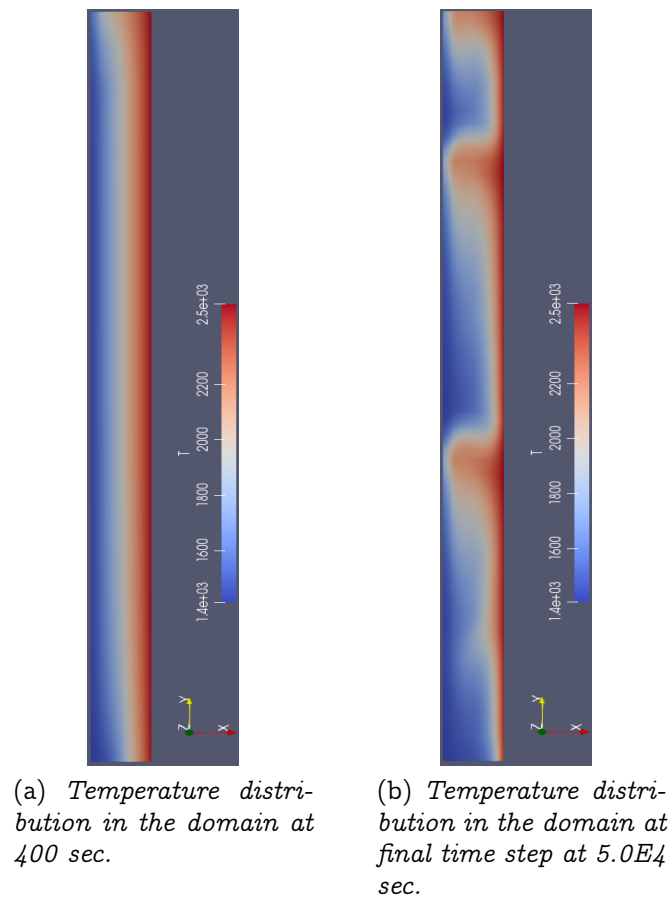


Figure 8.12: Evolution of the temperature profile in the domain in *case: 3*

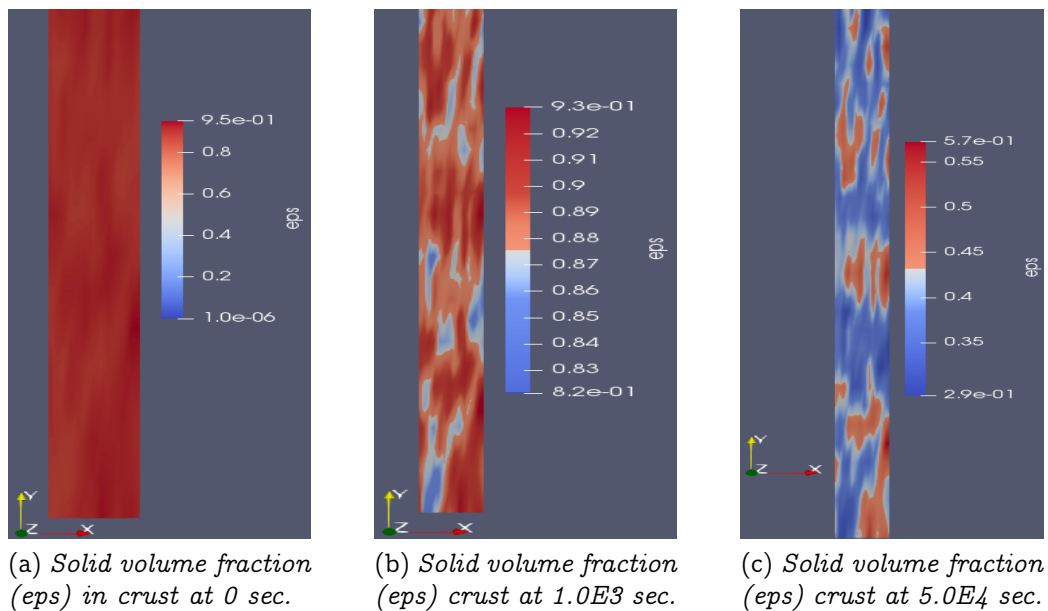


Figure 8.13: Evolution of liquid metal *channels* in the crust in *case: 3*

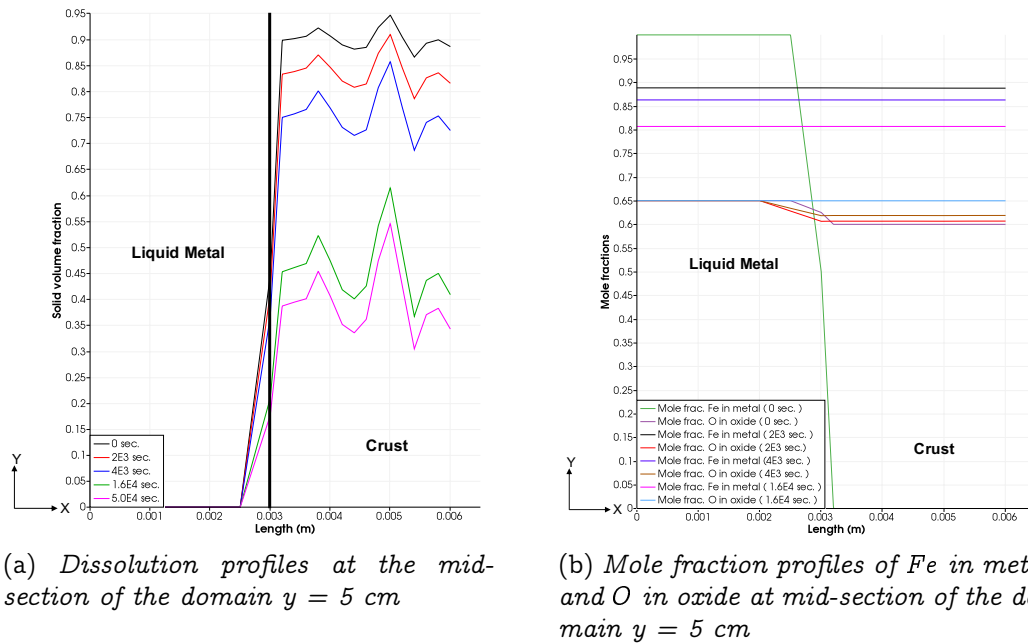


Figure 8.14: Results for dissolution and mole fractions profile evolution in the domain with time in case: 3

8.6.4 Case 4: Rayleigh-Bénard Convection

The last case is presented with *Rayleigh-Bénard Convection*. For this case, the computational domain is presented in Fig. 8.15. From the discussion in section (8.1), this case corresponds to $N^{Fe} = 10.0$ and thus, from section (8.2), the calculated equilibrium mole fractions are: $n_{ox}^{O*} = 0.65$ and $n_m^{Fe*} = 0.94$. The dimensions are: $H = 10$ cm, $A = 1$ cm and $B = 2$ mm. In this case, *Top* and *Bottom* boundaries are kept at 1400°C and 2500°C , respectively. *Left* and *Right* boundaries are adiabatic. *No mass transfer* and *No slip* B.Cs. are taken on all the boundaries for species and velocity, respectively. Similar to the other cases, here as well, $Ra_T > Ra_S$, with Ra_T and Ra_S having order of magnitudes to be 10^6 and 10^5 , respectively.

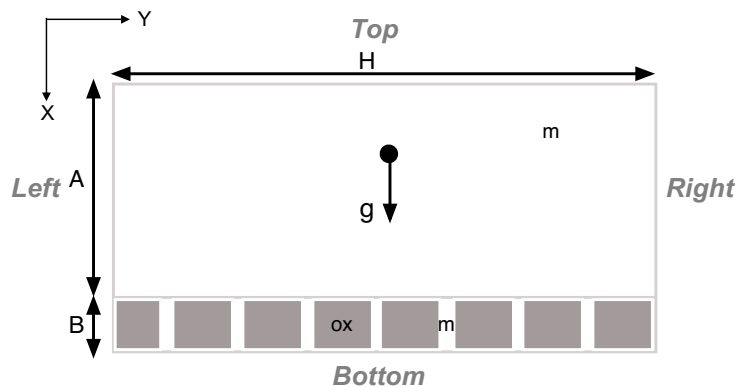
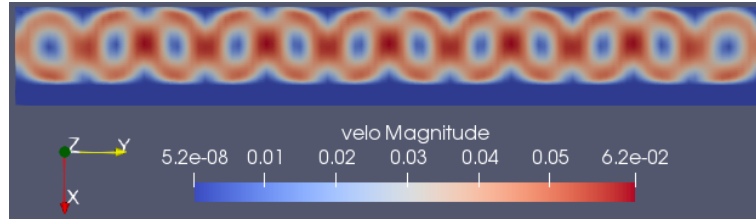
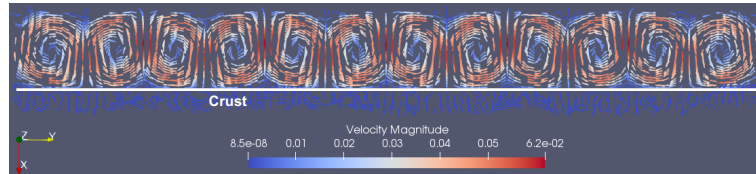


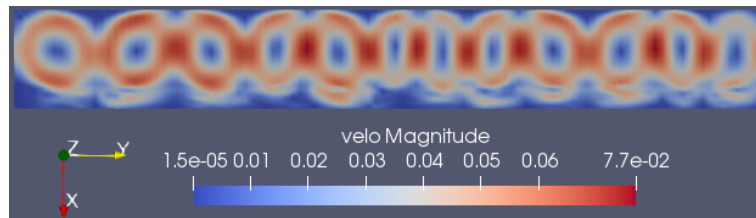
Figure 8.15: Computational domain for case: 4



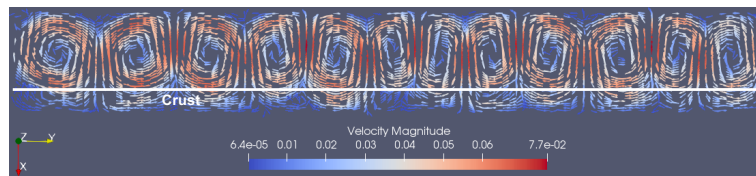
(a) Velocity profile in the domain at 400 sec.



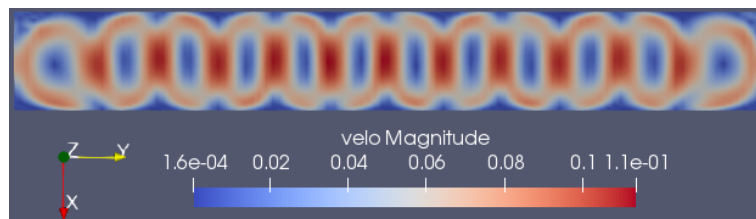
(b) Velocity vectors in the domain at 400 sec.



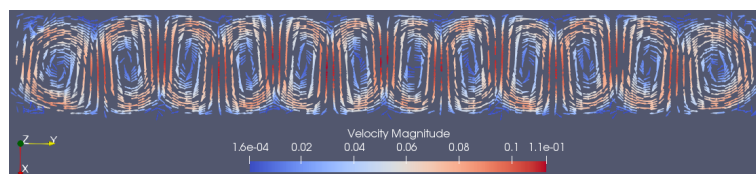
(c) Velocity profile in the domain at the time of flow penetration in the crust at $1.0E4$ sec.



(d) Velocity vectors in the domain at the time of flow penetration in the crust at $1.0E4$ sec.



(e) Velocity profile in the domain at final time step at $1.7E4$ sec.



(f) Velocity vectors in the domain at final time step at $1.7E4$ sec.

Figure 8.16: Evolution of the velocity in the domain in case: 4

Observing the Fig. 8.16 (a) it can be seen that there is a generation of *Bénard cells* in the top molten metal domain, with every odd cell having a clock-wise rotation and all even cells having a counter clock-wise rotation. The flow penetration in the crust is observed at 10,000 *sec.*, which is more than the time observed in *case: 2* and *case: 3*, which shows that the dissolution has a slower rate in the present case (see Fig. 8.19 (a)). This happens because the equilibrium value of *Fe* in metal is much higher than the *case: 2* and *case: 3*. This case having equilibrium value of $n_m^{Fe^*} = 0.94$ as opposed to other two cases, where equilibrium values were of $n_m^{Fe^*} = 0.8$. Thus, as evident from Fig. 8.19 (b), that the *Fe* in metal goes to equilibrium at 13,000 *sec.*, which is quicker compared to other two cases with convection. This leads to a slower dissolution. However, even though the metal reaches equilibrium early, there is still some dissolution because, *O* atoms in oxide reach to their equilibrium value of 0.65 later than *Fe* in metal, somewhere between 13,000 *sec.* and 16,000 *sec.* (see Fig. 8.19 (b)), which is almost equal to the time observed in *case: 2* and *case: 3*.

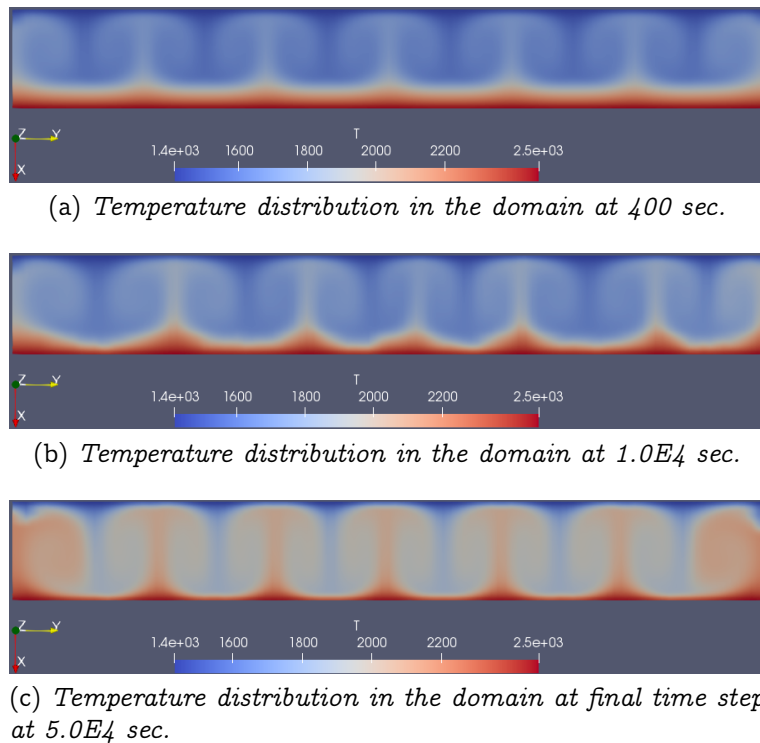


Figure 8.17: Evolution of the temperature profile in the domain in *case: 4*

Similar to the *case: 3*, here as well the dissolution profile in the crust is uniform with the amplification of the initial porosity field (see Fig. 8.19 (a)). This is again due to the fast diffusion in the thin crust in this case, making the mole fractions of *Fe* in metal and *O* in oxide to have uniform evolution towards their respective equilibrium values (see Fig. 8.19 (b)). This is also due to the more intense mixing in the metal layer due to natural convection. Also,

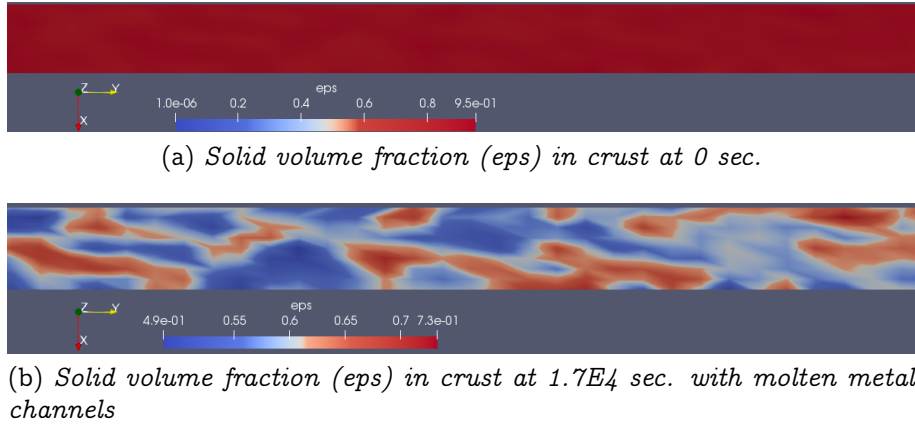


Figure 8.18: Evolution of liquid metal *channels* in the crust in *case: 4*

similar to *case: 3*, in Fig. 8.18 it can be seen that due to the amplification of the initial porosity field there is the formation of molten metal channels in the crust in this case as well.

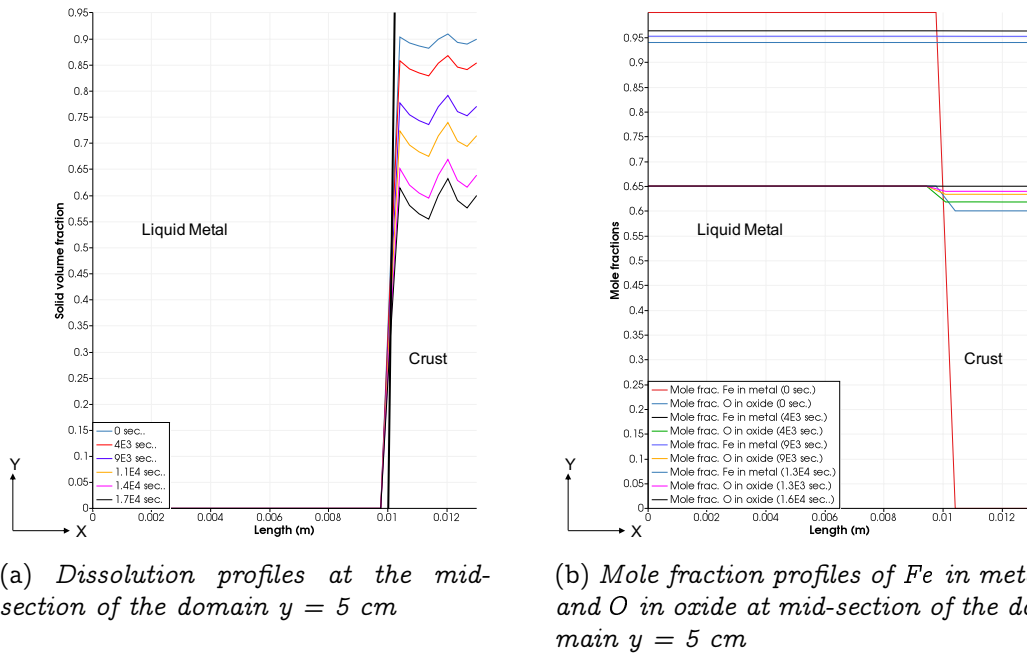


Figure 8.19: Results for dissolution and mole fractions profile evolution in the domain with time in *case: 4*

Chapter 9

Conclusions

Chapter 9

Conclusions

In this thesis, a macroscopic model was proposed for the dissolution of a (UO_2, ZrO_2, Zr) solid phase by liquid iron. This model includes a description of the distribution of liquid phase inside the solid as a quasi-periodic porous medium. The model was elaborated from the analysis of experimental observations and from a simplification of the quaternary diagram. This simplification was deduced from thermochemical equilibrium calculations.

Observations made in CORDEB and VITI-CORMET experiments have shown that dissolution of the crust is associated to the formation and growth of liquid metal channels inside the crust. Several experimental evidences tend to indicate that the dissolution process is driven by molecular diffusion of Fe and O atoms in the liquid and solid phases, respectively.

On the basis of those observations, a two-phase model was built, paying a particular attention to the description of species diffusion at two different scales. At the small (microscopic) scale, which was assumed to be the scale of ceramic (oxide) grains, the diffusion of species governs the displacement of the solid/liquid interface, and therefore, the local dissolution of grains (or their precipitation in some cases). At the scale of the crust (macroscopic), the effective diffusion of species controls the global time of dissolution and formation of metallic channels, leading to the possibility of percolation of liquid metal through the crust. When the model was written for the four species U, Zr, Fe, O , it was not possible to write explicitly the diffusion fluxes (they were linked).

In addition, several binary diffusion coefficients appear, but several of them were not known, for the species considered in this thesis. This issue had to be addressed owing to a simplification of the quaternary system. Boundary conditions also play an important role, in particular the conditions on the side of the crust which is not in contact with steel. If there is no way for O atoms to go out of the crust, this will limit the dissolution. Similarly, if there is not enough convection in the liquid metal to avoid saturation of the metal near the crust, dissolution may be limited. This implies that taking into account

the convective in the metal is also necessary, as it determines the boundary condition on one side of the crust.

To reduce the complexity of multi-species diffusion, a thermochemical study of the quaternary system U, Zr, Fe, O was made, estimating the fraction of phases and their respective compositions. This study was made with IRSN database NUCLEA and the solver *NUCLEA - Toolbox*. It was first observed that the results did not depend much on temperature, at least at high temperature, around the miscibility gap temperature. It was also observed that Fe was absent of the oxide phase and that the solubility of O in the metal phase was limited, and even negligible in many cases. Another important conclusion was that the atomic ratio U/Zr was approximately identical in both phases. This lead to a drastic simplification of the quaternary system. It may be viewed as two ternary systems, one in each phase.

Additionally, the uniform U/Zr ratio allows to consider that U and Zr atoms are always associated in the same proportion: therefore it is only necessary to know the mole fraction of one of those atoms and the other one can be directly deduced. Based on those conclusions, a simplified system was proposed, made of two "quasi-binary" systems: $(U, Zr) + Fe$ in the metal phase and $(U, Zr) + O$ in the oxide phase. For this simplified system, the diffusion transport depends on two main binary diffusion coefficients: the diffusivity of O in U, Zr (for the solid phase) and the diffusivity of Fe in U, Zr (for the liquid phase).

After reduction of the quaternary system, the macroscopic model becomes easier to solve numerically. In the first test cases, convective motion in the liquid phase were neglected. It was shown that the model could represent two different kinds of dissolution behaviour. If the characteristic time of effective diffusion is much lower than the characteristic time of dissolution at the microscopic scale, then it is possible to simulate the formation of metal macro-channels, as observed in experiments. If that condition is not verified, then the dissolution front is planar and there is not formation of metal channels within the solid phase. The consequence of the formation of channels is that, after some time of interaction, percolation of the metal through the crust is possible. Tests including the possible motion of the liquid have shown that when percolation occurs, the dissolution rate is increased around the percolating channels and the metallic phase can easily flow through the crust. This may explain some of the experimental results obtained in CORDEB experiments.

In order to be more accurate on the metal composition at the crust/liquid interface, the simulation of natural convection in the liquid phase was simulated. It was estimated that thermal convection is likely to be dominant over solutal convection. If the crust is vertical, large convection cells develop along the crust and this leads to a rather uniform dissolution front. If the crust is hor-

horizontal, Rayleigh-Bénard cells are formed and produce non-uniform patterns of dissolution along the crust. Finally, the sensitivity study to the boundary condition on the side opposite to the metal has brought interesting conclusions. If the boundary condition simulates the contact with a stoichiometric oxide, there is no mass flux of O through that boundary and it stabilizes the crust in the vicinity of that boundary: dissolution cannot be complete. If the boundary condition simulates the contact with a metal at equilibrium, there is again no mass flux of O through that boundary and the crust is stabilized and cannot be completely dissolved. On the contrary, if the boundary condition simulates the contact with a sub-stoichiometric oxide (i.e. O concentration is below its equilibrium value), there is a mass flux of O through that boundary and the dissolution front can progress up to that boundary (see Appendix (F)).

Therefore, even with a simplified model, we can conclude that the dissolution patterns can vary significantly and depend on several parameters: the evaluation of effective diffusivity, the boundary condition on the side opposite to the metal and the flow patterns generated by thermal convection in the metal layer.

Some theoretical difficulties of the modelling remain, in spite of the apparent relevance of the results produced by the developed model. The first theoretical difficulty is related to the concept of effective diffusivity at the macroscopic scale. In many models of the literature, the effective diffusivity is estimated as a combination of diffusivities in the liquid and solid phases. But, in our case, two different species are concerned for the two phases. In the solid, the diffusivity of O with respect to U, Zr is involved. In the liquid phase, the diffusivity of Fe with respect to U, Zr is involved. Therefore, it is justified to consider that effective diffusivity in each phase does not depend on the molecular diffusivity in the other phase. Only geometrical aspects should be taken into account in the closure of those terms. This is particularly true for Fe which is never present in the oxide phase. For O , a limited solubility in the metal exists and, therefore, the model could be improved by considering the diffusivity of O in the metal. But this would require to add an equation for the transport of O in the liquid metal phase. This option was not investigated in this thesis.

The second theoretical issue is related to the topology and geometry of the two-phase region. The channels seem to have a more or less periodic structure, at least when the solid volume fraction is larger than the liquid one. But the size and shape of the channels does not seem to be only related to the grain size. Other scales seem to appear. One interesting point of the developed model is that, with a particular choice of effective diffusivities, it is able to predict the formation of liquid channels, starting at the grain scale and evolving to other scales. But it must be kept in mind that the evolution of porosity predicted by the model is also necessarily scaled with the size of meshes because the model is not able to describe channels with a size smaller

than the mesh size. So, there is at least an implicit condition to be verified: the scale of the channels must be larger than the mesh size which must be larger than the grain size. This condition allows describing the formation of macro-channels. Due to the limited time of this work, it was not possible to study possible instability mechanisms generating those macro channels. But, clearly, they result from the coupling of the evolution of the local geometry and the dependence of effective diffusivities and local dissolution rate on that geometry.

There are several possible perspectives after this work. One of them would be to make a more detailed and systematic analysis of the model chosen for the effective diffusivities in each phase. It should include the dependence of binary diffusion coefficients with temperature, which was not taken into account in this work. Another important perspective would be to consider the solubility of O in the metal phase. This would allow some transport of O through the metal phase with a possible precipitation of oxides in regions that are not in direct contact with the crust itself.

Annexes

Appendix A

Discretization of Diffusion Form of Macroscopic Model

A.1 System of PDEs

The system of PDEs identified in section (5.2) is:

$$\frac{\partial}{\partial t}(\rho_{ox}\varepsilon_{ox}\langle n_{ox}^Y \rangle^{ox}) - n_{ox}^{Y*} \frac{\partial}{\partial t}(\rho_{ox}\varepsilon_{ox}) = \nabla \cdot (\rho_{ox}\varepsilon_{ox}D_{ox}^O \nabla \langle n_{ox}^Y \rangle^{ox}) + \rho_{ox}h_{ox}(n_{ox}^{Y*} - \langle n_{ox}^Y \rangle^{ox}) \quad (\text{A.1})$$

$$\frac{\partial}{\partial t}(\rho_m\varepsilon_m\langle n_m^Y \rangle^m) + n_m^{Y*} \frac{\partial}{\partial t}(\rho_{ox}\varepsilon_{ox}) = \nabla \cdot (\rho_m\varepsilon_mD_m^{Fe} \nabla \langle n_m^Y \rangle^m) + \rho_m h_m(n_m^{Y*} - \langle n_m^Y \rangle^m) \quad (\text{A.2})$$

$$\frac{\partial}{\partial t}(\rho_{ox}\varepsilon_{ox}) = \frac{1}{(n_m^{Y*} - n_{ox}^{Y*})} \left[\rho_m h_m(n_m^{Y*} - \langle n_m^Y \rangle^m) + \rho_{ox} h_{ox}(n_{ox}^{Y*} - \langle n_{ox}^Y \rangle^{ox}) \right] \quad (\text{A.3})$$

Assuming: $\rho_{ox}\varepsilon_{ox} = \widetilde{\rho_{ox}}$, where $\widetilde{\rho_{ox}}$ is termed as apparent density of oxide (solid) phase. Similarly apparent density of metal (liquid) phase is assumed to be: $\widetilde{\rho_m} = \rho_m\varepsilon_m$. Rewriting the Eqs. (A.1, A.2, A.3) with the assumptions:

$$\frac{\partial}{\partial t}(\widetilde{\rho_{ox}}\langle n_{ox}^Y \rangle^{ox}) - n_{ox}^{Y*} \frac{\partial}{\partial t}(\widetilde{\rho_{ox}}) = \nabla \cdot (\widetilde{\rho_{ox}}D_{ox}^O \nabla \langle n_{ox}^Y \rangle^{ox}) + \rho_{ox}h_{ox}(n_{ox}^{Y*} - \langle n_{ox}^Y \rangle^{ox}) \quad (\text{A.4})$$

$$\frac{\partial}{\partial t}(\widetilde{\rho_m}\langle n_m^Y \rangle^m) + n_m^{Y*} \frac{\partial}{\partial t}(\widetilde{\rho_{ox}}) = \nabla \cdot (\widetilde{\rho_m}D_m^{Fe} \nabla \langle n_m^Y \rangle^m) + \rho_m h_m(n_m^{Y*} - \langle n_m^Y \rangle^m) \quad (\text{A.5})$$

$$\frac{\partial}{\partial t}(\widetilde{\rho_{ox}}) = \frac{1}{(n_m^{Y*} - n_{ox}^{Y*})} \left[\rho_m h_m(n_m^{Y*} - \langle n_m^Y \rangle^m) + \rho_{ox} h_{ox}(n_{ox}^{Y*} - \langle n_{ox}^Y \rangle^{ox}) \right] \quad (\text{A.6})$$

Further making the following transformations for simplicity of notations:

1. $\langle n_{ox}^Y \rangle^{ox} = n^s$.
2. $n_{ox}^{Y*} = n^{seq}$.
3. $\widetilde{\rho_{ox}} = \widetilde{\rho^s}$.
4. $D_{ox}^O = D^s$.
5. $h_{ox} = h^s$.
6. $\langle n_m^Y \rangle^m = n^l$.
7. $n_m^{Y*} = n^{leq}$.
8. $\widetilde{\rho_m} = \widetilde{\rho^l}$.
9. $D_m^{Fe} = D^l$.
10. $h_m = h^l$.

With above transformations of notations, the system of PDEs looks like:

$$\frac{\partial}{\partial t}(\widetilde{\rho^s} n^s) - n^{seq} \frac{\partial}{\partial t}(\widetilde{\rho^s}) = \nabla \cdot (\widetilde{\rho^s} D^s \nabla n^s) + \rho^s h^s (n^{seq} - n^s) \quad (A.7)$$

$$\frac{\partial}{\partial t}(\widetilde{\rho^l} n^l) + n^{leq} \frac{\partial}{\partial t}(\widetilde{\rho^s}) = \nabla \cdot (\widetilde{\rho^l} D^l \nabla n^l) + \rho^l h^l (n^{leq} - n^l) \quad (A.8)$$

$$\frac{\partial}{\partial t}(\widetilde{\rho^s}) = \frac{1}{(n^{leq} - n^{seq})} \left[\rho^l h^l (n^{leq} - n^l) + \rho^s h^s (n^{seq} - n^s) \right] \quad (A.9)$$

Assuming: $Y^s = \widetilde{\rho^s} n^s$ and $Y^l = \widetilde{\rho^l} n^l$, the final set of PDEs transforms to Eqs. (A.10, A.11, A.12):

$$\frac{\partial}{\partial t}(Y^s) - n^{seq} \frac{\partial}{\partial t}(\widetilde{\rho^s}) = \nabla \cdot (D^s \nabla Y^s) - \nabla \cdot (D^s n^s \nabla \widetilde{\rho^s}) + \rho^s h^s (n^{seq} - n^s) \quad (A.10)$$

$$\frac{\partial}{\partial t}(Y^l) + n^{leq} \frac{\partial}{\partial t}(\widetilde{\rho^s}) = \nabla \cdot (D^l \nabla Y^l) + \nabla \cdot (D^l n^l \nabla \widetilde{\rho^s}) + \rho^l h^l (n^{leq} - n^l) \quad (A.11)$$

$$\frac{\partial}{\partial t}(\widetilde{\rho^s}) = \frac{1}{(n^{leq} - n^{seq})} \left[\rho^l h^l (n^{leq} - n^l) + \rho^s h^s (n^{seq} - n^s) \right] \quad (A.12)$$

Figure A.1: Final system of PDEs

A.2 Discretization Methodology

To discretize the system of PDEs summarized in Fig. A.1, standard Finite Volume method has been used. The system of PDEs has been discretized over a 2D Cartesian grid shown in Fig. A.2. The time discretization scheme is semi-implicit as evident from the equations below:

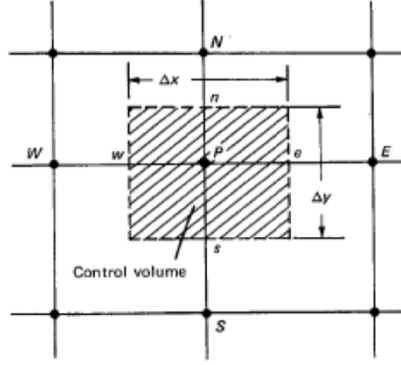


Figure A.2: A typical Finite Volume (FV) 2D cell

$$\frac{Y^s - Y^{s0}}{\Delta t} - n^{s^{eq}} \frac{\tilde{\rho}^s - \tilde{\rho}^{s0}}{\Delta t} = \nabla \cdot (D^s \nabla Y^s) - \nabla \cdot (D^s n^s \nabla \tilde{\rho}^s) + \rho^s h^s (n^{s^{eq}} - n^{s0}) \quad (\text{A.13})$$

$$\frac{Y^l - Y^{l0}}{\Delta t} + n^{l^{eq}} \frac{\tilde{\rho}^s - \tilde{\rho}^{s0}}{\Delta t} = \nabla \cdot (D^l \nabla Y^l) + \nabla \cdot (D^l n^l \nabla \tilde{\rho}^s) + \rho^l h^l (n^{l^{eq}} - n^{l0}) \quad (\text{A.14})$$

$$\frac{\tilde{\rho}^s - \tilde{\rho}^{s0}}{\Delta t} = \frac{1}{(n^{l^{eq}} - n^{s^{eq}})} \left[\rho^l h^l (n^{l^{eq}} - n^{l0}) + \rho^s h^s (n^{s^{eq}} - n^{s0}) \right] \quad (\text{A.15})$$

Further, the mass transfer coefficients and diffusivities are related to the apparent liquid and solid densities by the following simple relations:

$$h^k = h^{k0} (\tilde{\rho}^{k0} / \rho^k) (1 - (\tilde{\rho}^k / \rho^k)); \quad k = (s, l) \quad (\text{A.16})$$

$$D^k = D^{k0} (\tilde{\rho}^{k0} / \rho^k); \quad k = (s, l) \quad (\text{A.17})$$

The h^{k0} are constants whose values are chosen to be 10^{-3} for $k = l$ and 10^{-6} for $k = s$. Similarly, the D^{k0} are constants whose values are chosen to be $10^{-6} \text{ m}^2/\text{sec.}$ for $k = l$ and $10^{-9} \text{ m}^2/\text{sec.}$ for $k = s$. The final set of coupled algebraic system of linear equations are given in the following section.

A.2.1 Discretized form (Semi-implicit and coupled) for an Internal Finite Volume cell

Oxide phase:

$$\begin{aligned}
 a_P^{Y^s} Y_P^s + a_P^{\tilde{\rho}^s} \tilde{\rho}_P^s &= a_E^{Y^s} Y_E^s + a_W^{Y^s} Y_W^s + a_N^{Y^s} Y_N^s + a_S^{Y^s} Y_S^s + a_P^{Y^{s0}} Y_P^{s0} + a_E^{\tilde{\rho}^s} \tilde{\rho}_E^s + a_W^{\tilde{\rho}^s} \tilde{\rho}_W^s \\
 &\quad + a_N^{\tilde{\rho}^s} \tilde{\rho}_N^s + a_S^{\tilde{\rho}^s} \tilde{\rho}_S^s + a_P^{\tilde{\rho}^{s0}} \tilde{\rho}_P^{s0} + a_P^{n^{s0}} n_P^{s0} + S
 \end{aligned} \tag{A.18}$$

Coefficients are:

$$\begin{aligned}
 a_P^{Y^s} &= \left[\frac{\Delta x \Delta y}{\Delta t} + D^s \Delta y \left(\frac{1}{\Delta x_E} + \frac{1}{\Delta x_W} \right) + D^s \Delta x \left(\frac{1}{\Delta y_N} + \frac{1}{\Delta y_S} \right) \right] \\
 a_P^{\tilde{\rho}^s} &= \left[-n^{s^{eq}} \frac{\Delta x \Delta y}{\Delta t} - \frac{D^s n_P^{s0} \Delta y}{\Delta x_E} - \frac{D^s n_P^{s0} \Delta y}{\Delta x_W} - \frac{D^s n_P^{s0} \Delta x}{\Delta y_N} - \frac{D^s n_P^{s0} \Delta x}{\Delta y_S} \right] \\
 a_E^{Y^s} &= \left[\frac{D^s \Delta y}{\Delta x_E} \right] \\
 a_W^{Y^s} &= \left[\frac{D^s \Delta y}{\Delta x_W} \right] \\
 a_N^{Y^s} &= \left[\frac{D^s \Delta x}{\Delta y_N} \right] \\
 a_S^{Y^s} &= \left[\frac{D^s \Delta x}{\Delta y_S} \right] \\
 a_P^{Y^{s0}} &= \left[\frac{\Delta x \Delta y}{\Delta t} \right] \\
 a_E^{\tilde{\rho}^s} &= \left[\frac{-D^s n_P^{s0} \Delta y}{\Delta x_E} \right] \\
 a_W^{\tilde{\rho}^s} &= \left[\frac{-D^s n_P^{s0} \Delta y}{\Delta x_W} \right] \\
 a_N^{\tilde{\rho}^s} &= \left[\frac{-D^s n_P^{s0} \Delta x}{\Delta y_N} \right] \\
 a_S^{\tilde{\rho}^s} &= \left[\frac{-D^s n_P^{s0} \Delta x}{\Delta y_S} \right] \\
 a_P^{\tilde{\rho}^{s0}} &= \left[-n^{s^{eq}} \frac{\Delta x \Delta y}{\Delta t} \right] \\
 a_P^{n^{s0}} &= \left[-\rho^s h^s \Delta x \Delta y \right] \\
 S &= \left[\rho^s h^s n^{s^{eq}} \Delta x \Delta y \right]
 \end{aligned}$$

Metal phase:

$$\begin{aligned}
 a_P^{Y^l} Y_P^l + a_P^{\tilde{\rho}^s} \tilde{\rho}_P^s &= a_E^{Y^l} Y_E^l + a_W^{Y^l} Y_W^l + a_N^{Y^l} Y_N^l + a_S^{Y^l} Y_S^l + a_P^{Y^{l0}} Y_P^{l0} + a_E^{\tilde{\rho}^s} \tilde{\rho}_E^s + a_W^{\tilde{\rho}^s} \tilde{\rho}_W^s \\
 &\quad + a_N^{\tilde{\rho}^s} \tilde{\rho}_N^s + a_S^{\tilde{\rho}^s} \tilde{\rho}_S^s + a_P^{\tilde{\rho}^{s0}} \tilde{\rho}_P^{s0} + a_P^{n^{l0}} n_P^{l0} + S
 \end{aligned} \tag{A.19}$$

Coefficients are:

$$\begin{aligned}
 a_P^{Y^l} &= \left[\frac{\Delta x \Delta y}{\Delta t} + D^l \Delta y \left(\frac{1}{\Delta x_E} + \frac{1}{\Delta x_W} \right) + D^l \Delta x \left(\frac{1}{\Delta y_N} + \frac{1}{\Delta y_S} \right) \right] \\
 a_P^{\tilde{\rho}^s} &= \left[n^{leq} \frac{\Delta x \Delta y}{\Delta t} + \frac{D^s n_P^{s0} \Delta y}{\Delta x_E} + \frac{D^s n_P^{s0} \Delta y}{\Delta x_W} + \frac{D^s n_P^{s0} \Delta x}{\Delta y_N} + \frac{D^s n_P^{s0} \Delta x}{\Delta y_S} \right] \\
 a_E^{Y^l} &= \left[\frac{D^l \Delta y}{\Delta x_E} \right] \\
 a_W^{Y^l} &= \left[\frac{D^l \Delta y}{\Delta x_W} \right] \\
 a_N^{Y^l} &= \left[\frac{D^l \Delta x}{\Delta y_N} \right] \\
 a_S^{Y^l} &= \left[\frac{D^l \Delta x}{\Delta y_S} \right] \\
 a_P^{Y^{l0}} &= \left[\frac{\Delta x \Delta y}{\Delta t} \right] \\
 a_E^{\tilde{\rho}^s} &= \left[\frac{D^s n_P^{s0} \Delta y}{\Delta x_E} \right] \\
 a_W^{\tilde{\rho}^s} &= \left[\frac{D^s n_P^{s0} \Delta y}{\Delta x_W} \right] \\
 a_N^{\tilde{\rho}^s} &= \left[\frac{D^s n_P^{s0} \Delta x}{\Delta y_N} \right] \\
 a_S^{\tilde{\rho}^s} &= \left[\frac{D^s n_P^{s0} \Delta x}{\Delta y_S} \right] \\
 a_P^{\tilde{\rho}^{s0}} &= \left[n^{leq} \frac{\Delta x \Delta y}{\Delta t} \right] \\
 a_P^{n^{l0}} &= \left[-\rho^l h^l \Delta x \Delta y \right] \\
 S &= \left[\rho^l h^l n^{leq} \Delta x \Delta y \right]
 \end{aligned}$$

Rate of dissolution (\dot{m}) :

$$a_P^{\tilde{\rho}^s} \tilde{\rho}_P^s = a_P^{\tilde{\rho}^{s0}} \tilde{\rho}_P^{s0} + a_P^{n^{s0}} n_P^{s0} + a_P^{n^{l0}} n_P^{l0} + S \quad (\text{A.20})$$

Coefficients are:

$$\begin{aligned} a_P^{\tilde{\rho}^s} &= \left[\frac{\Delta x \Delta y}{\Delta t} \right] \\ a_P^{\tilde{\rho}^{s0}} &= \left[\frac{\Delta x \Delta y}{\Delta t} \right] \\ a_P^{n^{s0}} &= \left[-\rho^s h^s \frac{\Delta x \Delta y}{(n^{leq} - n^{seq})} \right] \\ a_P^{n^{l0}} &= \left[-\rho^l h^l \frac{\Delta x \Delta y}{(n^{leq} - n^{seq})} \right] \\ S &= \left[\frac{\rho^s h^s n^{seq} + \rho^l h^l n^{leq}}{(n^{leq} - n^{seq})} \Delta x \Delta y \right] \end{aligned}$$

A.3 Numerical Resolution

For numerical resolution of the coupled algebraic equations, a fully coupled solver has been programmed in Python using NumPy and SciPy libraries. Routines involving loops has been optimized with Python's Numba library. The global assembled matrix at each time step is sparse, positive definite and non-symmetric, thus, iterative scheme of Generalized Minimal Residual (GMRES) method has been adopted for the resolution of the system:

$$AX = B. \quad (\text{A.21})$$

Appendix B

Numerical Resolution of Coupled ODEs

The system of coupled ODEs identified in the section (5.1), is given as:

$$\frac{d(\rho_{ox}\varepsilon_{ox}\langle n_{ox}^Y \rangle^{ox})}{dt} - n_{ox}^{Y*}\dot{m} = \rho_{ox}h_{ox}(n_{ox}^{Y*} - \langle n_{ox}^Y \rangle^{ox}) \quad (\text{B.1})$$

$$\frac{d(\rho_m\varepsilon_m\langle n_m^Y \rangle^m)}{dt} + n_m^{Y*}\dot{m} = \rho_m h_m(n_m^{Y*} - \langle n_m^Y \rangle^m) \quad (\text{B.2})$$

$$\begin{aligned} \dot{m} &= \frac{d(\rho_{ox}\varepsilon_{ox})}{dt} \\ &= \frac{1}{(n_m^{Y*} - n_{ox}^{Y*})} \left[\rho_m h_m(n_m^{Y*} - \langle n_m^Y \rangle^m) + \rho_{ox}h_{ox}(n_{ox}^{Y*} - \langle n_{ox}^Y \rangle^{ox}) \right] \end{aligned} \quad (\text{B.3})$$

Assuming:

1. $\rho_{ox}\varepsilon_{ox} = \widetilde{\rho_{ox}}$
2. $\rho_m\varepsilon_m = \widetilde{\rho_m}$
3. $n_{ox}^{Y*} = n_{ox}^*$
4. $n_m^{Y*} = n_m^*$
5. $\langle n_{ox}^Y \rangle^{ox} = n_{ox}$
6. $\langle n_m^Y \rangle^m = n_m$

Thus, above system of ODEs can be further written as:

$$\frac{d(\widetilde{\rho}_{ox} n_{ox})}{dt} - n_{ox}^* \dot{m} = \rho_{ox} h_{ox} (n_{ox}^* - n_{ox}) \quad (\text{B.4})$$

$$\frac{d(\widetilde{\rho}_m n_m)}{dt} + n_m^* \dot{m} = \rho_m h_m (n_m^* - n_m) \quad (\text{B.5})$$

$$\begin{aligned} \dot{m} &= \frac{d(\widetilde{\rho}_{ox})}{dt} \\ &= \frac{1}{(n_m^* - n_{ox}^*)} \left[\rho_m h_m (n_m^* - n_m) + \rho_{ox} h_{ox} (n_{ox}^* - n_{ox}) \right] \end{aligned} \quad (\text{B.6})$$

Further, the mass transfer coefficients are related to the solid and liquid volume fractions by the following simple relations:

$$h_k = h_{k0} (\widetilde{\rho}_k / \rho_k) (1 - (\widetilde{\rho}_k / \rho_k)); \quad k = (ox, m) \quad (\text{B.7})$$

The h_{k0} are constants whose values are chosen to be 10^{-3} for $k = m$ and 10^{-6} for $k = ox$.

To numerically solve the Eqs. (B.4 - B.5), following algorithm has been used:

Knowing the values of $\widetilde{\rho}_{ox}^t$, $\widetilde{\rho}_m^t$, n_{ox}^t and n_m^t from previous time step (t):

Step 1: Calculate \dot{m} , $\widetilde{\rho}_{ox}^{t+1}$ and $\widetilde{\rho}_m^{t+1}$:

$$\dot{m} = \frac{1}{(n_m^* - n_{ox}^*)} \left[\rho_m h_m^t (n_m^* - n_m^t) + \rho_{ox} h_{ox}^t (n_{ox}^* - n_{ox}^t) \right]$$

$$\frac{\widetilde{\rho}_{ox}^{t+1} - \widetilde{\rho}_{ox}^t}{\Delta t} = \frac{1}{(n_m^* - n_{ox}^*)} \left[\rho_m h_m^t (n_m^* - n_m^t) + \rho_{ox} h_{ox}^t (n_{ox}^* - n_{ox}^t) \right]$$

$$\widetilde{\rho}_m^{t+1} = \rho_m (1 - \widetilde{\rho}_{ox}^{t+1} / \rho_{ox})$$

Step 2: Calculate n_{ox}^{t+1} :

$$\widetilde{\rho}_{ox}^t \frac{n_{ox}^{t+1} - n_{ox}^t}{\Delta t} = n_{ox}^* \dot{m} + \rho_{ox} h_{ox}^t (n_{ox}^* - n_{ox}^t)$$

Step 3: Calculate n_m^{t+1} :

$$\widetilde{\rho}_m^t \frac{n_m^{t+1} - n_m^t}{\Delta t} = -n_m^* \dot{m} + \rho_{ox} h_m^t (n_m^* - n_m^t)$$

Step 4:

$$\widetilde{\rho}_{ox}^t = \widetilde{\rho}_{ox}^{t+1}$$

$$\widetilde{\rho}_m^t = \widetilde{\rho}_m^{t+1}$$

$$n_{ox}^t = n_{ox}^{t+1}$$

$$n_m^t = n_m^{t+1}$$

Appendix C

Method of Volume Averaging

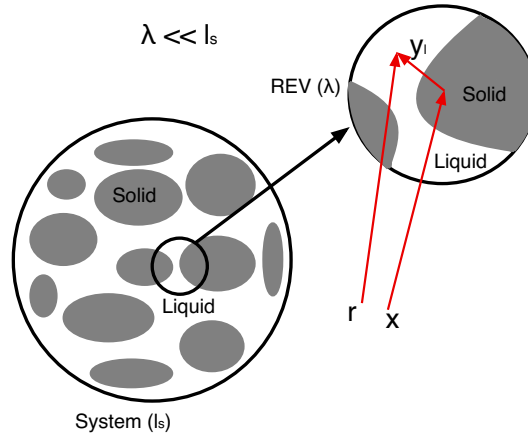


Figure C.1: Position vectors associated with Representative Elementary Volume (REV)

C.1 Volume Averaging

In the method of volume averaging, an averaging volume V is associated with every point in space, both in solid and liquid phase. This allows the association of an average value to every point in space. Most commonly this is called superficial average [124] and defined as:

$$\langle \Phi_l \rangle = \frac{1}{V} \int_{V_l} \Phi_l dV \quad (\text{C.1})$$

where: V_l represents the volume of the liquid (l) phase contained within the averaging volume V and Φ_l is some field defined at every point in the liquid domain.

Further, the average of the field Φ_l , represented by $\langle \Phi_l \rangle$, is assumed to

be associated to the centroid of the averaging volume (Fig. C.1). The centroid is located by the position vector \mathbf{x} , and points in the liquid (l) phase relative to the centroid are located by \mathbf{y}_l . Thus, it can be written that:

$$\langle \Phi_l \rangle_{\mathbf{x}} = \frac{1}{V} \int_{V_l(\mathbf{x})} \Phi_l(\mathbf{x} + \mathbf{y}_l) dV_{\mathbf{y}} \quad (\text{C.2})$$

From above it is clear that $\langle \Phi_l \rangle$ is associated with the centroid and that integration is carried out with respect to the components of the relative position vector, \mathbf{y}_l . In general, it is common to use the simpler notation indicated by the Eq. (C.1). In addition to the superficial averaging indicated by Eq. (C.1), another way of representation is the *intrinsic average* [124], which reads as:

$$\langle \Phi_l \rangle^l = \frac{1}{V_l} \int_{V_l} \Phi_l dV \quad (\text{C.3})$$

The superficial and intrinsic averages given by Eq. (C.1) and Eq. (C.3), respectively, are related as:

$$\langle \Phi_l \rangle = \varepsilon_l \langle \Phi_l \rangle^l \quad (\text{C.4})$$

In Eq. (C.4), quantity ε_l is the liquid (l) phase volume fraction or more generally, *porosity*.

C.2 Theorems

C.2.1 Spatial Averaging Theorem

This theorem gives the rule for interchanging the derivative with respect to space. The derivation of the *spatial averaging theorem* can be referred from [121]. The theorem reads as:

$$\langle \nabla \cdot \Phi_l \rangle = \nabla \cdot \langle \Phi_l \rangle + \frac{1}{V} \int_{A_{ls}(t)} \Phi_l \cdot \hat{\boldsymbol{\eta}}_{ls} dA \quad (\text{C.5})$$

C.2.2 General Leibniz Rule

This theorem gives the rule for differentiation under the integral sign. In volume averaging formulation, *general Leibniz rule* is used to interchange time derivative from inside of the averaging integral to outside of the averaging integral. The general form of the theorem reads as:

$$\frac{d}{dt} \int_{V(t)} \Phi dV = \int_{V(t)} \frac{\partial \Phi}{\partial t} dV + \int_{A_{ls}(t)} \Phi \mathbf{w}_{ls} \cdot \hat{\boldsymbol{\eta}}_{ls} dA \quad (\text{C.6})$$

In terms of volume averaging notation the theorem reads as:

$$\frac{d}{dt}\langle\Phi\rangle = \left\langle\frac{\partial\Phi}{\partial t}\right\rangle + \frac{1}{V} \int_{A_{ls}(t)} \Phi \mathbf{w}_{ls} \cdot \hat{\boldsymbol{\eta}}_{ls} dA \quad (\text{C.7})$$

where: \mathbf{w}_{ls} is the velocity of the interface between solid and liquid phase.

The derivation of the *general Leibniz rule* can be referred from [111].

Appendix D

Discrete Maximum Principle

In chapter 6, in section (6.2), it was explained that one of the features of the numerical scheme used, is the use of *time semi-discretization*, which essentially means that the density is shifted backward with respect to time. This discretization will satisfy the *discrete maximum principle*. Here, it will be proved that by applying the same discretization on a generic advection-diffusion equation for a variable Φ , it will satisfy the *discrete maximum principle*. Below is the generic advection-diffusion equation for a variable Φ . The equation reads:

$$\frac{\partial}{\partial t}(\rho\Phi) + \nabla \cdot (\rho\Phi\mathbf{v}) - \Delta\Phi = 0 \quad (\text{D.1})$$

where: ρ and \mathbf{v} are related by mass balance equation:

$$\frac{\partial}{\partial t}(\rho) + \nabla \cdot (\rho\mathbf{v}) = 0 \quad (\text{D.2})$$

The solution of the aforementioned equation Eq. (D.1) will be sought on a polygon domain ($d = 2$) of \mathbb{R}^d , of boundary $\partial\Omega = \partial\Omega_D \cup \partial\Omega_N$. Over $\partial\Omega_D$, Φ is assumed to be fixed and the flow is assumed to enter the domain i.e. $\mathbf{v} \cdot \boldsymbol{\eta}_{\partial\Omega_D} \leq 0$, where: $\boldsymbol{\eta}_{\partial\Omega_D}$ is the outward normal vector to $\partial\Omega_D$. Further, over $\partial\Omega_N$, Φ is assumed to satisfy the Neumann boundary condition, and flow is assumed to leave the domain i.e. $\mathbf{v} \cdot \boldsymbol{\eta}_{\partial\Omega_N} \geq 0$. Using, relation (D.2), a non-conservative form of Eq. (D.1) reads:

$$\rho \left[\frac{\partial}{\partial t}(\Phi) + \mathbf{v} \cdot \nabla\Phi \right] - \Delta\Phi = 0 \quad (\text{D.3})$$

The aforementioned equation is known to satisfy the maximum principle. The proof of the discrete analog of this principle relies on the following lemma:

Lemma D.0.1 *Let A be a matrix of $\mathbb{R}^{n \times n}$ such that:*

1. *For $1 \leq i \leq n$, $A_{i,i} > 0$, diagonal elements should be greater than 0.*
2. *For $1 \leq i, j \leq n$, $j \neq i$, $A_{i,j} \leq 0$, off-diagonal elements should be less than 0.*
3. *For $1 \leq i \leq n$, $\sum_{1 \leq i \leq n} A_{i,j} > 0$. Thus A is a diagonal dominant matrix.*

Then, matrix A will be invertible i.e. A^{-1} will exist.

Further, referring to the notation for the control volumes from Fig. D.1, let $(\rho_K)_{K \in M}$, $(\rho_K^*)_{K \in M}$ and $(F_K)_{K \in M, \sigma \in \varepsilon(K)}$ be the discrete quantities associated with density (ρ) and the flux ($F = \rho \mathbf{u}$), respectively. It is further supposed that these quantities will satisfy the following conditions:

$$\begin{aligned}
 & \forall K \in M, \rho_K > 0, \rho_K^* > 0; \\
 & \forall \sigma = K|L, F_{K,\sigma} = -F_{L,\sigma}, \\
 & \forall K \in M, \frac{|K|(\rho_K - \rho_K^*)}{\delta t} + \sum_{\sigma \in \varepsilon(K)} F_{K,\sigma} = 0
 \end{aligned} \tag{D.4}$$

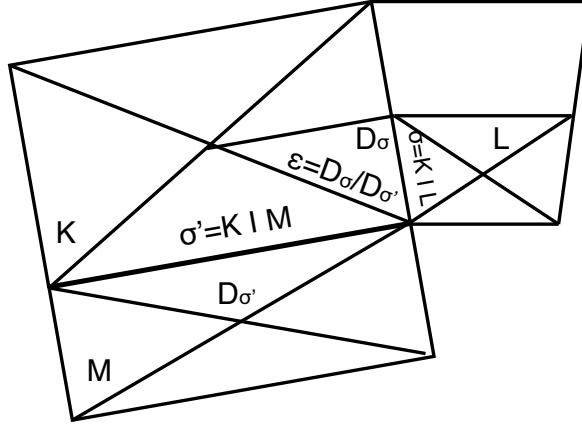


Figure D.1: Control volumes representation

The third relation of (D.4) is a discrete version of the mass balance equation given by Eq. (D.2). To solve the Eq. (D.1), implicit linear upwind scheme has been demonstrated. According to which:

Assuming the time semi-discretization by backward Euler method and an upwind discretization be used for the convection flux. Let $(\Phi_K^*)_{K \in M}$ be the known discrete solution at the previous time step. The set of faces decomposes in $\varepsilon = \varepsilon_{int} \cup \varepsilon_D \cup \varepsilon_N$, where ε_D and ε_N stand for faces included in $\partial\Omega_D$ and $\partial\Omega_N$, respectively. ε_{int} are set of internal faces. Thus, time semi-discretized form of Eq. (D.1) having unknowns $((\Phi_K)_{K \in M})$, looks like:

$$\forall K \in M, \frac{|K|(\rho_K \Phi_K - \rho_K^* \Phi_K^*)}{\delta t} + \sum_{\sigma \in \varepsilon(K)} F_{K,\sigma} \Phi_\sigma + \sum_{\sigma=K|L} \frac{|\sigma|(\Phi_K - \Phi_L)}{d_\sigma} + \sum_{\sigma \in \varepsilon(K) \cap \varepsilon_D} \frac{|\sigma|(\Phi_K - \Phi_\sigma)}{d_\sigma} = 0 \quad (\text{D.5})$$

Further:

$$\begin{aligned} \forall \sigma \in \varepsilon_{int}, \sigma = K|L, \Phi_\sigma = \Phi_K, \text{ if } F_{K,\sigma} \geq 0 \text{ and } \Phi_\sigma = \Phi_L \text{ else.} \\ \forall \sigma \in \varepsilon_N, \sigma = K|ext, \Phi_\sigma = \Phi_K, \text{ For these faces flux } F_{K,\sigma} < 0 \\ \forall \sigma \in \varepsilon_D, \Phi_\sigma = \Phi_{D,\sigma}, \text{ which is given at the boundaries.} \end{aligned}$$

Now, it will be shown that the system of algebraic equations obtained from time semi-discretization and given by Eq. (D.5) has one and only one solution satisfying:

$$\forall K \in M : \text{Minimum}(\Phi) \leq \Phi_K \leq \text{Maximum}(\Phi)$$

This is *Discrete Maximum Principle*.

Proof:

Assuming any real number R and defining $R^+ = \max(0, R)$ and $R^- = \min(0, R)$, such that $R = R^+ - R^-$. Thus, now advection fluxes through internal face $\sigma = K|L$ can be written: $F_{K,\sigma} \Phi_\sigma = F_{K,\sigma}^+ \Phi_K - F_{K,\sigma}^- \Phi_L$, and advection flux through $\sigma = K|ext \in \varepsilon_N$ takes the form: $F_{K,\sigma} \Phi_\sigma = F_{K,\sigma}^+ \Phi_K$. The diagonal elements for the system of Eq. (D.5) thus becomes:

$$A_{K,K} = \frac{|K| \rho_K}{\delta t} + \sum_{\sigma \in K\varepsilon(K)} F_{K,\sigma}^+ + \sum_{\sigma=K|L} \frac{|\sigma|}{d_\sigma} + \sum_{\sigma \in K\varepsilon(K) \cap \varepsilon_D} \frac{|\sigma|}{d_\sigma}$$

and off-diagonal entries will be:

$$A_{K,L} = -F_{K,K|L}^- - \frac{|K|L|}{d_{K|L}}$$

Thus, it can be seen that, $A_{K,K} > 0$, all diagonal values are positive and non-zero. Also, all off-diagonal values are negative or equal to zero, i.e. $A_{K,L} \leq 0$. It is also easy to see that the sum of diagonal and off-diagonal entries is positive. Hence, from Lemma D.0.1, the system of algebraic equations given by Eq. (D.5) will have a unique solution. Also, for proving the boundedness of the solution, on substituting $(\Phi_K - \text{Minimum}(\Phi))$ instead of Φ in Eq. (D.5), will also satisfy the Lemma D.0.1, and thus will yield a solution:

$$\Phi_K - \text{Minimum}(\Phi) \geq 0$$

Hence, $\Phi_K \geq \text{Minimum}(\Phi)$, always.

Similarly, on substituting $(\text{Maximum}(\Phi) - \Phi_K)$ instead of Φ in Eq. (D.5), will also satisfy the Lemma D.0.1, and thus will yield a solution:

$$\text{Maximum}(\Phi) - \Phi_K \geq 0$$

Hence, $\Phi_K \leq \text{Maximum}(\Phi)$, always.

Thus:

$$\forall K \in M : \text{Minimum}(\Phi) \leq \Phi_K \leq \text{Maximum}(\Phi)$$

Which essentially means, the solution will be bounded.

Appendix E

Test Cases

E.1 Validation of Implemented Navier-Stokes Equation for Partially Porous Domains in case of Forced Convection

The numerical validation of implemented macroscopic Navier-Stokes equation in *CALIF³S* [20] for partially porous region in case of forced convection has been done with the work of Vafai and Kim [114]. In this work, Vafai and Kim [114] had worked out an exact solution for describing the fluid mechanics of interface region between a porous medium and fluid layer. They had made the analysis of the fluid mechanics of the interface region by taking into account two parameters, which are:

1. $A = Re_H \Lambda_H$
2. $B = \frac{1}{Da_H}$

where: Re_H is the Reynolds number based on the fluid layer of height H shown in Fig. E.1, Da_H and Λ_H are the Darcy number and inertia parameter respectively, with definitions:

$$Da_H = \frac{K}{H^2} \quad (\text{E.1})$$

$$\Lambda_H = \frac{F \varepsilon H}{\sqrt{K}} \quad (\text{E.2})$$

where:

1. F is the function used in expressing terms, which depends on the Reynolds number and the microstructure of the porous medium.
2. ε is the porosity of the porous medium.
3. H is the height of the fluid layer shown in Fig. E.1.

4. K is the permeability of the porous medium.

However, in the present comparative study the contribution from F parameter will be neglected. Because of which the velocity profile are re-calculated from the formula derived by Vafai and Kim [114] by setting $F = 0$. The comparative study is done for a partially porous domain shown in Fig. E.1.

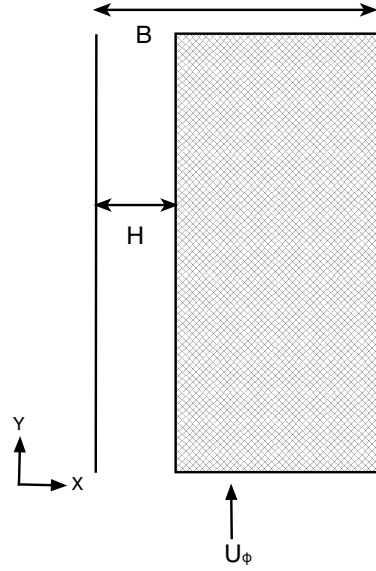


Figure E.1: Schematic of a partial porous cavity

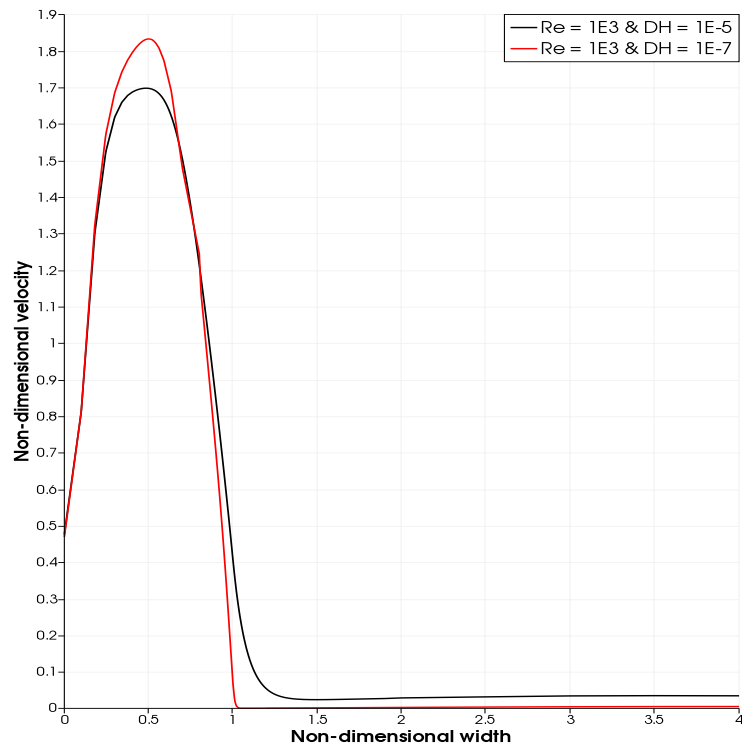
Fig. E.1 shows the physical domain having a porous region and a fluid channel of height H . A free stream velocity u_ϕ is imposed over the domain by imposing a *velocity inlet* boundary condition. The study has been performed for two values of Darcy number (Da_H) at a fixed channel Reynolds number (Re_H). These values of Da_H and Re_H are:

1. $Da_H = 10^{-5}$ and $Re_H = 10^3$.
2. $Da_H = 10^{-7}$ and $Re_H = 10^3$.

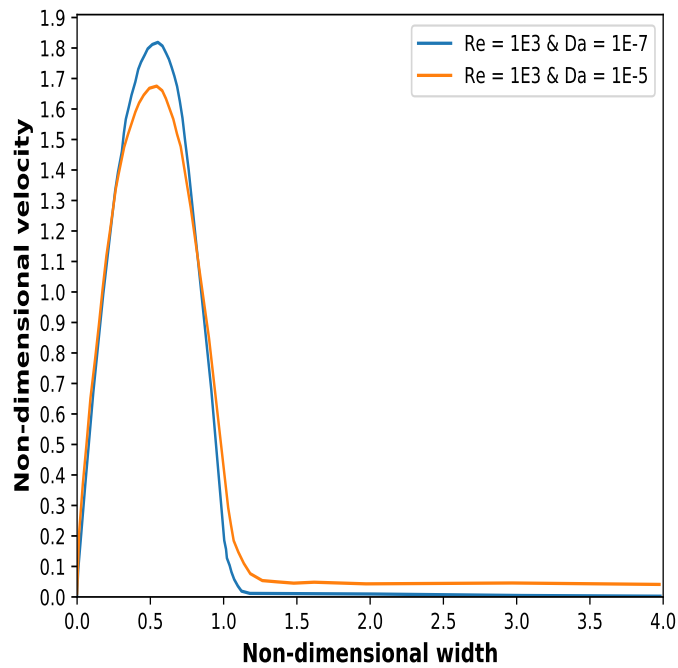
where: $Re_H = \frac{\rho U_\phi H}{\mu}$ and $Da_H = \frac{K}{l_d^2}$.

The dimensions taken for the partially porous schematic shown in Fig. E.1 are:

1. $H = 1$ m.
2. $B = 4$ m.



(a) Numerical results from CALI F³S



(b) Recalculated velocity profiles from the formula derived by Vafai and Kim [114]

Figure E.2: Effects of the permeability variations on the velocity field

Values of other physical parameters are:

1. $\rho = 10^3 \text{ kgm}^{-3}$.
2. $\mu = 10^{-3} \text{ kgm}^{-1}\text{sec}^{-1}$.
3. $\varepsilon = 0.1$

The closure model for permeability (K) is given by Konzey-Carman relation [12].

$$K = \frac{1}{180} \frac{l_d^2 \varepsilon^3}{(1 - \varepsilon)} \quad (\text{E.3})$$

The value of l_d^2 are taken to be 10 m^2 and 0.1 m^2 for $Da_H = 10^{-5}$ and $Da_H = 10^{-7}$, respectively.

Further, the velocity and width has been made dimensionless by inlet velocity (U_ϕ) and channel width (H).

The effect of the Darcy number can be seen in Fig. E.2. It can be seen that an decrease in the Darcy number, results in less permeability in the porous region. This decrease in permeability give rise to the lower mass flow rate through the porous region, thus resulting an increase in the velocity through the open region. From, Fig. E.2 it can also be seen that the numerical results shown in Fig. E.2 (a) are in good agreement with the recalculated velocity profiles from Kim and Vafai [114].

E.2 Validation Against Solutal Natural Convection in a Uniform Porous Medium

The numerical implementation of coupling between Navier-Stokes equation with the concentration equation by *Boussinesq approximation* [125] has been validated against a semi-analytical solution proposed by Marwan et. al. [34] for density driven flows in porous media. Fig. E.3 shows the square domain used by [34] having the fixed concentrations on the lateral boundaries. The gravity is downward pointed and porous media is water saturated.

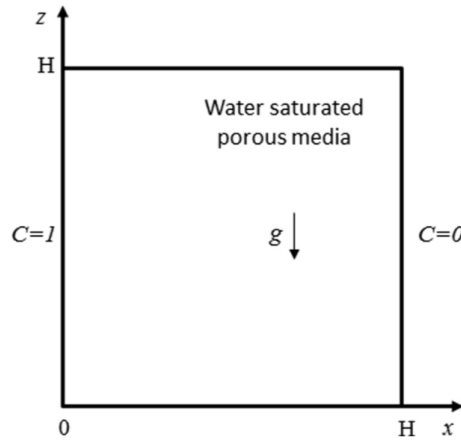


Figure E.3: Domain for porous cavity [34]

The benchmark shown here is for the case with solutal Rayleigh number $Ra = 380$, where solutal Rayleigh number for porous cavity is computed by the data given in the Table E.1, using the following expression:

$$Ra_s = \frac{\rho_0 g \beta_s H K_e}{\mu_m D_m} ; K_e = \frac{K}{\varepsilon} \quad (\text{E.4})$$

Square cavity dimension [34]	$H = 1 \text{ m}$
Porosity [34]	$\varepsilon = 0.35$
Permeability [34]	$K = 1.0204 \times 10^{-9} \text{ m}^2$
Molecular diffusion [34]	$D_m = 18.86 \times 10^{-7} \text{ m}^2 \text{ s}^{-1}$
Density [34]	$\rho_o = 1000 \text{ kg/m}^3$
Solutal expansion coefficient	$\beta_s = -2.5 \times 10^{-2} -$
Gravity	$g = 9.81 \text{ m/s}^2$
Viscosity [34]	$\mu_m = 10^{-3} \text{ kgm}^{-1} \text{ s}^{-1}$

Table E.1: Parameters for the porous cavity problem

E.2.0.1 $Ra = 380$

This case in [34] corresponds to a small Rayleigh number with high diffusion coefficient. The value for this diffusion coefficient is given in Table E.1. Fig. E.6, E.5 and Fig. E.4 show the comparison between the velocity and contours generated by the semi-analytical solution of [34] and $CALIF^3S$. The numerical results seems to have good agreement. The velocities has been made dimensionless by the product of $D_m H \varepsilon$.

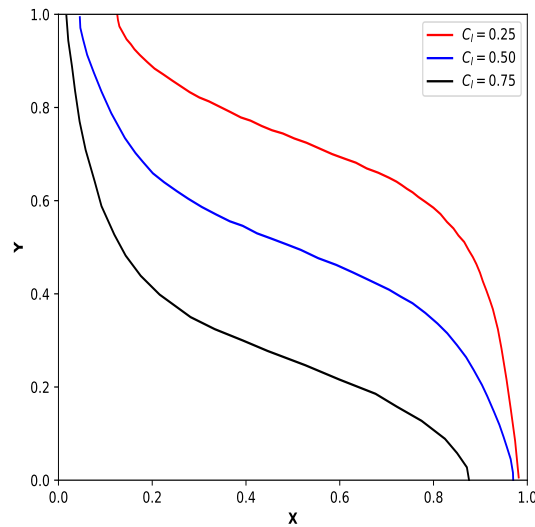
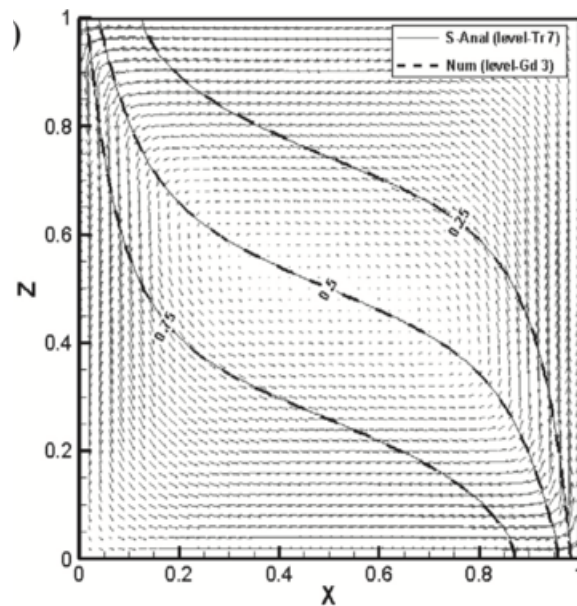
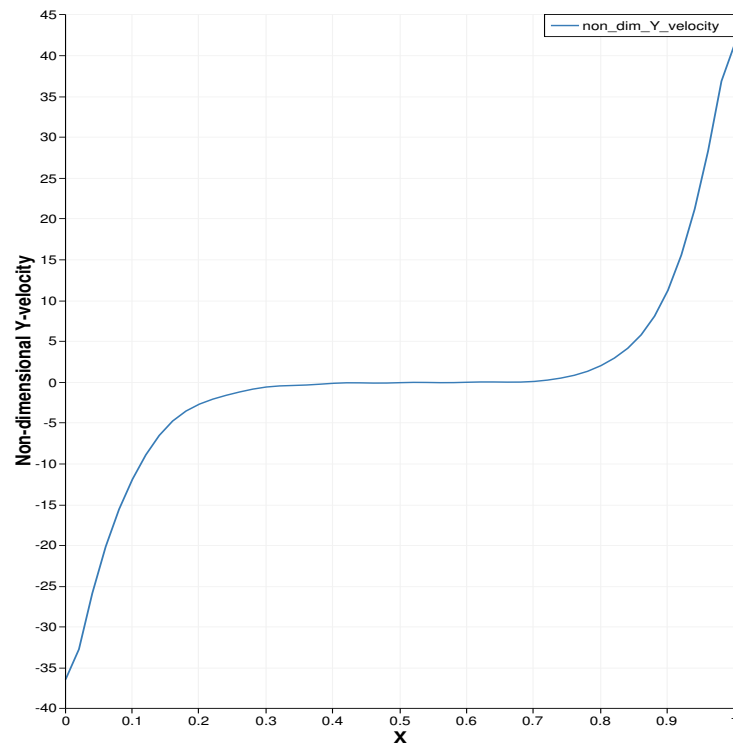
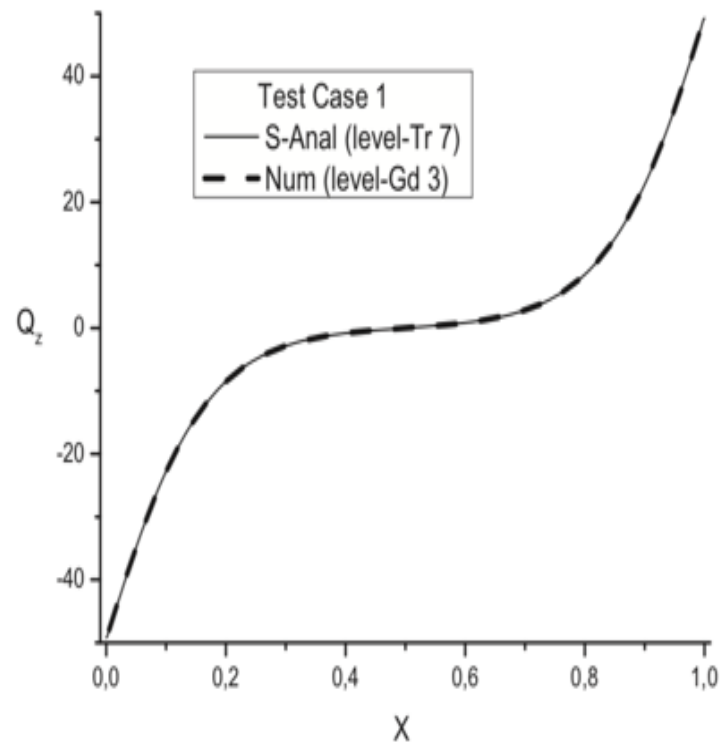
(a) *Liquid concentration contours*(b) *Liquid concentration contours [34]*

Figure E.4: Liquid concentration contours for case: 1

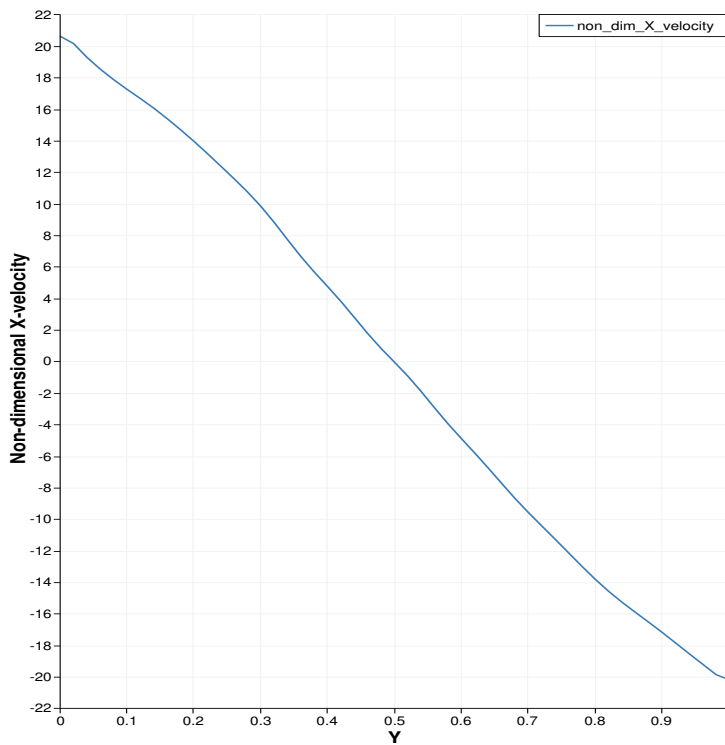


(a) Non-dimensional vertical (Y) velocity at mid-section $Y = 0.5$

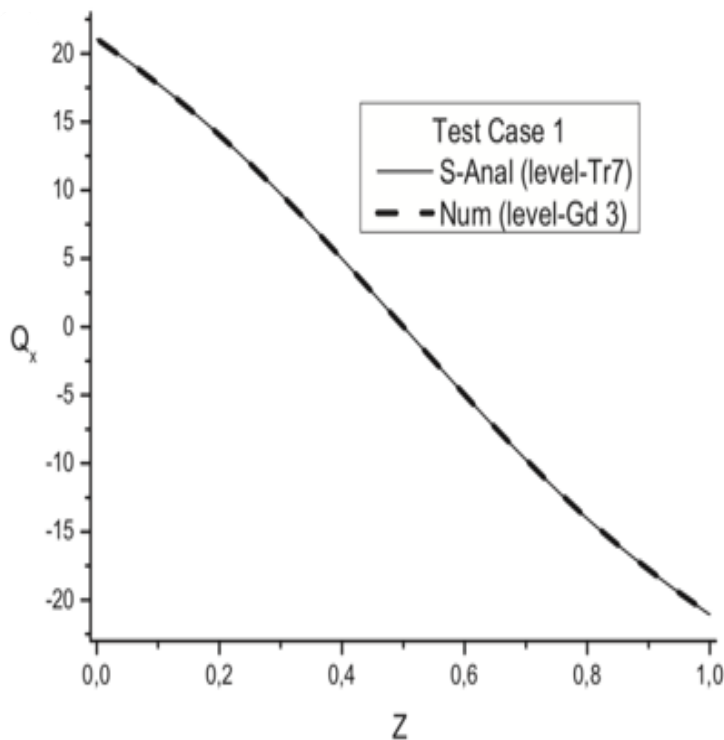


(b) Non-dimensional vertical (Y) velocity at mid-section $Y = 0.5$ [34]

Figure E.5: Non-dimensional vertical velocities for case: 1



(a) Non-dimensional horizontal (X) velocity at mid-section $X = 0.5$



(b) Non-dimensional horizontal (X) velocity at mid-section $X = 0.5$ [34]

Figure E.6: Non-dimensional horizontal velocities for case: 1

Appendix F

Different B.C. for Oxygen Atoms

This appendix shows the results for the Fixed B.C. for O atoms on the *Right* boundary of computational domain shown in Fig. 8.3. This Fixed B.C. corresponds to the initial value of O atoms in oxide, i.e. $n_{ox}^O = 0.6$. It is observed in this case when compared with the original case discussed in chapter 8, in section (8.6.1), that there is more dissolution. Fig. (F.1) (a)-(b) and Fig. (F.2) (a)-(b), shows the results for the present case and its comparison with the case shown in section (8.6.1).

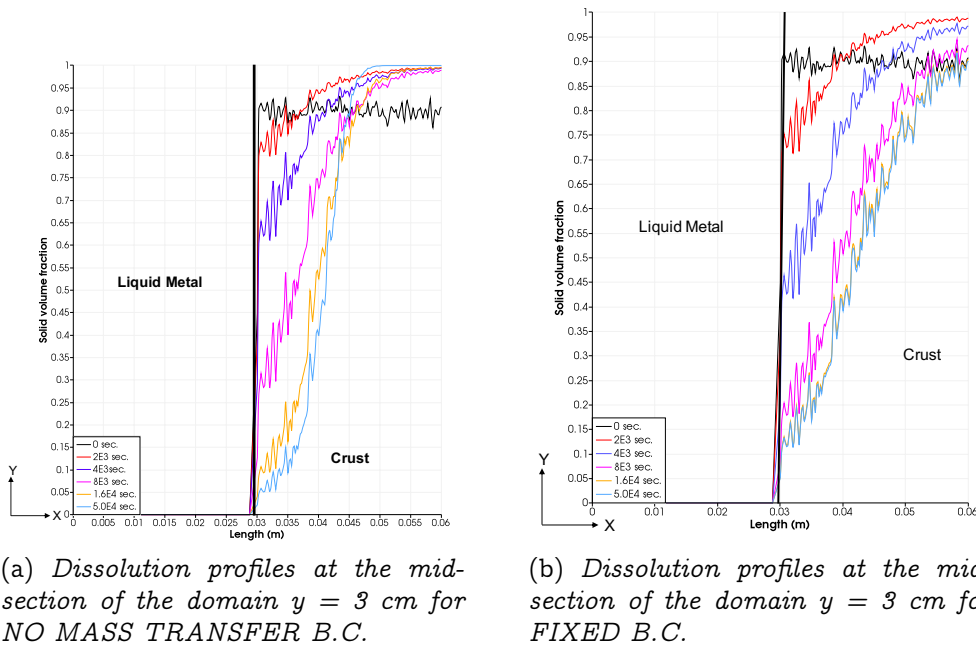
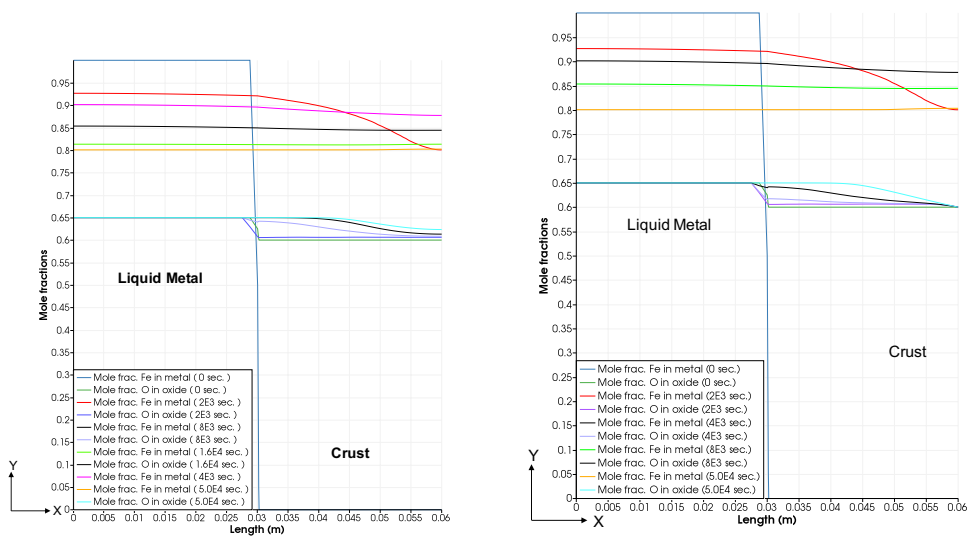


Figure F.1: Results for dissolution profiles with different B.Cs. for O atoms



(a) Mole fraction profiles of Fe in metal and O in oxide at mid-section of the domain $y = 3$ cm for NO MASS TRANSFER B.C.

(b) Mole fraction profiles of Fe in metal and O in oxide at mid-section of the domain $y = 3$ cm for FIXED B.C.

Figure F.2: Results for mole fractions profile evolution in the domain with different B.Cs. for O atoms

Bibliography

- [1] H. B. Aaron and G. R. Kotler. “Second phase dissolution”. In: *Metallurgical Transactions* 2.2 (Feb. 1971), pp. 393–408. DOI: 10.1007/BF02663326.
- [2] S. Abalin, I. Gnidoi, A. Surenkov, and V. Strizhov. *Database for 3rd and 4th series of RASPLAV salt tests*. Tech. rep. OECD RASPLAV Report, 1998.
- [3] O. Alderman, C. Benmore, J. Weber, L. Skinner, A. Tamalonis, S. Sendelbach, A. Hebden, and M. A. Williamson. “Corium lavas: Structure and properties of molten UO₂-ZrO₂ under meltdown conditions”. In: *Scientific Reports* 8 (Feb. 2018), p. 2434. DOI: 10.1038/s41598-018-20817-z.
- [4] V. Almjashev, V. Granovsky, V. Khabensky, S. Kotova, E. Krushinov, A. Sulatsky, S. Vitol, V. Gusarov, F. Fichot, B. Michel, P. Piluso, R. L. Teller, M. Fischer, C. L. Guennic, and N. Bakouta. “Experimental study of transient phenomena in the three-liquid oxidic-metallic corium pool”. In: *Nuclear Engineering and Design* 332 (2018), pp. 31–37. DOI: <https://doi.org/10.1016/j.nucengdes.2018.03.004>.
- [5] ANL. *Reactors Designed by Argonne National Laboratory*. <https://www.ne.anl.gov/About/reactors/early-reactors.shtml>.
- [6] M. A. Ansari and F. Stepanek. “The effect of granule microstructure on dissolution rate”. In: *Powder Technology* 181.2 (2008). Particulate Processes in the Pharmaceutical Industry, pp. 104–114. DOI: <https://doi.org/10.1016/j.powtec.2006.12.012>.
- [7] V. Asmolov, V. Khabensky, V. Beshta, V. Gusarov, S. Vitol, E. V. Krushinov, S. Y. Kotova, E. K. Kalyago, N. E. Kamensky, A. V. Lysenko, V. G. Bliznyuk, V. R. Bulygin, E. V. Shevchenko, V. S. Granovsky, V. V. Martynov, V. V. Gusarov, V. I. Almyashev, M. D. Tolkachyov, M. R. Pavlov, V. V. Vlasov, Y. G. Degaltsev, and Y. M. Utkin. *The MA-2 Experiment: Zirconium and Uranium partitioning between oxide and metallic phases of molten corium, MR-TR-6*. Tech. rep. Mar. 2001.
- [8] V. Asmolov, V. Khabensky, V. Beshta, V. Gusarov, S. Vitol, Y. Krushinov, Y. Degaltsev, V. Vlasov, and Y. Utkin. *MA-1 Experiment: Post-Test Analysis Results, MP-TR-1*. Tech. rep. Nov. 2001.

-
- [9] V. Asmolov, V. Zagryazkin, and D. F. Tsurikov. “The thermodynamics of U-Zr-Fe-O melts”. In: *High Temperature* 45.3 (June 2007), pp. 305–312. DOI: 10.1134/S0018151X07030042.
- [10] S. Bakardjieva, M. Barrachin, S. Bechta, P. Bezdicka, D. Bottomley, L. Brissonneau, B. Cheynet, O. Dugne, E. Fischer, M. Fischer, V. Gusarov, C. Journeau, V. Khabensky, M. Kiselova, D. Manara, P. Piluso, M. Sheindlin, V. Tyrpekl, and T. Wiss. “Quality improvements of thermodynamic data applied to corium interactions for severe accident modelling in SARNET2”. In: *Annals of Nuclear Energy* 74.C (2014), pp. 110–124. DOI: 10.1016/j.anucene.2014.06.023.
- [11] M. Barrachin, P. Chevalier, B. Cheynet, and E. Fischer. “New modelling of the U-O-Zr phase diagram in the hyper-stoichiometric region and consequences for the fuel rod liquefaction in oxidising conditions”. In: *Journal of Nuclear Materials* 375.3 (2008), pp. 397–409. DOI: 10.1016/j.jnucmat.2008.02.003.
- [12] J. Bear. *Dynamics of Fluids in Porous Media*. Dover Publication, 1972.
- [13] J. Belloni. “Modélisation des phénomènes de dissolution lors de la phase précoce d’un accident grave de réacteur nucléaire”. PhD thesis. Ecole Centrale Paris, Feb. 2009.
- [14] J. Belloni, F. Fichot, G. Benoit, D. Gobin, and M. Quintard. “A Two-Phase Model to Describe the Dissolution of ZrO₂ by Molten Zr”. In: Eurotherm 81: Reactive Heat Transfer In Porous Media, June 2007.
- [15] W. Bennon and F. Incropera. “A continuum model for momentum, heat and species transport in binary solid-liquid phase change systems—II. Application to solidification in a rectangular cavity”. In: *International Journal of Heat and Mass Transfer* 30 (Oct. 1987), pp. 2171–2187. DOI: 10.1016/0017-9310(87)90095-0.
- [16] P. Bousquet-Mélou. “Modélisation macroscopique et simulation numérique de la solidification de mélanges binaires”. PhD thesis. Université Paris VI, 2000.
- [17] P. Bousquet-Melou, A. Neculae, G. Benoit, and M. Quintard. “Averaged solute transport during solidification of a binary mixture: Active dispersion in dendritic structures”. In: *Metallurgical and Materials Transactions B* 33 (June 2002), pp. 365–376. DOI: 10.1007/s11663-002-0048-8.
- [18] M. E. Bunker. “Early Reactors: From Fermi’s Water Boiler to Novel Prototypes”. In: *Los Alamos Science* (1983).
- [19] V. C. Prantil and P. R. Dawson. “Application of mixture theory in continuous casting”. In: *Transport phenomenon in material processing* 36 (1983), pp. 469–484.
- [20] CALIF3S. <https://gforge.irsn.fr/gf/project/calif3s>.

-
- [21] R. Chen, Y. Li, K. Guo, X. Tian, S. Qiu, and G. Su. “Numerical investigation on the dissolution kinetics of ZrO₂ by molten zircaloy using MPS method”. In: *Nuclear Engineering and Design* 319 (Aug. 2017), pp. 117–125. DOI: 10.1016/j.nucengdes.2017.05.002.
- [22] F. Cheung. “Limiting factors for external vessel cooling.” In: *Proceeding of NURETH 10*. 2003.
- [23] P. Chevalier and E. Fischer. “Thermodynamic modelling of the O-U-Zr system”. In: *Journal of Nuclear Materials* 257 (1998), pp. 213–255.
- [24] N. Chikhi, G. Nguyen, and J. Fleurot. “Determination of the hydrogen source term during the reflooding of an overheated core: Calculation results of the integral reflood test QUENCH-03 with PWR-type bundle”. In: *Nuclear Engineering and Design* 250 (Sept. 2012), pp. 351–363. DOI: 10.1016/j.nucengdes.2012.05.026.
- [25] A. Ciobanas, R. P. Q. G, G. Benoit, D. Gobin, F. Fichot, M. Quintard, L. P, and Y. Fautrelle. “Modélisation des ségrégations en solidification d’alliages binaires”. In: Grenoble, France: Congrès Francais de Thermique, June 2003.
- [26] J. Crank. *Free and moving boundary problems*. Oxford: Clarendon Press, 1984.
- [27] *Degraded core after Three Mile Island nuclear accident*. https://commons.wikimedia.org/wiki/File:Graphic_TMI-2_Core_End-State_Configuration.png.
- [28] T. Dinh, T. Salmassi, and T. Theofanous. “The limit of coolability in AP 1000 related ULPU-2400 confi V facility.” In: *Proceeding of NURETH 11*. Seoul, Korea., Oct. 2003.
- [29] D. A. Drew. “Mathematical Modeling of Two-Phase Flow”. In: *Annual Review of Fluid Mechanics* 15.1 (1983), pp. 261–291. DOI: 10.1146/annurev.fl.15.010183.001401.
- [30] C. Duijn and I. Pop. “Crystal Dissolution and Precipitation in Porous Media: Pore Scale Analysis”. In: *Journal für die reine und angewandte Mathematik (Crelles Journal)* 577 (Jan. 2004), pp. 171–211. DOI: 10.1515/crll.2004.2004.577.171.
- [31] M. Edenius. *Study of reactivity temperature coefficient in Light Water Reactor*. 1976.
- [32] S. Eleonora, S. Maciej, S. Laurent, and L. Romain. “In vessel corium propagation sensitivity study of reactor pressure vessel rupture time with PROCOR platform”. In: *Journal of Power Technologies* 97.(2) (2017), pp. 110–116.
- [33] R. Eymard, G. Thierry, R. Herbin, D. Hilhorst, and M. Mainguy. “Instantaneous and non-instantaneous dissolution: approximation by the finite volume method”. In: *Proceedings of ESAIM* 6 (Jan. 1999), 41–55 (electronic). DOI: 10.1051/proc:1999045.

- [34] M. Fahs, A. Younes, and T. A. Mara. “A new benchmark semi-analytical solution for density-driven flow in porous media”. In: *Advances in Water Resources* 70 (2014), pp. 24–35. DOI: <https://doi.org/10.1016/j.advwatres.2014.04.013>.
- [35] B. Faugeras, J. Pousin, and F. Fontvieille. “An efficient numerical scheme for precise time integration of a diffusion-dissolution/precipitation chemical system”. In: *Math. Comput.* 75 (Jan. 2006), pp. 209–222. DOI: 10.1090/S0025-5718-05-01782-5.
- [36] F. Fichot and L. Carénini. “Some Consequences of Material Interactions for In-Vessel Melt Retention”. In: *Proceeding of ICAPP*. May 2015.
- [37] M. Fukasawa and S. Fukasawa. “Thermodynamic analysis for molten corium stratification test MASCA with ionic liquid U-Zr-Fe-O-B-C-FPs database”. In: *Journal of Nuclear Science and Technology* 44.9 (2007), pp. 1210–1219. DOI: 10.1080/18811248.2007.9711364.
- [38] M. Fukasawa, S. Tamura, and M. Hasebe. “Development of thermodynamic database for U-Zr-Fe-O-B-C-FPs system”. In: *Journal of Nuclear Science and Technology* 42.8 (2005), pp. 706–716. DOI: 10.1080/18811248.2004.9726440.
- [39] H. Fukuyama, H. Higashi, and H. Yamano. “Thermophysical Properties of Molten Stainless Steel Containing 5 mass % B4C”. In: *Nuclear Technology* 205.9 (2019), pp. 1154–1163. DOI: 10.1080/00295450.2019.1578572.
- [40] K. George. *The Oak Ridge Research Reactor (ORR), The Low-Intensity Testing Reactor (LITR), and The Oak Ridge Graphite Reactor (OGR) as experiment facilities*. Tech. rep. ORNL, 1962.
- [41] B. Goyeau, T. Benihaddadene, D. Gobin, and M. Quintard. “Averaged Momentum Equation for Flow Through a Nonhomogenous Porous Structure”. In: *Transport in Porous Media* 28.1 (July 1997), pp. 19–50. DOI: 10.1023/A:1006578602112.
- [42] B. Goyeau, D. Gobin, T. Benihaddadene, D. Gobin, and M. Quintard. “Numerical calculation of the permeability in a dendritic mushy zone”. In: *Metallurgical and Materials Transactions B* 30.4 (Aug. 1999), pp. 613–622. DOI: 10.1007/s11663-999-0022-9.
- [43] B. Goyeau, P. BOUSQUET-MELOU, D. Gobin, M. Quintard, and F. Fichot. “Macroscopic modeling of columnar dendritic solidification”. In: *Computational & Applied Mathematics* 23 (Dec. 2004). DOI: 10.1590/S0101-82052004000200015.
- [44] U. Grafe, B. Böttger, J. Eiken, and S. G. Fries. “Coupling of multicomponent thermodynamic databases to a phase field model: Application to solidification and solid state transformations of superalloys”. In: *Scripta Materialia - SCRIPTA MATER* 42 (June 2000), pp. 1179–1186. DOI: 10.1016/S1359-6462(00)00355-9.

- [45] W. G. Gray. "A derivation of the equations for multi-phase transport". In: *Chemical Engineering Science* 30.2 (1975), pp. 229–233. DOI: [https://doi.org/10.1016/0009-2509\(75\)80010-8](https://doi.org/10.1016/0009-2509(75)80010-8).
- [46] J. GUO. "MODELISATION NUMERIQUE DE LA DISSOLUTION DES CAVITES KARSTIQUES". PhD thesis. Université de Toulouse, Sept. 2015.
- [47] K. N. Han and M. C. Fuerstenau. "Dissolution behavior of metals from binary alloys". In: *International Journal of Mineral Processing* 72.1 (2003). Special Issue To Honor Professor Douglas W. Fuerstenau, pp. 355–364. DOI: [https://doi.org/10.1016/S0301-7516\(03\)00110-8](https://doi.org/10.1016/S0301-7516(03)00110-8).
- [48] M. Hillert. *Phase equilibria, phase diagrams and phase transformations, their thermodynamic basis*. Cambridge: Cambridge University Press, 1998.
- [49] R. Hubert. "Modelisation numerique de la croissance et de la dissolution des precipites dans l'acier". In: *ATB Metallurgie* 34-35 (Jan. 1995), pp. 4–14.
- [50] IAEA. *Guideline for Accident Analysis of WWER Nuclear Power Plants, Rep. IAEA-EBP-WWER-01*. Tech. rep. 1995.
- [51] IAEA. *Accident Analysis for Nuclear Power Plants, Safety Reports Series*. Tech. rep. 2002.
- [52] F. Incropera and D. Dewitt. *Fundamentals of Heat and Mass Transfer*. John Wiley and Sons, 2011.
- [53] M. J. Whelan. "On the kinetics of particle dissolution". In: *Material Science Journal* 3 (1969), pp. 95–97.
- [54] M. Joyce. "Chapter 6 - Moderation". In: *Nuclear Engineering*. Ed. by M. Joyce. Butterworth-Heinemann, 2018, pp. 111–127. DOI: <https://doi.org/10.1016/B978-0-08-100962-8.00006-8>.
- [55] L. K. Sepold, A. Miassoedov, G. Schanz, U. Stegmaier, M. Steinbrück, J. Stuckert, and C. Homann. "Hydrogen Generation in Reflooding Experiments with LWR-Type Rod Bundles (QUENCH Program)". In: *Nuclear technology* 147 (Aug. 2004), pp. 202–215. DOI: 10.13182/NT04-A3526.
- [56] Y. KANEKO and K. SUMITA. "Determination of Neutron Multiplication (1)". In: *Journal of Nuclear Science and Technology* 4:8 (1967), pp. 400–407. DOI: 10.1080/18811248.1967.9732775.
- [57] M. Kaviany. *Principles of heat transfer in porous media*. Springer-Verlag, 1991.
- [58] K. Kim and D. Olander. "Dissolution of UO_2 by molten Zircaloy". In: *Journal Of Nuclear Materials* 154 (1988), pp. 85–101.

- [59] P. Knabner, C. Duijn, and S. Hengst. “An analysis of crystal dissolution fronts in flows through porous media. Part 1: Compatible boundary conditions”. In: *Advances in Water Resources* 18 (July 1996), pp. 171–185. DOI: 10.1016/0309-1708(95)00005-4.
- [60] R. Kobayashi. “Modeling and numerical simulations of dendritic crystal growth”. In: *Physica D: Nonlinear Phenomena* 63.3 (1993), pp. 410–423. DOI: [https://doi.org/10.1016/0167-2789\(93\)90120-P](https://doi.org/10.1016/0167-2789(93)90120-P).
- [61] M. Kondo, M. Takahashi, T. Suzuki, K. Ishikawa, K. Hata, S. Qiu, and H. Sekimoto. “Metallurgical study on erosion and corrosion behaviors of steels exposed to liquid lead-bismuth flow”. In: *Journal of Nuclear Materials* (2005). DOI: 10.1016/j.jnucmat.2004.08.037.
- [62] A. Kupryazhkin, A. Zhiganov, D. Risovany, K. Nekrassov, V. Risovany, and V. Golovanov. “Simulation of diffusion of oxygen and uranium in uranium dioxide nanocrystals”. In: *Journal of Nuclear Materials* 372.2 (2008), pp. 233–238. DOI: <https://doi.org/10.1016/j.jnucmat.2007.03.176>.
- [63] U. L. Baty, R. A. Tanzilli, and R. W. Heckel. “Dissolution kinetics of CuAl₂ in an Al₄Cu alloy”. In: *Metallurgical Transactions* 1 (1970), pp. 1651–1656.
- [64] T. Laporte. *Synthèse des études réalisées au DMT sur les conséquences d'une explosion de vapeur en cuve ou hors cuve en cas d'accident grave de REP*. Tech. rep. CEA/DEN/DMT/LM2S/RT/00-039, 2000.
- [65] N. Lee and J. Cahoon. “Interdiffusion of Copper and Iron in Liquid Aluminum”. In: *Journal of Phase Equilibria and Diffusion* 32 (June 2011), pp. 226–234. DOI: 10.1007/s11669-011-9883-0.
- [66] H. Lei, H. Zhang, and J. He. “Flow, Solidification, and Solute Transport in a Continuous Casting Mold with Electromagnetic Brake”. In: *Chemical Engineering & Technology* 32 (June 2009), pp. 991–1002. DOI: 10.1002/ceat.200800346.
- [67] “Local thermal equilibrium for transient heat conduction: theory and comparison with numerical experiments”. In: *International Journal of Heat and Mass Transfer* 38.15 (1995), pp. 2779–2796. DOI: [https://doi.org/10.1016/0017-9310\(95\)00028-8](https://doi.org/10.1016/0017-9310(95)00028-8).
- [68] V. Mages, L. Casella, M. Simonet-Roda, D. Henkel, E. Griesshaber, A. Checa, and W. Schmahl. “The effect of microstructure in the dissolution and alteration kinetics of biogenic Carbonates”. In: *Proceedings of the 20th EGU General Assembly, EGU2018*. Vienna, Austria, Apr. 2018.
- [69] E. Maise and J. Pousin. “Diffusion and dissolution/precipitation in an open porous reactive medium”. In: *Journal of Computational and Applied Mathematics - J COMPUT APPL MATH* 82 (Sept. 1997), pp. 279–290. DOI: 10.1016/S0377-0427(97)00049-6.

-
- [70] *Manhattan Project*. <https://www.history.com/topics/world-war-ii/the-manhattan-project>.
- [71] M. Marion and R. Temam. “Navier-Stokes equations: Theory and approximation”. In: *Handbook of Numerical Analysis*. Ed. by P. Ciarlet and J. Lions. North Holland, 1998.
- [72] “Material Testing Reactor”. In: *JPhysics Today* 5 6 (1952). DOI: 10.1063/1.3067632.
- [73] N. Moelans, B. Blanpain, and P. Wollants. “An introduction to phase-field modeling of microstructure evolution”. In: *Calphad* 32.2 (2008), pp. 268–294. DOI: <https://doi.org/10.1016/j.calphad.2007.11.003>.
- [74] K. Müller, A. Goryachev, V. Smirnov, Svyatkin, J. Stuckert, M. Veshchunov, and A. Berdyshev. *Simultaneous Dissolution of UO₂ and ZrO₂ by Molten Zircaloy New Experiments and Modelling*. Tech. rep. Forschungszentrum Karlsruhe, Jan. 2004.
- [75] R. N. HILLS, D. Loper, and P. Roberts. “A thermodynamically consistent model of a mushy zone”. In: *The Quarterly Journal of Mechanics and Applied Mathematics* 36 (Nov. 1983), pp. 505–539. DOI: 10.1093/qjmam/36.4.505.
- [76] J. Ni and C. Beckermann. “A volume-averaged two-phase model for transport phenomena during solidification”. In: *Metallurgical Transactions B* 22.3 (June 1991), p. 349. DOI: 10.1007/BF02651234.
- [77] C. Noiriél, P. Gouze, and D. Bernard. “Investigation of porosity and permeability effects from microstructure changes during limestone dissolution”. In: *Geophysical Research Letters* 31.24 (2004), L24603 (4 p.) DOI: 10.1029/2004GL021572.
- [78] F. V. Nolfi, P. G. Shewmon, and J. S. Foster. “The dissolution and growth kinetics of spherical particles”. In: *Transactions of the metallurgical society of AIME* 245 (July 1969), pp. 1427–1433.
- [79] T. L. Noorden and I. Pop. “A Stefan problem modelling dissolution and precipitation in porous media”. In: *IMA Journal of Applied Mathematics* 73 (Aug. 2008), pp. 393–411.
- [80] NSAC. *Analysis of Three Mile Island (TMI)-Unit 2*. Tech. rep. Nuclear Safety Analysis Center NSAC 80-1, Electric Power Research Institute, 1980.
- [81] *Nuclear Fuel and its Fabrication*. <http://www.world-nuclear.org/information-library/nuclear-fuel-cycle/conversion-enrichment-and-fabrication/fuel-fabrication.aspx>.
- [82] D. R. Olander. “Interpretation of laboratory crucible experiments on UO₂dissolution by liquid zirconium”. In: *Journal of Nuclear Materials* (1995). DOI: 10.1016/0022-3115(95)00085-2.

- [83] D. R. Olander and W. E. Wang. "Thermodynamics of the U-O and Zr-systems and application to analysis of fuel liquefaction during severe accidents in light water reactors". In: *Journal of Nuclear Materials* (1997). DOI: 10.1016/S0022-3115(97)00052-4.
- [84] D. R. Olander and W. E. Wang. "Thermodynamics of the U-O and Zr-systems and application to analysis of fuel liquefaction during severe accidents in light water reactors". In: *Journal of Nuclear Materials* 247 (1997), pp. 258–264. DOI: 10.1016/S0022-3115(97)00052-4.
- [85] P. P. Brahma and T. Harmon. "The effect of multicomponent diffusion on NAPL dissolution from spherical ternary mixtures". In: *Journal of contaminant hydrology* 67 (Jan. 2004), pp. 43–60. DOI: 10.1016/S0169-7722(03)00087-1.
- [86] A. Passerone, M. L. Muolo, R. Novakovic, and D. Passerone. "Liquid metal/ceramic interactions in the (Cu, Ag, Au)/ZrB₂ systems". In: *Journal of the European Ceramic Society* 27.10 (2007), pp. 3277–3285. DOI: <https://doi.org/10.1016/j.jeurceramsoc.2006.12.008>.
- [87] A. Pivano, P. Piluso, N. Chikhi, J. Delacroix, P. Fouquart, and R. Le Tellier. "VITI-CORMET experiments". In: *Proceedings of the 4th annual meeting of the IVMR project*. Trnava, Slovakia, June 2019.
- [88] *Pressurised Water Reactor (PWR) Major Systems*. https://www.mhi.com/products/energy/reactor_coolant_pump.html.
- [89] M. Quintard and S. Whitaker. "One- and Two-Equation Models for Transient Diffusion Processes in Two-Phase Systems". In: ed. by J. P. Hartnett and T. F. Irvine. Vol. 23. *Advances in Heat Transfer*. Elsevier, 1993, pp. 369–464. DOI: [https://doi.org/10.1016/S0065-2717\(08\)70009-1](https://doi.org/10.1016/S0065-2717(08)70009-1).
- [90] M. Quintard and S. Whitaker. "Transport in ordered and disordered porous media I: The cellular average and the use of weighting functions". In: *Transport in Porous Media* 14.2 (Feb. 1994), pp. 163–177. DOI: 10.1007/BF00615199.
- [91] M. Quintard and S. Whitaker. "Transport in ordered and disordered porous media II: Generalized volume averaging". In: *Transport in Porous Media* 14.2 (Feb. 1994), pp. 179–206. DOI: 10.1007/BF00615200.
- [92] M. Quintard and S. Whitaker. "Transport in ordered and disordered porous media III: Closure and comparison between theory and experiment". In: *Transport in Porous Media* 15 (Apr. 1994), pp. 31–49. DOI: 10.1007/BF01046157.
- [93] O. Reiso, N. Ryum, and J. Strid. "Melting and dissolution of secondary phase particles in AlMgSi-alloys". In: *Metallurgical Transactions A* 24A (Jan. 1993), pp. 2626–2641.

-
- [94] S. Rippon. "History of the PWR and its worldwide development". In: *Energy Policy* 12.3 (1984), pp. 259–265. DOI: [https://doi.org/10.1016/0301-4215\(84\)90026-0](https://doi.org/10.1016/0301-4215(84)90026-0).
- [95] S. Rougé. "SULTAN test facility". In: *Proceeding of NURETH 7*. Saratoga Springs, Sept. 1995.
- [96] P. Roux, F. Fichot, S. De Pierrepont, B. Goyeau, and M. Quintard. "Modeling of binary mixture phase change: assesment on RASPLAV Salt Experiment". In: *Proceeding of NURETH 11*. Avignon, Oct. 2005.
- [97] P. Roux. "Modélisation de la solidification colonnaire at équiaxe de mélanges binaries". PhD thesis. Université Pierre-et-Marie-Curie, Dec. 2005.
- [98] P. Roux, G. Benoit, D. Gobin, F. Fichot, and M. Quintard. "Chemical non-equilibrium modelling of columnar solidification". In: *International Journal of Heat and Mass Transfer* 49 (Nov. 2006). DOI: 10.1016/j.ijheatmasstransfer.2006.05.020.
- [99] P. Roux, D. Gobin, G. Benoit, F. Fichot, and M. Quintard. "Macroscopic model for equiaxed solidification of binary mixtures". In: *Modeling of Casting, Welding and Advanced Solidification Processes - XI* 1 (May 2006).
- [100] S. B. Ryzhov, V. A. Mokhov, M. P. Nikitenko, G. G. Bessalov, A. K. Podshibyakin, D. A. Anufriev, J. Gadó, and U. Rohde. "VVER-Type Reactors of Russian Design". In: *Handbook of Nuclear Engineering*. Ed. by D. G. Cacuci. Boston, MA: Springer US, 2010, pp. 2249–2320. DOI: 10.1007/978-0-387-98149-9_20.
- [101] M. Sahal, J. Creus, R. Sabot, and X. Feaugas. "The effects of dislocation patterns on the dissolution process of polycrystalline nickel". In: *Acta Materialia* 54.8 (2006), pp. 2157–2167. DOI: <https://doi.org/10.1016/j.actamat.2006.01.006>.
- [102] D. Sapundjiev, S. V. Dyck, and W. Bogaerts. "Liquid metal corrosion of T91 and A316L materials in Pb–Bi eutectic at temperatures 400–600°C". In: *Corrosion Science* 48.3 (2006), pp. 577–594. DOI: <https://doi.org/10.1016/j.corsci.2005.04.001>.
- [103] B. Sehgal. *Nuclear Safety in Light Water Reactors*.
- [104] J. Seiler, K. Froment, F. Defoort, and F. Fichot. "The thermalhydraulics of corium undergoing a miscibility gap: Model development and reactor applications." In: *MASCA Seminar*. Aix-en-Provence, France, June 2004.
- [105] J. Seiler and G. Ducros. *Reflooding of a PWR core assessment of knowledge and R&D needs. Potential contribution by Phébus*. Tech. rep. DEN/DTN/SE2T/LPTM/05-117, 2005.
- [106] J. Seiler and K. Froment. "Material effects on multiphase phenomenon in late phase of severe accidents of nuclear reactor." In: *Multiphase Science and Technology*. 12 (2000).

-
- [107] *Severe accident in nuclear power plants*. <https://www.intechopen.com/books/nuclear-power-operation-safety-and-environment/research-on-severe-accidents-in-nuclear-power-plants>.
- [108] *Stefan Problem*. <https://www.encyclopediaofmath.org/index.php/Stefan-problem>.
- [109] J. Svoboda, F. Fischer, P. Fratzl, E. Gamsjäger, and N. Simha. “Kinetics of interfaces during diffusional transformations”. In: *Acta Materialia* (Apr. 2001), pp. 1249–1259.
- [110] T. Takeda, A. Ohwada, and H. Nakamura. “Measurement of non-condensable gas in a PWR small-break LOCA simulation test with LSTF for OECD/NEA ROSA Project and RELAP5 post-test analysis”. In: *Experimental Thermal and Fluid Science* 51 (2013), pp. 112–121. DOI: <https://doi.org/10.1016/j.expthermflusci.2013.07.007>.
- [111] *The Conservation Equations: Leibniz Rule for Differentiation of Integrals*. https://web.stanford.edu/cantwell/AA200_Course_Material/AA200_Course_Notes/AA200_Ch_06_The_Conservation_equations_Cantwell.pdf.
- [112] U. H. Tundal and N. Ryum. “Dissolution of particles in binary alloys: part I. computer simulations”. In: *Metallurgical Transactions A* 23.2 (Feb. 1992), pp. 433–444.
- [113] *Typical Pressurized Water Reactor (PWR) design and basic layout*. <https://www.nrc.gov/reactors/pwrs.html>.
- [114] K. Vafai and S. Kim. “Fluid mechanics of the interface region between a porous medium and a fluid layer—an exact solution”. In: *International Journal of Heat and Fluid Flow* 11.3 (1990), pp. 254–256. DOI: [https://doi.org/10.1016/0142-727X\(90\)90045-D](https://doi.org/10.1016/0142-727X(90)90045-D).
- [115] F. Vermolen and C. Vuik. “A mathematical model for the dissolution of particles in multi-component alloys”. In: *Journal of Computational and Applied Mathematics* 126.1 (2000), pp. 233–254. DOI: [https://doi.org/10.1016/S0377-0427\(99\)00355-6](https://doi.org/10.1016/S0377-0427(99)00355-6).
- [116] F. Vermolen and S. van der Zwaag. “A numerical model for the dissolution of spherical particles in binary alloys under mixed mode control”. In: *Materials Science and Engineering: A* 220.1 (1996), pp. 140–146. DOI: [https://doi.org/10.1016/S0921-5093\(96\)10441-X](https://doi.org/10.1016/S0921-5093(96)10441-X).
- [117] F. J. Vermolen, C. Vuik, and S. V. der Zwaag. *Mathematical models for particle dissolution in metallic alloys*. <http://resolver.tudelft.nl/uuid:493c3f79-da25-46c0-8c03-9cb5f3c8a098>. 2002.
- [118] J. M. Vitek, S. A. Vitek, and S. A. David. “Numerical modeling of diffusion-controlled phase transformations in ternary systems and application to the ferrite/austenite transformation in the Fe-Cr-Ni system”. In: *Metallurgical and Materials Transactions A* 26.8 (Aug. 1995), pp. 2007–2025. DOI: [10.1007/BF02670673](https://doi.org/10.1007/BF02670673).

- [119] A. Walker. *Natural Ventilation*. <http://www.wbdg.org/resources/natural-ventilation>.
- [120] W. Wang, J. Lin, Y. Wang, and G. Chen. “The corrosion of Fe3Al alloy in liquid zinc”. In: *Corrosion Science* 49.3 (2007), pp. 1340–1349. DOI: <https://doi.org/10.1016/j.corsci.2006.10.002>.
- [121] S. Whitaker. “A Simple Geometrical Derivation of the Spatial Averaging Theorem”. In: *Chemical Engineering Education* Winter (Dec. 1985), 18–21 and 50.
- [122] S. Whitaker. “Flow in porous media I: A theoretical derivation of Darcy’s law”. In: *Transport in Porous Media* 1.1 (Mar. 1986), pp. 3–25. DOI: 10.1007/BF01036523.
- [123] S. Whitaker. “Flow in porous media II: The governing equations for immiscible, two-phase flow”. In: *Transport in Porous Media* 1.2 (June 1986), pp. 105–125. DOI: 10.1007/BF00714688.
- [124] S. Whitaker. *The Method of Volume Averaging*. Vol. 13. Kluwer Academic Publishers, 1999.
- [125] R. Zeytounian. “The Boussinesq Approximation”. In: *Asymptotic Modeling of Atmospheric Flows*. Berlin, Heidelberg: Springer Berlin Heidelberg, 1990, pp. 142–176. DOI: 10.1007/978-3-642-73800-5_8.